Exploring the Energy Storage Applications of Transition Metals and Perovskite Based Nanomaterials

THESIS SUBMITTED FOR THE DEGREE OF
DOCTOR OF PHILOSOPHY (SCIENCE)

OF

JADAVPUR UNIVERSITY

By

Kausik Sardar

Index No.: D-7/ISLM/31/2017

School of Materials Science and Nanotechnology
Faculty of Interdisciplinary Studies, Law & Management
Jadavpur University
Kolkata, India

2024

CERTIFICATE FROM THE SUPERVISOR

This is to certify that the thesis entitled "**Exploring the energy storage applications of transition metals and perovskite based nanomaterials**" submitted by Sri Kausik Sardar, who got his name registered on **18/09/2017** for the award of **Ph.D. (Science) degree of Jadavpur University** is absolutely based upon his own work under the supervision of **Prof. Gautam Majumdar** and that neither his thesis nor any part of the thesis has been submitted for any degree/diploma or any other academic award anywhere before.

G. Majumdar 12.09.2024

(EX) Professor
Dept. of Mechanical Engineering
Jadavpur University, Kolkata-32

Prof. Gautam Majumdar

(Signature of the Supervisor, date with office seal)

"Statement of Originality"

I **Kausik Sardar** registered on **18/09/2017** do hereby declare that this thesis entitled "**Exploring the energy storage applications of transition metals and perovskite based nanomaterials**" contains literature survey and original research work done by the undersigned candidate as part of Doctoral studies.

All information in this thesis have been obtained and presented in accordance with existing academic rules and ethical conduct. I declare that, as required by these rules and conduct, I have fully cited and referred all materials and results that are not original to this work.

I also declare that I have checked this thesis as per the "Policy on Anti Plagiarism, Jadavpur University, 2019", and the level of similarity as checked by iThenticate software is 10%.

Signature of Candidate: Kausik Sardar

Date: 12.09.2024

Certified by Supervisor:

(Signature with date, seal)

Prof. Gautam Majumdar

Department of

Mechanical Engineering,

Jadavpur University,

Kolkata-700032

12.09.2024

(Ex) Professor
Dept. of Mechanical Engineering
Jadavpur University, Kolkata-32

To my beloved

Ma-Baba . . .

To my beloved wife

Sagarika Mondal . . .

"Knowledge is the light that guides the way to progress and success. It must be used with wisdom and vision."

— *Dr. A.P.J. Abdul Kalam*

Acknowledgements

I would like to express my deepest gratitude to those who have supported and guided me throughout the journey of my PhD.

First and foremost, I am profoundly grateful to my advisors, Prof. Gautam Majumdar and Prof. Kalyan Kumar Chattopadhaya, for their unwavering support, insightful feedback, and continuous encouragement. Your guidance has not only shaped this thesis but has also profoundly influenced my academic and professional growth.

I extend my heartfelt thanks to the members of my dissertation committee, for their time, expertise, and constructive critiques. Your diverse perspectives have greatly enriched my research and contributed to its depth and quality.

I am also indebted to Thin film and Nano science Laboratory, Jadavpur University for providing the resources and environment necessary for my research. I'd like to thank Dr. Subhasish Thakur for his valuable assistance during every stage of my Ph.D. journey. He reminded me more of a brother than a colleague. Few co-authored reports can truly capture the essence of our friendship. I must state Dr. Nripen Besra's name clearly here. He has been by my side from the day I arrived in the Nanotechnology department. He is not just my colleague, but also a trusted friend. I would like to thank Dr. Tufan Paul and Mr. Kausik Chanda for their invaluable assistance in carrying out my research. Their collaboration and camaraderie made the research process both enjoyable and intellectually stimulating. I am really grateful to Dr. Soumen Maiti, Dr. Diptonil Baneerjee, Dr. Partha Bairi, Dr. Pulak Pal, Dr. Nirmalya Sankar

Das, and all of my lab mates and younger colleagues for their continuous cooperation and helpful talks. I want to thank Dr. Bikram Kumar Das, Mr. Arnab Das and Dr. Souvik Bhattacharjee for their assistance with my work.

To my family and friends, your unwavering support and understanding have been a source of strength. I am particularly grateful to my parents, my beloved wife and my younger brother, whose patience, encouragement, and belief in me have been a constant source of motivation.

Finally, I would like to acknowledge University Grants Commission (UGC) for their financial support, which made this research possible.

Thank you all for your contributions to this journey. This thesis is as much a reflection of your support and belief in me as it is of my own efforts.

September 2024

School of Materials Science & Nanotechnology,

Jadavpur University, Kolkata –700032, India. **Kausik Sardar**

Contents

Abstract

We are searching for green renewable energy sources like solar and wind energy to support sustainable growth because of the world's ongoing use of fossil fuels and rising environmental degradation. In the current period of civilisation, innovative, affordable, and environmentally friendly alternative energy storage solutions are required; supercapacitors fall into this category. In the race against rechargeable batteries, supercapacitors still face significant challenges in maintaining high power with high energy density and long cyclic stability. Because of their reversible faradic processes for charge storage, transition metal oxides (TMOs) can meet the aforementioned requirements with high capacitance. Mixed transition metal oxides (MTMOs) and their hybrid with nanocarbons as electrode material should improve TMOs' sluggish redox reaction rate and poor inherent electrical conductivity. Rich redox reactions and enhanced electronic conductivity are provided by MTMOs, which are advantageous for electrochemical energy storage applications. High surface area and porosities can be achieved by carbonization. One of the most exciting new materials, perovskite, has a big impact on energy applications. In this dissertation, the synthesis of TMOs, MTMOs and their hybrid with nanocarbon material like amorphous carbon nanotubes (aCNTs) along with perovskite material is discussed in detail, since their well-controlled shape aided electron transmission and therefore increased electrochemical energy storage.

The main idea of supercapacitors is introduced in this dissertation, along with the ways that TMOs, MTMOs, and their hybrids with nanocarbons and perovskites are constantly developing as supercapacitive electrode materials. After then, a detailed discussion of the issues raised throughout the research period and its successful resolution has taken place. An easy method for synthesising TMOs and its hybrid with nanocarbon material has been developed here in the first experimental attempt. In this study, amorphous carbon nanotubes ($MnWO_4$-aCNT) and manganese tungstate hybrids are realised and used as solid-state asymmetric supercapacitor

electrodes. The budgetary solid-state reaction was used to synthesise aCNTs on a large scale at low temperature. $MnWO_4$ nanorods were then added to the walls of these nanotubes by an in situ hydrothermal approach that did not require surfactants. High specific capacitance of 542.18 Fg^{-1} at a scan rate of 2 mVs^{-1} was delivered by the produced electrode based on this hybrid over nickel foam, which is significantly better than the same of other structural units separately. Even after 15,000 cycles of operation, this $MnWO_4$-aCNT based electrode demonstrated a high-rate capacity with around 100% capacitance retention and almost 100% coulombic efficiency. On this combination, the solid-state asymmetric supercapacitor achieved a power density of 893.6 W kg^{-1} and an energy density of 5.6 Wh kg^{-1}. The hybrid sample's significantly improved electrochemical behaviour is explained by its increased surface area, which results in a higher number of redox reaction sites, as well as the beneficial synergistic effect of the building blocks.

In second experimental work Our findings describe the synthesis of $MnWO_4$ nanostructures with varying aspect ratios achieved by careful adjustment of reaction temperature and reaction duration. One direct application of size control nanostructures is as supercapacitor electrode material. X-ray diffraction, field emission scanning electron microscopy, and Raman spectroscopy were among the characterisation techniques used to examine the effects of reaction parameters, specifically growth time and processing temperature, on the size of $MnWO_4$ nanorods. The results indicate that all of the samples have very good charge storage characteristics, with the greatest specific capacitance values recorded at 2 mVs^{-1} and 1 Ag^{-1}, respectively, being 455.07 Fg^{-1} and 239.07 Fg^{-1}. Additionally, even after 10,000 charge-discharge cycles, the matching sample exhibits a notable capacitance retention of approximately 94%, demonstrating the electrode's great electrochemical stability. Density functional theory study conducted theoretically indicates that the remarkable charge storage

potential of the synthesised $MnWO_4$ is mostly due to the higher quantum capacitance and the existence of electronic states close to the Fermi level.

In third experimental work we present the use of $CsPb_2Br_5$ as a material for supercapacitor electrodes. A specific capacitance of 886 Fg^{-1} is displayed by the $CsPb_2Br_5$-based manufactured electrode at a scan rate of 2 mVs^{-1}. It showed a Columbic efficiency of around 99% after 5000 operating cycles, and it kept 76% of its initial specific capacitance. The observed capacitive behaviour is explained in detail and the charge transfer mechanism is investigated using Mott-Schottky analysis based on real C'(ω) and imaginary C''(ω) capacitances as a function of frequency. This important perspective from the dissertation may encourage future scholars to work on some creative ideas that could advance emerging alternative energy technology.

List Of Publications

1. Amalgamation of $MnWO_4$ nanorods with amorphous carbon nanotubes for highly stabilized energy efficient supercapacitor electrodes, Kausik Sardar, Subhasish Thakur, Soumen Maiti, Nripen Besra, Partha Bairi, Kausik Chanda, Gautam Majumdar, Kalyan Kumar Chattopadhyay, *Dalton Transactions*, 2021, *50*(15), 5327-5341.
2. Synthesis of different manganese tungstate nanostructures for enhanced charge-storage applications: theoretical support for experimental findings, Kausik Sardar, Subhasish Thakur, Arnab Das, Nripen Besra, Diptonil Banerjee, Gautam Majumdar and Kalyan Kumar Chattopadhyay, *Physical Chemistry Chemical Physics*, 2022, *24*(46), 28271-28282.
3. Two-dimensional layered $CsPb_2Br_5$ perovskite as high-performance electrode material for supercapacitor application, Kausik Sardar, Tufan Paul, Soumen Maiti, Subhasish Thakur, Aditi Sahoo, Gautam Majumdar and Kalyan Kumar Chattopadhyay, *MRS Communications*, 2023, *13*(6), 1131-1138.
4. Incorporation of V_2O_5 nanorods into perovskite photodetectors as an alternative approach to enhance device performance: a step towards stability against ambient water species, Nripen Besra, Kausik Sardar, Soumen Maiti, Pranab Kumar Sarkar, Tufan Paul, Subhasish Thakur, Gautam Majumdar, Kalyan Kumar Chattopadhyay, *Dalton Transactions*, 2020, *49*(44), 15788-15799.
5. Shape-shifting via salt crystallization: conversion of a nanostructured polymer into a site-selective nitrogen-doped carbon sheet with enhanced supercapacitive performance, Partha Bairi, Kausik Sardar, Kausik Chanda, Madhupriya Samanta, Subhasish Thakur, Karamjyoti Panigrahi, Saikat Sarkar, Tufan Paul, and Kalyan Kumar Chattopadhyay, *ACS Applied Energy Materials*, 2020, 3(6), 5984-5992.
6. $CH_3NH_3PbI_3$ as a radio frequency decoupling capacitor: interplay between Maxwell–Wagner polarization and a pseudo inductive response, Nripen Besra, Kausik Sardar, Nilesh Mazumder, Souvik Bhattacharjee, Anjan Das, Bikram Das, Saikat Sarkar, Kalyan Kumar Chattopadhyay, *Journal of Physics D: Applied Physics*, 2021, *54*(17), 175105.

7. Nanoporous nitrogen-doped graphitic carbon hollow spheres with enhanced electrochemical properties, Partha Bairi, Kausik Sardar, Madhupriya Samanta, Kausik Chanda, Kalyan Kumar Chattopadhyay, *Materials Chemistry Frontiers*, 2021, *5*(20), 7645-7653.
8. New class of trimetallic oxide hierarchical mesoporous array on woven fabric: electrode for high-performance and stable battery type ultracapacitor, Subhasish Thakur, Soumen Maiti, Kausik Sardar, Nripen Besra, Partha Bairi, Karamjyoti Panigrahi, Kausik Chanda, Tufan Paul and Kalyan Kumar Chattopadhyay, *Journal of Energy Storage*, 2021, *35*, 102249.
9. Hierarchical assembly of MnO_2 nanosheet on $CuCo_2O_4$ nanoflake over fabric scaffold for symmetric supercapacitor, Kausik Chanda, Soumen Maiti, Samrat Sarkar, Partha Bairi, Subhasish Thakur, Kausik Sardar, Nripen Besra, Nirmalya Sankar Das and Kalyan Kumar Chattopadhyay, *ACS Applied Nano Materials*, 2021, *4*(2), 1420-1433.
10. Site specific nitrogen incorporation in reduced graphene oxide using imidazole as a novel reducing agent for efficient oxygen reduction reaction and improved supercapacitive performance, Dipayan Roy, Saikat Sarkar, Kaustav Bhattacharjee, Karamjyoti Panigrahi, Bikram Kumar Das, Kausik Sardar, Sourav Sarkar, Kalyan Kumar Chattopadhyay, *Carbon*, 2020, *166*, 361-373.
11. Charge-Carrier Dynamics and Relaxation in Cs_2SnI_6 Perovskite for Energy Storage: Existence of Anharmonic Rattling-Assisted Polaron Dynamics, Moumita Ghosh, Pulak Pal, Tufan Paul, Soumen Maiti, Souvik Bhattacharjee, Kausik Sardar, Aditi Sahoo, Aswini Ghosh, Kalyan Kumar Chattopadhyay, *Physical Review Applied*, 2023, *20*(5), 054032.
12. Morphology tuned electrochemical properties of $CuBO_2$ nanostructures, Pulok Das, Nirmalya Sankar Das, Kausik Sardar, Brahami Das, Ashadul Adalder, Kalyan Kumar Chattopadhyay, *Materials Chemistry and Physics*, 2023, *301*, 127642.
13. Hierarchical Heterostructure of MoS_2 Flake Anchored on TiO_2 Sphere for Supercapacitor Application, Kausik Chanda, Subhasish Thakur, Soumen Maiti, Anubhab Acharya, Tufan Paul, Nripen Besra, Saikat Sarkar, Anjan Das, Kausik Sardar and Kalyan Kumar Chattopadhyay, *AIP Conference Proceedings*, 2018, 1953, 030138.

14. Efficient blue emission from ambient processed all-inorganic $CsPbBr_2Cl$ perovskite cubes, Tufan Paul, Biplab Kumar Chatterjee, Soumen Maiti, Nripen Besra, Subhasish Thakur, Saikat Sarkar, Kausik Chanda, Anjan Das, Kausik Sardar and Kalyan Kumar Chattopadhyay, *AIP Conference Proceedings*, 2018, 1942, 120026.

15. Luminescence behaviour of room temperature chemical processed all-inorganic $CsPbCl_3$ perovskite cubes, Tufan Paul, Biplab Kumar Chatterjee, Soumen Maiti, Nripen Besra, Subhasish Thakur, Saikat Sarkar, Kausik Chanda, Anjan Das, Pranab Kumar Sarkar, Kausik Sardar and Kalyan Kumar Chattopadhyay, *AIP Conference Proceedings*, 2018, 1953, 030085.

16. Low dimensional $CH_3NH_3PbBr_3$ cubes for persistent luminescence: Energy variation of electron excitation, Nripen Besra, Tufan Paul, Subhasish Thakur, Saikat Sarkar, Kausik Sardar, Kausik Chanda, Anjan Das and Kalyan Kumar Chattopadhyay, *AIP Conference Proceedings*, 2018, 1942, 120027.

17. Room temperature solution processed low dimensional $CH_3NH_3PbI_3$ NIR detector, Nripen Besra, Tufan Paul, Pranab Kumar Sarkar, Subhasish Thakur, Saikat Sarkar, Anjan Das, Kausik Chanda, Kausik Sardar and Kalyan Kumar Chattopadhyay, *AIP Conference Proceedings*, 2018, 1953, 030210.

Paper Presented in National/ International Conferences

1. Impact of Water Adsorbates on Field Electron Emission from Vanadium Oxide Nanorods, National Conference on Recent Developments in Nanoscience & Nanotechnology ***NCRDNN-2019***, organized by School of Materials Science and Nanotechnology, Jadavpur University, 29-31st January, 2019.

2. Low temperature processed $CoGeO_4$@ZnO core shell for electron field emission, International Conference on Condensed Matter Physics ***IEMPHYS-19***, organized by Institute of Engineering & Management in collaboration with IEM-Society of Physics Student Chapter (AIP), Kolkata, 14^{th}- 16^{th} November, 2019.
3. Designing of high performance pseudocapacitive sulfurized $NiWO_4$ material for advanced supercapacitors, XX^{th} INTERNATIONAL WORKSHOP ON THE PHYSICS OF SEMICONDUCTOR DEVICES ***IWPSD-2019***, organized at Novotel Hotel & Residences, Kolkata, 17-20^{th} December, 2019.
4. Aspect ratio controlled $MnWO_4$ nanorods for supercapacitor application, 6^{th} International Conference on Nanoscience and Nanotechnology ***ICONN-2021***, organized by Department of Physics and Nanotechnology, SRM IST, India, February 1-3, 2021.
5. Bipolar Resistive Switching and Synaptic Characteristics of V_2O_5-Organic Composite Based Flexible Memristor for Neuromorphic Computing Application, International Conference on Advanced Materials and Mechanical Characterization ***ICAMMC-2021***, organized by Department of Physics and Nanotechnology and Department of Mechanical Engineering, SRM IST, India 2-4 December, 2021.

Chapter 1: Introduction & Objectives

1.1 Background

Global energy consumption is rapidly increasing due to technological advancements, population growth, and other factors [1–3]. Energy consumption in a typical U.S. home has already doubled since 1980 [4], with the International Energy Agency (IEA) predicts it will double again by 2022 and treble by 2030 [1]. Over the past few decades, the steadily declining availability of fossil fuel energy sources, such as coal and petroleum, makes the development of suitable, high-performing renewable energy sources is of utmost importance [5–9]. Despite their widespread availability, growing environmental effect, and worry over climate change, researchers have discovered alternative energy sources like solar power, wind energy, hydro power, tidal power and biogas. There are unique difficulties associated with these energy sources. While wind and tidal energy sources are intermittent and have limited geographical availability, sources like solar energy have extremely low efficiency. Proper energy storage is essential to obtaining consistent and dependable power from these sources. As the world moves towards electric mobility, electrochemical storage technologies like batteries, fuel cells, and supercapacitors are becoming more popular [10–14]. Among all, supercapacitors are an environmentally safe, non-toxic, and economically viable renewable energy source with fast charge discharge process, high energy density, and long-life cycle stability that has shown to be the best of its kind [15]. Supercapacitors, which absorb and release charge at a high rate of acceleration, are regarded as one of the major energy storage systems because of their effective electrical charge storage capacity [16,17]. Supercapacitors are commonly referred to by several names, including electrical double layer capacitors (EDLCs), ultracapacitors, gold capacitors, electrochemical capacitors, pseudocapacitors, power capacitors, and power caches. The remarkable qualities of supercapacitors and their potential uses in a variety of domains have drawn researchers from a range of disciplines [18,19]. Hence, supercapacitors have gained recognition as revolutionary energy conversion and storage devices that have the potential to

function as power backup sources in numerous fields. Electrochemical supercapacitors (ECs) are divided into two groups based on their charge storage mechanisms. 1) Electrochemical Double Layer Capacitors (EDLCs) and 2) Pseudocapacitors (PCs). The superior performance of Supercapacitors (SCs) over conventional capacitors and batteries can be attributed to their unique charge storage mechanism, which allows for faster charging and discharging times (SCs: 1-10 s vs. Battery: 0.5-5 h), higher power densities (SCs: 500–10,000 WKg^{-1} vs. battery < 1000 WKg^{-1}), longer lifespans (SCs > 500,000 h vs. Battery: 500–1000 h), superior reversibility (90–95% or higher), and safer operation [20–23]. The primary challenge for SCs replacing battery technology is low energy density (1-10 $WhKg^{-1}$ vs. Battery: 10-100 $WhKg^{-1}$) [24–26]. The performance of the SCs is represented on a graph coined as the "Ragone plot" in Figure 1.1. This type of graph shows the power densities and energy densities of various energy storage technologies on the vertical and horizontal axes, respectively.

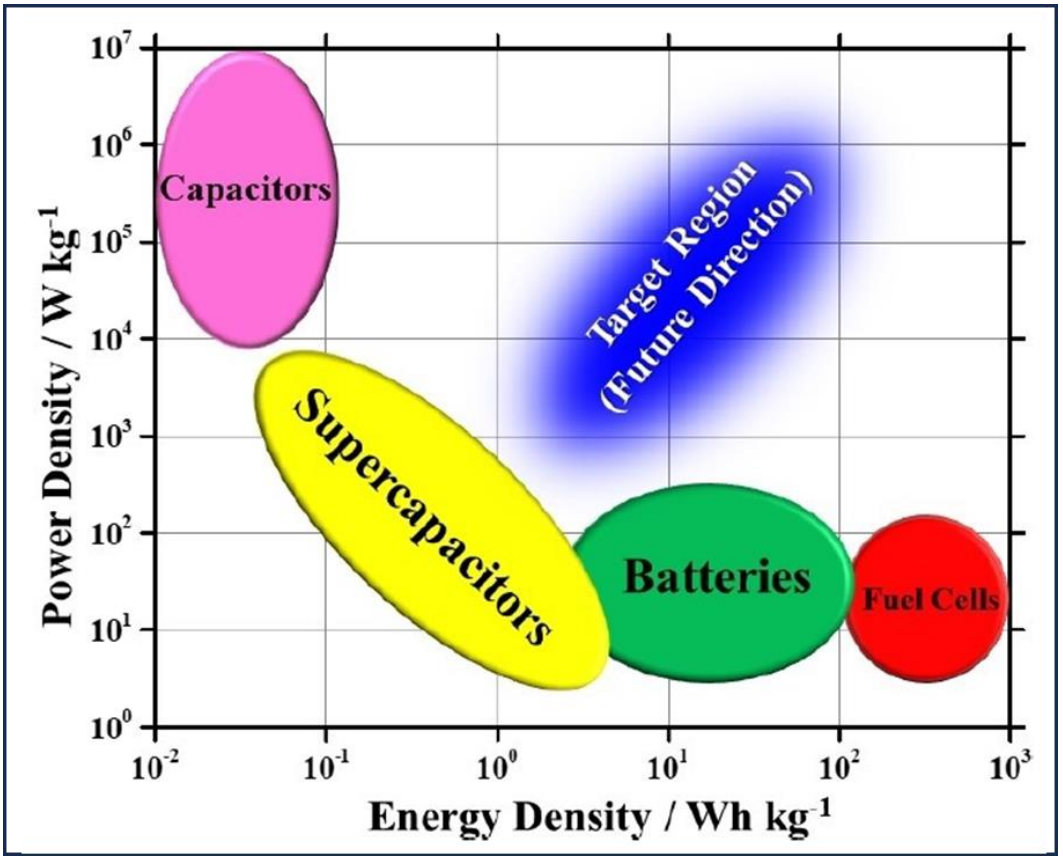

Figure 1.1: A Ragone plot for various energy storage systems[27]**.**

Figure 1.1 shows the SCs reside between batteries and conventional capacitors [22]. Supercapacitors are still unable to match the energy density of mid- to high-end batteries and fuel cells, despite having larger capacitances than ordinary capacitors.

1.2 Supercapacitors: The journey so far

Supercapacitors, also known as Electrochemical Capacitors, have received substantial research during the last few decades [22]. Supercapacitors, with their high-power density, long cyclic stability, and great reversibility, have shown promise in alternative energy storage technology. Supercapacitors are now widely used in a wide range of applications, such as consumer electronics, grid balancing, transportation, aerospace and military, and power backup, to enhance, protect, and/or replace batteries [17,28–33]. H. I. Becker of General Electric Company invented a high surface-area carbon-coated metallic current collector in an aqueous H_2SO_4 solution, resulting in the first SC patent in 1957. In 1969, the Standard Oil Company of Ohio (SOHIO) became the first to commercialize SCs [17,29–31]. SOHIO was unable to commercialise the innovation. The Nippon Electric Company (NEC) was granted a license by SOHIO to utilize this double-layer capacitor technology in 1971. NEC was able to produce the first double-layer capacitor for commercial use, which they called a "supercapacitor" [34]. Between 1973 and 1990, Russian and Japanese businesses manufactured supercapacitor cells with high energy densities ($WhKg^{-1}$) and power densities (WKg^{-1}). It became evident in the 1990s when SCs were employed in conjunction with rechargeable batteries to provide additional power to electric and hybrid electric vehicles (HEVs). By accumulating and storing regenerative braking energy, these SCs powered vehicle acceleration. The applications of SCs have grown dramatically during the last few decades. These include improving the production process and developing electrolyte and electrode materials even further. In 1978, Panasonic developed a special kind of supercapacitor known as a "Gold capacitor" that was used in memory backup systems. In the mid-1980s, Panasonic started

manufacturing button-cell capacitors in 1/2 and 1/3 farad (F) sizes. Panasonic started manufacturing larger SCs in the 1990s, including the 470F, 2.3V, and 1500F, 2.3V. In 1982, Pinnacle Research Institute (PRI) designed the first high-power double-layer capacitors known as "PRI Ultracapacitors" by using metal oxide in the electrode.

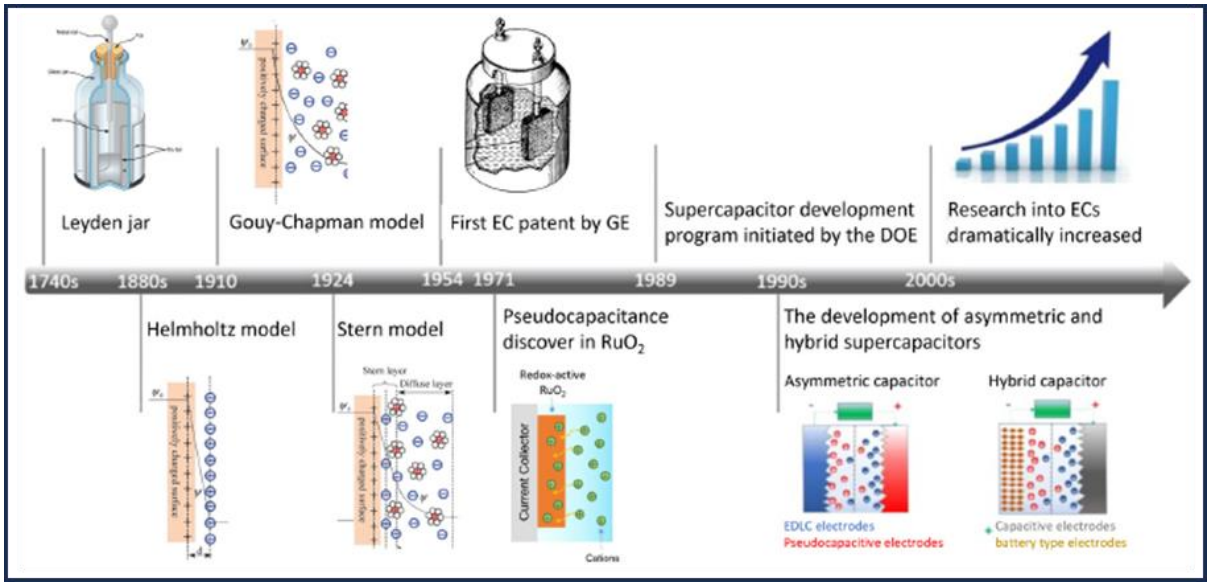

Figure 1.2: A historical chronology of the development of supercapacitors [34]

B. E. Convey developed pseudocapacitors, a novel concept in charge storage mechanism, between 1975 and 1981. It was based on rapid and reversible redox reactions adjacent to the electrode surface. RuO2 was investigated by Convey as a pseudocapacitive substance. The first ideal pseudocapacitor was the ruthenium oxide (RuO2) electrode-based device with long cycle life, significant reversibility, and capacitive behaviour [35,36]. In 1987, ELNA began producing "Dynacap" double-layer capacitors. Maxwell Laboratories created the Ultracapacitor Development Programme in 1992 as part of a study on hybrid electric cars conducted by the US Department of Energy [37]. In light of the expanding global demand for alternative energies, several businesses are already producing supercapacitors. Electric double-layer capacitor (EDLC) components have been created by companies such as Panasonic, NEC, Epcos, ELNA, Cooper, and AVX in Japan and America. Additionally, integrated modules containing voltage-balancing circuitry are produced by companies such as Evans and Maxwell.

For use in electric vehicle and power quality development applications, ESMA Russia provides a variety of EDLC module types. Modern energy harvesting applications for commercial supercapacitors include standby power for random access memory devices, uninterruptible power supplies for computers, and energy harvesters to gather and store solar energy from solar cells [38,39]. Also, commercial supercapacitors are a major component of solid-state drives (SSD), cell-phones, electric hybrid cars, electric tools, and communication equipment. Table 1.1 represents some features of the supercapacitors that are available in global market.

Table 1.1: Supercapacitor (SC) features that are marketed globally [40]

Manufacturer companies	Voltage (V)	ESR (mΩ)	Capacitance (F)
PowerStor	16.20	7.00	65
Yunasko	2.75	0.11	1275
Asahi Glass	2.75	2.50	1375
Ioxus	2.70	0.54	2000
LS Mtron	2.80	0.25	3200
NessCap	2.70	0.30	3640

1.2.1 Supercapacitors and Batteries: A Comparison

A supercapacitor is a high-capacity capacitor with an energy density intermediate between normal capacitors and batteries. It has a higher power density than batteries. The key problem is replacing batteries in power systems with supercapacitors, which have the potential to charge and discharge in seconds and retain charging capacity over time. Supercapacitors may charge/discharge order of 10^2 or 10^3 times more than batteries, which eventually experience "charging fatigue" due to energy storage and release via chemical reaction. Figure 1.3 indicates that supercapacitors have a rapid charge and discharge cycle, whereas batteries discharge at a

consistent rate. The researchers' long-term goal is to replace batteries with supercapacitors in electric vehicles, smartphones, and other devices, based on the supercapacitor's ability to charge/discharge in seconds as well as retain charging capacity over time.

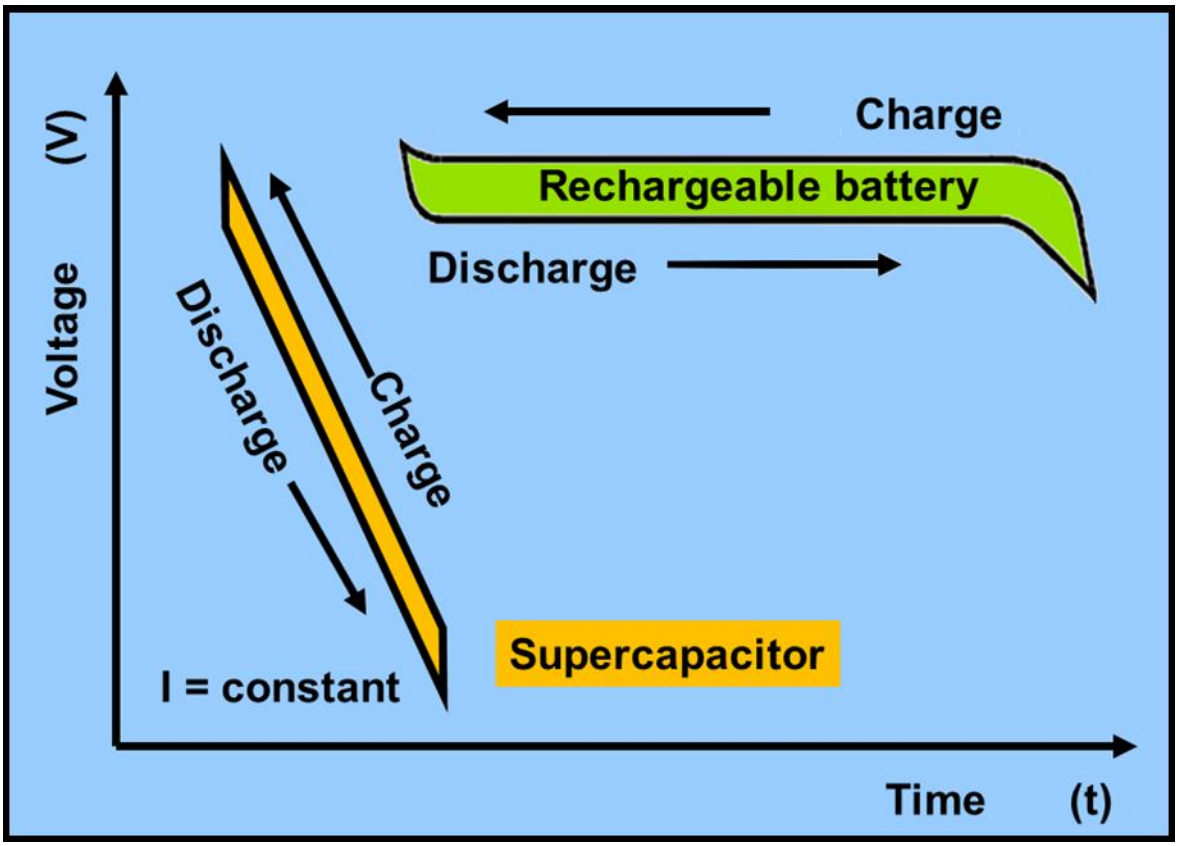

Figure 1.3: Charge-discharge Characteristics curve between Supercapacitor and battery (*Wikimedia Commons*).

Supercapacitors outperform batteries in a number of different ways in addition to having higher power densities, including long cycling lives, high efficiency, high performance stability, and excellent operational safety. The fact that there is always a linear voltage increase with constant current charge (or reduction upon discharge), with the charge stored (released) from supercapacitor electrodes, is another important electrochemical trait that sets supercapacitors apart from batteries, as depicted in Figure 1.4. Supercapacitors often exhibit a potential-independent capacitance in response to potential scanning. As a result, during charge and discharge operations, a supercapacitor's CV curve should retain a rectangular form and the

current should be almost constant. In contrast, batteries exhibit distinct and noticeable peaks with noteworthy Faradaic responses. A supercapacitor's galvanostatic charge/discharge (GCD) curve has a sloping shape with a constant slope value. Comparatively, during a constant voltage stage, a battery usually displays a quite flat charge/discharge plateau. Supercapacitors must be used with a DC-DC converter in order to control and stabilise the output voltage for applications that demand a steady output voltage. Because of this variation in the charge-storage process, the energy stored in these two types is defined differently and has a distinct unit (capacitance vs. capacity).

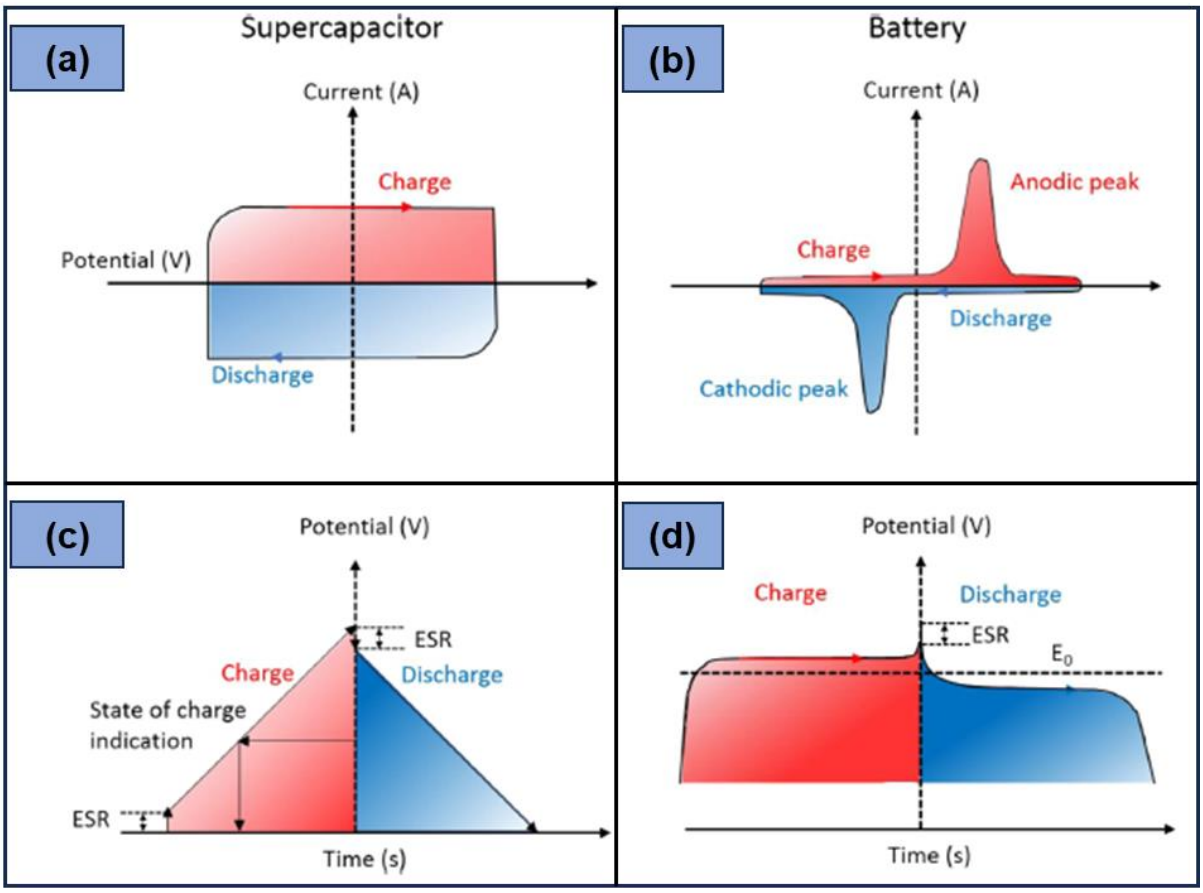

Figure 1.4: cyclic voltammogram curves (a, b) and galvanostatic charge-discharge curves (c, d) comparison for a supercapacitor and a battery [34].

1.2.2 Fundamental Principle of Supercapacitors

Supercapacitors store energy in an electric double-layer (EDL) at the electrolyte-electrode interface, while normal capacitors store energy on the dielectric-separated electrode surface. Electrochemical capacitors typically acquire charges at the electrolyte and electrode solution contact. Charges are gathered into an electric double layer separated by a few Angstroms. Figure 1.2 illustrates how a basic electrochemical capacitor stores energy. A typical capacitor consists of two conducting electrodes separated by a dielectric [41].

1.2.3 Classification of Supercapacitors

Supercapacitors can be divided into three categories: EDLC, pseudocapacitor, and hybrid capacitor. These classes are characterised by their specific charge storage method [42]. Figure 1.5 illustrates the charge storage technique for supercapacitors.

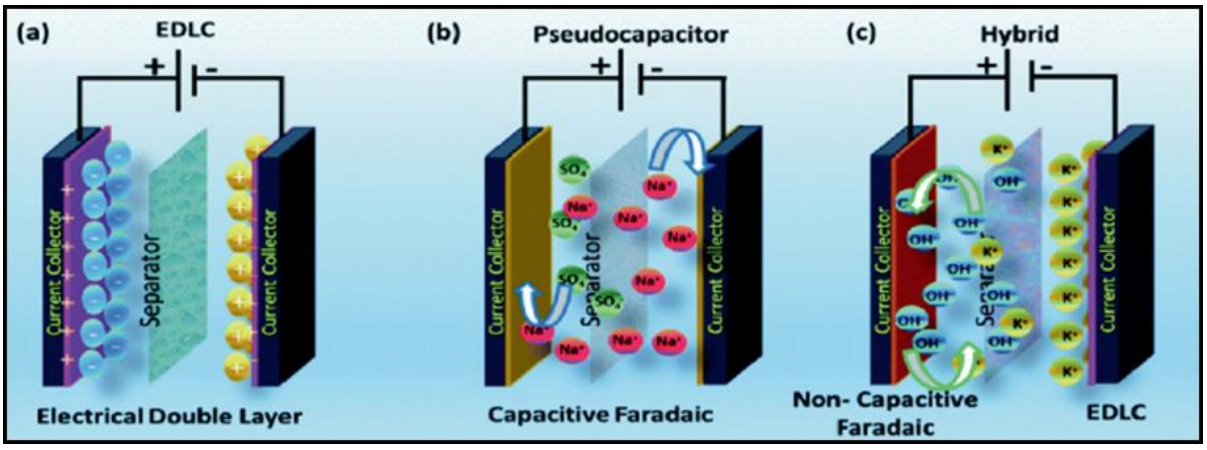

Figure 1.5: Schematic diagram of Charge storage mechanism of (a) EDLCs (b) Pseudocapacitors and (c) Hybrid supercapacitors [43].

There are several charge storage techniques, including faradic, non-faradic, and a combination of both. EDLCs store charges using a non-faradic process and are composed of carbon-based materials [44,45]. Pseudocapacitors store charges through a faradic process on the surface or in the bulk of active material. Pseudocapacitors are constructed of metal oxides and conductive polymers [46]. Hybrid capacitors work in both faradic and non-faradic modes. Hybrid

capacitors can be created by combining carbon-based materials with conducting polymers, metal oxides, or both [47]. Figure 1.6 depicts different forms of supercapacitors, including classes and sub-classes. The charge storage mechanisms in SCs are described in detail below.

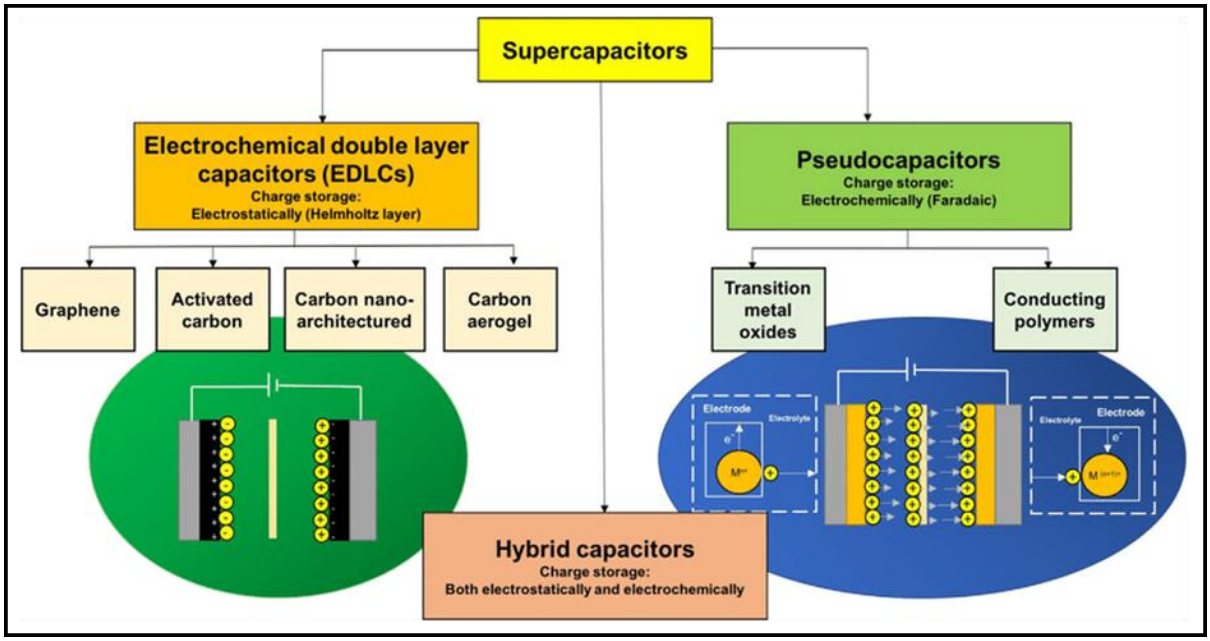

Figure 1.6: Different forms of supercapacitors [48].

1.2.4 Charge storage mechanism in EDLCs:

An EDLC is made up of two carbon-based electrodes, a separator, and an electrolyte. A boundary among two separate constituents or phases creates an interface. EDLCs store energy by adsorbing and desorbing ions at the electrode/electrolyte interface, resulting in a double layer of charges on the electrode surface [49]. EDLCs store charge at nanoscale distances, enabling rapid charging and discharging [50]. Compared to traditional dielectric capacitors, SCs based on the EDLC mechanism offer a significantly larger energy storage capacity because of their large interfacial area and atomic-scale charge separation distances. Surface electrode charges are formed through surface dissociation and ion adsorption from electrolyte and crystal lattice defects. These methods rely on electrostatic surface charges [51]. EDLC electrodes require high electrical conductivity and a large specific surface area. As was previously

established, non-Faradaic reactions do not alter the chemical composition of the electrolyte or electrode because there is no charge transfer between them. In the absence of any chemical change, the system is reversible and possesses extremely high cycle stabilities. Up to 10^6 charge-discharge cycles can occasionally be performed by the EDLCs with stable performance characteristics. Nevertheless, electrochemical batteries only have about 10^3 cycle life. Because of its great cycling stability, EDLCs are used in deep-sea or hilly environments that are inappropriate for manual handling.

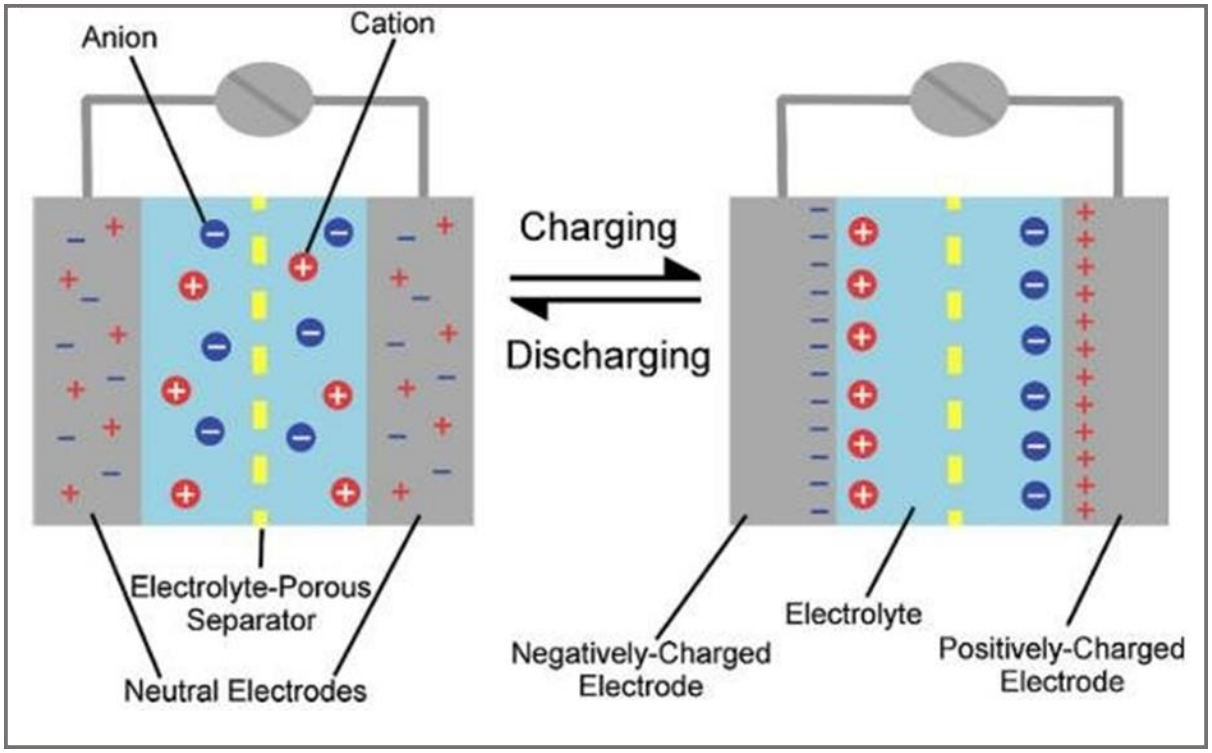

Figure 1.7: Charging Discharging Process of EDLC [52].

In Figure 1.7, electrode particles, such as carbon particles at an electrolyte interface, generate capacitance due to an electric charge surplus or deficit on the electrode surfaces, while ions with the corresponding charge accumulate on the electrolyte side to achieve electroneutrality [53,54]. Electrons transfer from the negative electrode to the positive electrode using an external load during the charging process. In an electrolyte, cations travel towards the negative electrode and anions towards the positive. The opposite procedure occurs during discharge.

This type of ES does not include charge transfers or ion exchanges between the electrode and electrolyte. During charging and discharging, the electrolyte concentration remains constant. As a result, energy is stored in the double-layer contact. More recently, it was discovered that increasing the specific capacitance is more influenced by the pore size and carbon nanostructure than by the specific surface area [55,56]. Different forms of carbon electrodes, including carbon nanotubes, graphene, activated carbon, and carbon aerogel, have been extensively researched and found to be effective [57].

Models to explain the charge storage mechanism in an EDLC:

When a charged object is immersed in a liquid, an electric double-layer structure forms at the electrode-electrolyte interface. To balance the charged surface, counter-charges arise in the liquid and concentrate around it. This solid-liquid interface is explained by three models and hypotheses. The three models are: Helmholtz, Gouy-Chapman, and Stern model.

Helmholtz Model:

The concept of a double layer at the electrode/electrolyte interface was first introduced by Helmholtz in 1853. Positive and negative charges held at the interfaces separated by a distance (in the order of Å) may be thought of as corresponding to a basic parallel plate capacitor in accordance with the Helmholtz model. Figure 1.8a shows the working principle of a double-layer capacitor based on the Helmholtz model.

The differential Capacitance of the EDL Capacitors according to this model is given by

$$C_H = \frac{\partial \sigma^M}{\partial \varphi} = \frac{\epsilon \epsilon_0}{d} \quad (1)$$

$$\text{Where } \sigma = \frac{\epsilon \epsilon_0}{d} \varphi \quad (2)$$

σ^M is the surface charge density.

φ is the voltage drop across the double layer.

ϵ is the dielectric constant of the medium

ϵ_0 is the free space permittivity.

d is the spacing between interlayer.

This model fails because it assumes a constant differential capacitance at the interface. However, for real systems, it is not constant; it fluctuates with potential. As a result, the assumption of constant interlayer spacing is incorrect.

Gouy-Chapman or diffuse model

While the Helmholtz model accurately describes high ionic concentrations, it fails to account for low concentrations. Gouy and Chapman developed the first statistical double-layer theory at the turn of the century. This idea is similar to the Debye-Huckel theory, developed decades later.

The Gouy-Chapman theory is based on the following presumptions and involves a planar metal electrode in contact with an ionic solution:

(1) The metal is a perfect conductor with its excess charge dispersed uniformly on the surface.

(2) The solvent is a dielectric continuum with a dielectric constant of e.

(3) The Poisson–Boltzmann equation determines the distribution of the ions, which are point particles.

This model indicates that the capacitance in the double layer is not constant, but rather varies with the applied potential across the electrode and the electrolyte concentration. As per this model, the electrolyte ions' polarity and tendency to move thermally to randomize the electrolyte ions between the electrode and the electrolyte ions determine the type of electric forces that exist. Consequently, the electrolytic side of the interface forms the diffuse layer of charges, and the average ion separation within the diffuse layer should replace the constant diffuse layer separation in the Helmholtz model. From this, they deduced that the capacitance

depends upon the electrode's applied potential because an increase in applied voltage causes the diffuse layer to become compact.

According to Guoy-Chapman Model, differential capacitance across the double layer interface is given by the following equation:

$$C_G = \frac{d\sigma^M}{d\varphi_0} = \left(\frac{2z^2e^2n^0\epsilon\epsilon_0}{KT}\right)^{1/2} \cosh\left(\frac{ze\varphi_0}{2KT}\right) \quad (3)$$

Where σ^M is the excess of electrons per unit area at the electrode interface.

Where φ_0 is the potential drop at the electrode surface.

Where n^0 is the concentration of ion in the bulk of solution.

Z is the magnitude of charge of the ion

K is Boltzman constant.

T is sbsolute temperature in Kelvin scale.

Since ions are treated as point charges in this model, they can approach the surface of electrode at any point, which causes the capacitance to enhance infinitely with an increase in potential. This behaviour cannot be observed in real systems [49,58].

Stern Modification of Previous Models:

Stern created a new model by modifying the earlier research conducted by Helmhotz, Gouy, and Chapman [58]. Stern postulated in this concept that ions cannot approach the electrode surface endlessly but can approach the surface close to their ionic radius due to their finite sizes. The technique would also depend on the ion's solvation in the solvent, increasing the ionic radius. The outer Helmholtz plane (OHP) is the distance at which the closest approach occurs. The inner Helmholtz plane (IHP) is created by the locus of the centres of the particularly adsorbed ions. Solvated ions can only reach the electrode's surface up to the IHP. The inner compact layer, also known as the stern layer, and the diffuse layer comprise the two distinct ion distribution regions in the modified stern model. Solvated ions, also known as non-

specifically adsorbed ions, can interact with the electrode only through long-range electrostatic forces and are independent of the ions' chemistry. Particularly, the inner Helmholtz plane (IHP) of a compact layer is where deposited hydrated ions are found. The distribution of ions in the electrolyte solution around the electrode is controlled by thermal motion. Point charges are believed to be the ions in the diffuse layer. The experimental value is well-fitted with the double-layer capacity as per the Stern model.

The total double-layer capacitance (C_{DL}) consists of the Helmholtz layer capacitance (C_H) and the Gouy-Chapman layer capacitance (C_{GC}) coupled in series, can be understood by the following equation:

$$\frac{1}{C_{DL}} = \frac{1}{C_H} + \frac{1}{C_{GC}} \tag{4}$$

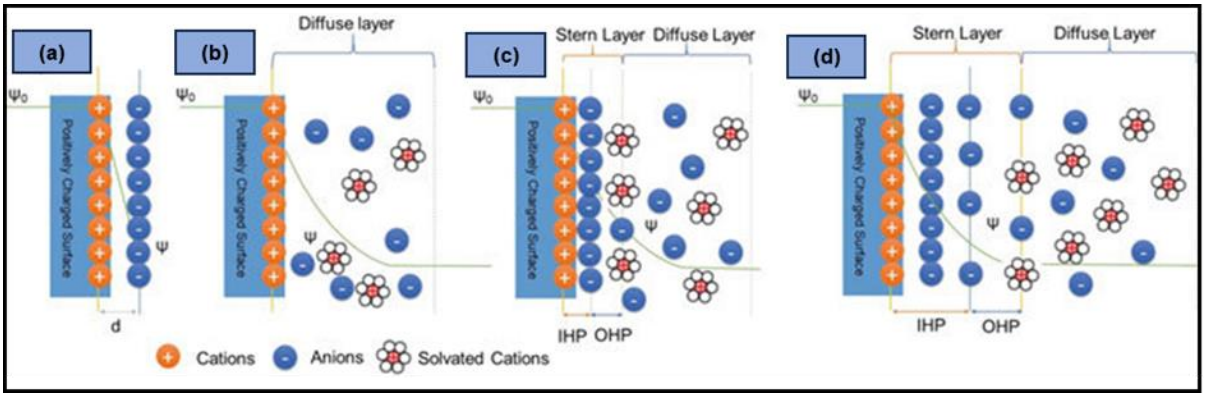

Figure 1.8: (a) Helmholtz model, (b) Gouy-Chapman model, (c) Stern model and (d) modified Gouy-Chapman-Stern model of the EDL at a positively charged electrode[59].

In most real-world scenarios, this equation yields results that are fairly similar to the experimental values. Helmholtz capacitance dominates diffusion layer thickness when the electrolyte concentration is high or the applied potential is high. In contrast, diffusion layer capacitance is higher than Helmholtz capacitance when the electrolyte solution is very diluted or the electrode potential is low because a very loose compact layer forms in these circumstances. The Helmholtz, Gouy-Chapman, and Stern models are shown in Figure 1.8. where Ψ, Ψ_0, IHP, d and OHP stand for the potential, electrode potential, electric double-layer distance, inner Helmholtz plane and outer Helmholtz plane, respectively.

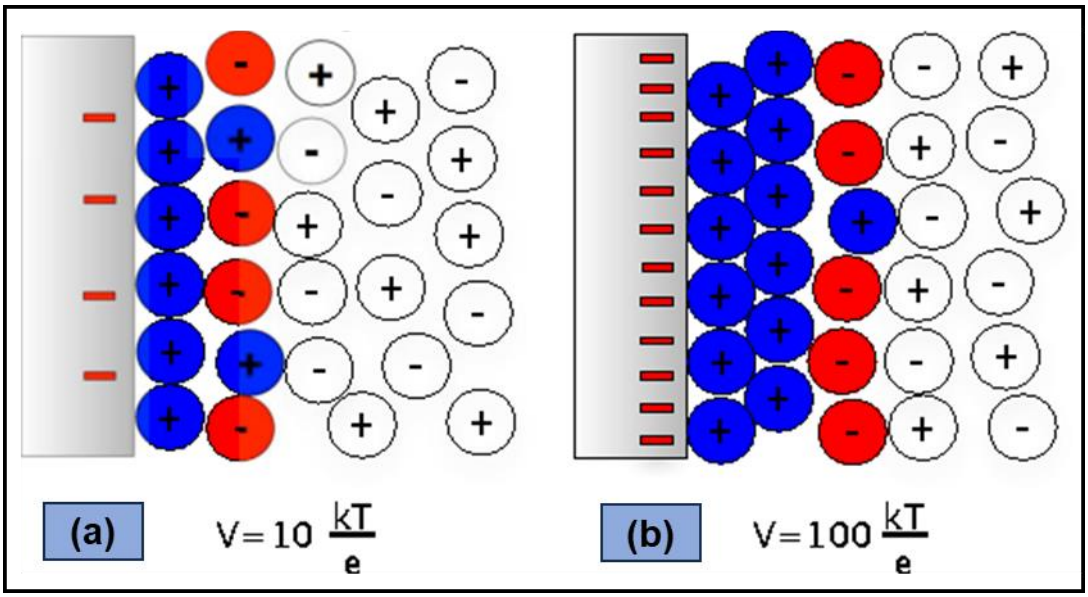

Figure 1.9: Structure of ionic liquid layer (a) at a moderate voltage, $V = 10\ k_B T/e$, and (b) at a high voltage, $V = 100\ k_B T/e$ (*Wikimedia Commons*).

The standard EDLC hypotheses assume that the electrolyte is a diluted solution. These ideas, however, do not apply to ionic liquids or high concentration electrolytes due to considerable short-range Coulomb correlations. Ionic liquids with low potential exhibit a more prominent overscreen effect [60,61]. This is due to the fact that the first layer overscreens again because it displays a smaller net charge of the opposite ion, and the second layer overscreens again because it contains more counter-ions than are required to neutralize the electrode surface. As electro-neutrality is attained, this process keeps going (Figure 1.9a). The overscreening structure is eventually replaced by the condensed layer produced by counter-ions as the voltage rises (Figure 1.9b), reaching complete lattice saturation at a large potential in the process. The repulsive forces between ions with the same charge make it difficult for these ions to accumulate. According to Kondrat et al. [62,63], the image forces exponentially screen out the repulsive forces between ions in the pores, creating the superionic state. Utilising the hybrid reverse Monte Carlo (HRMC) simulation-aided X-ray scattering method, Simon et al. have

verified the existence of the super-ion state in the pores that can only contain a single layer of ions [64].

1.2.5 Charge storage mechanism in Pseudocapacitor

Pseudocapacitance is a Faradic charge storage process that can be either reversible or irreversible. The faradaic charge transfer that occurs between the electrode and the electrolyte is what allows pseudocapacitors to store electric energy. Pseudocapacitance is the ratio of charge acceptance (∇q) to change in potential (∇V) in differential form. It is a sort of capacitance originating from thermodynamic considerations.

$$C = \frac{d(\nabla \mathrm{q})}{d(\nabla \mathrm{V})} \tag{5}$$

The pseudocapacitance mechanism involves the reversible or irreversible oxidation or reduction of a chemical species at the electrode interface, resulting in electron transport. In the irreversible process, new chemical species are created during oxidation/reduction, whereas no new chemical species develop during chemical reactions in the reversible phase. Pseudocapacitors exhibit specific capacitances ten to hundred times greater than those of electric double-layer capacitors. Pseudocapacitors have also been observed to exhibit higher operating voltages than electric double-layer capacitors. Pseudocapacitors function as charge storage devices that resemble battery charging and discharging without changing the phase of the electrode material because the electrochemical process takes place close to the surface, resulting in a thin layer of electrode material that is faradaically active [65,66]. But compared to electric double-layer capacitors, pseudocapacitors typically possess higher energy densities, shorter cycling lives, and lower power densities. The material's pseudocapacitance may be extrinsic or intrinsic [67]. Although extrinsic pseudocapacitance in nanomaterials is only observed under specific conditions, the intrinsic pseudocapacitance is dependent on the particle size and morphologies; this is because the material does not exhibit pseudocapacitive behaviour

in bulk due to phase transformations during ion storage [67–69]. While a surface-related mechanism limits the kinetics of pseudocapacitive materials, diffusion-controlled reactions restrict the electrochemical response of battery electrodes [70]. It is possible to distinguish between battery-type and pseudocapacitive materials using electroanalytical analysis. The followings are the charge storage methods found in pseudocapacitive materials [71]:

i. Redox pseudocapacitance of transition metal oxide

ii. Intercalation pseudocapacitance

iii. Underpotential deposition

Redox pseudocapacitance

Charges are consistently stored via the traditional "redox pseudocapacitance" method, which involves fast and reversible electron transfer and the electrochemical ions adsorption at or near the electrode material's surface. Redox pseudocapacitive materials include conducting polymers like polyaniline and polypyrrole [72,73] and metal oxides like RuO_2 [74], NiO [75].

Intercalation Pseudocapacitance

Intercalation pseudocapacitance occurs when ions are inserted into electroactive material layers or channels without undergoing any phase transformation. Examples of intercalation pseudocapacitive electrodes for SCs include V_2O_5 [76], Nb_2O_5 [77], $TiNb_2O_7$ [78], Li_3VO_4 [79], MXenes [80] and MoS_2 [81]. Figure 1.10 depicts the intercalation/insertion of Li^+ ions into Nb_2O_5.

Underpotential deposition

The formation of monolayers at the metal-electrolyte interface by adsorbed metal ions at a potential lower than the metal's reduction potential is known as underpotential deposition. On the surface of gold (Au), for instance, there are lead ions (Pb^{2+}), while on platinum (Pt), there are hydrogen ions (H^{+}). The diagram in Figure 1.10 shows this method. Other examples of underpotential deposition are hydrogen (H) electrosorption on noble metal substrates as platinum, Rh, or Ru. SCs are rarely made with electrode materials that use the underpotential deposition method because to their unique background and poor specific capacitance [71,82].

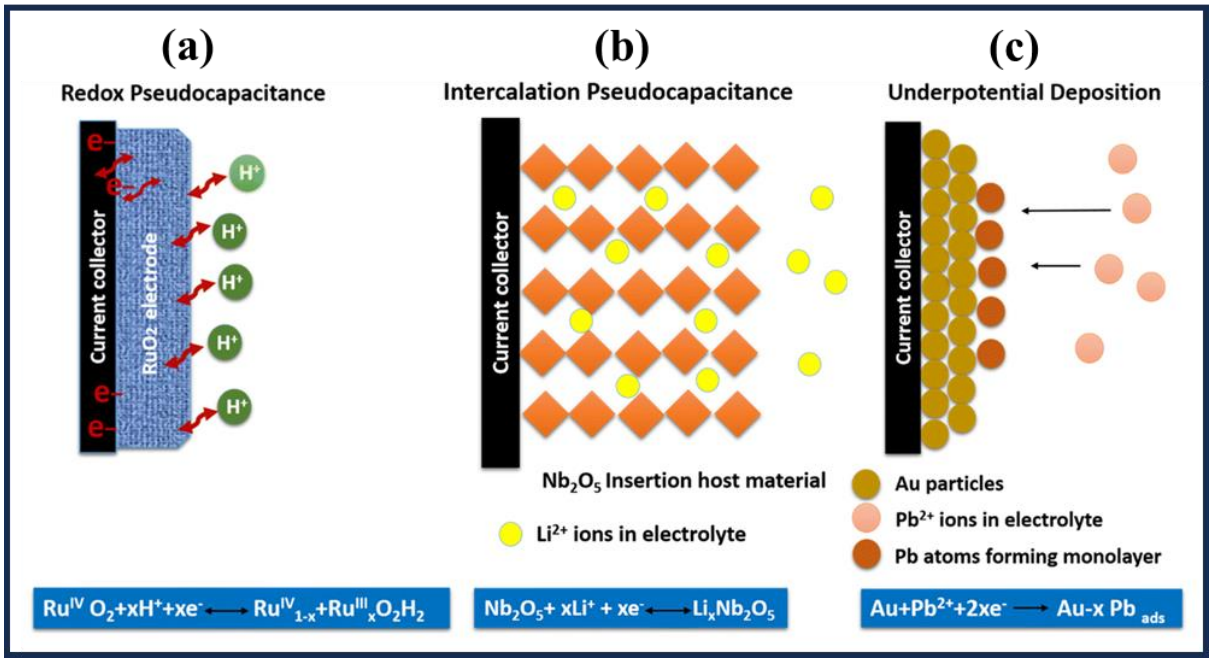

Figure 1.10: Types of storage mechanisms in pseudocapacitors (a) Redox pseudocapacitance (b) Intercalation pseudocapacitance (c) Underpotential deposition [83].

1.2.6 Hybrid Capacitors

A hybrid system can be a good replacement for conventional SCs. HCs aim to maximise the advantages and minimise the disadvantages of EDLCs and pseudocapacitors using both Faradaic and non-Faradaic techniques in order to obtain superior Supercapacitive capabilities. Without losing the cycling stability and affordability that have impeded the deployment of pseudocapacitors, HCs have achieved energy densities and power densities higher than EDLCs.

Research has been conducted on three different types of hybrid capacitors: composite, asymmetric, and battery-type capacitors. These capacitor types can be distinguished by the design of their electrodes. These unusual configurations highlight the need for stronger batteries and higher energy SCs.

Composite electrode

By mixing materials made from carbon with conducting polymer or transition metal-based semiconductors, composite electrodes integrate chemical (Faradaic) and physical (non-Faradaic) charge storage mechanisms into a unitary electrode. In addition to providing a high-surface-area scaffold that enhances the interaction between the pseudocapacitive materials and the electrolyte, the carbon-based materials also facilitate a capacitive double-layer of charge. The use of pseudocapacitive materials through redox-induced Faradaic reactions might further increase the capacitance of the composite electrode [84–87].

Asymmetric hybrids

Asymmetric hybrids integrate both Faradaic and non-Faradaic mechanisms by connecting an EDLC electrode with a pseudocapacitor electrode. A great deal of emphasis has been focused on the combination of transition metal-based semiconductors as the positive electrode and activated carbon as the negative electrode [88–91].

Battery-type hybrid

Similar to an asymmetric hybrid, battery-type hybrids connect two different electrodes. Battery-type hybrids are created by combining a supercapacitor electrode and a battery electrode. This novel arrangement combines battery energy qualities with supercapacitor power, cycle life, and recharge times to fulfil the growing demand for greater energy supercapacitors and batteries. The research has mostly focused on two electrodes: activated

carbon and nickel hydroxide, Lithium titanate (LTO) ($Li_4Ti_5O_{12}$), and lead dioxide [92–96]. Experimental evidence suggests that battery-type hybrids may be able to bridge the void across batteries and supercapacitors. Despite the promising results, most experts concur that further research is needed to fully comprehend the potential of battery-type hybrids.

1.2.7 Evaluation of Parameters of Supercapacitors:

Three-electrode configuration

Supercapacitors with three-electrode arrangement are made up of a working electrode, a reference electrode, and a counter electrode immersed in a solution of electrolyte (Figure 1.11a). In this design, the materials to be examined serve as working electrodes, with the reference electrode employed to assess the working electrode potential. The counter electrode's role is to conduct the current to close the circuit. The primary electrochemical reactions occur between the working and counter electrodes.

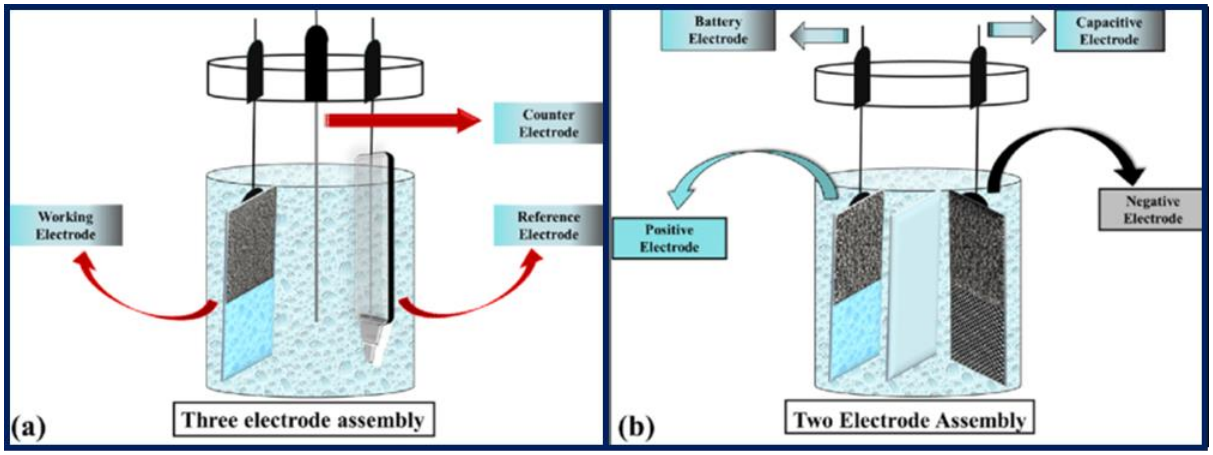

Figure 1.11: (a) Three-electrode configuration and (b) two-electrode configuration.

Two-electrode configuration

The two-electrode cell arrangement offers a better knowledge of the electrochemical process and is a near prototype of the supercapacitor unit cell design for real-world applications (Figure

1.11b). Since the reference and counter electrodes in a two-electrode cell design are shorted, the voltage that is applied to the system is equally distributed across both electrodes.

Using two electrodes in contact with an electrolyte solution and a separator, a single-cell supercapacitor was constructed. Two capacitors in series with one resistance allow for projection of this entire setup. With the anode and cathode capacitances indicated by C_a and C_c, respectively, the RC circuit created by this arrangement is depicted in Figure 1.12. The letter R_s stands for the cell's equivalent series resistance, or ESR. Here is the equation that calculates the cell's total capacitance:

$$\frac{1}{C} = \frac{1}{C_a} + \frac{1}{C_C} \tag{6}$$

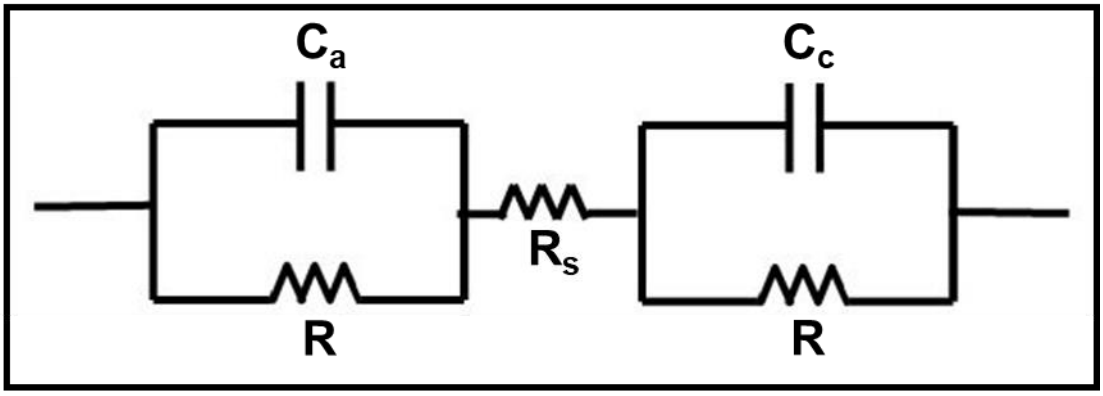

Figure 1.12: RC equivalent circuit illustrating the supercapacitor cell.

The following equation can be used to express the maximum energy stored (E) as well as the power densities given as output.

$$E = \frac{1}{2}CV^2 \tag{7}$$

$$P_{max} = \frac{V^2}{4R_s} \tag{8}$$

Where each parameter has its typical meaning. These three parameters, R_s, C, and V, are all essential for achieving optimal device performance from a supercapacitor cell. The cell potential is determined by the type of electrode and the thermodynamic stability of the solution. In general, aqueous electrolytes cannot produce potential more than 1.2 V. Organic electrolytes

might be employed to get a higher working voltage. ESR is caused by a variety of resistances, including solution resistance, parasitic resistance, and mass transfer resistance of ions in the matrix [97]. In summary, the ESR should be minimised, and a high working cell potential and capacitance value are necessary to provide the best results from the Supercapacitor cell.

1.3 The Objectives and Scope of the Thesis:

Transition metals and perovskite-based materials electrochemistry are becoming more and more popular, which makes them a good option for usage as outstanding electrode materials for energy storage applications and next-generation portable devices. All of these advantages can be obtained from transition metal-based systems because of their availability, low environmental toxicity, high energy state, and several metal ion oxide states. Because of its many oxide states, it can readily give and accept electrons from other molecules. Additionally, because of an even relationship among the pore size at the surface of the electrode and the ionic-size of the electrolyte, these materials have a higher energy density over carbonaceous materials and better electrochemical endurance than polymers. The synthesis, thorough characterisation, and property study of these transition metal oxides (TMOs), perovskite-based nanomaterials, and novel types of nanocarbon materials such amorphous carbon nanotubes (aCNTs) and their hybrid with TMOs will therefore be the main focusses of this research. Direct growth of this TMOs across multiple different nanoforms is a well-known technique compared to bulk composite. The realisation of this kind of hierarchical nanoform frequently leads to distinct interface phenomena, a sizable surface area, several functionalities, and a synergistic influence from each individual that suppresses all individual flaws. Either two transition metal-based systems or carbonaceous and transition metal-based systems can be used for this. Furthermore, composites will be created and thoroughly examined. TMOs often have a lower energy density than ordinary batteries. Compositionally related perovskite may be an attractive alternative in the hunt for future energy materials with device-level performance.

This thesis includes the following research goals:

- Developing wet chemical and hydrothermal synthesis methods for transition metal oxides, aCNTs, and perovskite-based nanomaterials.
- Advanced techniques like as XRD, HRTEM, FESEM, and XPS will be employed to characterise the generated materials to structural and morphological study.
- Synthesised nanomaterials such as aCNTs, TMOs, and perovskites, along with composites, would be used to develop and test structures for unique material properties and novel applications.
- Synthesised nanomaterials will also be examined for energy storage applications by building appropriate electrodes.
- Theoretical models and extensive data analysis will be built to better understand electrical and electronic processes.

1.4 Thesis Structure:

This thesis consists of 7 well-documented chapters focused on research ideas and applications. Chapter 1 introduces supercapacitors in the research track, working principle, and their classification based on charge storage. Their real-life uses are addressed in detail, which serves as the foundation for this thesis.

Chapter 2 provides a literature overview of earlier studies on electrode materials for supercapacitors, as well as an introduction to carbon, TMO and perovskite-based supercapacitors and their limitations, which set the way for MTMO and perovskite-based supercapacitors.

Chapter 3 provides a detailed documentation of the experimental apparatus utilised for the thesis study.

Chapter 4 marks the beginning of the experimental work. This work suggests creating a new

class of hybrids using low-temperature synthesised amorphous CNT and $MnWO_4$. Here, a bulk-scale CNT was developed via an economical technique. The hydrothermal method was used to decorate $MnWO_4$ nanorods using this low temperature. A thorough analysis of the electrochemical characteristics of the pure aCNT, $MnWO_4$, and hybrid samples was done. When compared to the C_s value for the separate building components, the hybrid sample's value is found to be greatly boosted. Electrolyte diffusion is enhanced by the intrinsic porosity of conducting 1D tubular backbone, which facilitates electron transport. The total surface area is greatly increased concurrently when $MnWO_4$ grows over a CNT backbone.

We have synthesised $MnWO_4$ nanostructures with varying aspect ratios in chapter 5 by carefully adjusting the reaction temperature and reaction time. The electrochemical characteristics of the as-synthesised $MnWO_4$ nanostructures have been investigated as an immediate application of the size-controlled nanostructures. The detailed analysis demonstrates that the samples with the longest synthesised times have far higher specific capacitance (Cs) values. It has been found that altering the synthesis conditions significantly affects surface area, which in turn controls the samples' capacity to store charge. As supported by experimental evidence, density functional theory (DFT) discovered that $MnWO_4$ possesses a number of advantageous properties that contribute to the system's ability to function as an effective energy storage material.

Exploring potential materials for sustainable energy generation and storage application has emerged as a significant problem of this century. Perovskite, one of the most promising new materials, has a significant impact on energy applications. Chapter 6 describes a straightforward solution-based approach for synthesising perovskite material $CsPb_2Br_5$ at ambient temperature. We discuss promising findings and advances in our knowledge of electrochemical charging in nanostructured material lead halide perovskite. The contact surface of the $CsPb_2Br_5$ electrode plays an essential role to charge storage within the SC.

Last but not least is Chapter 7, which provides a summary of the entire dissertation as well as a vision for future study directions that may benefit future scholars in this field.

1.5 References:

[1] Chatterjee DP, Nandi AK. A review on the recent advances in hybrid supercapacitors. J Mater Chem A Mater 2021; 9: 15880–918.

[2] Choi H-J, Jung S-M, Seo J-M, Chang DW, Dai L, Baek J-B. Graphene for energy conversion and storage in fuel cells and supercapacitors. Nano Energy 2012; 1: 534–51.

[3] Chen T, Dai L. Carbon nanomaterials for high-performance supercapacitors. Materials Today 2013; 16: 272–80.

[4] Fanara A, Clark R, Duff R, Polad M. How small devices are having a big impact on US utility bills. Environmental Protection Agency and ICF International: Washington, DC 2006.

[5] Wang Y, Qiao M, Mamat X. Nitrogen-doped macro-meso-micro hierarchical ordered porous carbon derived from ZIF-8 for boosting supercapacitor performance. Appl Surf Sci 2021; 540: 148352.

[6] Sun Z, Li F, Ma Z, Wang Q, Qu F. Battery-type phosphorus doped FeS_2 grown on graphene as anode for hybrid supercapacitor with enhanced specific capacity. J Alloys Compd 2021; 854: 157114.

[7] Sethi M, Shenoy US, Bhat DK. Simple solvothermal synthesis of porous graphene-NiO nanocomposites with high cyclic stability for supercapacitor application. J Alloys Compd 2021; 854: 157190.

[8] Prakash D, Manivannan S. Unusual battery type pseudocapacitive behaviour of graphene oxynitride electrode: High energy solid-state asymmetric supercapacitor. J Alloys Compd 2021; 854: 156853.

[9] Liu P-Y, Zhao J-J, Dong Z-P, Liu Z-L, Wang Y-Q. Interwoving polyaniline and a metal-organic framework grown in situ for enhanced supercapacitor behavior. J Alloys Compd 2021; 854: 157181.

[10] Kumar KS, Choudhary N, Pandey D, Hurtado L, Chung H-S, Tetard L, et al. High-performance flexible asymmetric supercapacitor based on rGO anode and WO_3/WS_2 core/shell nanowire cathode. Nanotechnology 2020; 31: 435405.

[11] Gao Y-P, Zhai Z-B, Wang Q-Q, Hou Z-Q, Huang K-J. Cycling profile of layered $MgAl_2O_4$/reduced graphene oxide composite for asymmetrical supercapacitor. J Colloid Interface Sci 2019; 539: 38–44.

[12] Liu Y, Murtaza I, Shuja A, Meng H. Interfacial modification for heightening the interaction between PEDOT and substrate towards enhanced flexible solid supercapacitor performance. Chemical Engineering Journal 2020; 379: 122326.

[13] Shin S, Shin MW. Nickel metal–organic framework (Ni-MOF) derived NiO/C@CNF composite for the application of high performance self-standing supercapacitor electrode. Appl Surf Sci 2021; 540: 148295.

[14] Yu J, Gao X, Cui Z, Jiao Y, Zhang Q, Dong H, et al. Facile synthesis of binary transition metal sulfide tubes derived from NiCo-MOF-74 for high-performance supercapacitors. Energy Technology 2019; 7: 1900018.

[15] Zhang LL, Zhao XS. Carbon-based materials as supercapacitor electrodes. Chem Soc Rev 2009; 38: 2520–31.

[16] Hall PJ, Bain EJ. Energy-storage technologies and electricity generation. Energy Policy 2008; 36: 4352–5.

[17] Conway BE. Electrochemical supercapacitors: scientific fundamentals and technological applications. Springer Science & Business Media; 2013.

[18] Lewandowski A, Galinski M. Practical and theoretical limits for electrochemical double-layer capacitors. J Power Sources 2007; 173: 822–8.

[19] Bohlen O, Kowal J, Sauer DU. Ageing behaviour of electrochemical double layer capacitors: Part I. Experimental study and ageing model. J Power Sources 2007; 172:

468–75.

[20] Raza W, Ali F, Raza N, Luo Y, Kim K-H, Yang J, et al. Recent advancements in supercapacitor technology. Nano Energy 2018; 52: 441–73.

[21] Hashemi M, Rahmanifar MS, El-Kady MF, Noori A, Mousavi MF, Kaner RB. The use of an electrocatalytic redox electrolyte for pushing the energy density boundary of a flexible polyaniline electrode to a new limit. Nano Energy 2018; 44: 489–98.

[22] Kötz R, Carlen M. Principles and applications of electrochemical capacitors. Electrochim Acta 2000; 45: 2483–98.

[23] Burke A. Ultracapacitors: why, how, and where is the technology. J Power Sources 2000; 91: 37–50.

[24] Kumar S, Saeed G, Zhu L, Hui KN, Kim NH, Lee JH. 0D to 3D carbon-based networks combined with pseudocapacitive electrode material for high energy density supercapacitor: A review. Chemical Engineering Journal 2021; 403: 126352.

[25] Gao X, Wang P, Pan Z, Claverie JP, Wang J. Recent progress in two-dimensional layered double hydroxides and their derivatives for supercapacitors. ChemSusChem 2020; 13: 1226–54.

[26] Zhao C, Zheng W. A review for aqueous electrochemical supercapacitors. Front Energy Res 2015; 3: 23.

[27] Naskar P, Chakraborty P, Kundu D, Maiti A, Biswas B, Banerjee A. Envisaging future energy storage materials for supercapacitors: an ensemble of preliminary attempts. ChemistrySelect 2021; 6: 1127–61.

[28] Wu H Bin, Zhang G, Yu L, Lou XWD. One-dimensional metal oxide–carbon hybrid nanostructures for electrochemical energy storage. Nanoscale Horiz 2016; 1: 27–40.

[29] Wu Z, Li L, Yan J, Zhang X. Materials design and system construction for conventional and new-concept supercapacitors. Advanced Science 2017; 4: 1600382.

[30] Yang Z, Ren J, Zhang Z, Chen X, Guan G, Qiu L, et al. Recent advancement of nanostructured carbon for energy applications. Chem Rev 2015; 115: 5159–223.

[31] Naoi K, Naoi W, Aoyagi S, Miyamoto J, Kamino T. New generation "nanohybrid supercapacitor." Acc Chem Res 2013; 46: 1075–83.

[32] Yu A, Chabot V, Zhang J. Electrochemical supercapacitors for energy storage and delivery: fundamentals and applications. Taylor & Francis; 2013.

[33] Yang S, Bachman RE, Feng X, Müllen K. Use of organic precursors and graphenes in the controlled synthesis of carbon-containing nanomaterials for energy storage and conversion. Acc Chem Res 2013; 46: 116–28.

[34] Shao Y, El-Kady MF, Sun J, Li Y, Zhang Q, Zhu M, et al. Design and mechanisms of asymmetric supercapacitors. Chem Rev 2018; 118: 9233–80.

[35] Conway BE. Transition from "supercapacitor" to "battery" behavior in electrochemical energy storage. J Electrochem Soc 1991; 138: 1539.

[36] Conway BE, Conway BE. Similarities and differences between supercapacitors and batteries for storing electrical energy. Electrochemical Supercapacitors: Scientific Fundamentals and Technological Applications 1999: 11–31.

[37] Bullard GL, Sierra-Alcazar HB, Lee HL, Morris JL. Operating principles of the ultracapacitor. IEEE Trans Magn 1989; 25: 102–6.

[38] Sharma P, Bhatti TS. A review on electrochemical double-layer capacitors. Energy Convers Manag 2010; 51: 2901–12.

[39] Schneuwly A, Gallay R. Properties and applications of supercapacitors from the state-of-the-art to future trends. Proceeding PCIM, vol. 2, Citeseer; 2000, p. 1.

[40] Yassine M, Fabris D. Performance of commercially available supercapacitors. Energies (Basel) 2017; 10: 1340.

[41] Frackowiak E, Beguin F. Carbon materials for the electrochemical storage of energy in

capacitors. Carbon N Y 2001; 39: 937–50.

[42] Shinde SK, Jalak MB, Ghodake GS, Maile NC, Kumbhar VS, Lee DS, et al. Chemically synthesized nanoflakes-like NiCo2S4 electrodes for high-performance supercapacitor application. Appl Surf Sci 2019; 466: 822–9.

[43] Joseph A, Thomas T. Pseudocapacitance: An Introduction. Pseudocapacitors: Fundamentals to High Performance Energy Storage Devices, Springer; 2023, 1–17.

[44] Rodriguez-Romero J, Ruiz de Larramendi I, Goikolea E. Nanostructured manganese dioxide for hybrid supercapacitor electrodes. Batteries 2022; 8: 263.

[45] Guo Y, Wang K, Hong Y, Wu H, Zhang Q. Recent progress on pristine two-dimensional metal–organic frameworks as active components in supercapacitors. Dalton Transactions 2021; 50: 11331–46.

[46] Qin Z, Liu J, Sun B, Zou H, Chen L, Xu Y, et al. AC/$Ni(OH)_2$ as a porous electrode material for supercapacitors with high-performance. Electrochim Acta 2022; 435: 141370.

[47] Wang C, Zeng X, Cullen PJ, Pei Z. The rise of flexible zinc-ion hybrid capacitors: advances, challenges, and outlooks. J Mater Chem A Mater 2021; 9: 19054–82.

[48] Abdah MAAM, Azman NHN, Kulandaivalu S, Sulaiman Y. Review of the use of transition-metal-oxide and conducting polymer-based fibres for high-performance supercapacitors. Mater Des 2020; 186: 108199.

[49] Conway BE. Electrochemical supercapacitors: scientific fundamentals and technological applications. Springer Science & Business Media; 2013.

[50] Burke A. R&D considerations for the performance and application of electrochemical capacitors. Electrochim Acta 2007; 53: 1083–91.

[51] Wang G, Zhang L, Zhang J. A review of electrode materials for electrochemical supercapacitors. Chem Soc Rev 2012; 41: 797–828.

[52] Khawaja MK, Khanfar MF, Oghlenian T, Alnahar W. Fabrication and Electrochemical Characterization of Carbon Based Supercapacitor Electrodes. 2019 10th International Renewable Energy Congress (IREC), IEEE; 2019, 1–4.

[53] Saikia BK, Benoy SM, Bora M, Tamuly J, Pandey M, Bhattacharya D. A brief review on supercapacitor energy storage devices and utilization of natural carbon resources as their electrode materials. Fuel 2020; 282: 118796.

[54] Shi F, Li L, Wang X, Gu C, Tu J. Metal oxide/hydroxide-based materials for supercapacitors. RSC Adv 2014; 4: 41910–21.

[55] Merlet C, Rotenberg B, Madden PA, Taberna P-L, Simon P, Gogotsi Y, et al. On the molecular origin of supercapacitance in nanoporous carbon electrodes. Nat Mater 2012; 11: 306–10.

[56] Deschamps M, Gilbert E, Azais P, Raymundo-Piñero E, Ammar MR, Simon P, et al. Exploring electrolyte organization in supercapacitor electrodes with solid-state NMR. Nat Mater 2013; 12: 351–8.

[57] Zhang LL, Zhao XS. Carbon-based materials as supercapacitor electrodes. Chem Soc Rev 2009; 38: 2520–31.

[58] Bard AJ, Faulkner LR. Electrochemical methods: fundamentals and applications. Surf Technol 1983; 20: 91–2.

[59] He H, Liu Y, Shearing PR, He G, Brett DJL. Mesoporous Carbon for Supercapacitors. Nanostructured Materials for Supercapacitors, Springer; 2022, 147–63.

[60] Bazant MZ, Storey BD, Kornyshev AA. Double layer in ionic liquids: Overscreening versus crowding. Phys Rev Lett 2011; 106: 046102.

[61] Kornyshev AA. Double-layer in ionic liquids: paradigm change? J Phys Chem B 2007; 111: 5545–57.

[62] Kondrat S, Kornyshev A. Corrigendum: Superionic state in double-layer capacitors with

nanoporous electrodes. J Phys: Condens Matter 2013; 25: 1pp.

[63] Kondrat S, Georgi N, Fedorov M V, Kornyshev AA. A superionic state in nano-porous double-layer capacitors: insights from Monte Carlo simulations. Physical Chemistry Chemical Physics 2011; 13: 11359–66.

[64] Futamura R, Iiyama T, Takasaki Y, Gogotsi Y, Biggs MJ, Salanne M, et al. Partial breaking of the Coulombic ordering of ionic liquids confined in carbon nanopores. Nat Mater 2017; 16: 1225–32.

[65] Wang G, Zhang L, Zhang J. A review of electrode materials for electrochemical supercapacitors. Chem Soc Rev 2012; 41: 797–828.

[66] Kang J, Zhang S, Zhang Z. Three-dimensional binder-free nanoarchitectures for advanced pseudocapacitors. Advanced Materials 2017; 29: 1700515.

[67] Augustyn V, Simon P, Dunn B. Pseudocapacitive oxide materials for high-rate electrochemical energy storage. Energy Environ Sci 2014; 7: 1597–614.

[68] Yoshida N, Yamada Y, Nishimura S, Oba Y, Ohnuma M, Yamada A. Unveiling the origin of unusual pseudocapacitance of $RuO_2 \cdot n\ H_2O$ from its hierarchical nanostructure by small-angle x-ray scattering. The Journal of Physical Chemistry C 2013; 117: 12003–9.

[69] Kim JW, Augustyn V, Dunn B. The effect of crystallinity on the rapid pseudocapacitive response of Nb_2O_5. Adv Energy Mater 2012; 2: 141–8.

[70] González A, Goikolea E, Barrena JA, Mysyk R. Review on supercapacitors: Technologies and materials. Renewable and Sustainable Energy Reviews 2016; 58: 1189–206.

[71] Sarno M. Nanotechnology in energy storage: The supercapacitors. Stud Surf Sci Catal, vol. 179, Elsevier; 2020, 431–58.

[72] Girija TC, Sangaranarayanan M V. Analysis of polyaniline-based nickel electrodes for

electrochemical supercapacitors. J Power Sources 2006; 156: 705–11.

[73] Li X, Zhitomirsky I. Electrodeposition of polypyrrole–carbon nanotube composites for electrochemical supercapacitors. J Power Sources 2013; 221: 49–56.

[74] Hu C-C, Wang C-C. Improving the utilization of ruthenium oxide within thick carbon–ruthenium oxide composites by annealing and anodizing for electrochemical supercapacitors. Electrochem Commun 2002; 4: 554–9.

[75] Lang J-W, Kong L-B, Wu W-J, Luo Y-C, Kang L. Facile approach to prepare loose-packed NiO nano-flakes materials for supercapacitors. Chemical Communications 2008: 4213–5.

[76] Chen Z, Augustyn V, Wen J, Zhang Y, Shen M, Dunn B, et al. High-performance supercapacitors based on intertwined CNT/V_2O_5 nanowire nanocomposites. Advanced Materials 2011; 23: 791–5.

[77] Li H, Zhu Y, Dong S, Shen L, Chen Z, Zhang X, et al. Self-assembled Nb_2O_5 nanosheets for high energy–high power sodium ion capacitors. Chemistry of Materials 2016; 28: 5753–60.

[78] Wang X, Shen G. Intercalation pseudo-capacitive $TiNb_2O_7$@ carbon electrode for high-performance lithium ion hybrid electrochemical supercapacitors with ultrahigh energy density. Nano Energy 2015; 15: 104–15.

[79] Shen L, Lv H, Chen S, Kopold P, van Aken PA, Wu X, et al. Peapod-like Li_3VO_4/N-doped carbon nanowires with pseudocapacitive properties as advanced materials for high-energy lithium-ion capacitors. Advanced Materials 2017; 29: 1700142.

[80] Wang X, Kajiyama S, Iinuma H, Hosono E, Oro S, Moriguchi I, et al. Pseudocapacitance of MXene nanosheets for high-power sodium-ion hybrid capacitors. Nat Commun 2015; 6: 6544.

[81] Wang R, Wang S, Peng X, Zhang Y, Jin D, Chu PK, et al. Elucidating the intercalation

pseudocapacitance mechanism of MoS_2–carbon monolayer interoverlapped superstructure: toward high-performance sodium-ion-based hybrid supercapacitor. ACS Appl Mater Interfaces 2017; 9: 32745–55.

[82] Sun J, Guo L, Sun X, Zhang J, Hou L, Li L, et al. One-dimensional nanostructured pseudocapacitive materials: design, synthesis and applications in supercapacitors. Batter Supercaps 2019; 2: 820–41.

[83] Tiwari P, Janas D. Emergent pseudocapacitive behavior of single-walled carbon nanotube hybrids: a materials perspective. Mater Chem Front 2022; 6: 2386–412.

[84] Frackowiak E, Khomenko V, Jurewicz K, Lota K, Béguin F. Supercapacitors based on conducting polymers/nanotubes composites. J Power Sources 2006; 153: 413–8.

[85] Zheng JP, Jow TR. A new charge storage mechanism for electrochemical capacitors. J Electrochem Soc 1995; 142: L6.

[86] Zheng JP, Cygan PJ, Jow TR. Hydrous ruthenium oxide as an electrode material for electrochemical capacitors. J Electrochem Soc 1995; 142: 2699.

[87] Jurewicz K, Delpeux S, Bertagna V, Beguin F, Frackowiak E. Supercapacitors from nanotubes/polypyrrole composites. Chem Phys Lett 2001; 347: 36–40.

[88] Lei Z, Zhang J, Zhao XS. Ultrathin MnO_2 nanofibers grown on graphitic carbon spheres as high-performance asymmetric supercapacitor electrodes. J Mater Chem 2012; 22: 153–60.

[89] Yang J, Yu C, Fan X, Liang S, Li S, Huang H, et al. Electroactive edge site-enriched nickel–cobalt sulfide into graphene frameworks for high-performance asymmetric supercapacitors. Energy Environ Sci 2016; 9: 1299–307.

[90] Tang X, Jia R, Zhai T, Xia H. Hierarchical Fe_3O_4@ Fe_2O_3 core–shell nanorod arrays as high-performance anodes for asymmetric supercapacitors. ACS Appl Mater Interfaces 2015; 7: 27518–25.

[91] Ding B, Wu X. Transition metal oxides anchored on graphene/carbon nanotubes conductive network as both the negative and positive electrodes for asymmetric supercapacitor. J Alloys Compd 2020; 842: 155838.

[92] Li H, Cheng L, Xia Y. A hybrid electrochemical supercapacitor based on a 5 V Li-ion battery cathode and active carbon. Electrochemical and Solid-State Letters 2005; 8: A433.

[93] Wang X, Zheng JP. The optimal energy density of electrochemical capacitors using two different electrodes. J Electrochem Soc 2004; 151: A1683.

[94] Du Pasquier A, Plitz I, Menocal S, Amatucci G. A comparative study of Li-ion battery, supercapacitor and nonaqueous asymmetric hybrid devices for automotive applications. J Power Sources 2003; 115: 171–8.

[95] Pell WG, Conway BE. Peculiarities and requirements of asymmetric capacitor devices based on combination of capacitor and battery-type electrodes. J Power Sources 2004; 136: 334–45.

[96] Amatucci GG, Badway F, Du Pasquier A, Zheng T. An asymmetric hybrid nonaqueous energy storage cell. J Electrochem Soc 2001; 148: A930.

[97] Zhang LL, Zhao XS. Carbon-based materials as supercapacitor electrodes. Chem Soc Rev 2009; 38: 2520–31.

Chapter 2: Literature Review

2.1 Electrode materials for Supercapacitor application

Electrode materials strongly influence the performance and properties of supercapacitors. The following conditions for electrode materials are important for high-performance supercapacitors.

- The active electrode's preparation should be inexpensive and non-toxic.
- Should ensure high thermal and chemical stability for maximum electrochemical stability.
- Improve electrode conductivity for optimal performance.
- A large surface area leads to more electroactive material in electrochemical processes.

2.1.1 Carbon Based Materials

Because of their distinct chemical and physical characteristics, carbon compounds play a significant role in electrochemical energy storage devices. Better specific surface area (up to 3000 m^2g^{-1}), electric conductivity, corrosion resistance, chemical stability, changeable pore size, and accessibility to electrochemically active sites are a few of these [1,2]. The performance of EDLC supercapacitors is enhanced by carbon-based electrodes such as carbon nanotubes, carbon aerogel, and activated carbon [3]. At the moment, activated carbon (AC) having a large surface area but a little storage capacity, makes up EDLC [4].

Activated carbons

Activated carbons are widely employed as supercapacitor electrode materials because to their high surface area (> 1000 m^2g^{-1}), excellent electrical conductivity, chemical stability, and affordability [5]. Activated carbons can be produced using coal, wood, nutshells, and charcoal as precursors. The right activation technique, such as hybrid activation, physical activation, or

chemical activation, is used to activate materials with poor porosity [6,7]. The particular surface area and pore size distribution of activated carbon (AC) supercapacitors dictate their efficiency. The connected pore structure with short pore length and narrower pore size dispersal improves the supercapacitor efficiency [8].

Carbon nanotubes (CNTs)

CNTs are hollow nanostructures made of cylinder-shaped carbon allotropes. Because of their remarkable properties such as strong thermal and chemical endurance, high conductivity, and very porous architectures, CNTs have attracted the attention of researchers working on the construction of supercapacitor electrodes [9]. Owing to their unique open tubular shape, high aspect ratio, and mechanical resilience, CNTs provide good substrates for other materials. Single-walled and multi-walled carbon nanotubes (CNTs) are both possible. In improved power density devices, carbon nanotubes are frequently used as the electrode material. There are several methods for producing CNTs, including as chemical vapour deposition (CVD), arc discharge, laser ablation, and others. More so than the other two approaches, CVD's affordability and simplicity make it an easy route to scale up to bottom-scale production.

Carbon aerogels

Carbon aerogels are also used as electrode materials for EDLCs owing to their favourable qualities such as large surface area, tunable pore structure, and excellent electrical conductivity [10]. Carbon aerogels are composed of biomass-derived chemicals like humic acids. Carbon aerogels are composed of a continuous network of conductive carbon nanoparticles. Carbon aerogels can form chemical bonds with current collectors, reducing the requirement for additional binding agents [11,12]. Carbon aerogels show an inferior ESR than activated carbon and therefore offers a higher power density. Carbon-based materials' specific capacitance (C_{Sp})

is determined by electrode surface properties such as pore size distribution, volume, shape, and area [13].

2.1.2 Conducting Polymers

A wide potential window, low cost, good conductivity, flexibility, and ease of production are only a few benefits of using conductive polymer as an electrode material for supercapacitors (SCs) [14]. The polymers used in SC electrode materials are polythiophene, polypyrrole (PPy), polyaniline (PANI), and poly (3,4-ethylene-dioxythiophene) [15,16]. A few S cm^{-1} to 500 S cm^{-1} in the doped state is the range of conducting polymers' strong intrinsic conductivity, which makes them attractive [17]. Appropriate operating potential window is crucial for polymers. Incorrect potential window exposure causes conducting polymers to degrade and lose their conductivity [18]. For conducting polymers to operate better in supercapacitors, potential range is therefore crucial. Many efforts have been made to enhance the electrochemical performance of conducting polymers [19]

2.1.3 Transition Metal Oxides

Metal oxides are thought to be very desirable and advantageous materials for supercapacitor electrodes. In pseudo-capacitance research and applications, transition metal oxides (TMOs) like ruthenium, manganese, copper, cobalt, iron, vanadium, and tin are commonly used [20]. This is largely because of their remarkable properties, which are better than conducting polymers in terms of specific capacitance, energy density, and cycling stability. Metal oxides are capable of displaying several oxidation states at once. Metal oxides can be converted into different oxidation states during charging or discharging, which permits ions to be added or removed from the active material [21,22]. Ruthenium dioxide (RuO_2) is a popular transition metal oxide used as an active electrode material in supercapacitors [23]. Its noteworthy

properties, which include a broad potential window (1.4V), high electrical conductivity, and a good theoretical specific capacitance (2000 Fg^{-1}) are the main reasons for this selection [24,25]. However, ruthenium precursors are extremely expensive and have toxic characteristics that prevent their continued usage in the consumer sector. The potential electrode materials for supercapacitors have been explored, and these include transition metal oxides such as MnO_2 [26], V_2O_5 [27], NiO [28], CuO [29], Co_3O_4 [30], $NiCO_2O_4$ [31], and $MnCo_2O_4$ [32].

Metal Tungstate based supercapacitors

The common formula XWO_4, where 'X' is a divalent cation (X^{2+} = Ni, Mn, Co, Fe, Cu transition metals-d), represents transition metal tungstates. These states are more intriguing than other forms of metal oxide because of their structural, chemical, physical, and photoluminescent characteristics [33]. because of its vast reserves, specific capacity, environmental friendliness, and appropriate working voltage. The usage of tungsten (W) in oxysalts, oxides, and nitrides has been discovered to be advantageous for electrochemical energy storage over the past few years. Excellent cycle operation, high reversible capacity, and rate capability are among the many electrochemical qualities displayed by the $NiWO_4$, $CoWO_4$, $CuWO_4$, and $MnWO_4$ electrodes.

Nickel tungstate ($NiWO_4$)

Due to its significant features, including its high stability and electrochromic capabilities, nickel tungstate ($NiWO_4$) is suitable for use as both a catalyst and an electrode. $NiWO_4$ exhibits a monoclinic wolframite type crystal structure, as seen in Figure. 2.1 Ni^{2+}, with a space group of P2/c and a tiny ionic radius of 0.69 Å [34]. A transition metal oxide (TMO) nano-composition known as $NiWO_4$ has outstanding conductivity (10^{-7}–10^{-2} S cm^{-1}). $NiWO_4$ Nanoparticles have been employed as a supercapacitor material due to their inexpensive cost,

narrow band gap, and strong electrochemical characteristics. The wolframite-type (monoclinic) structure of $NiWO_4$ makes it useful in a variety of applications, including microwave, optical fibre, humidity sensor, and catalysis [35]. The integration of W atoms into the NiO structural pattern enhances conductivity, stability, and electrochemical characteristics in $NiWO_4$ nanoparticles [36]. Figure 2.1 displays the monoclinic geometry of the $NiWO_4$ crystal structure.

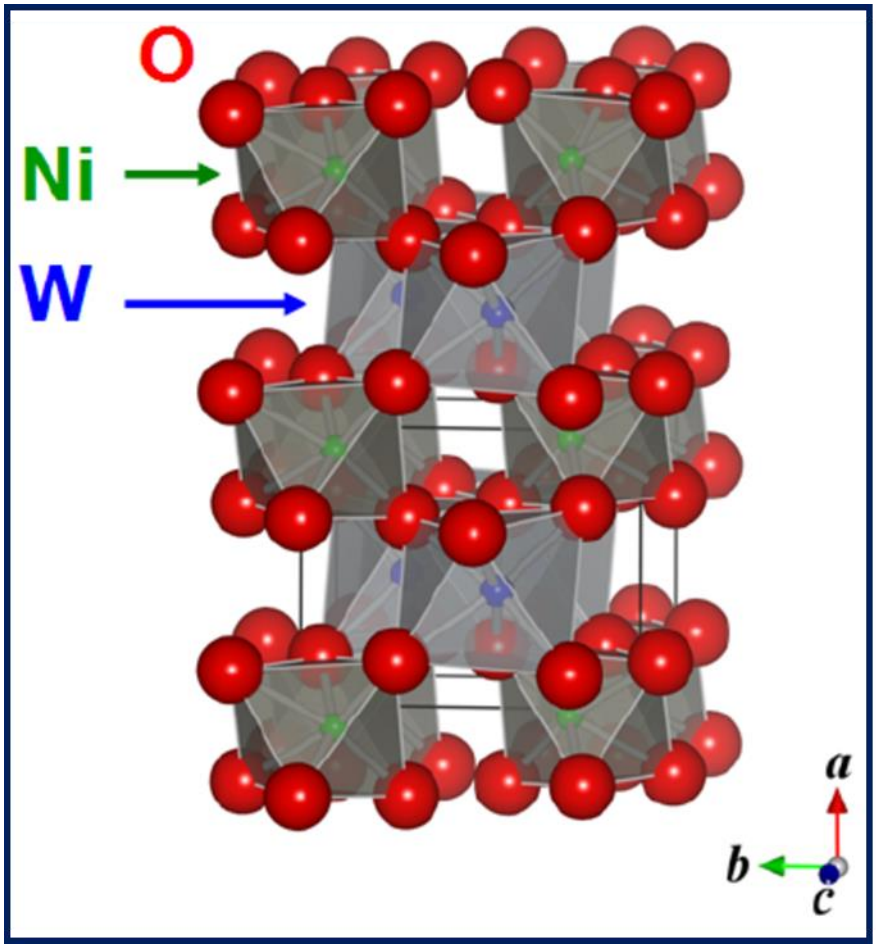

Figure 2.1: The $NiWO_4$ monoclinic (P 2/c) crystal structure [37]. The crystallographic unit cell is illustrated.

Table 2.1 displays the electrochemical properties of $NiWO_4$ based electrodes, including specific capacitance, current density, and manufacturing technique. According to the literature assessment, hydrothermally produced $NiWO_4$ electrodes are more suited for supercapacitor applications.

Table. 2.1: Electrochemical performance comparison of $NiWO_4$ based electrodes.

Electrode material	Electro lyte	Specific capacitance (Fg^{-1})	Current density (Ag^{-1})	Potential window (V)	Cycling stability	Ref.
$NiWO_4$ spherical shape	1 M KOH	437.2	0.1	0-0.6	>94%) after 500 cycles	[38]]
$NiWO_4$ nano-spheres	2 M KOH	427	1	0-0.5	99% after 1000 cycles	[39]
Zn doped amorphous $NiWO_4$ nanoparticle	2 M KOH	653.75	1	0.1-0.7	64.1% after 1000	[40]
$NiWO_4$	3 M KOH	specific capacity of 284 mC cm^{-2}	0.2	- 0.2 to 0.6	80% after 5500 cycles	[41]
$NiWO_4$ agglomerated hydrangea flower	6 M KOH	170	1	0-0.5	61.1% after 5000 cycles	[42]
$NiWO_4$ cauliflower like	2 M KOH	586	0.5	0-0.6	91.4% after 5000 cycles	[43]
$NiWO_4$ hill-like hemisphere	2 M KOH	797.8	1	0-0.6	55.6% after 6000	[44]
$NiWO_4$ spheric morphology	6 M KOH	750	1	0.1-0.6	93.2% after 6000	[45]
$NiWO_4$ burl-like	6 M KOH	1190.2	2	-0.1-0.6	92% after 1,000 cycles	[46]
$NiWO_4$ Nano-berry cycles	1 M KOH	1115.05	20 mA cm^{-2}	0–0.7	80% after 2000	[47]

Cobalt tungstate ($CoWO_4$)

Researchers are interested in cobalt tungstates, a key component of ABO_4-type ternary metal oxides, due to their low cost, environmental friendliness, abundance of resources, and excellent

catalytic and electrochemical capabilities [48]. Monoclinic wolframite crystalline $CoWO_4$ has hexagonal oxygen atoms and octahedral sites that are occupied by W^{6+} and Co^{2+} cations [49,50]. Additionally, due to the addition of W atoms, which significantly raises their conductivity in comparison to pure metal oxide, the binary metal oxides (MO) of tungstate have conductivities on the scale of 10^{-7}-10^{-3} S cm^{-1} [51]. For materials used in pseudo-capacitors, $CoWO_4$ is a suitable electrode material. Figure 2.2 shows the crystal structure of $CoWO_4$ with monoclinic geometry.

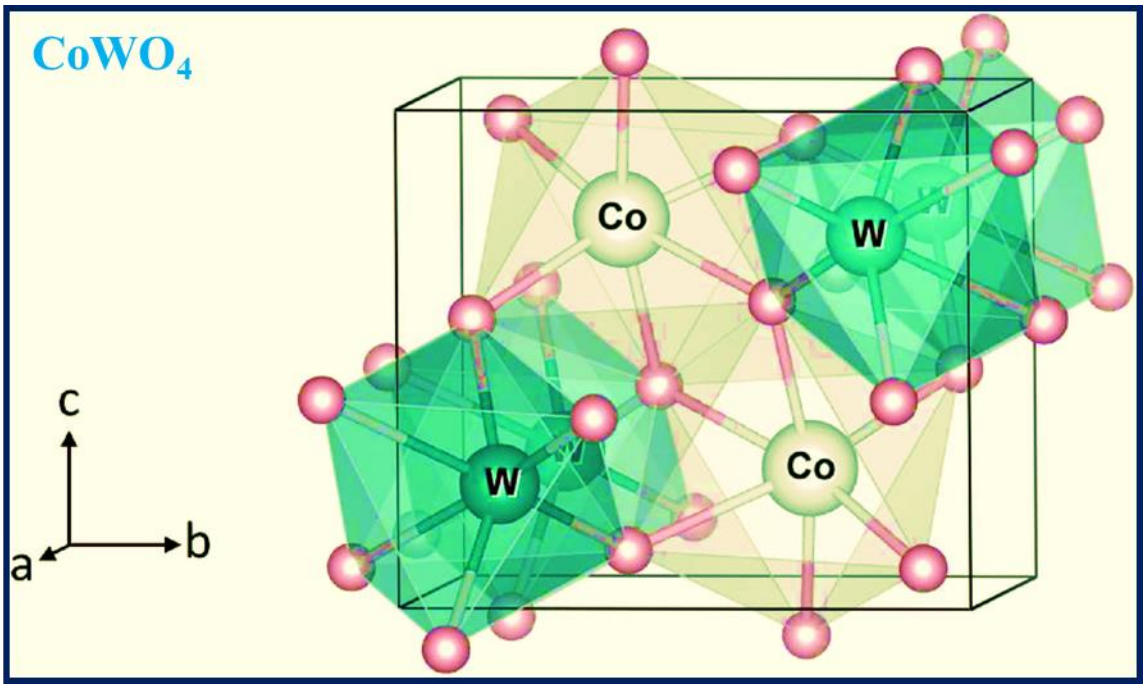

Figure 2.2: Crystal structure of monoclinic $CoWO_4$ [52]. The crystallographic unit cell is illustrated.

Table 2.2 displays the electrochemical properties of $CoWO_4$ based electrodes, including specific capacitance, current density, and manufacturing technique. According to the literature assessment, hydrothermally produced $CoWO_4$ electrodes are more suited for supercapacitor applications.

Table. 2.2: Electrochemical performance comparison of $CoWO_4$ based electrodes.

Electrode material	Electro lyte	Specific capacitance (Fg^{-1})	Current density (Ag^{-1})/ Scan rate (mVS^{-1})	Potential window (V)	Cycling stability	Ref.
$CoWO_4$ nanoparticles	2 M H_2SO_4	378	2 mVS^{-1}	-0.3-0.4	95.5% after 4000 cycles	[53]
$CoWO_4$ shuttle-like	2 M KOH	764.4	0.5	0-0.6	50% after 6000	[44]
$CoWO_4$ Flower like	2 M KOH	156	0.5	0-0.5	85.2% retention at 10 Ag^{-1}	[54]
$CoWO_4$ Flower like	6 M KOH	1395	0.5	0-0.6	89% after 3000 cycles	[55]
$CoWO_4$ nanocrystals	1 M Na2SO 4	249	5 mVS^{-1}	0-1	-	[56]
$CoWO_4$ porous nanospheres	1 M KOH	177.25	1.33	0-0.5	94% after 10000 cycles	[57]
$CoWO_4$ Flower like	1 M KOH	712	0.5	0-0.6	84.2% after 5000 cycles	[58]
$CoWO_4$ Carambola like microspheres	6 M KOH	493.7 Cg^{-1}	1 mVS^{-1}	0-0.7	95.7% after 12000 cycles	[59]
$CoWO_4$ nanoparticles	2 M KOH	403	0.5	0-0.6	-	[60]
$CoWO_4$ nanosheets	1 M KOH	1127.6	1	0-0.6	92.4% after 3000 cycles	[61]

Copper tungstate ($CuWO_4$)

The two metal atoms that make up copper tungstate (Cu and W) are surrounded by six oxygen atoms. The M-O distances in the octahedra of WO_6 and CuO_6 are, respectively, ~0.176-0.221

and ~0.196-0.245 nm. This molecule exhibits low dimensional magnetic behaviour due to the thinly connected zigzag chains containing copper (Cu) ions [62]. There are many uses for copper tungstate, such as photoanode material, laser host, photo-electrolysis, electrode material for sensors, and optical fibres [62–65]. Figure 2.3 displays the triclinic geometry crystal structure of $CuWO_4$.

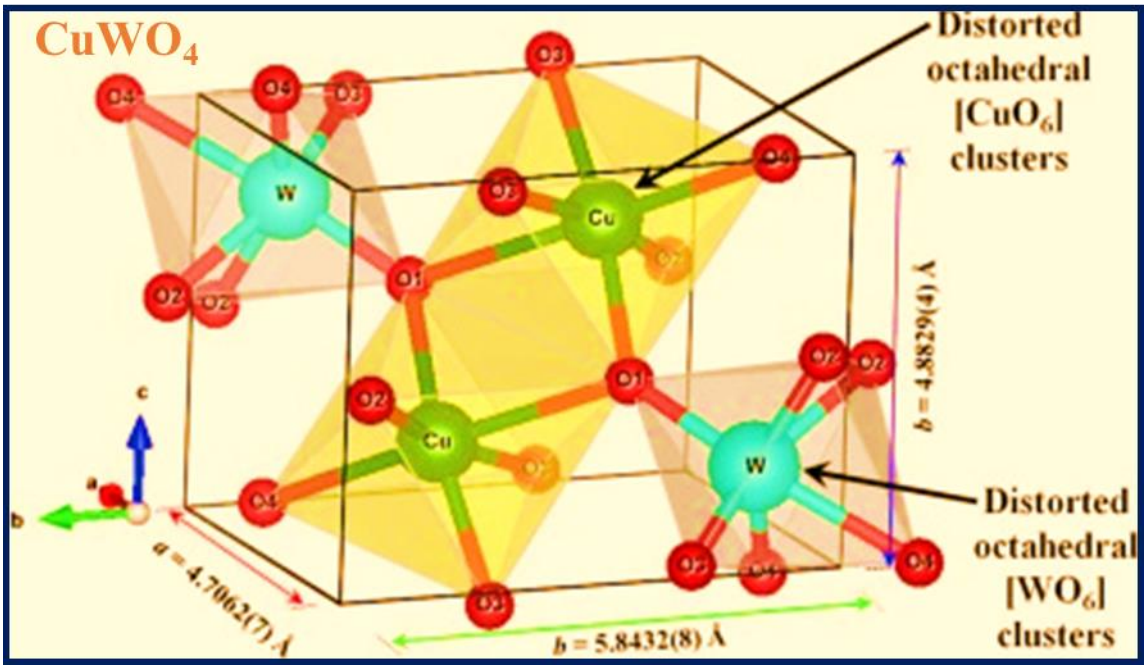

Figure 2.3: Crystal structure of triclinic $CuWO_4$ [66]. The crystallographic unit cell is illustrated.

Table 2.3 displays the electrochemical properties of $CuWO_4$ based electrodes, including specific capacitance, current density, and manufacturing technique. According to the literature assessment, hydrothermally produced $CuWO_4$ electrodes are more suited for supercapacitor applications.

Table. 2.3: Electrochemical performance comparison of $CuWO_4$ based electrodes.

Electrode material	Electro lyte	Specific capacitance (Fg^{-1})	Current density (Ag^{-1})/ Scan rate (mVS^{-1})	Potential window (V)	Cycling stability	Ref.
$CuWO_4$ nanoparticles	1 M KOH	215	2	-0.2-0.4	75% after 2000 cycles	[67]
$CuWO_4$ nanoparticles	3 M KOH	360	1	0-0.5	-	[68]
$CuWO_4$ micro-sphere like	6 M KOH	168.08	1	-0.1-0.4	80% after 1000 cycles	[69]
$CuWO_4$ nanoparticles	3 M KOH	35.71	0.25	-0.1 to 0.4	-	[70]
$CuWO_4$ nanoporous	2 M KOH	15.08	0.25	0-0.6	-	[71]
$CuWO_4$ cube-shaped	1 M KOH	230	-	-0.2 - 0.45	-	[72]
$CuWO_4$ nanosheet	3 M H_2SO_4	620.1	-	-0.1 -0.9	97.1% after 3000 cycles	[73]

Manganese tungstate ($MnWO_4$)

The remarkable catalytic, magnetic, and electrochemical properties of manganese tungstate ($MnWO_4$) have garnered significant attention as a bimetallic oxide. As a result, the material has found use in a wide range of industries, including sensing, optical communication, and photocatalysis [74]. The structure of $MnWO_4$ is monoclinic, with six O atoms around an octahedral coordination formed by the Mn and W atoms. Due to their arrangement, these oxygen atoms form a deformed, closely packed hexagonal shape [75,76]. Its binary form exhibits greater conduction compared to pure tungstate oxides due to the addition of the second atom [77]. Consequently, $MnWO_4$ is a good option for an electrode material for SCs due to the

simultaneous existence of W and Mn atoms [78]. There are numerous publications about the electrochemical properties of $MnWO_4$ in the literature. Still, such electrode materials' capacitive capabilities are not up to par [79,80]. Furthermore, one of the key obstacles to the material's application in real-world, industry-scale operations continues to be its long cycle stability [75]., As a result, electrode materials with improved electrochemical characteristics like a long cycle stability and high specific capacitance are required.

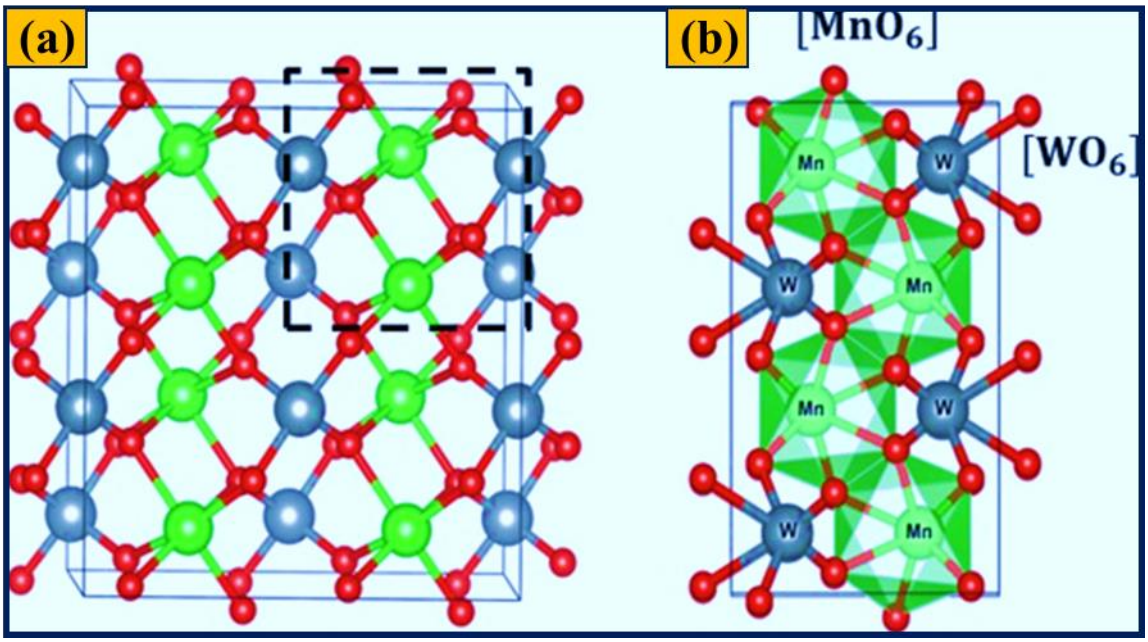

Figure 2.4: Crystal structure of monoclinic $MnWO_4$ [81]. Mn atoms are in green, W atoms are in blue and O atoms are in red.

The current imperative is the rational design of hybrid structured electrode materials with enhanced electrochemical properties. Electron transport could be facilitated by a hybrid structure consisting of nanorods or nanotubes with a 1D backbone. In this sense, a combination of carbonaceous material and multi-metallic oxides is highly exciting, as it might combine the benefits of both high-power density EDLCs and high energy density pseudocapacitors in one unit. A multilayer MnWO4/reduced graphene oxide-based SC with a specific capacitance of 288 Fg^{-1} at a scan rate of 5 mVs^{-1} has been reported by Tang et al. [77]. Phase-pure $MnWO_4$@MWCNTs were employed by Shim et al. as an electrode material for Li storage that

is reversible [82]. The monoclinic geometry of the crystal structure of $MnWO_4$ is depicted in Figure 2.4. Table 2.3 displays the electrochemical properties of $MnWO_4$ based electrodes, including specific capacitance, current density, and manufacturing technique. According to the literature assessment, hydrothermally produced $MnWO_4$ electrodes are more suited for supercapacitor applications.

Table. 2.4: Electrochemical performance comparison of $MnWO_4$ based electrodes.

Electrode material	Electro lyte	Specific capacitance (Fg^{-1})	Current density (Ag^{-1})/ Scan rate (mVS^{-1})	Potential window (V)	Cycling stability	Ref.
$MnWO_4$ Micro flowers	1 M KOH	698 Fg^{-1}	5 mA cm^{-2}	0 to 0.5 V	-	[83]
$MnWO_4$ -CNF@H	6 M KOH	451.3 mAh g^{-1}	1 A g^{-1}	0 to 0.5 V	95% after 5000 cycles	[84]
Ni-doped $MnWO_4$ Micro flowers	1 M KOH	222.7 Fg^{-1}	1 A g^{-1}	−0.1 to 0.6 V	> 100% after 10,000 cycl es	[85]
$MnWO_4$	1 M KOH	295 Fg^{-1}	5 mVs^{-1}	-0.2 to 0.6 V	> 100% after 3000 cycles	[86]
$MnWO_4$ (using DNA scaffold)	0.1 M Na_2SO_4	34 Fg^{-1}	0.5 mA cm^{-2}	0 to 1 V	-	[87]
$MnWO_4$	1 M Na_2SO_4	386 Fg^{-1}	5 mVs^{-1}	0 to 1 V	90% after 2000 cycles	[88]
$MnWO_4$	0.1 M NaOH	199 Fg^{-1}	2 mVs^{-1}	0 to 0.5 V	62% after 1200 cycles	[89]
$MnWO_4$ (using CTAB)	1 M H_2SO_4	27 Fg^{-1}	5 mVs^{-1}	-0.2 to 1 V	> 100% after 1000 cycles	[90]
$MnWO_4$ micro flower	1 M Na_2SO_4	324 Fg^{-1}	1 mA cm^{-2}	0 to 1 V	93% after 8000	[91]
$MnWO_4$/RG O	6 M KOH	288 Fg^{-1}	5 mV s^{-1}	-0.35 to 0.55 V	14.9% after 6000 cycles	[92]

2.1.4 Perovskite Materials as Supercapacitor

The perovskite materials have gained the attraction among research community over recent years owing to their low cost, characteristics of oxygen vacancies, multiple oxidation states with swift and reversible faradic response [93]. Until 2014 perovskite-based energy materials have not been cultivated broadly. Mefford.et al. [94] in 2014 published a breakthrough result on the mechanism of oxygen anion intercalation of nanostructured $LaMnO_3$ oxides. The proposed mechanism is as follows; Following the oxidation of two Mn^{2+} centers to two Mn^{3+}, OH^- groups fill the oxygen vacancies and spread through the crystal along the octahedral edges, producing water as a byproduct. The second stage of the reaction involves the oxidation of two Mn^{3+} centers to two Mn^{4+} centers and the diffusion of manganese to the surface, which intercalates excess oxygen at the surface (Figure. 2.5) [95]. As previously stated, the majority of perovskite oxide is utilized for charge storage; hence, a high surface area is not necessary for perovskite oxide to achieve high energy storage. The reaction mechanism is as follows [94];

$$La[Mn^{2+}_{2\delta}\ ;\ Mn^{3+}_{1-2\delta}]O_{3-\delta} + 2\delta OH^- \leftrightarrow LaMn^{3+}O_3 + 2\delta e^- + \delta H_2O \quad (2.1)$$

$$LaMn^{3+}O_3 + 2\delta OH^- \leftrightarrow La[Mn^{4+}_{2\delta}\ ;\ Mn^{3+}_{1-2\delta}]O_{3+\delta} + 2\delta e^- + H_2O \quad (2.2)$$

Theoritically, O^{2-} can carry two negative charges per unit in each which indicates the intercalation pseudocapacitance leads to store twice the charge in each charge/discharge cycle compared to Li^+ ion intercalation. Perovskite oxides are therefore thought to be extremely attractive candidate materials for Supercapacitors owing to its structural and compositional advantages.

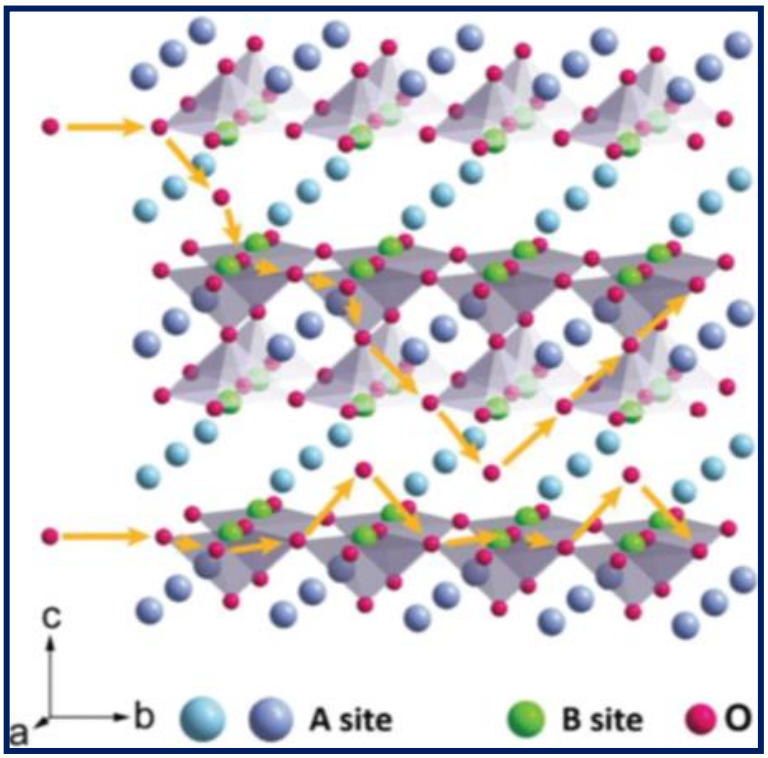

Figure 2.5: Oxygen intercalation mechanism in perovskite oxides [96].

Single Perovskite oxides (ABO_3 type):

Lanthanum Based perovskite Oxides: In recent years Lanthanum based perovskite oxides are explored extensively owing to their abundance, low cost, good electrical conductivity.Mefford.et.al. [94] reported Specific capacitance of 609.8 Fg^{-1} at the scan rate of 2 mVs^{-1} with the Energy density of 23.4 W h kg^{-1} at power density of 4.21 W kg^{-1} for $LaMnO_3$.Wie Che.et.al [97] synthesized novel $LaNiO_3$ powder by sol-gel method and measured their supercapacitance which shows with a specific capacitance of 478.7 Fg^{-1} at 0.1 mV s^{-1}, $LaNiO_3$ has excellent pseudocapacities. After 15000 cycles, it also demonstrates strong cycling stability, with a 5.5% reduction in charge-discharge efficiency. Charge storage in this type of perovskite pseudocapacitor electrode is linked to the intercalation of oxygen-ion into oxygen vacancies, which is primarily originated from the variation of different valence states of B site Ni in perovskite ABO_3 structure. The oxygen intercalation and extrusion mechanism of the $LaNiO_3$ electrode is also revealed.

Zhang.et.al [98] reported the performance of mesoporous perovskite $LaFeO_3$ nanostructure (Figure 2.6) as an electrode material which yielded a noteworthy Supercapacitive performance with specific capacitance of 241.3 Fg^{-1} at 1 Ag^{-1} and 68% capacitance retention at higher current density of 20 Ag^{-1}.Based on this material, a two-electrode symmetric SC cell (SSC) showed a high energy density of 34 W h kg^{-1} at a power density of 900 W kg^{-1} with 92.2% preservation of capacitance after 5,000 cycles. As the Fe^{3+} has more stable electronic configuration of $3d^5$than Ni^{3+} $LaFeO_3$ is more stable than $LaNiO_3$.

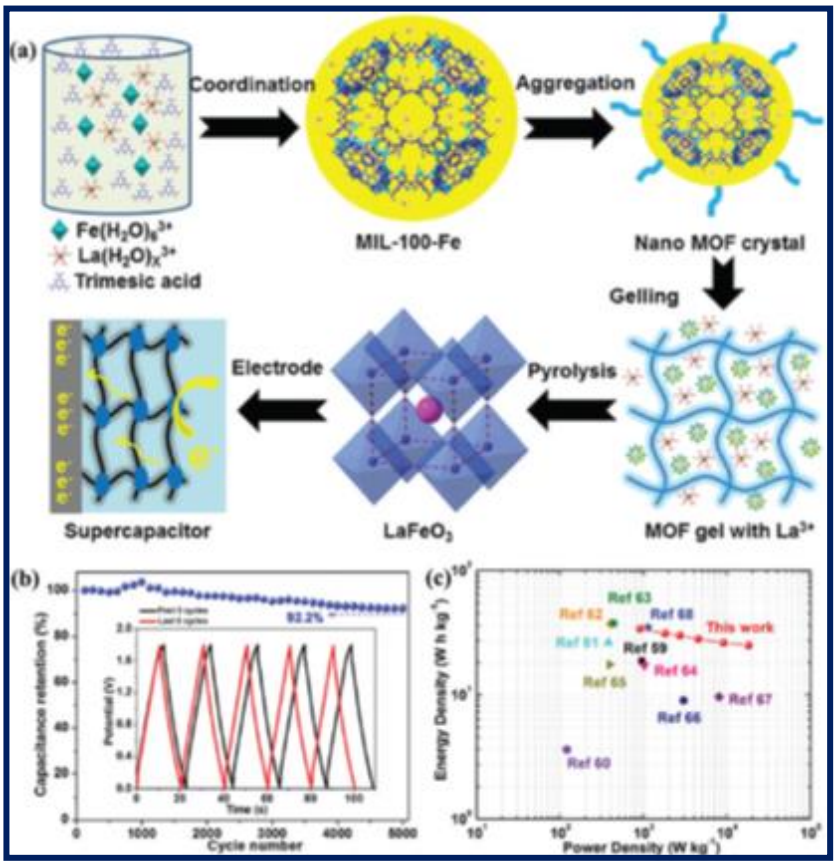

Figure 2.6: (a) Synthesis approach of Perovskite $LaFeO_3$, (b) Cyclic Stability graph; inset: first and last five charge/discharge cycles, (c) Ragone plot of this device [99].

Strontium based Perovskite Oxides:

Strontium based perovskite oxides have gained researcher's attraction since 1999 when Garche.et.al [100] reported the specific capacitance of 270 Fg^{-1} of the as synthesized novel $SrRuo_3$ oxide. $SrMnO_3$ nanofibers were synthesized by George et.al [101] using sol-gel assisted

electrospinning method and thereafter calcinations were done at different temperature ranges(600°-800°C).The nanofibers with porous structure synthesized at 700°C exhibited superlative performance with specific capacitance of 321.7 Fg^{-1} at current density of 0.5 Ag^{-1}.Mesoporous $SrTiO_3$ having pore diameter of 15.18 nm and porous volume of 0.249 cm^3 g^{-1} was synthesized by Sharma.et.al [102].Such porous structure with numerous active sites facilitates efficient charge storage and it registered the specific capacitance of 592 Fg^{-1} at the scan rate of 5 mVs^{-1}.When a Symmetric supercapacitor device is constructed with this electrode it delivered maximum energy density of 27.8 W h kg^{-1} at a power density of 1921 W kg^{-1} with excellent capacitance retention of 99% even after 5000 charge /discharge cycles.

Other single perovskite oxides:

Owing to the possession of high band gap, variable valence states between Ce^{3+} and Ce^{4+} [103], high dielectric constant cerium-based perovskites have gained attraction among research community over the years.Hu.et.al. [104] synthesized $CeMO_3$ (M=Co, Ni, cu) nanostructures via electrospinning process and the electrochemical study revealed that the specific capacitances of $CeCoO_3$, $CeNiO_3$, and $CeCuO_3$ perovskites are 128, 189, and 117 Fg^{-1} at the current density of 0.5 Ag^{-1}. BiFeO3 nanoplates were synthesized by Yin.et.al. [105] via hydrothermal method and it registered the specific capacitance of 254.6 Fg^{-1} at a scan rate of 1 mVs^{-1} when used as electrode and retained 84% capacitance even after 1000 cycles.Kim.et.al [106] prepared $NiMnO_3$ perovskite hydrothermally and even after 7000 cycles, the synthesized NiMnO3 perovskite oxide demonstrated outstanding cycle stability with a coulombic efficiency of 77% and a high specific capacitance of 99.03 Fg^{-1}.

2.1.5 Enhancement approach for perovskite oxides:

The oxygen vacancies are potential sites for charge storage in Perovskite Oxides. Therefore, to enhance the capacitance the number of oxygen vacancies are needed to increase. The number of Oxygen vacancies are also structural and compositional in nature. Increasing oxygen vacancies and integration with composite materials are imperative to get the optimized Supercapacitance from Perovskite Materials. The effective ways to improve the oxygen vacancies of perovskite oxides include [107]:

- Stoichiometry modulation of Cation or Anion.
- A-Site Doping.
- B-Site doping.

2.1.6 Halide perovskite materials for Supercapacitor applications:

Metal halide perovskites having formula ABX_3 (Where X= F, Cl, Br, I) registered their footprint firmly in the field of Solar Cells, LED devices etc. [108] Very few reports are available where halide perovskites are used as electrode in Supercapacitor applications. The metal hailde perovskites possess higher ionic conductivity than electronic conductivity which is beneficial for the design of Supercapacitor [109]. Considering this, Zhou.et.al. [110] designed $MAPbI_3$ based thin film electrochemical capacitor where the perovskite layer played the role of solid electrolyte and polarized electrode both. Popoola. et. al. [111] for the first time studied the integration of solid electrolyte with $MAPbI_3$.The detailed synthesis approach is depicted in Figure 2.7. The sysmmetric Supercapacitor device registered highest areal capacitance of 21.50 $\mu F\ cm^{-2}$. In order to create supercapacitors, Slonopas et. al. [112] press and sinter $MAPbI_3$ powders positioned between two gold contacts and the resulting device exhibited energy density of 34.2 $Wh\ kg^{-1}$ with mean areal capacitance of 432 $mF\ cm^{-2}$.

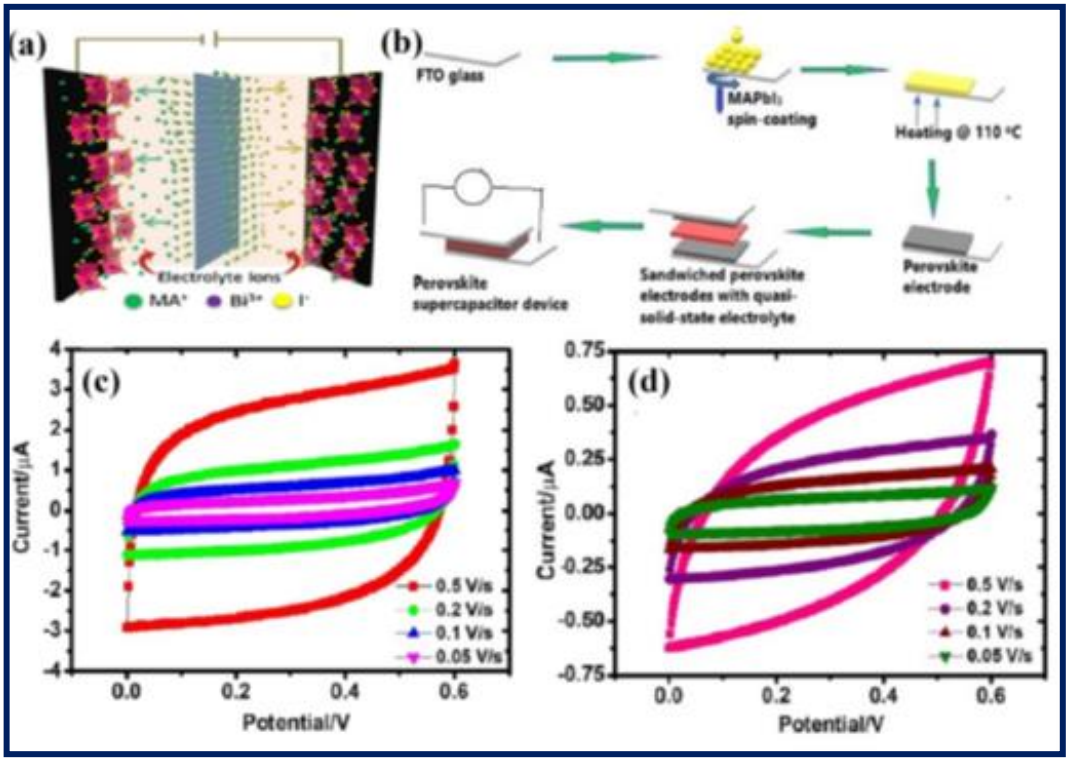

Figure 2.7: (a) Schematic representation of the super capacitor, (b) stepwise design of symmetric $MAPbI_3$ supercapacitor device, (c) CV curves of one-step process, (d) CV curves of two-step process (web page).

Considering the toxicity and environmental hazards the use of lead-free Supercapacitors are being encouraged. The use of $(CH_3NH_3)_3Bi_2I_9$ (MBI) as an electrode material for Supercapacitor was reported by Pious. et. al. [113] MBI based supercapacitor displayed areal capacitance of 5.5 mF cm^{-2} and the device kept 84.8% of its initial maximum capacitance even after 10000 charge–discharge cycles. Apart from these efforts Maji. et. al. [114] reported the use of $CsPbI_3$ microwires as an electrode material for Supercapacitor Application. With a specific capacitance of 7.23 mF cm^{-2} at a scan rate of 2 mV S^{-1} and 65.5% cyclic stability after 1000 cycles, the device exhibits good electrochemical properties.

All of the above-mentioned restricted investigations have certain shortcomings, including low specific capacitance, poor cycle stability with no proper charge storage mechanism explanation

till date. Our study to use the halide perovskite materials for Supercapacitor application have attempted to uncover the issues in this thesis.

2.2 References:

[1] Sharma V, Mishra S, Upadhyay P, Kulshrestha V. Carbon-based electrode materials with ion exchange membranes for enhanced membrane capacitive deionization. Colloids Surf A Physicochem Eng Asp 2023; 676: 132064.

[2] Ahmad F, Zahid M, Jamil H, Khan MA, Atiq S, Bibi M, et al. Advances in graphene-based electrode materials for high-performance supercapacitors: a review. J Energy Storage 2023; 72: 108731.

[3] Rustamaji H, Prakoso T, Devianto H, Widiatmoko P. Optimization of Electrode Material Composition from Activated Carbon, MWCNT & Graphene to Enhance Performance of Supercapacitor. Journal of Engineering and Technological Sciences 2022; 54: 220505.

[4] Borenstein A, Hanna O, Attias R, Luski S, Brousse T, Aurbach D. Carbon-based composite materials for supercapacitor electrodes: a review. J Mater Chem A Mater 2017; 5: 12653–72.

[5] Said B, Bacha O, Rahmani Y, Harfouche N, Kheniche H, Zerrouki D, et al. Activated carbon prepared by hydrothermal pretreatment-assisted chemical activation of date seeds for supercapacitor application. Inorg Chem Commun 2023; 155: 111012.

[6] Wang D, Geng Z, Li B, Zhang C. High performance electrode materials for electric double-layer capacitors based on biomass-derived activated carbons. Electrochim Acta 2015; 173: 377–84.

[7] Ramalingam G, Priya AK, Gnanasekaran L, Rajendran S, Hoang TKA. Biomass and waste derived silica, activated carbon and ammonia-based materials for energy-related applications–A review. Fuel 2024; 355: 129490.

[8] Kumari R, Singh V, Kant CR. Enhanced performance of activated carbon-based supercapacitor derived from waste soybean oil with coffee ground additives. Mater Chem Phys 2023; 305: 127882.

[9] Raphey VR, Henna TK, Nivitha KP, Mufeedha P, Sabu C, Pramod K. Advanced biomedical applications of carbon nanotube. Materials Science and Engineering: C 2019; 100: 616–30.

[10] Thuy UTD, Nam PV, Van Chi N, Duong TX, Van Hoa N. Chitosan-derived carbon aerogel nanocomposite as an active electrode material for high-performance supercapacitors. Journal of Science: Advanced Materials and Devices 2023; 8: 100586.

[11] Lee J-H, Lee S-Y, Park S-J. Highly porous carbon aerogels for high-performance supercapacitor electrodes. Nanomaterials 2023; 13: 817.

[12] Hu J, Zhao C, Si Y, Hong C, Xing Y, Wang Y, et al. Preparation of ultrafine microporous nitrogen self-doped chitosan (CS) carbon aerogel based on a Zn-Zn system for high-performance supercapacitors. Appl Surf Sci 2023; 637: 157910.

[13] Asfaw HD, Kucernak A, Greenhalgh ES, Shaffer MSP. Electrochemical performance of supercapacitor electrodes based on carbon aerogel-reinforced spread tow carbon fiber fabrics. Compos Sci Technol 2023; 238: 110042.

[14] Lota K, Khomenko V, Frackowiak E. Capacitance properties of poly (3, 4-ethylenedioxythiophene)/carbon nanotubes composites. Journal of Physics and Chemistry of Solids 2004; 65: 295–301.

[15] Boota M, Jung E, Ahuja R, Hussain T. MXene binder stabilizes pseudocapacitance of conducting polymers. J Mater Chem A Mater 2021; 9: 20356–61.

[16] Ambade RB, Ambade SB, Shrestha NK, Nah Y-C, Han S-H, Lee W, et al. Polythiophene infiltrated TiO_2 nanotubes as high-performance supercapacitor electrodes. Chemical Communications 2013; 49: 2308–10.

[17] Snook GA, Kao P, Best AS. Conducting-polymer-based supercapacitor devices and electrodes. J Power Sources 2011; 196: 1–12.

[18] Mastragostino M, Arbizzani C, Soavi F. Polymer-based supercapacitors. J Power Sources 2001; 97: 812–5.

[19] Gurunathan K, Murugan AV, Marimuthu R, Mulik UP, Amalnerkar DP. Electrochemically synthesised conducting polymeric materials for applications towards technology in electronics, optoelectronics and energy storage devices. Mater Chem Phys 1999; 61: 173–91.

[20] Yadav MS. Metal oxides nanostructure-based electrode materials for supercapacitor application. Journal of Nanoparticle Research 2020; 22: 367.

[21] Guan C, Liu J, Wang Y, Mao L, Fan Z, Shen Z, et al. Iron oxide-decorated carbon for supercapacitor anodes with ultrahigh energy density and outstanding cycling stability. ACS Nano 2015; 9: 5198–207.

[22] Boyd S, Augustyn V. Transition metal oxides for aqueous sodium-ion electrochemical energy storage. Inorg Chem Front 2018; 5: 999–1015.

[23] Arunachalam R, Prataap RKV, Pavul Raj R, Mohan S, Vijayakumar J, Péter L, et al. Pulse electrodeposited RuO_2 electrodes for high-performance supercapacitor applications. Surface Engineering 2019; 35: 102–8.

[24] Ji S-H, Chodankar NR, Kim D-H. Aqueous asymmetric supercapacitor based on RuO_2-WO_3 electrodes. Electrochim Acta 2019; 325: 134879.

[25] Jeon S, Jeong JH, Yoo H, Yu HK, Kim B-H, Kim MH. RuO_2 nanorods on electrospun carbon nanofibers for supercapacitors. ACS Appl Nano Mater 2020; 3: 3847–58.

[26] Wu D, Xie X, Zhang Y, Zhang D, Du W, Zhang X, et al. MnO_2/carbon composites for supercapacitor: synthesis and electrochemical performance. Front Mater 2020; 7: 2.

[27] Sutrave S, Konda S, Velpula D, Volety SA, Ravula SR, Chidurala SC, et al. A simple solution combustion method for the synthesis of V_2O_5 nanostructures for supercapacitor applications. Applied Surface Science Advances 2022; 12: 100331.

[28] Kunhikrishnan L, Shanmugham R, Sivashanmugam G. Electrochemical performance evaluation of template-assisted and morphology-modified ultra-small-sized NiO as electrodes for supercapacitors. Journal of Solid State Electrochemistry 2021; 25: 1–11.

[29] Zhang J, Huang R, Dong Z, Lin H, Han S. An illumination-assisted supercapacitor of rice-like CuO nanosheet coated flexible carbon fiber. Electrochim Acta 2022; 430: 140789.

[30] Maile N, Shinde SK, Patil SS, Kim D-Y, Fulari A V, Lee DS, et al. Capacitive property studies of electrochemically synthesized Co_3O_4 and Mn_3O_4 on inexpensive stainless steel current collector for supercapacitor application. Ceram Int 2020; 46: 14640–9.

[31] Pore OC, Fulari A V, Chavare CD, Sawant DS, Patil SS, Shejwal R V, et al. Synthesis of $NiCo_2O_4$ microflowers by facile hydrothermal method: Effect of precursor concentration. Chem Phys Lett 2023; 824: 140551.

[32] Chen Y, Yang H, Sun Y, Li Y, Wei M. High-performanced flexible solid supercapacitor based on the hierarchical $MnCo_2O_4$ micro-flower. Electrochim Acta 2022; 429: 141037.

[33] M Zawawi SM, Yahya R, Hassan A, Mahmud HNME, Daud MN. Structural and optical characterization of metal tungstates (MWO_4; M= Ni, Ba, Bi) synthesized by a sucrose-templated method. Chem Cent J 2013; 7: 1–10.

[34] Rosal FJO, Gouveia AF, Sczancoski JC, Lemos PS, Longo E, Zhang B, et al. Electronic structure, growth mechanism, and sonophotocatalytic properties of sphere-like self-assembled $NiWO_4$ nanocrystals. Inorg Chem Commun 2018; 98: 34–40.

[35] Pourmortazavi SM, Rahimi-Nasrabadi M, Karimi MS, Mirsadeghi S. Evaluation of photocatalytic and supercapacitor potential of nickel tungstate nanoparticles synthesized by electrochemical method. New Journal of Chemistry 2018; 42: 19934–44.

[36] Hosseini S, Farsi H, Moghiminia S, Zubkov T, Lightcap I V, Riley A, et al. Nickel tungstate ($NiWO_4$) nanoparticles/graphene composites: preparation and photoelectrochemical applications. Semicond Sci Technol 2018; 33: 055008.

[37] Kuzmin A, Kalinko A, Evarestov R. First-principles LCAO study of phonons in $NiWO_4$. Open Physics 2011; 9: 502–9.

[38] Huang Y, Gao Y, Liu C, Cao Z, Wang Y, Li Z, et al. Amorphous $NiWO_4$ nanospheres with high-conductivity and-capacitive performance for supercapacitors. The Journal of Physical Chemistry C 2019; 123: 30067–76.

[39] Packiaraj R, Devendran P, Venkatesh KS, Nallamuthu N. Investigation on the structural, morphological and electrochemical properties of nickel tungstate for energy storage application. Inorg Chem Commun 2021; 126: 108490.

[40] Tang J, Chen M, Xu H. Zn Ion-Doped Amorphous $NiWO_4$ Nanospheres as Cathode Material for High-Performance Asymmetric Supercapacitors. J Electron Mater 2021; 50: 7240–9.

[41] Hekmat F, Tutel Y, Unalan HE. Wearable supercapacitors based on nickel tungstate decorated commercial cotton fabrics. Int J Energy Res 2020; 44: 7603–16.

[42] Yang M, Zheng C, Wang Q, Yin J, Yang L, Wang O, et al. Improvement of specific capacitance and rate performance of $NiWO_4$ synthesized through modified chemical precipitation. Journal of Materials Science: Materials in Electronics 2021; 32: 12232–40.

[43] Niu L, Li Z, Xu Y, Sun J, Hong W, Liu X, et al. Simple synthesis of amorphous $NiWO_4$ nanostructure and its application as a novel cathode material for asymmetric supercapacitors. ACS Appl Mater Interfaces 2013; 5: 8044–52.

[44] He G, Li J, Li W, Li B, Noor N, Xu K, et al. One pot synthesis of nickel foam supported self-assembly of $NiWO_4$ and $CoWO_4$ nanostructures that act as high performance electrochemical capacitor electrodes. J Mater Chem A Mater 2015; 3: 14272–8.

[45] Han K, Zhong Z, Zhang W, Wu J, Liu S. Rational Design and Construction of Nanoporous and Nanosize $NiWO_4$ for High-Performance Supercapacitors. Russian Journal of Physical Chemistry A 2022; 96: S122–31.

[46] Nagaraju G, Kakarla R, Cha SM, Yu JS. Highly flexible conductive fabrics with hierarchically nanostructured amorphous nickel tungsten tetraoxide for enhanced electrochemical energy storage. Nano Res 2015; 8: 3749–63.

[47] Chebrolu VT-V, Balakrishnan B, Cho I, Bak J-S, Kim H-J. Selenium vacancies enriched the performance of supercapacitors with excellent cycling stability via a simple chemical bath deposition method. Dalton Transactions 2019; 48: 8254–63.

[48] Ling C, Zhou LQ, Jia H. First-principles study of crystalline $CoWO_4$ as oxygen evolution reaction catalyst. RSC Adv 2014; 4: 24692–7.

[49] Rajagopal S, Nataraj D, Khyzhun OY, Djaoued Y, Robichaud J, Mangalaraj D. Hydrothermal synthesis and electronic properties of $FeWO_4$ and $CoWO_4$ nanostructures. J Alloys Compd 2010; 493: 340–5.

[50] Jia H, Stark J, Zhou LQ, Ling C, Sekito T, Markin Z. Different catalytic behavior of amorphous and crystalline cobalt tungstate for electrochemical water oxidation. RSC Adv 2012; 2: 10874–81.

[51] Li A, Tu Y, Zhu Y, Li D, Zhou W, Zhu X, et al. $CoWO_4$ nanoparticles prepared in different solvents and their pseudocapacitant performances. Int J Electrochem Sci 2017; 12: 5646–56.

[52] Hoang K, Oh M, Choi Y. Electronic structure, polaron formation, and functional properties in transition-metal tungstates. RSC Adv 2018; 8: 4191–6.

[53] Adib K, Rahimi-Nasrabadi M, Rezvani Z, Pourmortazavi SM, Ahmadi F, Naderi HR, et al. Facile chemical synthesis of cobalt tungstates nanoparticles as high performance supercapacitor. Journal of Materials Science: Materials in Electronics 2016; 27: 4541–50.

[54] Fan X, Chen X. Hydrothermal synthesis of flower-like $CoWO_4$ with good supercapacitive performances. Proceedings 11th International Conference on Nanomaterials-Research & Application, 2019, 215–20.

[55] Chu D, Guo D, Xiao B, Tan L, Ma H, Pang H, et al. 3D Hollow Flower-like $CoWO_4$ Derived from ZIF-67 Grown on Ni-foam for High-Performance Asymmetrical Supercapacitors. Chemistry–An Asian Journal 2020; 15: 1750–5.

[56] Oliveira YL, Gouveia AF, Costa MJS, Lopes FHP, Sczancoski JC, Longo E, et al. Investigation of electronic structure, morphological features, optical, colorimetric, and

supercapacitor electrode properties of $CoWO_4$ crystals. Mater Sci Energy Technol 2022; 5: 125–44.

[57] Patil SJ, Chodankar NR, Huh YS, Han Y, Lee DW. Bottom-up Approach for Designing Cobalt Tungstate Nanospheres through Sulfur Amendment for High-Performance Hybrid Supercapacitors. ChemSusChem 2021; 14: 1602–11.

[58] Patil SS, Chougale UM, Kambale RK, Fulari VJ. Hydrothermal synthesis of $CoWO_4$ nanoparticles and evaluation of their supercapacitive performance. J Energy Storage 2023; 67: 107517.

[59] Sun Y, Liu S, Huang N, Wang X, Liu J, Bi J, et al. Regulation preferred crystal plane and oxygen vacancy of $CoWO_4$ with morphology remolding to boost electrochemical performances for battery-supercapacitor hybrid device electrode. J Power Sources 2022; 545: 231911.

[60] Xing X, Gui Y, Zhang G, Song C. $CoWO_4$ nanoparticles prepared by two methods displaying different structures and supercapacitive performances. Electrochim Acta 2015; 157: 15–22.

[61] Chen S, Yang G, Jia Y, Zheng H. Facile synthesis of $CoWO_4$ nanosheet arrays grown on nickel foam substrates for asymmetric supercapacitors. ChemElectroChem 2016; 3: 1490–6.

[62] Aneesh K, Berchmans S. Enhanced peroxidase-like activity of $CuWO_4$ nanoparticles for the detection of NADH and hydrogen peroxide. Sens Actuators B Chem 2017; 253: 723–30.

[63] Lhermitte CR, Bartlett BM. Advancing the chemistry of $CuWO_4$ for photoelectrochemical water oxidation. Acc Chem Res 2016; 49: 1121–9.

[64] Hu X, Gao D, Li Y, Dong H, Zhou W, Yang L, et al. Fabrication of novel $CuWO_4$ nanoparticles (NPs) for photocatalytic degradation of methylene blue in aqueous solution. SN Appl Sci 2019; 1: 1–10.

[65] Mohammadikish M, Masteri-Farahani M, Mahdian T. Optical properties of copper tungstate nanoparticles prepared by microemulsion method. Inorganic and Nano-Metal Chemistry 2019; 49: 63–8.

[66] Souza ELS, Sczancoski JC, Nogueira IC, Almeida MAP, Orlandi MO, Li MS, et al. Structural evolution, growth mechanism and photoluminescence properties of $CuWO_4$ nanocrystals. Ultrason Sonochem 2017; 38: 256–70.

[67] Pourmortazavi SM, Rahimi-Nasrabadi M, Khalilian-Shalamzari M, Ghaeni HR, Hajimirsadeghi SS. Facile chemical synthesis and characterization of copper tungstate nanoparticles. J Inorg Organomet Polym Mater 2014; 24: 333–9.

[68] Roshani R, Tadjarodi A, Ghaffarinejad A. The effect of annealing temperature on the structure and supercapacitive properties of copper tungstate. Mater Lett 2021; 293: 129644.

[69] Balasubramanian V, Kannan S, Nishanthi ST, Sivakumar G, Mohanraj K. Elucidate the pseudocapacitive behaviour of $CuWO_4$ electrode synthesized by solid-state reaction. Journal of Materials Science: Materials in Electronics 2020; 31: 10142–50.

[70] Samantaray KS, Sahoo S, Rout CS. Hydrothermal synthesis of $CuWO_4$-reduced graphene oxide hybrids and supercapacitor application. Am J Eng Applied Sci 2016; 9: 584–90.

[71] Kumar RD, Karuppuchamy S. Microwave-assisted synthesis of copper tungstate nanopowder for supercapacitor applications. Ceram Int 2014; 40: 12397–402.

[72] Ahmed J, Ahamad T, Alhokbany N, Almaswari BM, Ahmad T, Hussain A, et al. Molten salts derived copper tungstate nanoparticles as bifunctional electro-catalysts for electrolysis of water and supercapacitor applications. ChemElectroChem 2018; 5: 3938–45.

[73] Roshani R, Tadjarodi A. Preparation of nanocomposite with different component ratios of $CuWO_4$ nanoparticles and nitrogen-doped reduced graphene oxide to compare their supercapacitive properties. J Alloys Compd 2021; 856: 157302.

[74] Muthamizh S, Suresh R, Giribabu K, Manigandan R, Kumar SP, Munusamy S, et al. $MnWO_4$ nanocapsules: synthesis, characterization and its electrochemical sensing property. J Alloys Compd 2015; 619: 601–9.

[75] Yao S, Xing L, Dong Y, Wu X. Hierarchical WO_3@$MnWO_4$ core-shell structure for asymmetric supercapacitor with ultrahigh cycling performance at low temperature. J Colloid Interface Sci 2018; 531: 216–24.

[76] Harichandran G, Divya P, Radha S, Yesuraj J. Facile and controllable CTAB-assisted sonochemical synthesis of one-dimensional $MnWO_4$ nanorods for supercapacitor application. J Mol Struct 2020; 1199: 126931.

[77] Tang J, Shen J, Li N, Ye M. Facile synthesis of layered $MnWO_4$/reduced graphene oxide for supercapacitor application. J Alloys Compd 2016; 666: 15–22.

[78] Raj BGS, Acharya J, Seo M-K, Khil M-S, Kim H-Y, Kim B-S. One-pot sonochemical synthesis of hierarchical $MnWO_4$ microflowers as effective electrodes in neutral electrolyte for high performance asymmetric supercapacitors. Int J Hydrogen Energy 2019; 44: 10838–51.

[79] Naik KK, Gangan AS, Pathak A, Chakraborty B, Nayak SK, Rout CS. Facile Hydrothermal Synthesis of $MnWO_4$ Nanorods for Non-Enzymatic Glucose Sensing and Supercapacitor Properties with Insights from Density Functional Theory Simulations. ChemistrySelect 2017; 2: 5707–15.

[80] Li F, Xu X, Huo J, Wang W. A simple synthesis of $MnWO_4$ nanoparticles as a novel energy storage material. Mater Chem Phys 2015; 167: 22–7.

[81] Assis M, Tello ACM, Abud FSA, Negre P, Ribeiro LK, Ribeiro RAP, et al. Bridging experiment and theory: Morphology, optical, electronic, and magnetic properties of $MnWO_4$. Appl Surf Sci 2022; 600: 154081.

[82] Shim H, Lim A, Kim J, Lee G, Kim D. Hydrothermal realization of a hierarchical, flowerlike $MnWO_4$@ MWCNTs nanocomposite with enhanced reversible Li storage as a new anode material. Chemistry–An Asian Journal 2013; 8: 2851–8.

[83] Shembade U V, Moholkar RA, Ambi NH, Nikam KS, Wategaonkar SB, Padalkar NS, et al. Ion-by-Ion Adsorption Process and Reaction for the Synthesis of Hierarchical Manganese Tungstate ($MnWO_4$) Microflowers as an Energy-Efficient Electrode for Supercapacitors. ACS Applied Engineering Materials 2024; 2: 672–82.

[84] Roy N, Mangiri R, Reddy GP, Manohar A, Chung E, Raju BDP, et al. Carbon nanofiber-supported elongated square bipyramid-like $MnWO_4$ composite electrodes for high-performance battery-type supercapacitors: Enhanced electrochemical performance via synergistic effect. Journal of Electroanalytical Chemistry 2023; 947: 117764.

[85] Karuppaiah B, Sukanya R, Chen S-M, Chavan PR, Karthik R, Hasan M, et al. Morphological and electrocatalytic studies on Ni^{2+} doped $MnWO_4$ microflowers: A dual mode catalyst for the electrochemical sensor and supercapacitor application. J Energy Storage 2024; 79: 110145.

[86] Li F, Xu X, Huo J, Wang W. A simple synthesis of $MnWO_4$ nanoparticles as a novel energy storage material. Mater Chem Phys 2015; 167: 22–7.

[87] Nithiyanantham U, Ede SR, Kesavan T, Ragupathy P, Mukadam MD, Yusuf SM, et al. Shape-selective formation of $MnWO_4$ nanomaterials on a DNA scaffold: magnetic, catalytic and supercapacitor studies. RSC Adv 2014; 4: 38169–81.

[88] Yesuraj J, Elanthamilan E, Muthuraaman B, Suthanthiraraj SA, Merlin JP. Bio-assisted hydrothermal synthesis and characterization of $MnWO_4$ nanorods for high-performance supercapacitor applications. J Electron Mater 2019; 48: 7239–49.

[89] Naik KK, Gangan AS, Pathak A, Chakraborty B, Nayak SK, Rout CS. Facile Hydrothermal Synthesis of $MnWO_4$ Nanorods for Non-Enzymatic Glucose Sensing and Supercapacitor Properties with Insights from Density Functional Theory Simulations. ChemistrySelect 2017; 2: 5707–15.

[90] Saranya S, Senthilkumar ST, Sankar KV, Selvan RK. Synthesis of $MnWO_4$ nanorods and its electrical and electrochemical properties. J Electroceram 2012; 28: 220–5.

[91] Raj BGS, Acharya J, Seo M-K, Khil M-S, Kim H-Y, Kim B-S. One-pot sonochemical synthesis of hierarchical $MnWO_4$ microflowers as effective electrodes in neutral electrolyte for high performance asymmetric supercapacitors. Int J Hydrogen Energy 2019; 44: 10838–51.

[92] Tang J, Shen J, Li N, Ye M. Facile synthesis of layered $MnWO_4$/reduced graphene oxide for supercapacitor application. J Alloys Compd 2016; 666: 15–22.

[93] Tan P, Liu M, Shao Z, Ni M. Recent advances in perovskite oxides as electrode materials for nonaqueous lithium–oxygen batteries. Adv Energy Mater 2017; 7: 1602674.

[94] Mefford JT, Hardin WG, Dai S, Johnston KP, Stevenson KJ. Anion charge storage through oxygen intercalation in $LaMnO_3$ perovskite pseudocapacitor electrodes. Nat Mater 2014; 13: 726–32.

[95] Cao Y, Liang J, Li X, Yue L, Liu Q, Lu S, et al. Recent advances in perovskite oxides as electrode materials for supercapacitors. Chemical Communications 2021; 57: 2343–55.

[96] Liu Y, Jiang SP, Shao Z. Intercalation pseudocapacitance in electrochemical energy storage: recent advances in fundamental understanding and materials development. Mater Today Adv 2020; 7: 100072.

[97] Che W, Wei M, Sang Z, Ou Y, Liu Y, Liu J. Perovskite $LaNiO_3$-δ oxide as an anion-intercalated pseudocapacitor electrode. J Alloys Compd 2018; 731: 381–8.

[98] Zhang Y, Ding J, Xu W, Wang M, Shao R, Sun Y, et al. Mesoporous $LaFeO_3$ perovskite derived from MOF gel for all-solid-state symmetric supercapacitors. Chemical Engineering Journal 2020; 386: 124030.

[99] Hou X, Sun J, Lian M, Peng Y, Jiang D, Xu M, et al. Emerging Synthetic Methods and Applications of MOF-Based Gels in Supercapacitors, Water Treatment, Catalysis, Adsorption, and Energy Storage. Macromol Mater Eng 2023; 308: 2200469.

[100] Wohlfahrt-Mehrens M, Schenk J, Wilde PM, Abdelmula E, Axmann P, Garche J. New materials for supercapacitors. J Power Sources 2002; 105: 182–8.

[101] George G, Jackson SL, Luo CQ, Fang D, Luo D, Hu D, et al. Effect of doping on the performance of high-crystalline $SrMnO_3$ perovskite nanofibers as a supercapacitor electrode. Ceram Int 2018; 44: 21982–92.

[102] Tomar AK, Joshi A, Singh G, Sharma RK. Triple perovskite oxide as an advanced pseudocapacitive material: multifarious element approach with an ordered structure. J Mater Chem A Mater 2020; 8: 24013–23.

[103] Chen J, He Z, Li G, An T, Shi H, Li Y. Visible-light-enhanced photothermocatalytic activity of ABO_3-type perovskites for the decontamination of gaseous styrene. Appl Catal B 2017; 209: 146–54.

[104] Hu Q, Yue B, Shao H, Yang F, Wang J, Wang Y, et al. Facile syntheses of cerium-based $CeMO_3$ (M= Co, Ni, Cu) perovskite nanomaterials for high-performance supercapacitor electrodes. J Mater Sci 2020; 55: 8421–34.

[105] Yin S, Wu Y, Chen J, Chen Z, Hou H, Liu Q, et al. Facile hydrothermal synthesis of s$BiFeO_3$ nanoplates for enhanced supercapacitor properties. Functional Materials Letters 2018; 11: 1850013.

[106] Kim H-Y, Shin J, Jang I-C, Ju Y-W. Hydrothermal synthesis of three-dimensional perovskite NiMnO3 oxide and application in supercapacitor electrode. Energies (Basel) 2019; 13: 36.

[107] Cao Y, Liang J, Li X, Yue L, Liu Q, Lu S, et al. Recent advances in perovskite oxides as electrode materials for supercapacitors. Chemical Communications 2021; 57: 2343–55.

[108] Narayanan S, Parikh N, Tavakoli MM, Pandey M, Kumar M, Kalam A, et al. Metal halide perovskites for energy storage applications. Eur J Inorg Chem 2021; 2021: 1201–12.

[109] Yang T, Gregori G, Pellet N, Grätzel M, Maier J. The significance of ion conduction in a hybrid organic–inorganic lead-iodide-based perovskite photosensitizer. Angewandte Chemie 2015; 127: 8016–21.

[110] Cheng Y, Li H-W, Qing J, Yang Q-D, Guan Z, Liu C, et al. The detrimental effect of excess mobile ions in planar $CH_3NH_3PbI_3$ perovskite solar cells. J Mater Chem A Mater 2016; 4: 12748–55.

[111] Popoola I, Gondal M, Oloore L, Popoola A, AlGhamdi J. Fabrication of organometallic halide perovskite electrochemical supercapacitors utilizing quasi-solid-state electrolytes for energy storage devices. Electrochim Acta 2020; 332: 135536.

[112] Slonopas A, Ryan H, Norris P. Ultrahigh energy density $CH_3NH_3PbI_3$ perovskite based supercapacitor with fast discharge. Electrochim Acta 2019; 307: 334–40.

[113] Pious JK, Lekshmi ML, Muthu C, Rakhi RB, Vijayakumar C. Zero-dimensional methylammonium bismuth iodide-based lead-free perovskite capacitor. ACS Omega 2017; 2: 5798–802.

[114] Maji P, Ray A, Sadhukhan P, Roy A, Das S. Fabrication of symmetric supercapacitor using cesium lead iodide ($CsPbI_3$) microwire. Mater Lett 2018; 227: 268–71.

Chapter 3: Instruments & Apparatus

3.1 Brief description about general synthesis apparatus:

3.1.1 Furnace and Oven:

Solid state reactions or sample annealing were carried out in open air using a simple muffle furnace. The furnace was front-loading and could reach temperatures of up to 1100˚C. The furnace's heating rate may be adjusted with an accuracy of ± 0.2˚C using an electronic temperature controller. Samples were loaded using an alumina boat or crucible. A basic hot air oven was employed for hydrothermal or wet chemical reactions with temperatures below 250˚C. Temperature was controlled by a thermostat fitted to these ovens. Aside from synthesis, ovens were employed to dry samples. Figure 3.1 shows an image of a furnace and oven.

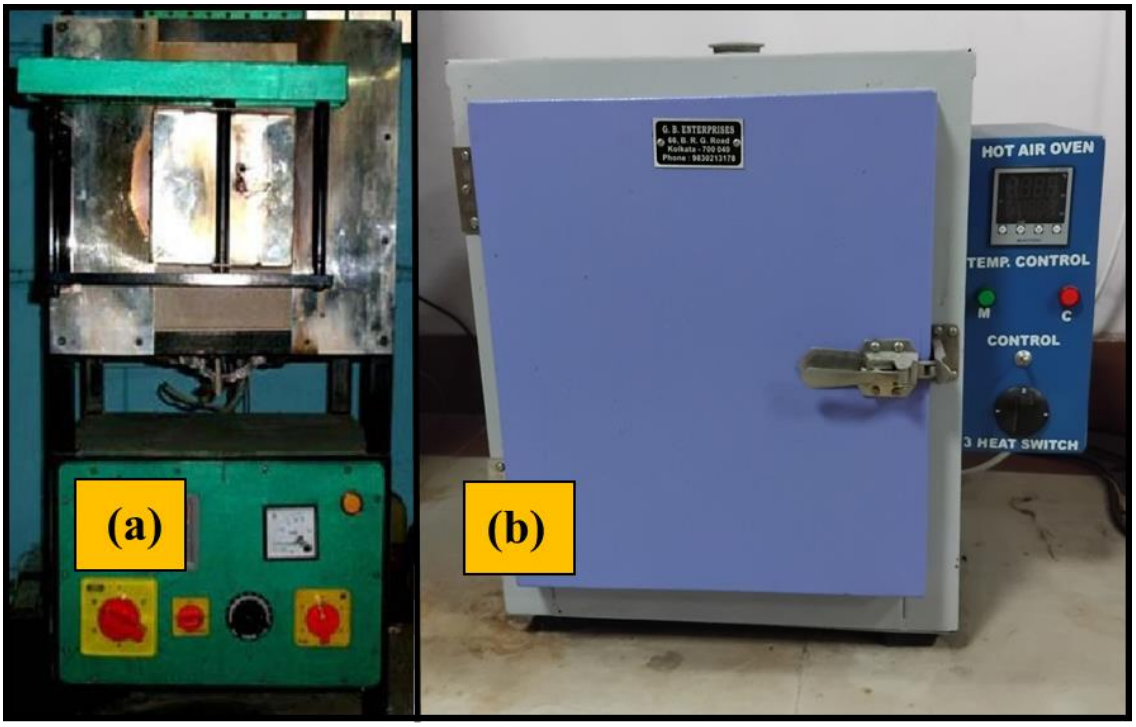

Figure 3.1: Image of a furnace and hot air oven.

3.1.2 Autoclave reactor for hydrothermal synthesis:

Chemical reactions are carried out at high pressure and high temperature in hydrothermal autoclave reactors, which are similar to pressure cookers. Because it operates at such high temperatures, it is also known as a hydrothermal bomb. The two most common types of hydrothermal reactors are the PPL lined autoclave and the Polytetrafluoroethylene (PTFE) or Teflon lined autoclave. The two primary components of a hydrothermal reactor are an outside jacket made of premium stainless steel and an inside Teflon liner, sometimes known as a Teflon chamber. In an autoclave lined with Teflon, the maximum reaction temperature is 240°C (428 F), while the safe temperature for hydrothermal reactions is 200°C (392 F). The majority of the experiments in this thesis are carried out as safely as possible below 200°C.In this thesis, temperature and reaction time are optimised in a hydrothermal reactor to create nanostructures with regulated morphology. Figure 3.2 represents image of a teflon lined autoclave.

Figure 3.2: Image of a teflon lined autoclave.

3.2 Major Accessories for applications:

3.2.1 Instrument for electrochemical measurements:

Autolab PGSTAT Multi Autolab/(M204) is used to measure the electrochemical properties of the as-prepared electrode. This apparatus can perform Cyclic Voltametry (CV), Galvanostatic Charge Discharge (GCD), Nyquist, and Mott Schottky measurements. This instrument has been used to perform both three (3) and two (2) electrode measurements, with Ag/AgCl serving as the reference electrode, Pt wire serving as the counter electrode, and as synthesised nanomaterials in a flexible substrate serving as the working electrode, with an acidic/basic aqueous electrolyte serving as the required electrolyte. This high-end, high-current multichannel galvanostat has a compliance voltage of 20 V, a bandwidth of 1 MHz, and a maximum current of 0.4 A. It can do many measurements at the same time. The current ranges can be adjusted from 10nA to 100mA, for a total of eight ranges. Gamry Interface 1000 cell was also used for electrochemical studies. Figure 3.3 shows the diagram of instruments used.

Figure 3.3: (a) Autolab PGSTAT (M204) and (b) Gamry Interface 1000 instrument diagram.

3.3 Major instruments for characterizations:

3.3.1 X-Ray Diffractometer (XRD):

X-ray diffraction (XRD) was used to determine the phase of synthesised materials using a D8 Advanced Bruker apparatus. Diffraction traces were collected in intensity vs. 2θ mode. A Germanium (022) monochromator was employed for CuKα (1.5406 Å) radiation from a highly stabilised Bruker X-ray generator (K780). Bragg's equation for first order diffraction can be used to determine the lattice spacing corresponding to a specific hkl plane.

$$2d_{hkl} \sin\theta = \lambda$$

In this equation, d_{hkl} represents inter-planar spacing, λ represents electron wavelength, and θ represents glancing angle. Rigaku XRD (MiniFlex 600) set-up was also used. A photograph of the instrument is shown in Figure 3.4

.

Figure 3.4: Image of X-rays diffractometers (a) D8 Advance Bruker set-up and (b) Rigaku MiniFlex 600 set-up.

3.3.2 X-ray photoelectron spectrometer:

X-ray photoelectron spectroscopy (XPS, Specs, Germany) was used to analyse the chemical composition of the nanostructure, the charge state of the dopants, and the purity of the sample. Surface study of thin films up to 3-600 atomic layers is performed using X-ray photoelectron

spectroscopy. The idea behind X-ray photoelectron spectroscopy, which is based on Einstein's photoelectric effect, is to illuminate a sample with an X-ray beam, which causes the material to emit photoelectron. Figure 3.5a shows a schematic representation of this electron emission mechanism. The binding energy (E_b) and the kinetic energy (E_k) of the released core electrons are connected by the formula E_b=hv-Ek-φsp, where φsp is the spectrometer work function and hν is the X-Ray energy that may be measured as a function of the number of electrons. The most accurate method for identifying the elements on the surface up to a few atomic layers is XPS since each element has a distinct set of binding energies. Moreover, elemental concentration in the sample can be measured using the area under the curve at nominal binding energies, which is also reliant on the sensitivity factor. Slight changes in these binding energies (chemical shifts) reveal details about the sample's chemical states and short-range chemistry. Higher positive oxidation states have higher binding energy due to the increased coulombic interaction between photoemitted electrons and the ion core atoms.

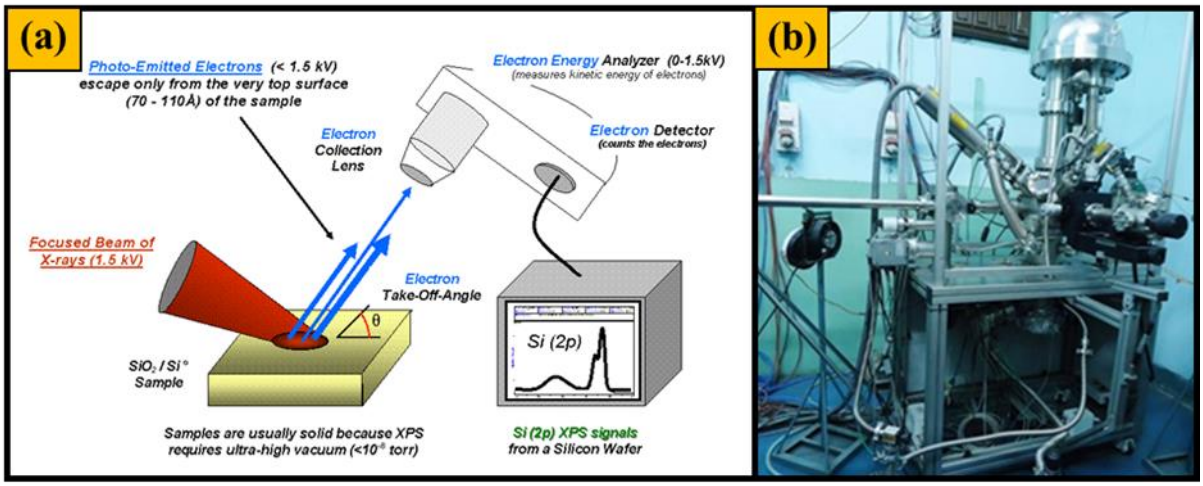

Figure 3.5: (a) Schematic presentation (source: webpage) and (b) image of XPS instrument.

The sample was analysed using a SPECS with a hemispherical energy analyser (HAS 3500). Photoelectron excitation was done using a monochromatic Mg Kα X-ray (1253.6 eV) or Al Kα X-ray (eV) source at 10 kV and 17 mA anode current. The system's residual pressure was

greater than ~10^{-9} mbar. Electrons disperse between the inner and outer hemispheres in spectroscopic mode. The 165 mm radius and eight-channel detector ensure great spectral resolution and sensitivity. The surface study and stoichiometric ratio of the synthesised nanocomposites were examined using the instrument's kinetic energy distribution. Figure 3.5b depicts a photo of X-ray photoelectron spectroscopy.

3.3.3 High resolution transmission electron microscope:

A transmission electron microscope (TEM) is a characterization tool that uses diffraction and imaging techniques to analyse both the crystal structure and microstructure of materials. However, high resolution transmission electron microscopy (HRTEM) is another imaging mode of the transmission electron microscope (TEM) that provides more precise and resolute images of the sample's crystallographic structure at the atomic scale, allowing researchers to determine the crystallinity of the sample. A thin sample is subjected to an electron beam with a constant current density in a conventional TEM. The electron gun emits electrons through numerous holes, while the lens illuminates the sample. The objective lens creates a diffraction pattern on the rear focal plane, which can be characterized as the Fourier transform of the wave function at the object exit surface, Ψ(r)n. The collimated beam passes through the sample, focusing the picture on the phosphor screen. Lastly, a CCD camera, direct exposure of the photographic emulsion, and other technologies are used to record the image digitally. The electric field accelerates the electron beam produced by the electron gun (which is often eliminated with tungsten or LaB6). The electron beam is often substantially greater than the ones used in HRTEM (150-250 kV) and SEM (5-30 kV). The beam can now travel through the sample in this manner. The objective lens creates an image that is first 25 times larger than the original, then the next lens keeps enlarging it until the final image is 106 times larger than the original. The sample is subject to separate interactions from every particle in the electron beam.

The positive atomic potential of the atomic nuclei attracts the beam when it enters the sample, which it channels along the lattice atomic column. Bragg diffraction is simultaneously caused by the interaction of electron waves in distinct atomic columns. To replicate electron microscope images more correctly, it is helpful to understand the basic principles of electron scattering and electron imaging. Brightfield imaging and darkfield imaging are the two imaging modalities that are frequently employed in TEM. In bright field imaging, a diaphragm stops the diffracted electrons, allowing just electrons to pass through without any diffraction to generate an image. However, the diffracted beam is employed for imaging in the dark field imaging mode.

Figure 3.6: Image of TEM instrument.

In this work, a transmission electron microscope (JEOL-JEM-2100) was used to study the crystalstructure and microstructure of thin films deposited on various substrates. This model

has three independent condensers, for any given probe size, can generate high probe current, thereby enhancing analysis and diffraction capabilities. This model offers a variety of pumping options, including dry/turbo pumps for laboratory environments. Oil-based or rotary pumps are not allowed. The instrument has a guaranteed resolution of 0.1 nm however the attained during routine measurements is 8–10 Å. The magnification of this model can vary from 50 X to 1,500,000 X, and the acceleration voltage is 80-200 kV. The suspension of the sample was dropped onto a carbon-coated copper mesh, and the solvent was allowed to evaporate, preparing the TEM sample. The HRTEM photo is displayed in Figure 3.6.

3.3.4 Field emission scanning electron microscope:

The field emission scanning electron microscope (FESEM), an electron microscope similar to the transmission electron microscope (TEM) but with many differences, was used to perform detailed morphological examinations of TMOs as well as MTMOs. In a raster scan pattern, the sample surface is scanned by a concentrated electron beam from a field emission source that has energy that is relatively lower than that of a TEM. The field emission gun emits electrons with energies between a few hundred and 50 KeV. Different deflection coils focus and accelerate the beam in a strong electrical field gradient after it is generated from the gun. Ultimately, the sample surface is struck by the collimated beam, which interacts with it and causes the sample to release electrons and photons. When the sample and electron beam exchange energy, the sample emits secondary electrons through inelastic scattering, electromagnetic radiation is released, and high-energy electrons are reflected by elastic scattering. These electrons can be collected by certain detectors and transformed into signals that reveal the composition of the sample, its surface topography, and many other of other properties. A variety of signals were produced by the FESEM, including transmitted electrons, characteristic X-rays, light (cathodoluminescence), secondary electrons, and back-scattered

electrons (BSE). FESEM is coupled to an EDX detector, which uses X-rays as a signal to provide chemical information about the material. The sample under research must be vacuum compatible and electrically conductive in order to facilitate conventional imaging in the FESEM by preventing the buildup of electrostatic charge at the surface. Before the imaging procedure, an ultrathin layer of gold or platinum is applied on nonconductive objects using sputtering or evaporation. Throughout the thesis project, surface morphology and film thickness are determined using a FESEM (HITACHI S4800). One might change the magnification from 30 X to 300,000 X with FESEM resolution is close to 5 nm. With a 35 mm single-lens reflex type camera (MP 35051, CSI 3) and a 50 mm focal length, this instrument offers both the Secondary Electron picture (SEI) and Backscattered Electron Image (BEI) picture modes. The final image may include details regarding the film's thickness and homogeneity. Figure 3.7 shows an example of the SEM instrument's image.

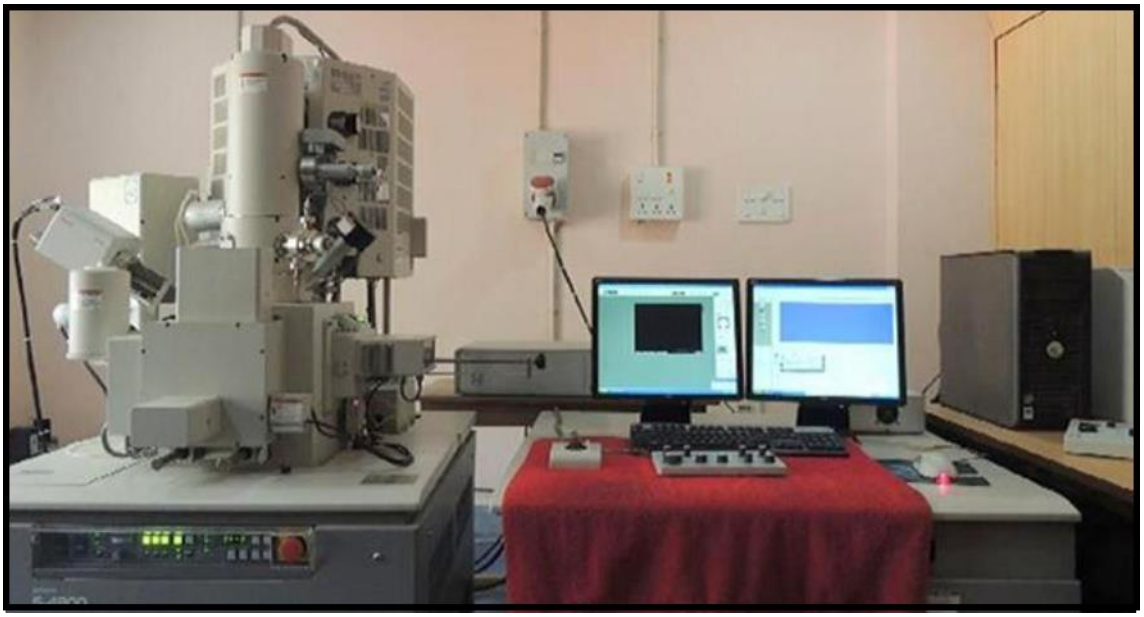

Figure 3.7: Image of FESEM instrument with EDX attachment.

3.3.5 Energy dispersive x-ray (EDX):

This method depends on characteristic X-ray peaks that arise from interactions between a sample and a high-energy electron beam. The characteristic X-rays that each element produces can be utilized to determine whether or not the element is present in the area under inspection. The relative concentration of each element in the sample can be found by comparing the X-ray peaks' relative intensities. In general, elements having atomic numbers smaller than six (Z = 6) are undetectable. The sample's composition is examined using an energy-dispersive X-ray (HITACHI S4800; operating at 15 kV). The device can identify elements ranging from uranium (92) to lithium (3). It is linked to a Hitachi S-4800 field emission scanning electron microscope (FESEM). The image can be found in Figure 3.7.

3.3.6 RAMAN Analysis:

Raman spectroscopy is used to examine the vibrational, rotational, and electronic modes that correspond to the molecular energy level of the nanostructures. The technique is based on the Raman Effect, which results in the deformation of the electron cloud upon the incidence of intense laser light. This consequently alters the molecule's polarizability, which is an outcome of a certain energy transition in molecules that gives rise to Raman modes. A test sample is exposed to a high-intensity monochromatic light beam, sometimes known as a laser beam. To remove the signal from the laser source within a very specific frequency band, notch filters are utilized. The photons' energy shift is either higher or lower than the incident energy owing to inelastic scattering. Thus, a shift known as the Raman Shift is observed. There is a possibility that some of the scattered radiation has frequencies that are either higher or lower than the incident frequency. Stokes lines and anti-Stokes lines are the names given to these, respectively. The Rayleigh scattering component has a scattering intensity that is approximately 105 times stronger than that of the Stokes lines. Compared to anti-Stokes lines, Stokes-shifted Raman spectra are more intense because they show transitions from lower to

higher vibrational energy levels. In turn, Stokes lines are evaluated in traditional Raman spectroscopy. Here, a Raman spectrometer (alpha 300R WI Tec Germany) equipped with a 532 nm laser source was used to get the Raman measurements. The image of the RAMAN Spectrometer in use is displayed in Figure 3.8.

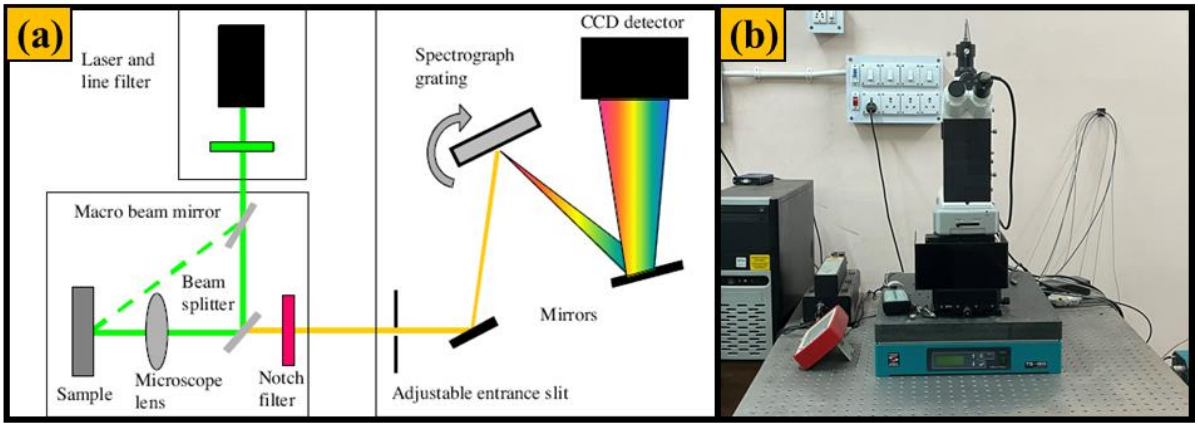

Figure 3.8: (a) Schematic presentation (source: webpage) and (b) image of RAMAN instrument.

3.3.7 BET Analysis:

The technique is used to get an estimate of a material's specific surface area. The BET theory is an expansion of the Langmuir theory, which was devised by Irving Langmuir in 1916 and relates the monolayer adsorption of gas molecules as a function of both temperature and pressure. It is based on the findings of Stephen Brunauer, Paul Emmett, and Edward Teller in 1938. As a result, the specific surface area can be determined by correlating the amount of gas that is adsorbed (not to be confused with absorption) on the surface of the adsorbent material. The pressure of the gas, temperature, and strength of the interaction between the gas and solid are some of the variables that regulate the adsorption process. While Langmuir theory is applied to the ideal monolayer adsorption system, BET theory is applicable to the multilayer adsorption system. Because of its strong interaction with the majority of solids and its high purity availability In BET surface analysis, nitrogen (N_2) gas is typically utilised; however,

other gases, such as Ar or CO_2, or even organic vapours (dynamic vapour sorption), may also be employed. Since the interactions between the solid and gaseous phases are often weak, the adsorbent material's surface undergoes cooling by N_2 gas to produce observable adsorption. Next, a known volume of nitrogen gas is gradually delivered into the sample cell. To reduce relative pressure below atmospheric pressure, partial vacuum conditions are established. Once the saturation pressure is reached, no more adsorption takes place, regardless of increasing pressure. Once the adsorption layers are established, the sample must be taken out of the nitrogen atmosphere and heated to liberate the adsorbed nitrogen from the substance and become quantized.

Figure 3.9: Image of the BET instrument.

The BET isotherm-which plots the amount of gas adsorbed against the relative pressure (P/P_0) data obtained from the instrument, is used to calculate the sample's specific surface area. The samples must be degassed to exclude water and other impurities before the surface area can be measured with precision. The sample's crystal structure is broken by setting the degassing temperature as high as possible, which will ultimately shorten the degassing time.

Electrochemical energy storage relies heavily on the determination of specific surface area and the size distribution of pores, both of which can be ascertained using BET theory. The macropores (>50 nm), mesopores (2-50 nm), and micropores (< 2 nm) of the isotherm can be identified by the shape of their hysteresis loop. The employed BET instrument is depicted in Figure 3.9.

Chapter 4: Amalgamation of $MnWO_4$ Nanorods with Amorphous Carbon Nanotubes for Highly Stabilized Energy Efficient Supercapacitor Electrode

4.1. Introduction

In consideration of the projected energy demands, increase in the level of the greenhouse gases globally and imminent consumption of fossil fuels, there is an indispensable necessity for alternative approaches capable of providing clean, sustainable and environmentally benign solution to cater our energy requirements [1]. Among all the documented systems regarding energy storage and conversion, supercapacitors (SCs) have been considered as most significant. In particular, electrochemical supercapacitors, also coined as supercapacitor, can store greater energy density in comparison with the capacitors usually found. With several advantageous traits such as fast charging discharging rates [2], long cycle lifetime [3], high-rate capability [4], wide operating temperature ranges [5], and safe operation, SCs have found widespread utility in hybrid electric vehicles [6], aircrafts [7], mobile communications [8], and smart grids etc. [9,10]. Depending on the charge storage principle, SC is generally classified into two categories: namely electrochemical double layer capacitor (EDLC) and pseudocapacitor. The former one stores charges electrostatically through reversible ion adsorption in electrolyte while capacitance of a pseudocapacitor originates from fast and revisable redox reaction process at interface. Carbonaceous materials in several nanoforms like particles, tubes and graphene are frequently used as the electrode materials for EDLC [11–13]. EDLC based on carbonaceous materials singularly offers high power density but often suffers from relatively low specific capacitance (C_s) [14–16]. Quite the reverse, pseudocapacitors largely based on transition metal oxides (TMOs), transition metal sulfides deliver much superior energy storage capacity and high-rate capability as compared to EDLCs [17–19]. TMOs have attracted substantial attention in recent times as electrode of supercapacitors due to their large abundance, suitable redox reaction of the transition metals, environmental friendliness, less toxicity, and high theoretical capacity [20].

Several kinds of TMOs like Co_3O_4, MnO_2, NiO, V_2O_5 and SnO_2 etc. have been studied extensively in this regard [21–23]. Unfortunately, low electrical conductivity associated with these mono metallic oxides limit them from easing the electron transport process towards high rate capability [24]. To overcome this issue as well as to bridge up the performance gap between the EDLC and pseudocapacitor, several attempts have been made in rational designing of new electrode materials via different routes. Enhancement of C_s values by considering multi-metallic oxides is very intriguing as they could exhibit better electronic conductivity and provide multiple oxidation state induced richer redox reactions than the single-component TMOs [25]. Being a bimetallic oxide, Manganese tungstate ($MnWO_4$) has drawn considerable attention owing to its extraordinary magnetic, catalytic and electrochemical characteristics and thereby its usage in optical fibres, photocatalysts, and humidity sensors [26]. $MnWO_4$ possesses monoclinic structure in which each Mn and W atom is in octahedral arrangement enclosed by six oxygen atoms. These oxygen atoms form a distorted hexagonal close packed structure with Mn and W atoms [22,24]. Compared to pure tungsten oxide, binary metal oxides of tungsten generally offer higher electrical conductivity where the incorporation of W atoms in the system enhances their conductivity [27]. Furthermore, because of the simultaneous presence of electrochemically active Mn and W atoms, $MnWO_4$ indeed offers promises as electrode material for SCs [28]. Several documentations on the electrochemical aspects of $MnWO_4$ are already available in literature. However, the energy densities as well as the capacitive performances of these electrodes made of the single materials are still unsatisfactory [29,30]. Additionally, cycling stabilities of these electrodes singularly remained an issue, constrained by the redox reaction sites and lesser contact between the active material and electrolyte [22]. Thus, rational design of hybrid structured electrode materials with improved electrochemical features is the need of hour. Hybrid structure with 1D backbone in the form of nanorod or nanotube could create stable

and easy pathways for electron transport. Amalgamation of carbonaceous material with multi-metallic oxides is very intriguing in this regard which could combine the advantage of high energy density of pseudocapacitors with high power density of EDLC in a single unit. Tang et al. have reported layered $MnWO_4$/reduced graphene oxide-based SC which delivered specific capacitance of 288 Fg^{-1} at scan rate of 5 mVs^{-1} [27]. Shim et al. have utilized phase-pure $MnWO_4$@MWCNTs as an electrode material for reversible Li storage [31]. To the best of our knowledge, presentation of such kind of hybrid with $MnWO_4$ and carbon or its derivative materials is rare in literature. Furthermore, in these reports the carbonaceous component of the hybrids was mostly prepared via complex route with stringent process controlling at high temperature which hindered its widespread usage.

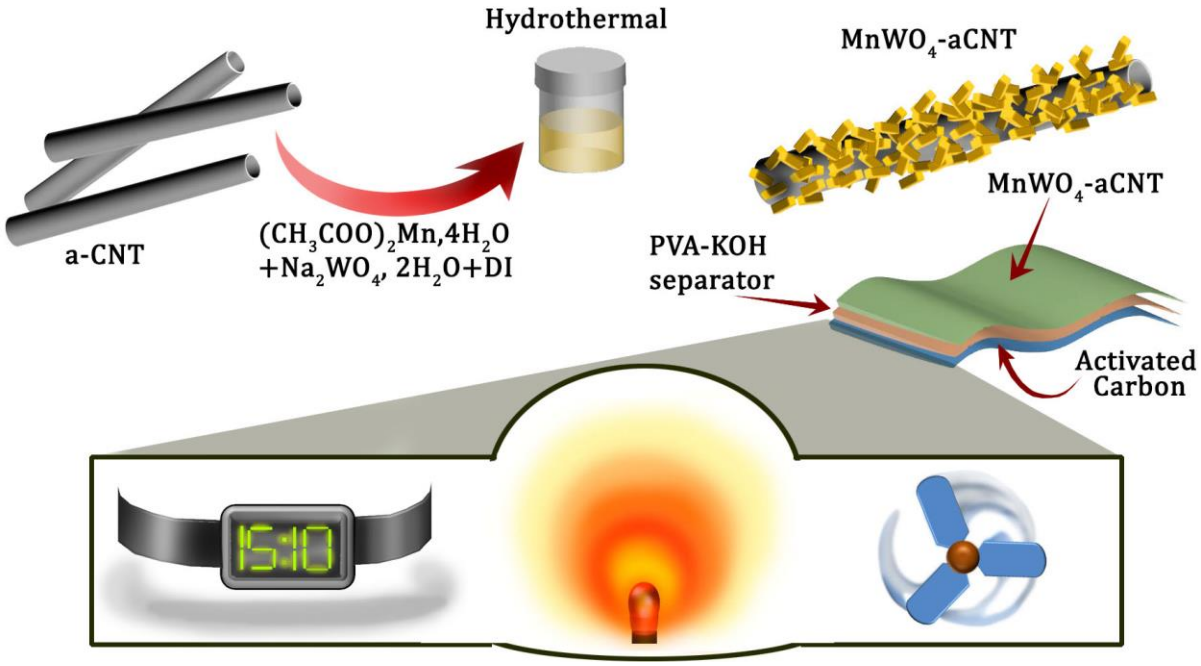

Scheme 4.1: Schematic diagram of $MnWO_4$−aCNT hybrid and its usage in Supercapacitor.

This work proposes the fabrication of a new class of hybrid comprising $MnWO_4$ and low temperature synthesized amorphous CNT. aCNT can be considered as a fitting

alternative of crystalline CNTs. Here, aCNT was realized via cost effective method in bulk scale. $MnWO_4$ nanorods were decorated with this low temperature proceeded aCNT via hydrothermal process. Electrochemical properties of pure aCNT, $MnWO_4$ and hybrid samples were carried out in detail. C_s value for the hybrid sample is found to be enhanced significantly as compared to that for the individual building blocks. Presence of conducting 1D tubular back bone eases the electron transport process and the inherent porosity of it increases the electrolyte diffusion. Simultaneously, growth of $MnWO_4$ over aCNT backbone increases the overall surface area significantly. Such elevated electrochemical performance registered from the hybrid sample will motivate for rational designing of other electrode materials using different multi-metallic oxides and carbonaceous material. This entire work in brief is schematically presented in Scheme 4.1.

4.2. Experimental

4.2.1. Materials

Manganese (II) acetate tetrahydrate crystals ($(CH_3COO)_2Mn,4H_2O$), sodium tungstate dihydrate (Na_2WO_4, $2H_2O$), ferrocene ($(C_5H_5)_2Fe$), ammonium chloride (NH_4Cl) and hydrochloric acid (HCl) are of analytical grade and used without any further purification.

4.2.2. Synthesis of aCNT

Firstly, NH_4Cl and $(C_5H_5)_2Fe$ were taken in appropriate weight ratio (2:1), and mixed rigorously in a mortar for 1h. The mixture was transferred to a quartz beaker with mica sheet on top of the beaker and treated in a laboratory oven at 225°C for 30 minutes. Mica sheet was placed to restrict the immediate evaporation of $(C_5H_5)_2Fe$ during heating. Thereafter, the sample was allowed to cool down naturally and washed by diluted HCl and deionized (D. I.)

water for multiple times. The product obtained after filtration was further dried for overnight at 80°C.

4.2.3. Synthesis of $MnWO_4$

0.5 M of $(CH_3COO)_2Mn$, $4H_2O$ and 0.5 M of Na_2WO_4, $2H_2O$ were mixed in 40 mL of D.I. water via magnetic stirring at ambient. The solution was further transferred to a Teflon lined autoclave which was further kept at 200 °C for 20 h. Finally, when it had cooled naturally to room temperature, the product was washed by D.I. water and dried at 80 °C for overnight.

4.2.4. Synthesis of $MnWO_4$- aCNT composite

The as synthesized aCNT was further used for the preparation of $MnWO_4$-aCNT hybrid. For the synthesis of the hybrid, the above-mentioned approach was adopted exactly except the addition of aCNT. 30 mg of as prepared aCNT was added with the aforesaid mixture. Thereafter the whole mixture was treated hydrothermally for similar time duration.

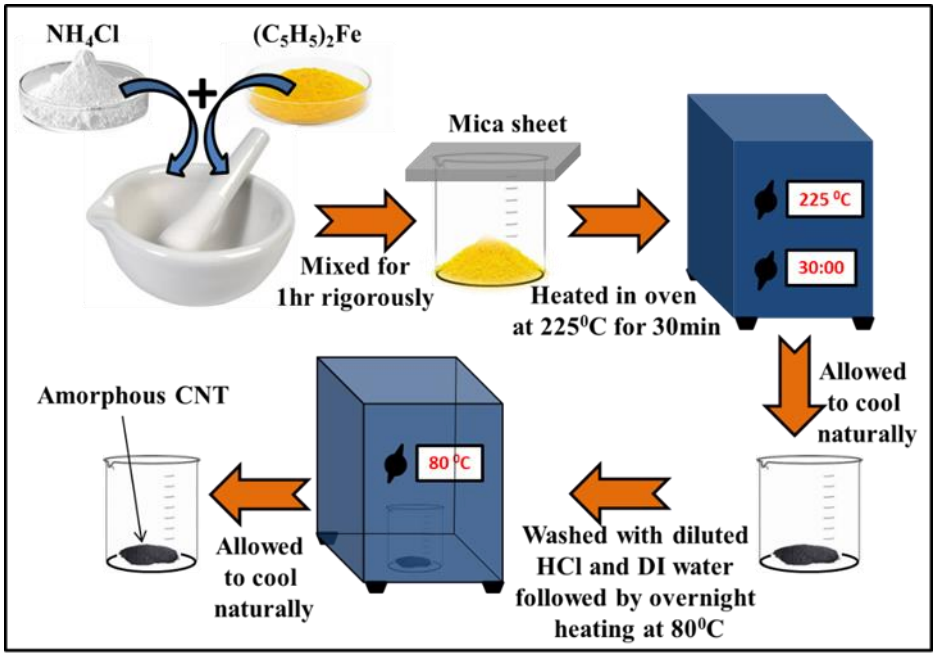

Figure 4.1: Schematic of synthesis protocol of aCNT.

The sample was then collected via same procedure. A schematic diagram showing step by step the synthesis protocol of aCNT and $MnWO_4$-aCNT hybrid are included in Figure 4.1 and Figure 4.2 respectively.

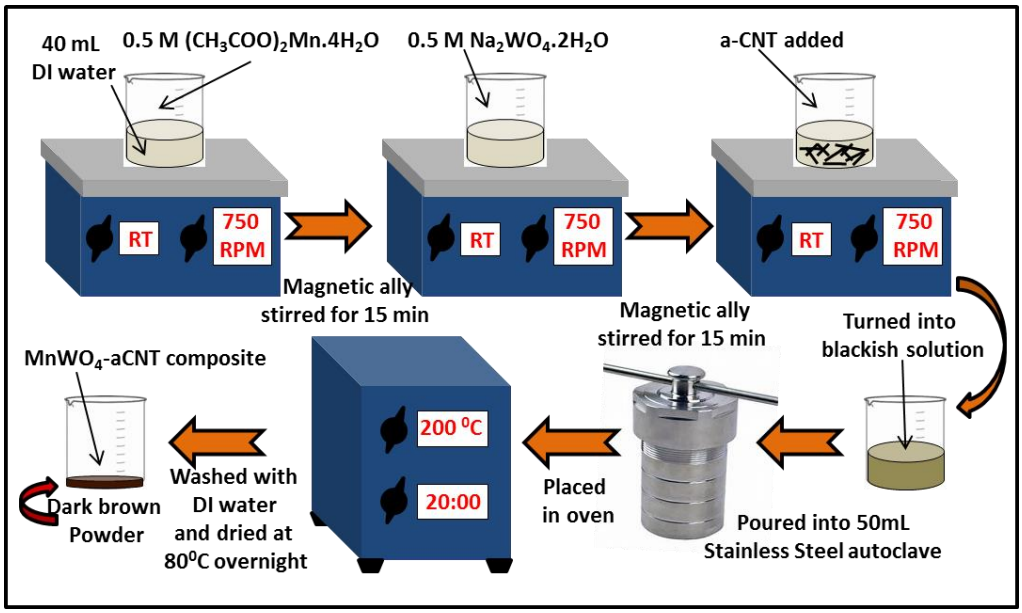

Figure 4.2: Schematic of synthesis protocol of $MnWO_4$-aCNT hybrid.

4.2.5. Electrode prepartaion

The working electrodes were prepared using of $MnWO_4$-aCNT, polytetrafluoroethylene (PVDF) and carbon black with a ratio of 8:1:1. The aforesaid reagents were mixed with 300 µL NMP and stirred for 6 hours to obtain a black paste. This mixture was coated on precleaned and dry Ni Foam and dried at 70 ˚C for 12 hours.

4.2.6. Electrochemical Measurements

Electrochemical features of all the fabricated electrodes were investigated in aqueous KOH (1M) electrolyte at ambient temperature using PGSTAT302N Autolab in three-electrode configuration where nanoform paste over nickel foam was used as working electrode. Pt wire is chosen as counter electrode and Ag/AgCl acted as reference electrode.

Cyclic voltammetry (CV) was performed with in potential range of -0.1 to 0.6 V (vs. Ag/AgCl) at different scan rates. Galvanostatic charge discharge (GCD) studies were also performed at different current densities. Electrochemical impedance spectroscopy (EIS) analysis was also performed using the same instrument.

4.2.7. Electrolyte gel preparation for ASC device

For the preparation of electrolyte gel, PVA, KOH and DI water was used. A mixture of PVA, KOH and DI water was stirred vigorously. Mixture temperature was maintained at 90 ºC and the solution was stirred until the solution became transparent and homogeneous. After the gel formation, it was cooled to room temperature which eliminated the as formed excess bubbles.

4.2.8. Characterizations

X-ray diffraction study was performed using X-ray diffractometer (Bruker D8: Advance). Morphology of the products was examined by field emission scanning electron microscope (FESEM, Hitachi S-4800). EDS study was performed using energy dispersive spectroscopy (EDS, Thermo Scientific attached with the FESEM). To get more details about morphology and crystal structure transmission electron microscope (JEOL, JEM 2100) study was further performed. Raman spectra were recorded using Raman spectrometer (alpha 300, Witec). BET measurements were carried out using Nova 1000e, Quantachrome. Electrochemical tests were studied in Gamry Interface 1000 (potentiostat/galvanostat/ZRA).

4.3. Results and discussion

X-ray diffraction (XRD) profiles of $MnWO_4$ and $MnWO_4$-aCNT are presented in Figure 4.3a whereas the same for aCNT is presented in Figure 4.4a. XRD profile for the aCNTs shows a single hump centred at ~ 26.4° which can be index to (002) plane of graphitic

carbon [32]. This indicates the amorphous nature of the CNTs. No discernible differences in the XRD profiles of $MnWO_4$ and $MnWO_4$-aCNT are observed. All the diffraction peaks in Figure 4.3a are corresponds to the monoclinic structure of $MnWO_4$ [JCPDS Card No 13-0434] with lattice parameters a = 4.829 Å, b = 5.759 Å, c = 4.998 Å, and β = 91.16° [33]. Strong intensity of these Bragg's peaks reveals high crystallinity of $MnWO_4$. Despite nearly same appearance of diffraction patterns, zoom in view of the 2θ range from 26° to 28° for the hybrid sample suggested a hump which corresponds to the presence of aCNT in the sample (Figure 4.3a inset). This result confirms the simultaneous presence of $MnWO_4$ and aCNT. Absence of any impurity related peaks in all three patterns demonstrates high purity of the synthesized samples.

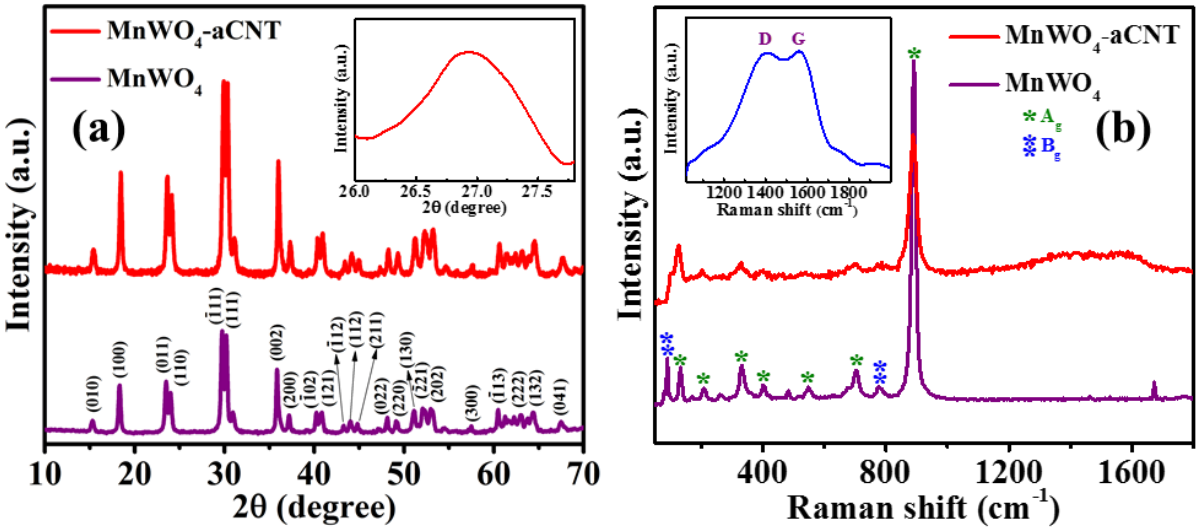

Figure 4.3: (a) XRD (b) RAMAN spectra of $MnWO_4$ and $MnWO_4$-aCNT; insets show zoom in view of a particular region.

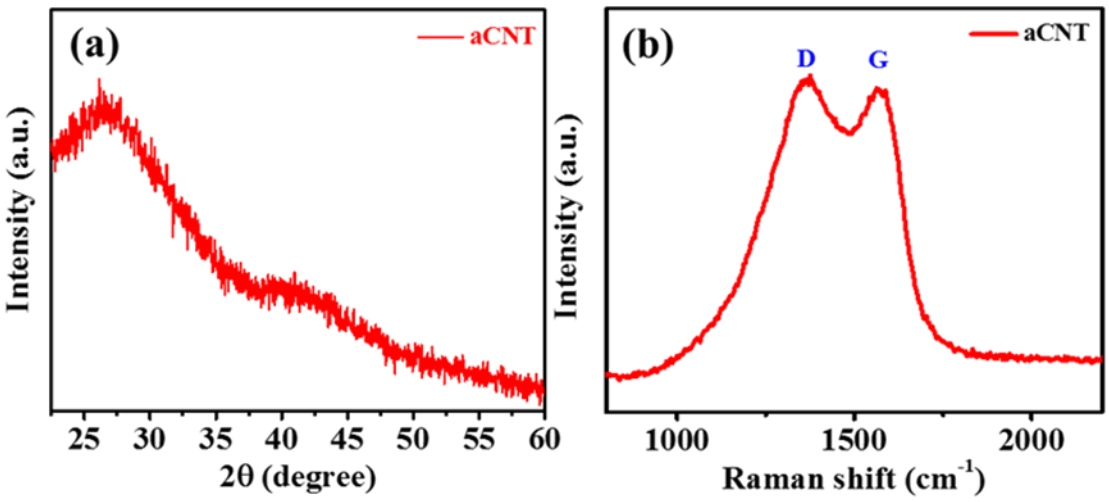

Figure 4.4: (a) XRD and (b) RAMAN spectra of aCNT.

For validation of the hybrid formation, room temperature Raman analysis of all the samples was further carried out. Raman spectrum of aCNT (Figure 4.4b) suggests presence of D and G bands at ~1355 and ~1585 cm^{-1} respectively. Well-known G band is related to doubly degenerate E_{2g} phonon modes and the D band arises due to disorder induced mode [34]. Almost symmetric peak related to second order is also observed at 2680 cm^{-1}. Absence of any impurity peaks in the spectrum suggests phase pure preparation of aCNT. Raman spectra of $MnWO_4$ and $MnWO_4$-aCNT are shown in Figure 4.3b. Most intense peak centered at 878 cm^{-1} is accredited to the symmetric stretching vibration of short W-O bond in $MnWO_4$[35]. Peaks appearing at 768 and 691 cm^{-1} denote the occurrence of asymmetric stretching vibration and symmetric stretching vibration of a short terminal W–O–W bond. The band at ~123 cm^{-1} is associated with the translational mode of tungsten [26]. Remaining peaks in the spectra of $MnWO_4$ are also in accordance with the literature [26,35]. As compared to pristine $MnWO_4$, an additional hump arises in the spectrum of the hybrid sample within the range of 1200-1700 cm^{-1}. Zoom in view of this hump in the inset of Figure 4.3b

reveals typical D and G band of the aCNT. Presence of these two peaks along with other prominent peaks related to $MnWO_4$ in the RAMAN spectra of $MnWO_4$-aCNT confirms successful formation of hybrid and corroborates with XRD results.

FESEM images of the synthesized nanoforms are shown in Figure 4.5. Image corresponding to aCNT in Figure 4.5a suggests uniform growth of one-dimensional (1D) tube-like structure with smooth side surfaces over a large area. These nanoforms are formed in bunch and closely attached with their neighbors. Average outer diameter of the 1D nanoforms is ~120 nm whereas their length varies in few micrometer ranges. Hollowness in these nanoforms is noticeable from the Figure 4.5b. Red marked circular areas confirm that the synthesized nanoforms pristine aCNTs. The external diameter of $MnWO_4$ nanorods coated aCNTs also increased to ~200–300 nm.

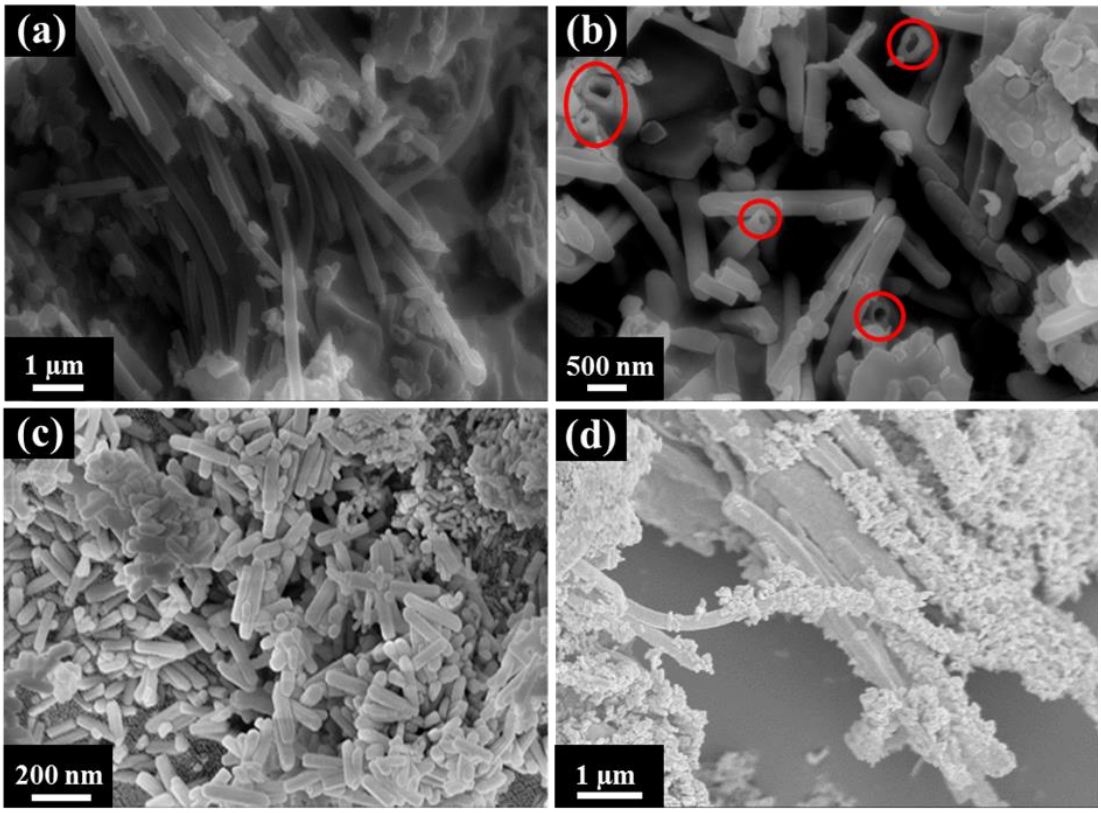

Figure 4.5: FESEM of (a) aCNT, (c) $MNWO_4$ and (d) $MnWO_4$-aCNT. (b) High magnification image of aCNT; circular rings indicate the hollowness of the tube.

To get more detail about the heterostructure morphology and its crystal structure, TEM investigation was carried out. Figure 4.6a and 4.6b present TEM images of $MnWO_4$-aCNT where the distinct morphological features of aCNT backbone and the attachment of $MnWO_4$ over it is obvious. Several number of $MnWO_4$ nanorods are found to co-exist on the surface of aCNT.

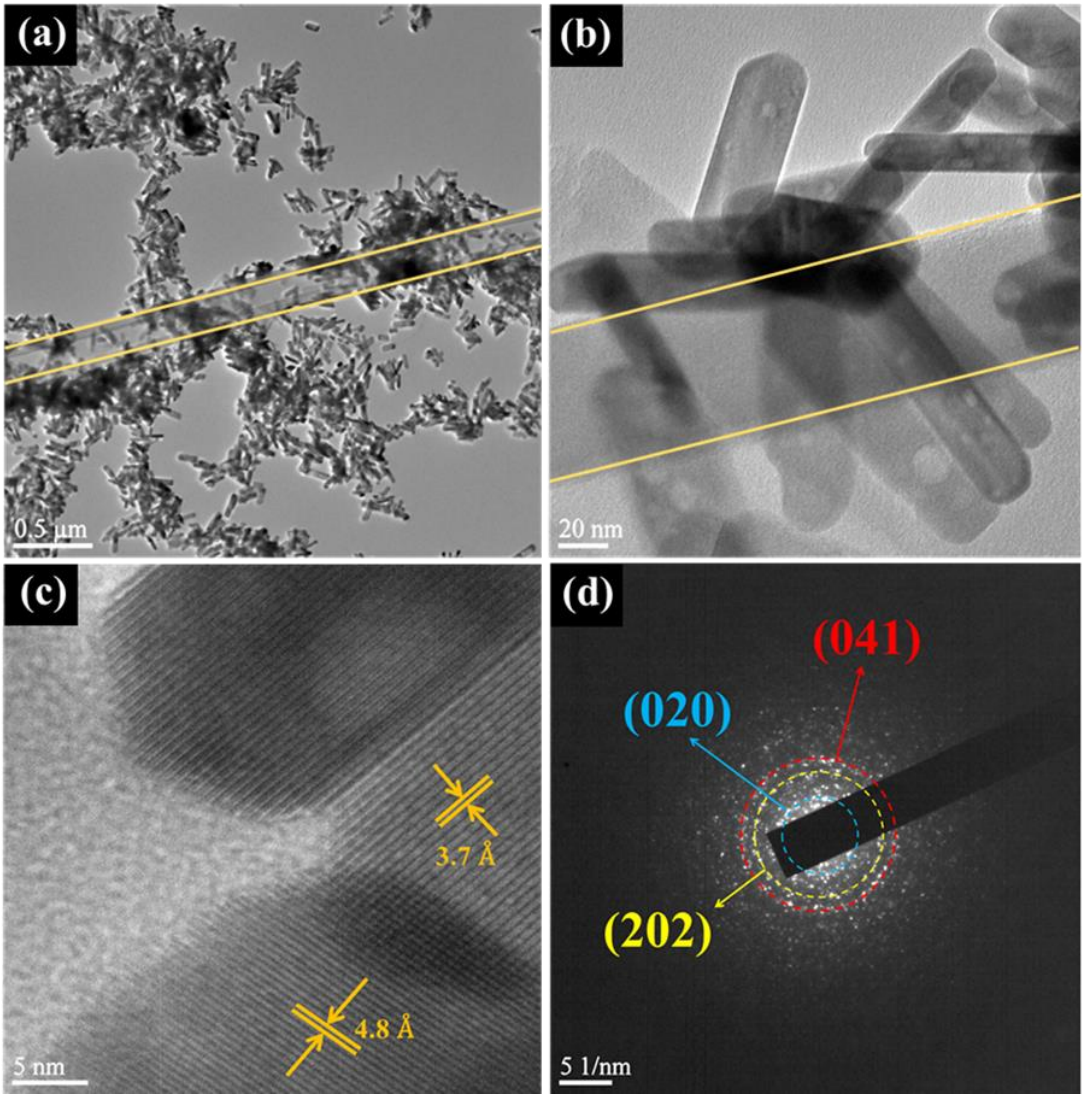

Figure 4.6: (a, b) TEM image at different magnification (c) HRTEM and (d) SAED pattern of $MnWO_4$-aCNT**.**

Average length of these randomly oriented $MnWO_4$ nanorods are within the range of 80 to 150 nm whereas their average diameter varies within 20-40 nm. HRTEM investigation of these nanorods in Figure 4.6c discloses the crystalline nature of $MnWO_4$. Assessed value of

inter-fringe spacing of 4.8 and 3.7 Å are consistent with the (100) and (011) crystal planes of $MnWO_4$ [JCPDS Card No 13-0434]. Selected area electron diffraction (SAED) pattern in Figure 4.6d taken over the nanorod discloses circular ring patterns which suggest the polycrystalline nature of these nanorods.

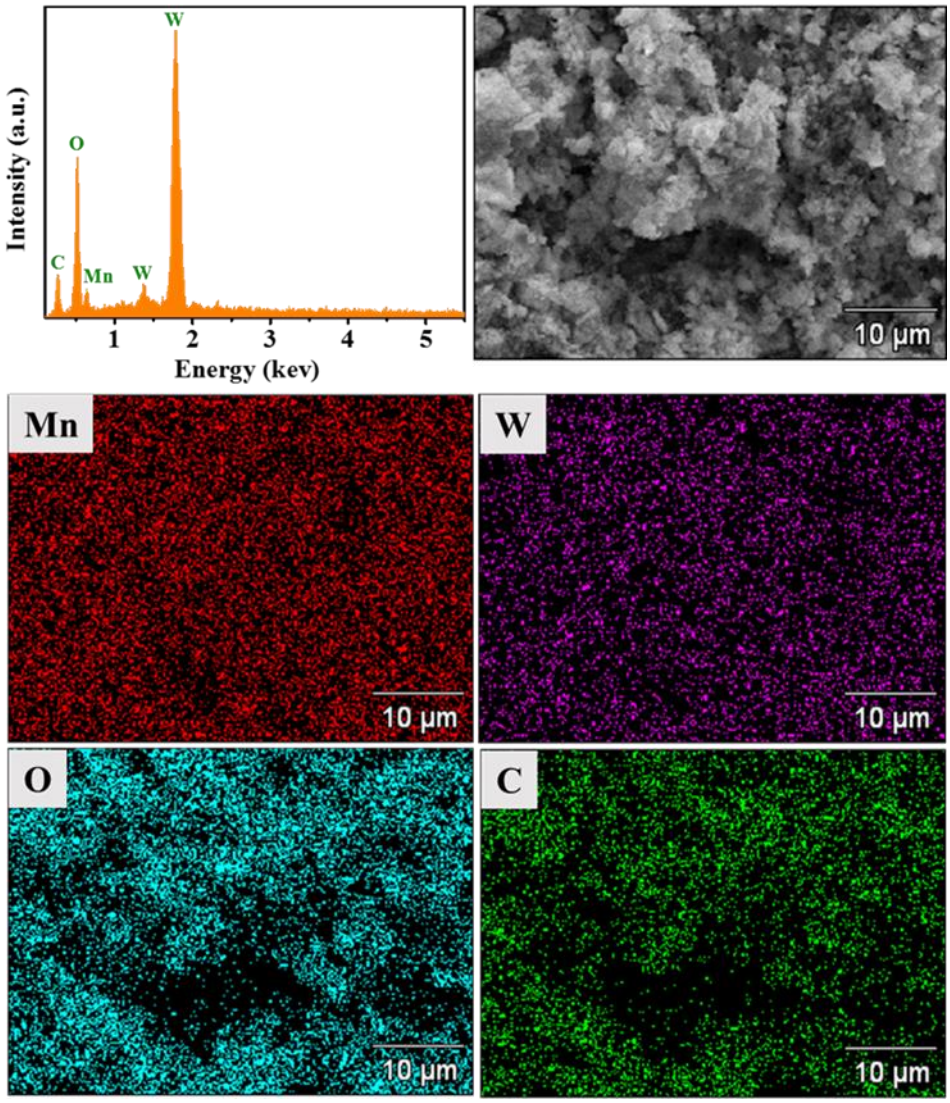

Figure 4.7: EDS spectrum and associated elemental mapping of $MnWO_4$-aCNT.

Furthermore, to evaluate the elemental composition of hybrid sample, EDX analysis of $MnWO_4$-aCNT was performed and shown in Figure 4.7. EDX spectra presented in Figure 4.7 confirms the sole existence of C, Mn, W and O in the sample. Corresponding elemental

mapping in the same figure discloses homogenous distribution of the constituents over the inspected area.

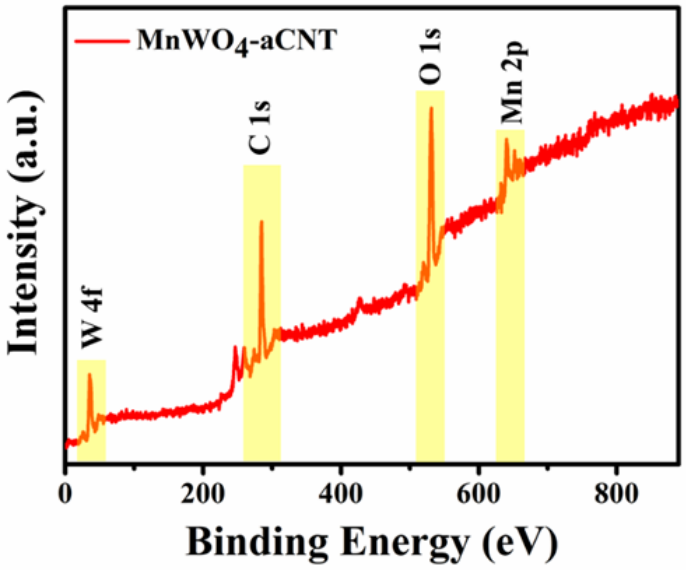

Figure 4.8: XPS survey scan of $MnWO_4$-aCNT.

For in-depth analysis of the constituting elements and to examine their respective oxidation states, XPS investigation of $MnWO_4$-aCNT was carried out. Survey spectrum of the sample presented in Figure 4.8 shows the only occurrence of Mn, W, O and C and corroborates with the findings of EDX analysis. High resolution XPS spectrum of C1s in Figure 4.9a is asymmetric and well fitted with two Gaussian curves. One prominent peak at binding energy ~284.6 eV is related to C-C whereas the other at ~288.8 eV is related to C=O [36]. Peak in higher binding energy reveals the presence of oxygen comprising functional groups. Presence of these kind of oxygen containing species in the defective aCNT networks, in general facilities growth of secondary nanoform over tubular aCNT nanostructures [37]. High resolution spectrum of Mn 2p shows two prominent peaks at ~641.5 and ~653.5 eV for Mn $2p_{3/2}$ and Mn 2p ½respectively (Figure 4.9b). The spin orbit coupling difference of 11.8 eV between these two peaks matches well with the literature [38].

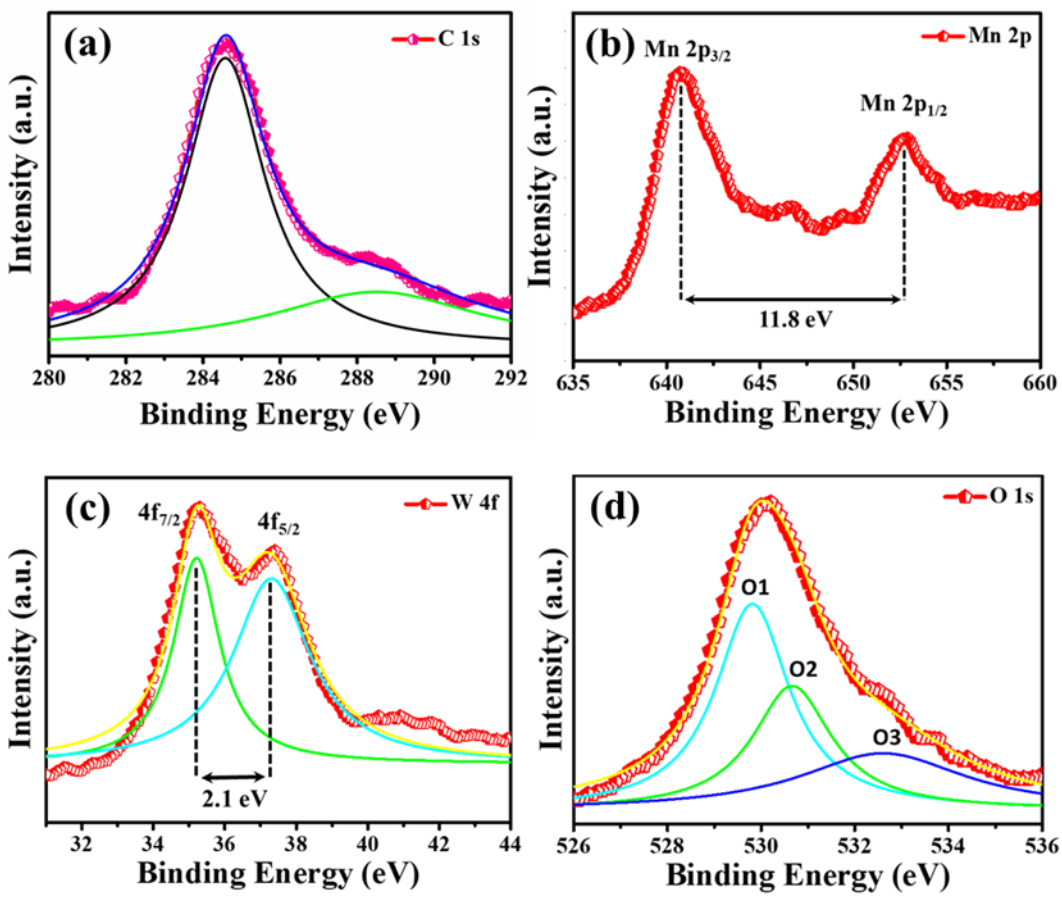

Figure 4.9: XPS spectra of (a) C1s (b) Mn 2p (c) W 4f (d) O1s of $MnWO_4$-aCNT.

A very small satellite peak also appeared in between these two peaks. Such positioning of the peaks confirms the presence of Mn in +2 oxidation state in the $MnWO_4$. Additionally, W 4f spectra presented in Figure 4.9c shows doublet features. Peaks appeared at ~35.3 and ~37.4 eV are associated with the W $4f_{7/2}$ and W $4f_{5/2}$ respectively. Furthermore, the as observed spin-orbit coupling of 2.1 eV between the aforesaid two peaks corroborates well with the previous reports and suggests the +6-oxidation state of W in the $MnWO_4$. Finally, the O 1s spectrum in Figure 4.9d displays two dominant component peaks along with a slight hump in higher wavelength side. Most dominant peak in the deconvoluted O1s spectra at ~529 eV is related to Mn-O-W bond in $MnWO_4$ [28], while the other prominent peak in higher binding energy side in the same spectrum are related to the O_2 forming oxide with Mn and W both. Little hump located at ~532.3 eV corresponds to surface hydration, inevitably present in the

nanoforms, particularly when wet chemical synthesis techniques are adopted. This elemental analysis thus validates the successful formation of $MnWO_4$ with Mn in +2 and W in +6 oxidation state in it [38]. Assessed atomic % of the constituent elements in $MnWO_4$ from the XPS results is found to follow the ratio of 16: 15: 70 for Mn: W: O, which matches well with the literature [26].

Electrochemical features of an electrode material depend on numerous factors, among which surface area and porosity are very vital. Surface textural properties of $MnWO_4$ and $MnWO_4$-aCNT were studied by nitrogen sorption measurements. N_2 adsorption–desorption

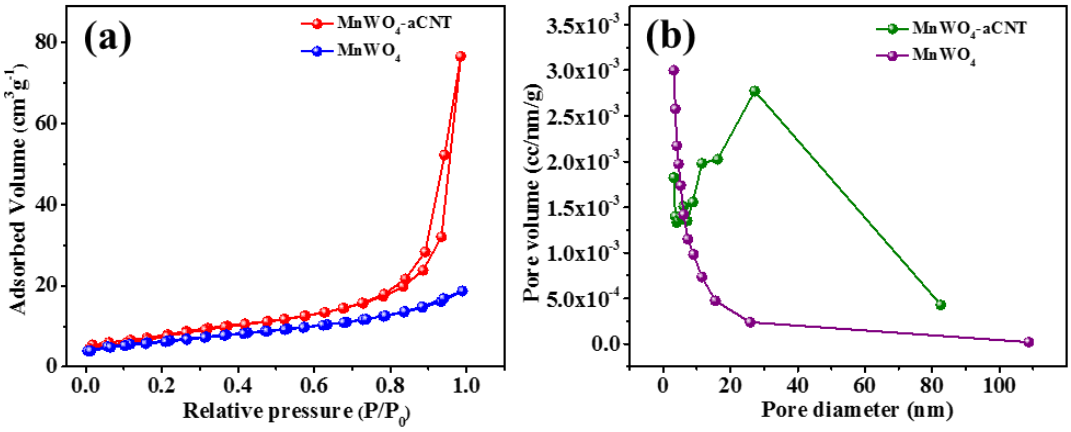

Figure 4.10: (a) N_2 adsorption–desorption isotherms and (b) pore distributions of $MnWO_4$-aCNT and $MnWO_4$.

isotherms of the samples are depicted in Figure 4.10a. The specific surface areas of $MnWO_4$ and $MnWO_4$-aCNT were found to be 22.5 and 29.1m^2 g^{-1} respectively. Higher surface area for hybrid sample is arises due to the decoration of aCNT with $MnWO_4$. Pore volume vs pore diameter plots for both samples of are shown in Figure 4.10b. Accessed value of the specific pore volume and pore diameter of $MnWO_4$-aCNT is found to be 0.114 cc/g and 27.24 nm respectively, both being much higher than those of the pristine $MnWO_4$. Nanoform with high surface area and porosity in it are advantageous for ion and electron transport. Moreover, high surface area also surges the contact area between the active materials and electrolyte.

Thus, the hybrid with high surface area and porosity has better potential to be used in electrochemical applications.

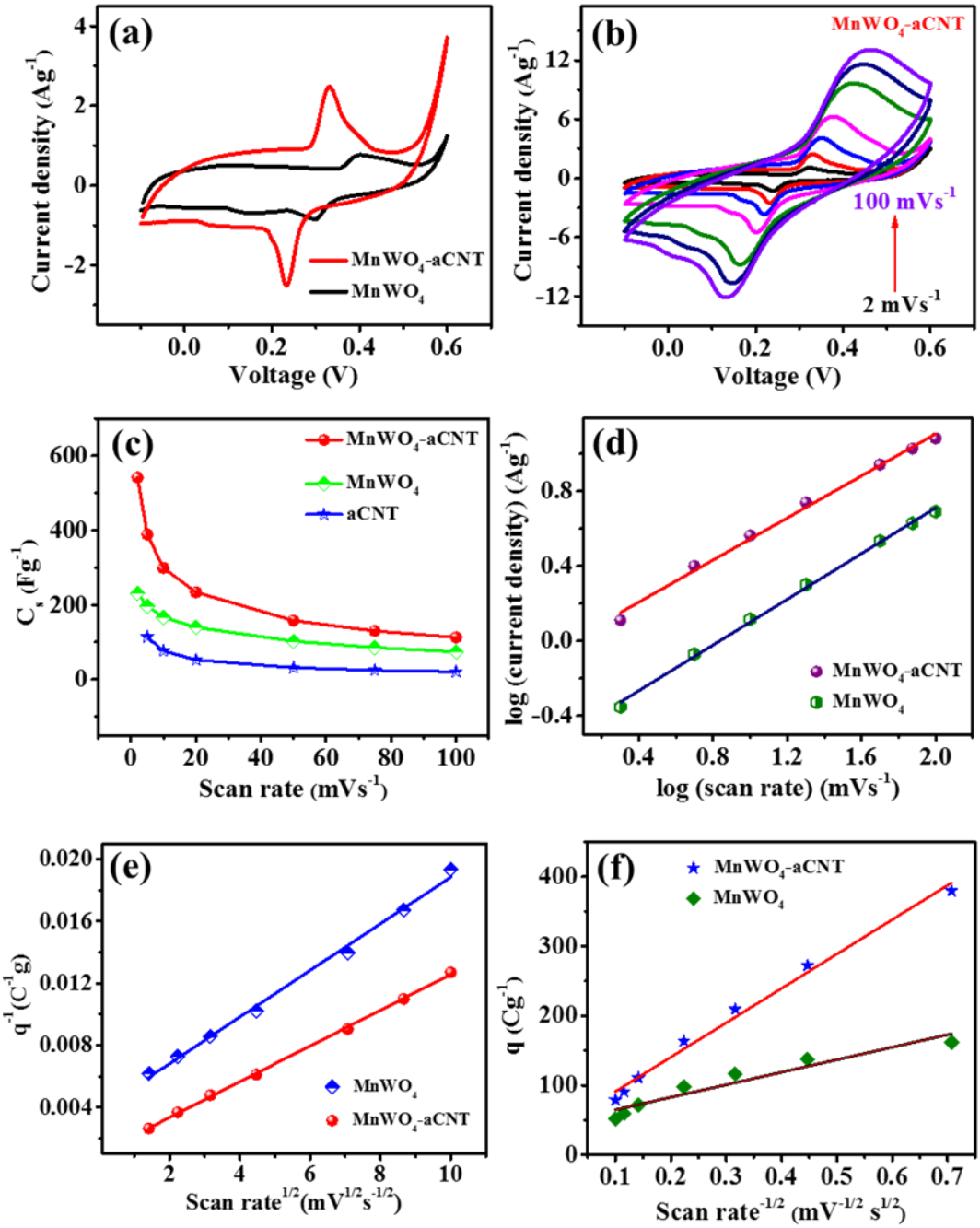

Figure 4.11: CV curves of (a) $MnWO_4$ and $MnWO_4$-aCNT electrode at a scan rate of 5 mVs^{-1} (b) $MnWO_4$-aCNT electrode at different scan rates. (c) variation of C_s with scan rate of all samples (d) log (current density) vs. log (scan rate) plot (e) Inverse voltammetric charge (q^{-1}) vs. square root of scan rate and (f) Voltammetric charge (q) vs. inverse square root of scan rate of $MnWO_4$ and $MnWO_4$-aCNT electrode.

4.3.1 Electrochemical analysis

Electrochemical behaviour of the synthesized samples was examined in three-electrode configuration. CV curves for $MnWO_4$ and $MnWO_4$-aCNT is presented in Figure 4.11a whereas the same for aCNT is displayed in Figure 4.12a.

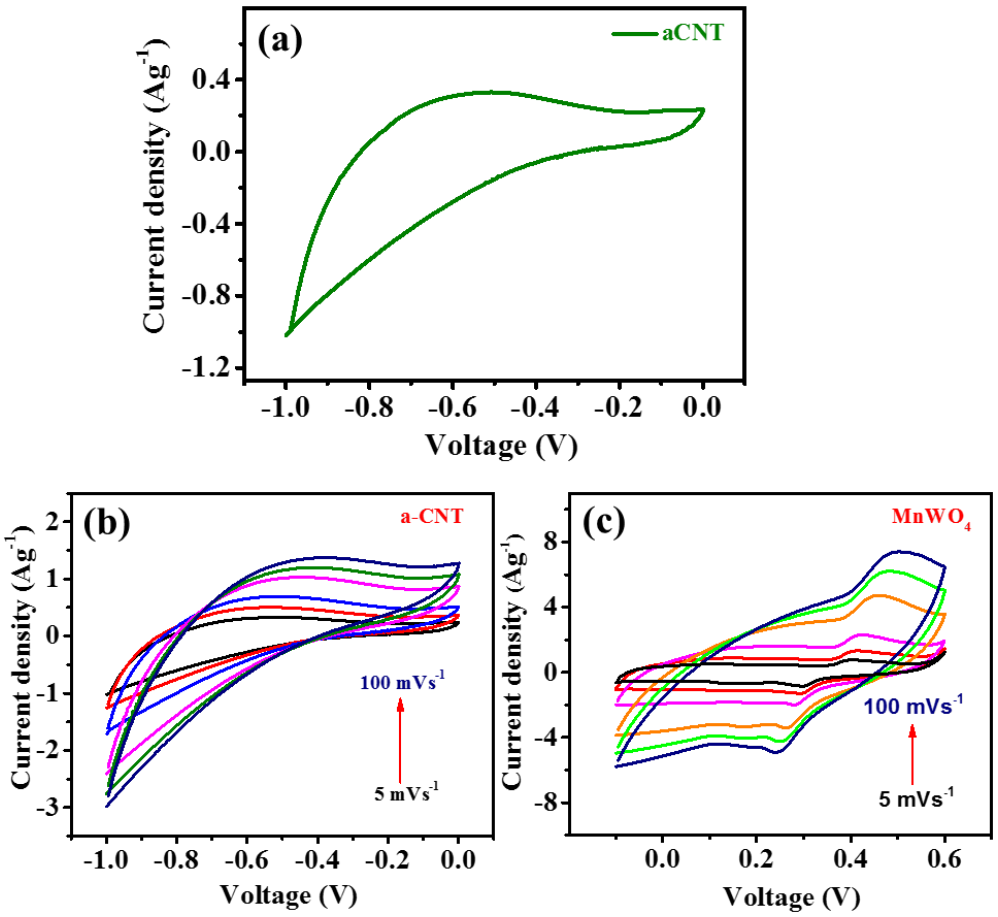

Figure 4.12: CV curves of (a) aCNT at 5mVs^{-1}; (b) aCNT and (b) $MnWO_4$ at different scan rates.

EDLC behaviour of electrode based on aCNT is prominent through the rectangular shaped CV curves in Figure 4.12a. Pristine $MnWO_4$ exhibited reversible redox behaviour whereas $MnWO_4$-aCNT hybrid electrode displayed the combination of both the aforesaid (Figure 4.11a). No significant changes in the shape were observed even at higher scan rates (Figure

4.11b). However, enhancement in the C_s values is registered with the increase of scan rate which indicates high supercapacitive behaviour of the hybrid electrode material.

Table 4.1: C_s values of all other electrodes.

Sample	Scan rate (mVs^{-1})	Specific capacitance (Fg^{-1})
aCNT	**5**	**113.86**
	10	**76.34**
	20	**52.18**
	50	**31.27**
	75	**24.31**
	100	**20.35**
$MnWO_4$	**2**	**231.15**
	5	**196.13**
	10	**166.58**
	20	**139.72**
	50	**102.38**
	75	**85.43**
	100	**73.88**
$MnWO_4$-aCNT	**2**	**542.18**
	5	**388.81**
	10	**298.95**
	20	**233.88**
	50	**157.94**
	75	**130.04**
	100	**112.52**

Similar kind of increment in specific current is also observed for other two electrodes (Figure 4.12b and 4.12c. Intercalation/de-intercalation of K^+ ions to active sites of electrode may be accredited to the reversible redox mechanism at electrode and electrolyte interface [39–41].

C_s value of the fabricated electrodes was calculated according to the following equation:

$$C_s = \frac{Q}{V} = \frac{\int I(V)dV}{\Delta V \times \upsilon \times \Delta m}$$

where $\int I(V)dV$ denotes the area under CV curve, υ denotes scan rate (mVs^{-1}), ΔV (V) and Δm (g) represent potential window and mass of active working electrode respectively. Accessed value of C_s for $MnWO_4$-aCNT is found to be 542.18, 388.81, 298.95, 233.88, 157.94, 130.04, 112.52 Fg^{-1} at 2, 5, 10, 20, 50, 75 and 100 mVs^{-1} respectively. Variation in C_s values with scan rate is presented in Figure 4.11c. C_s values of all other electrodes are tabulated in Table 4.1.

Galvanometric charge-discharge (GCD) profiles for $MnWO_4$ and $MnWO_4$-aCNT at a current density of 1 Ag^{-1} are displayed in Figure 4.13a, whereas the same for aCNT is shown in Figure 4.14a. Non-faradic aCNT electrode exhibited nearly triangular shaped charging-discharging profile. GCD profile of $MnWO_4$ and $MnWO_4$-aCNT is quite different from the aforesaid. Very prominent non-linearity in the shapes of decay profiles of the $MnWO_4$-aCNT electrode is accounted to following: IR drop triggered by the internal resistance, linear decay owing to the electrochemical double layer action and curved portion due to reversible electrochemical activities [23]. Similar kind of decay profile was also observed by Jagadale et al. [42]. Reduction of IR drop for $MnWO_4$-aCNT than the $MnWO_4$ electrodes may be accredited to the inner resistance minimization due to the amalgamation of aCNTs in sample which offers conducting paths to the Ni-foam substrate. C_s value was further estimated from GCD profile following the equation:

$$C_s = \frac{i\Delta t}{m\Delta V}.$$

Here i (A) symbolizes discharging current, Δt (s) denotes discharge time. ΔV (V) is the optimized potential window and m (g) is the effective mass of electrode. From Figure 4.13a, value of the $MnWO_4$-aCNT and $MnWO_4$ electrodes are found to be 178.6 and 105.7 Fg^{-1} at current density 1 Ag^{-1} respectively. GCD curves of $MnWO_4$-aCNT electrode at different current densities are presented in Figure 4.13b, whereas the same for other two electrodes are presented in Figure 4.14b and 4.14c. Calculated C_s value from each profile is 203.7, 178.7, 139.6, 100.6, 81.4, 70.4, 60.8, 55.5, 50.6 and 43 Fg^{-1} at 0.5, 1, 2, 3, 4, 5, 6, 7, 8 and 10 Ag^{-1} respectively.

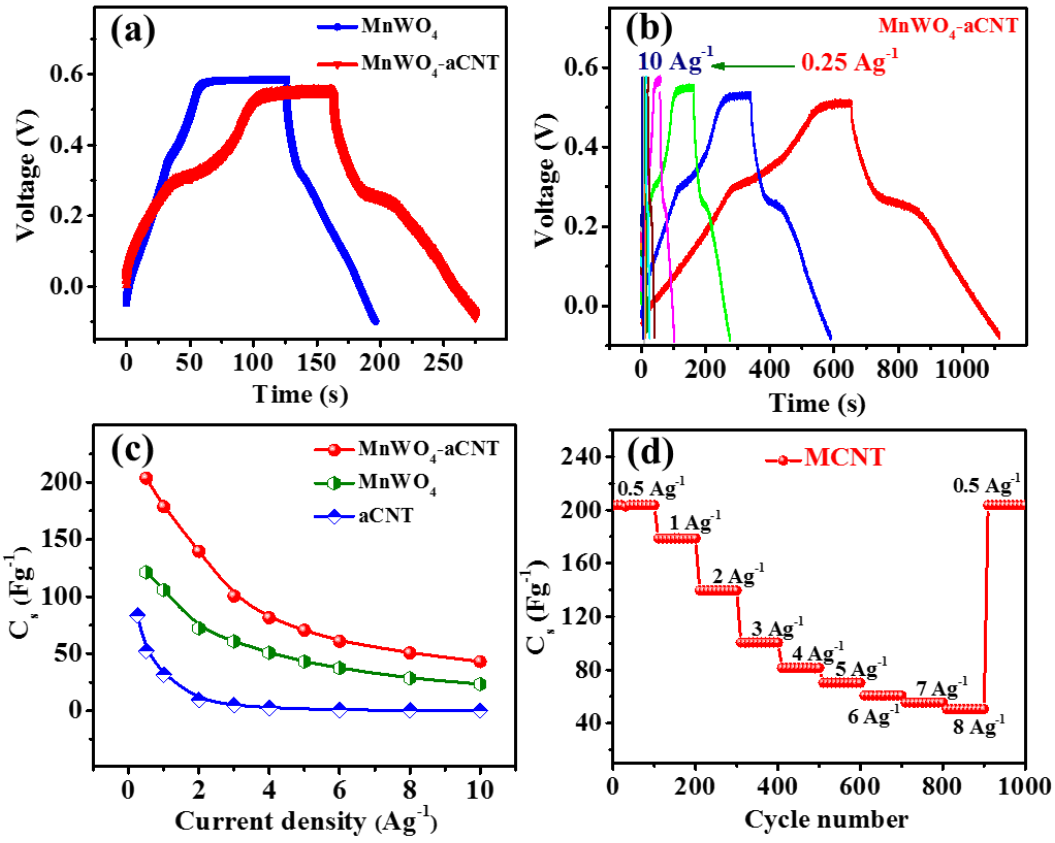

Figure 4.13: GCD curves of (a) $MnWO_4$-aCNT and $MnWO_4$ and (b) $MnWO_4$-aCNT at different current densities (c) Specific capacitance variation vs current density plot (d) cyclic stability of $MnWO_4$-aCNT with varied current density.

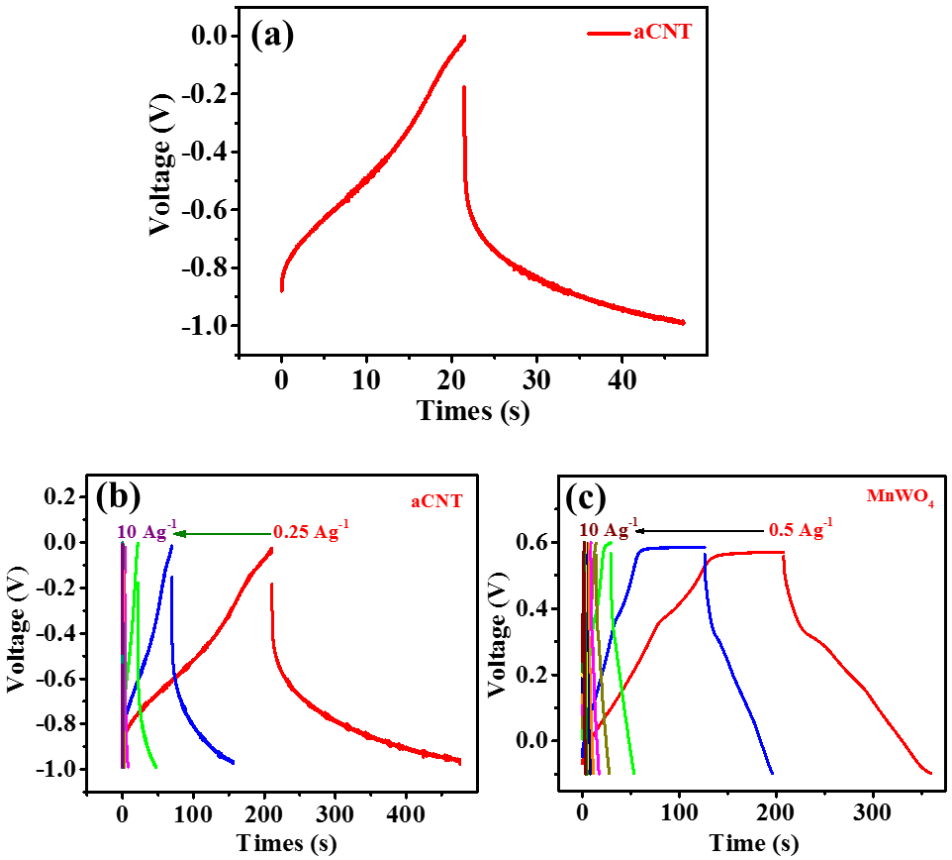

Figure 4.14: GCD curves of (a) aCNT at 1 Ag^{-1}; (b) aCNT and (c) $MnWO_4$ at different current density.

$MnWO_4$ nanorod decoration over aCNT facilitates more electroactive sites for electrolyte ion diffusion. As a consequence of this, ions can easily penetrate thorough nanorod and encounter inner aCNT which ensures maximum utilization of the electrode material. Furthermore, presence of defects of the aCNTs may also contribute in additional storage of potassium ion. A comparative summary of the C_s values at different current densities for all the fabricated electrodes is displayed in Figure 4.13c. Gradual decrement in the C_s values as a function of current density for all the samples is obvious from this image. Such variation in C_s values is more noticeable in $MnWO_4$-aCNT than the pristine samples. This Figure corroborates well with Figure 4.11c and confirms a good agreement between

GCD measurements and CV results. Lesser amount of active material usage at higher current density ensues such gradual decrement. Cycling stability, an important criterion which SCs must fulfil for their widespread utilization has been examined by executing the GCD study in finite interval of cycle number (1000 cycles) as a function of increased and decreased current density (Figure 4.14d). A uniform decrement of C_s values with the full recovery of initial capacitance after 1000 cycles from 0.5 to 8 Ag^{-1} is obvious from this Figure. These results suggest high cyclic stability as well as high-rate capability of the $MnWO_4$-aCNT electrode.

To understand the interfacial chemistry between the electrode and electrolyte in details, Electrochemical impedance spectroscopy (EIS) study was further performed. EIS measurements within the frequency range of 10 mHz to 100 kHz were performed with an a.c. amplitude of 5 mV and the results are shown in Figure 4.15a. The intersection of these curves in real impedance axis correspond to solution resistance (R_s). Value R_s for $MnWO_4$-aCNT electrode (~1.4 Ω) whereas the same for $MnWO_4$ electrode is ~2.0 Ω. Diameter of the semicircle in high to medium frequency regime plot indicates charge transfer resistance (R_{ct}) of electrode. The R_{ct} values of $MnWO_4$-aCNT and $MnWO_4$ electrodes are ~0.57 Ω and ~0.78 Ω respectively (Figure 4.15a: inset). Low R_{ct} value for hybrid indicates faster redox reactions rate in it than the same for $MnWO_4$ at electrode-electrolyte interface. At low frequency region, slope of the plot for $MnWO_4$-aCNT becomes sharper and parallel with the Y-axis, which indicates ideal capacitive nature of this electrode. Such linearity of the curve at low frequency region also indicates ion diffusion at the aforementioned interface. For in depth understanding of the electrochemical features, EIS data is further analysed by the equivalent circuit fitting. Equivalent circuit elements are responsible for the electrochemical activities. According to mechanism, electrolyte ions migrate within the layers sequentially in the electrochemical system. This ion migration in the electrolyte produces active electrolyte resistance (R_{el}). Geometrical capacitance term (C_s) is contributed by the surface layer of solid

electrode covered up by the intercalated ions. Another important element, diffusion impedance (W_s) is also influenced by the concentration gradient at surface layer [43,44].

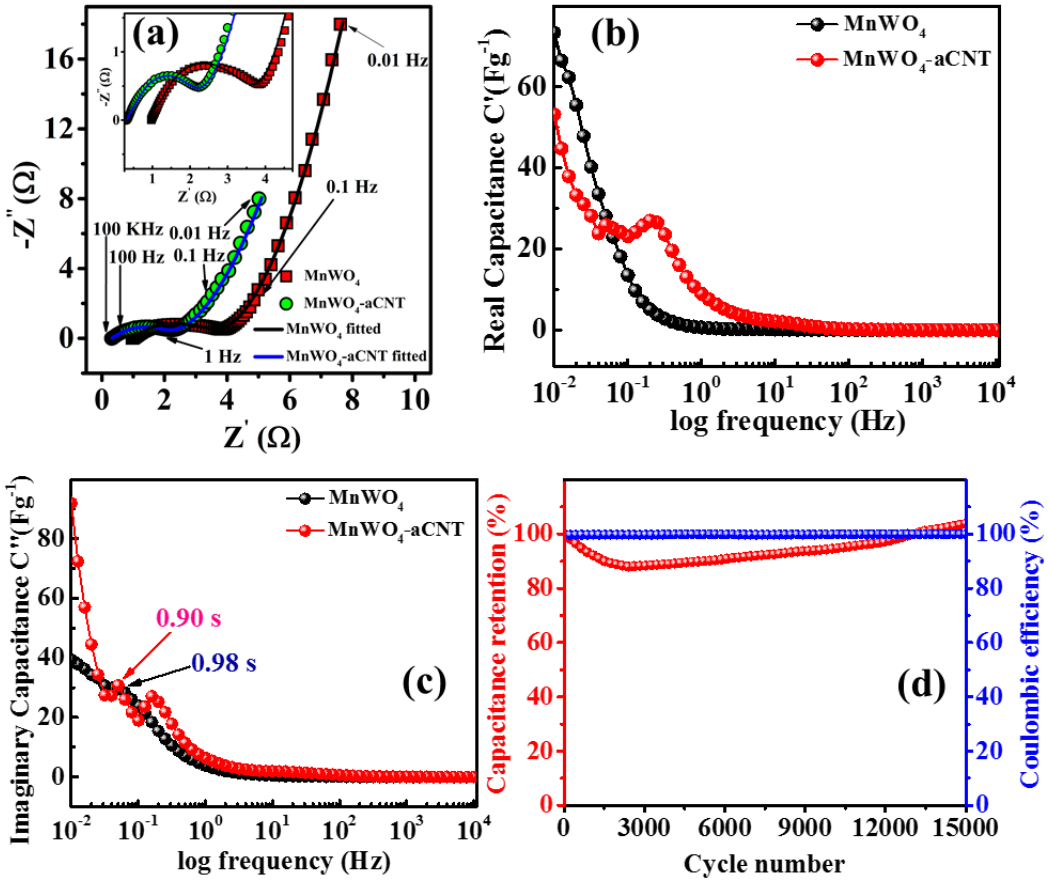

Figure 4.15: (a) Electrochemical impedance spectra; (b) real capacitance and (c) imaginary capacitance vs. log (frequency) of $MnWO_4$-aCNT and $MnWO_4$; (d) retention capacity and coulombic efficiency; inset of (a) shows the zoom in view of the high frequency region of EIS plot.

The bulk resistance of electrolyte solution, inherent resistance of electrode material and electrode-electrolyte contact resistance are collectively coined as equivalent series resistance (R_s). The abovesaid R_s, C_s, W_s in parallel combination contributed to the overall system. The mid frequency region of the presented EIS spectra is dispensed by double layer capacitance (C_{dl}) and charge transfer resistance (R_{ct}). The double layer arises at interface in between the

conductive electrode and the intercalated particles which are dissolved or solvated in form of ions in the electrolyte. In the high frequency region, as formed double layer initiates further diffusion of electrolyte ions within electrodes due to chemical composition differences and structural features variances which includes diffusion impedance (W_k) connected with the aforesaid elements in series combination [45]. Intercalated capacitance (C_{int}) is also involved which arises due to gathering of electrolyte ion with the intercalated materials. In the fitted circuit presented in Figure 4.16, R_1, R_2, R_3 stand for R_{el}, R_s, R_{ct} respectively. W_s and W_k are presented as W_1 and W_2 respectively. Finally, the capacitances C_s, C_{dl} and C_{int} are termed as C_1, C_2, C_3 respectively. Values of the aforesaid elements are tabulated in Table 4.2.

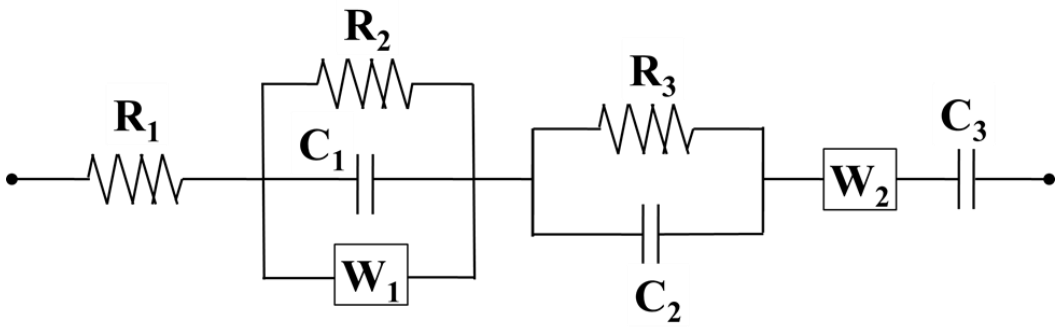

Figure 4.16: Equivalent circuit which is used to fit the EIS spectra.

In order to obtain more insights about the capacitive behaviour of the fabricated electrode in different frequency region, we have plotted real and imaginary capacitances vs. frequency of the $MnWO_4$-aCNT and the graphs are presented in Figure 4.15b and 4.15c. Total impendence of a system can be written as:

$$Z(\omega) = Z'(\omega) + Z''(\omega)$$

Here $Z'(\omega)$ and $Z''(\omega)$ denote real and imaginary impedance of the electrode material. $Z(\omega)$ signifies the overall a.c. complex impedance of the system. Furthermore, the complex capacitance of the SCs can be expressed as:

$$C(\omega) = C'(\omega) + C''(\omega)$$

Where $C'(\omega) = \frac{Z''(\omega)}{\omega|Z|^2}$ and $C''(\omega) = \frac{Z'(\omega)}{\omega|Z|^2}$. Here, C' denotes real part of complex capacitance, which is considered as the capacitance of the system assessed by GCD at very low frequency. C" in the aforementioned equation comprises the loss part of the capacitance and related with energy dissipation in charging process [46,47]. The assessed values of real capacitance of the cell form Figure 4.15b for both $MnWO_4$-aCNT and $MnWO_4$ match well with the capacitance measured form GCD profile at 10 mHz. Figure 4.15c depicts the variation of C" as a function of frequency. C" attains maximum value at peak frequency (f_0), beyond which its decreases. Inverse of peak frequency is coined as dielectric relaxation time constant (τ_0). τ_0 represents the time at which cell changes its behaviour from resistive to capacitive. It also denotes the

Table 4.2: Values of equivalent circuit components.

Component	Value	
	$MnWO_4$-aCNT	**$MnWO_4$**
R_1 (ohm)	**0.3265**	**0.9711**
R_2 (ohm)	**1.434**	**2.033**
R_3 (ohm)	**0.5731**	**0.7835**
W_1 (ohm $S^{-1/2}$)	**11.13**	**28.7**
W_2 (ohm $S^{-1/2}$)	**0.7003**	**0.9812**
C_1 (F)	**0.162×10^{-3}**	**0.6021×10^{-24}**
C_2 (F)	**8.366×10^{-3}**	**2.479×10^{-3}**
C_3 (F)	**3.039**	**1.121**

Figure of merit of the SCs [46,48]. Accessed values of time constant value for $MnWO_4$-aCNT and $MnWO_4$ electrodes are 0.90 s and 0.98 s respectively. Reduced time constant value for $MnWO_4$-aCNT electrode suggests faster charging as compared to $MnWO_4$ electrode. Dissipative nature of both SC cells was further examined considering the following frequency dependent complex power equation:

$$S(\omega) = P(\omega) + j\, Q(\omega)$$

where $P(\omega) = \omega\, C''(\omega)\, |\Delta Vrms|^2$ and $Q(\omega) = -\omega\, C'(\omega)\, |\Delta Vrms|^2$. In this equation, $P(\omega)$ and $Q(\omega)$ stands for active power and reactive power respectively. Normalized active power denotes power dissipated in cell. Change of the cell behaviour from capacitive to resistive state with the frequency increment ($\omega \rightarrow \infty$) led to such power dissipation [48,49]. On the contrary, normalized reactive power decreases with frequency increment. This is due to the pure capacitive nature at lower frequencies ($\omega \rightarrow 0$). The cell oscillates between two extreme frequencies. The change-over from capacitive to resistive phase occur after an interval of 0.91 s and 0.97 s for $MnWO_4$-aCNT and $MnWO_4$ (Figure 4.17a and 4.17b respectively. Such

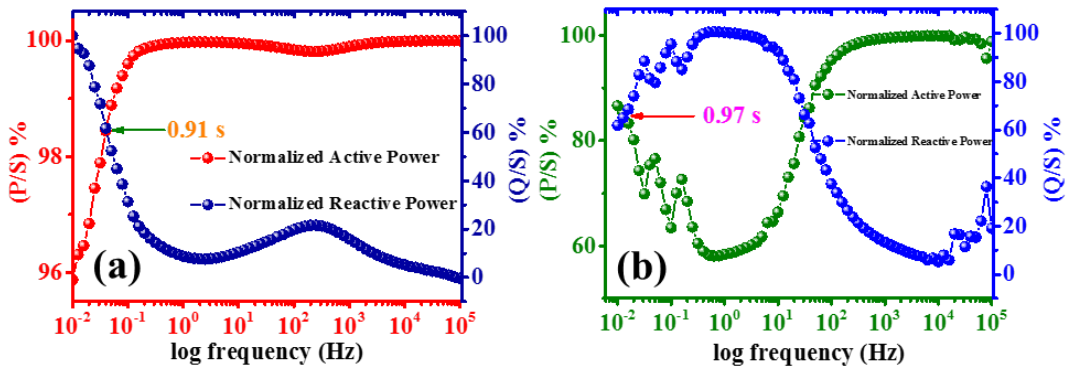

Figure 4.17: Active power and reactive power of (a) $MnWO_4$-aCNT and (b) $MnWO_4$.

values are in well accordance with the dielectric relaxation time constant (τ_0) values as calculated from Figure 4.15c.

Long term stability of the fabricated electrode based on the synthesized hybrid was further assessed at current density of 5 Ag^{-1} for 15000 cycles (Figure 4.15d). Initially, the specific

capacitance value decreases over first few hundred cycles which may be attributed to the presence of oxygen containing functional groups on the surface of hybrid nanoforms. These functional species prevent the interaction of electrolyte and electrode [50]. However, after 2400 cycles it increases gradually with cycle number. With the progress in charging discharging cycle, total activation of ionic species as well as gradual activation of the electroactive surface was ensued [3,50]. Furthermore, steady activation of the electrode surfaces with the increasing cycles is accounted to the easy access of electrolyte ions into pores, crevices as well as cracks at surface. $MnWO_4$-aCNT exhibited ~100% retention of its initial capacitance even after 15000 long cycles. Coulombic efficiency of hybrid sample also remained ~100% even after 15000 cycles. These results may originate from overall enhancement in conductivity and electroactive surface area owing to the amalgamation of multicomponent oxides with aCNTs. Such cycling stability and long life nominate the hybrid as the promising electrode material for SC. FESEM image of the hybrid before and after 15000 cycles operation is presented in Figure 4.18a-b. Change in the electrode after cycles operation is also manifested from the assessed value R_s and R_{ct} which are found to surge to ~1.43 and ~0.68 Ω respectively after 15000 cycles.

Charge transfer process plays an important role in the overall charge storage of the junction capacitor formed at electrode-electrolyte interface. Mott-Schottky analysis represents the behaviour of junction capacitance as a function of applied bias. This analysis was carried out in same experimental set up with 0.5 M Na_2SO_4 as electrolyte. In this set up, $MnWO_4$-aCNT paste on nickel foam was acted as working electrode. Pt wire and Ag/AgCl were used as counter and reference electrode respectively. Mott-Schottky plot for $MnWO_4$-aCNT and $MnWO_4$ electrode is shown in (Figure 4.19a-b) which confirms N-type behaviour for both. Flat-band potential is further assessed from this plot using following equation [51,52]

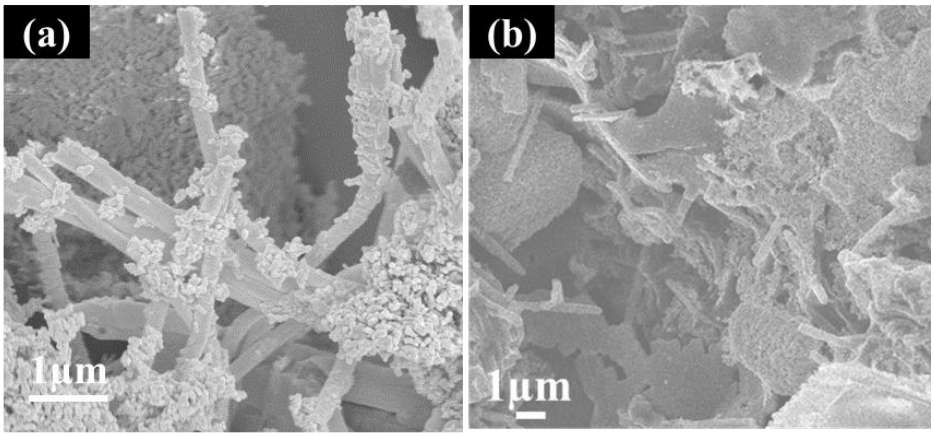

Figure 4.18: FESEM image of the hybrid (a) before and (b) after 15000 cycles.

$$\frac{1}{C^2} = \frac{2}{\varepsilon\varepsilon_0 e A^2 N_A}\left(V\text{-}V_{fb}\text{-}\frac{kT}{e}\right)$$

where C stands for capacitance. ε and ε_o denotes for dielectric constant of material and free space permittivity respectively. A and N_A represent active surface area and donor density. V symbolizes applied potential whereas V_{fb} stands for flat band potential. K, T and e denote Boltzmann constant, temperature and elementary charge respectively. Flat band potential

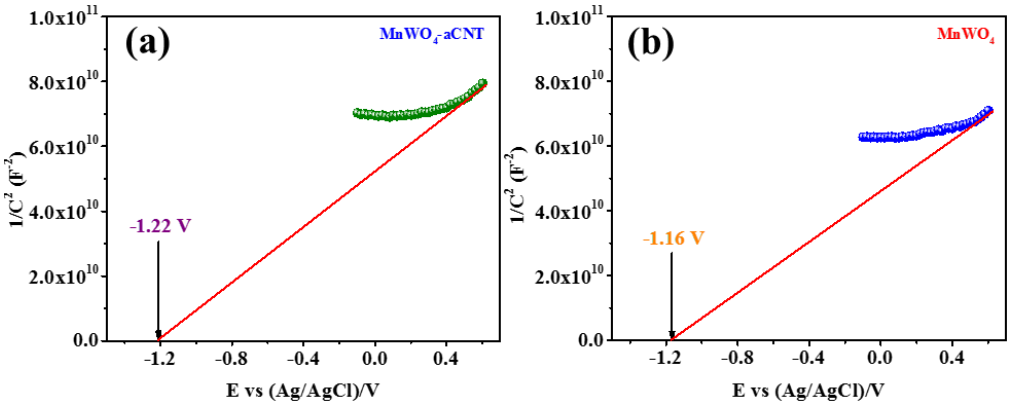

Figure 4.19: Mott Schottky plot of the (a) $MnWO_4$-aCNT and (b) $MnWO_4$.

value for $MnWO_4$-aCNT and $MnWO_4$ are found to be -1.22 V and -1.16 V respectively. Donor density of the electrode is also assessed from the inverse of the slope of linear fitting of aforesaid plot. Higher donor density for $MnWO_4$-aCNT is registered compare to the $MnWO_4$ electrode. Higher donor density as well as the flat band potential at more negative

side of $MnWO_4$-aCNT electrode boosted the charge transfer across electrode-electrolyte interface which in turn resulted in superior electrochemical performance than the other electrode.

A solid-state asymmetric supercapacitor (ASC) was devised using $MnWO_4$-aCNT and activated carbon electrode. With the help of polymer gel electrolyte (PVA/KOH), two electrodes were pasted together keeping cellulose filter paper in between as a separator. CV and GCD measurement of the ASC were performed to examine its electrochemical performance. For performance comparison we have also fabricated another ASC using activated carbon only. CV curves of the $MnWO_4$-aCNT and activated carbon performed at the scan rate of 5 mVs^{-1} within the potential window of -0.1 to 0.6 V and -1 to 0 V respectively, is presented in Figure 4.20a. Keeping in mind that both MnWO4-aCNT and activated carbon electrodes were glued together in single device, the potential range for the device characterization was chosen accordingly. The as fabricated device showed perfect capacitive activity within the inspected potential window. Figure 4.20b displays the CV curves of $MnWO_4$-aCNT based ASC device at different potential windows precisely at 0-0.6, 0-0.8, 0-1.0, 0-1.2, 0-1.4, 0-1.6, 0-1.7 V at a scan rate of 10 mVs^{-1}. Quasi rectangular nature of these curves is remained unchanged even at higher potential window. This result suggests the contribution of EDLC and pseudocapacitive materials both on overall performance. CV performance of ASC was further recorded at various scan rates and the results are shown in Figure 4.20c. Gradual increment of current density with scan rate is obvious from this image. Shapes of CV curves remained nearly same. These curves also showed reversibility even at

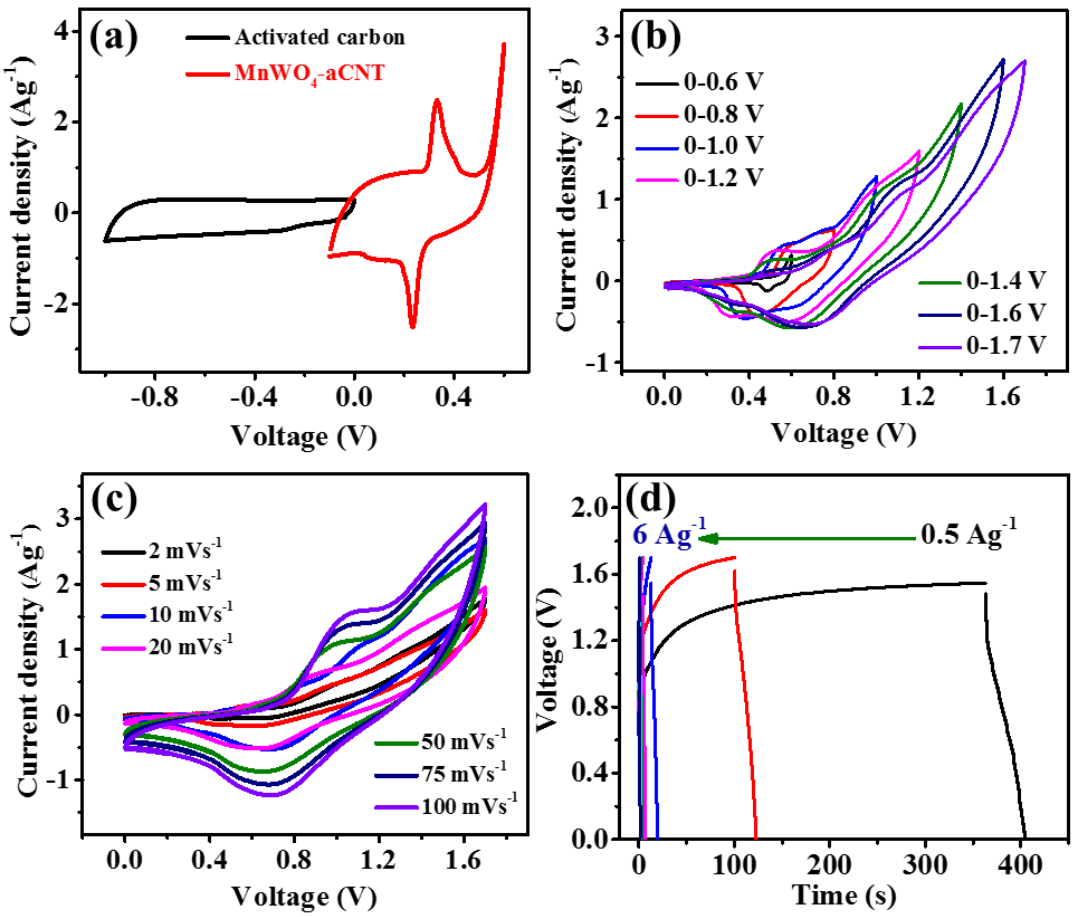

Figure 4.20: CV curves of (a) activated carbon and $MnWO_4$-aCNT at 5 mV s^{-1} (b) ASC at different potential windows (c) ASC at various scan rate (d) GCD profiles of ASC at various current densities.

low scan rate which indicates prominent supercapacitive behaviour. C_s values are also calculated from this curve and then plotted in a graph as function of scan rate (Figure 4.21a). Typical decrement in C_s values with scan rate increment was also registered for the ASC device. Figure 4.20d displays the GCD curves of this device as a function of current densities within the potential window of 0-1.7 V. The maximum capacitance value calculated from the GCD curve is 14.18 Fg^{-1} at a current density of 0.5 Ag^{-1}. Variation in the C_s values with the current density here mimicked the same as registered from the GCD measurement of the

single electrode (Figure 4.21b). Decrease of C_s values with current density is associated with diffusion limited charge transfer process.

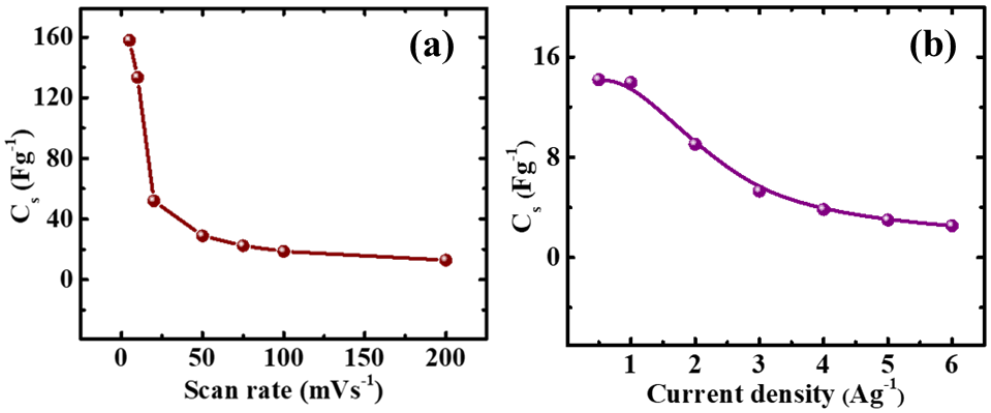

Figure 4.21: Variation in C_s of ASC with respect to (a) scan rate (b) current density.

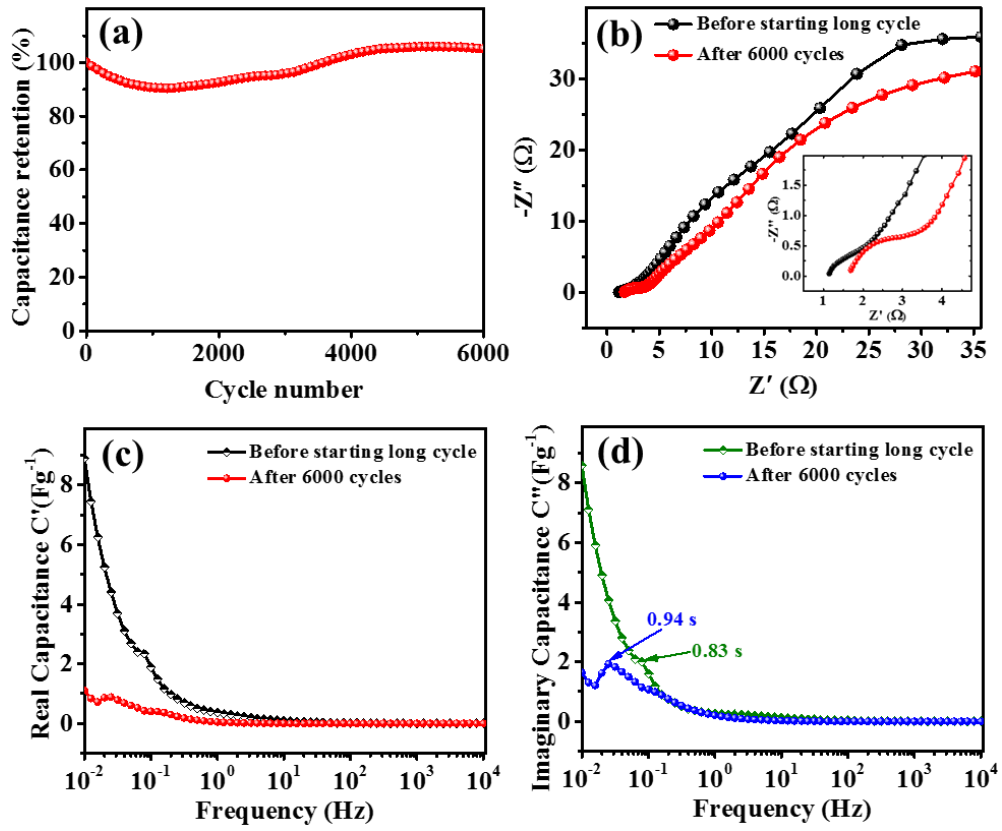

Figure 4.22:(a) Retention capacity (b) Nyquist plot before and after 6000 cycles (c) real capacitance and (d) imaginary capacitance vs frequency of ASC device.

Practical implementation of ASC device strongly depends on its cycling stability. Cycle reliability of the ASC device was further verified up to 6000 cycles at a current density of 2 Ag^{-1} (Figure 4.22a). A primary drop in C_s values was observed initially. However, after several charging discharging cycles the complete activation of ionic species occurred and specific capacitance increases with cycle number. The ASC device showed capacitance retention ~100% even after 6000 cycles clearly establishes the noticeable electrochemical stability of the device. EIS curves of the ASC device (Figure 4.22b) before and after 6000 long cycles process exhibited nearly similar behaviour in low frequency region, indicating identical Warburg impedance for both cases. At high frequency region, R_s value of the device changes from 1.1 to 1.7 Ω. Simultaneously, the R_{ct} value also increases from 3.4 to 4.8 Ω for before and after cycles operation (Figure 4.22b inset). After 6000 GCD cycles operation, gel resistance increases due to the loss in binding strength of PVA polymer which further resulted a increment in the R_{ct} value [53]. Similar nature of Nyquist plots for both is also another signature of good electrochemical stability. No discernible changes of nickel foam before and after 6000 cycles operation is feasible from the FESEM image of the electrode in Figure 4.23a-b. Plot for real capacitances and imaginary capacitances of the ASC as a function of frequency are depicted in Figure 4.22c and 4.22d respectively.

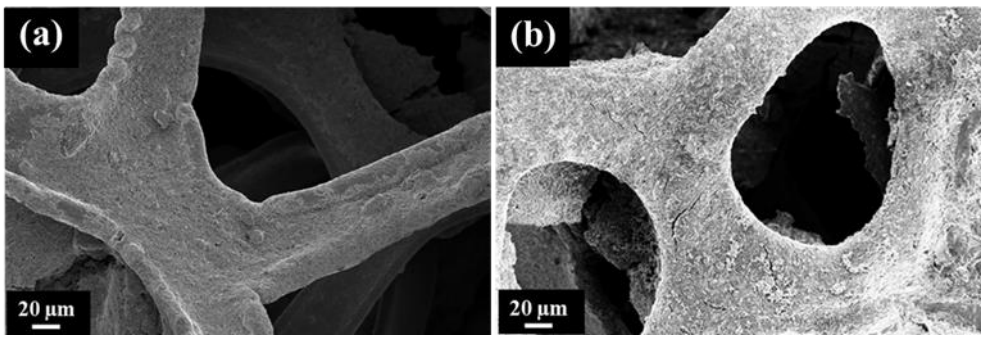

Figure 4.23: FESEM image of the nickel foam (a) before and (b) after 6000 cycles operation.

Specific capacitances calculated from plot in Figure 4.22c are in well accord with the calculated values of the same

from GCD profile. Dielectric relaxation time constant of the devices was also calculated from the plot in Figure 4.22d before and after the long cycle test. Accessed values of time constant for before and after long cycle run are 0.83 and 0.94 s respectively.

Energy and power density, two vital parameters enumerating the rate of charge transfer and storage ability of the device respectively determine the practical utility of SCs. Energy and power density were also evaluated using the following equations:

$$\mathrm{E} = \frac{1}{2} \times \mathrm{C_{sp}} \times (\Delta \mathrm{V})^2 \text{ and } \mathrm{P} = \frac{\mathrm{E}}{\Delta \mathrm{t}}$$

where E denotes energy density ($Whkg^{-1}$), C_{sp} represents specific capacitance (Fg^{-1}) and ΔV symbolizes the working potential window of the discharge process. P denotes power density (Wkg^{-1}) and Δt symbolizes discharging time.

Figure 4.24a displays Ragone plot of the device. As fabricated ASC device registered an energy density of 5.6 W h Kg^{-1} at a power density of 893.6 W Kg^{-1} at current density 1 Ag^{-1}. At higher current density of 6 Ag^{-1}, the energy density remains at 1.02 W h Kg^{-1} at a power density of 6.89 KW Kg^{-1}. Such values are comparable/superior to the other reported carbon-based composite devices [54–59]. Further, we have compared the electrochemical performance of the several carbon-based electrodes in Table 4.3 which highlights the figure of merit of the as fabricated devices. Such electrochemical results motivated us to examine its commercial utility. Further, the electrochemical performance of the ASC in series and parallel combination was explored. We have combined two devices and performed their CV and GCD measurements (Figure 4.24b and 4.24c). Operating window of the fabricated device (1.7 V) is superior than the same of regular alkaline cells (1.5 V). However, single ACS device cannot fulfil the current and voltage requirements for small electronic systems like

LEDs, digital display clock etc. Thus, it is necessary to connect two or more ASC devices in series mode (SM) or parallel mode (PM) or both which could drive those small appliances. Two

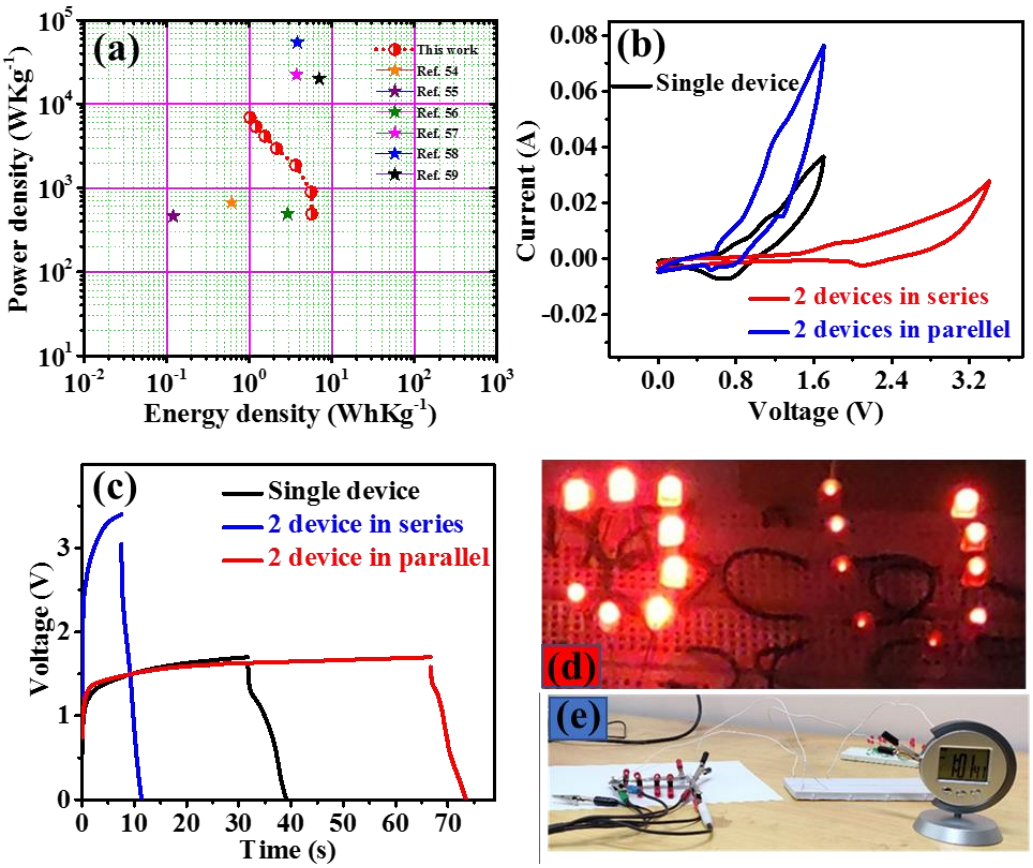

Figure 4.24:(a) Ragone plot of ASC. (b) CV and (c) GCD profiles of devices in series and parallel combination. Snapshots of (d) the glowing red LED (e) digital clock.

ASC devices in SM is charged to get two times of the potential window (3.4 V) of a single device (1.7 V) as well as to get higher the energy density. Also, to obtain a greater current for better running of the appliances two such series assemblies in parallel were used. CV measurement results of both series mode (SM) and parallel mode (PM) are compared with the same of single device in Figure 4.24b. CV performance of the devices in SM within the range 0–3.6 V showed the good tolerance limit. Specific capacitances in PM were found to be greater than that in single device whereas the same in SM was found lower.

Table 4.3: Electrochemical performance comparison.

Electrode material	Electrolyte	Specific capacitance	Potential window	Energy density	Cycling stability	Ref.
SWCNT	KOH + p-phenylenediamine	162.66 Fg^{-1} at 1 Ag^{-1}	-0.8 to 0.2 V	4.23 W h kg^{-1}	96.51% after 4000 cycles	[60]
MWCNTs	KOH + m-phenylenediamine	78 Fg^{-1} at 0.5 Ag^{-1}	-0.5 to 0.5 V	9.99 W h kg^{-1}	90.68% after 10000 cycles	[61]
MWCNTs	H_2SO_4 + indigo carmine	50 Fg^{-1} at 0.88 mA cm^{-2}	0 to 1 V	1.7 W h kg^{-1}	30% after 10000 cycles	[62]
NGPC15	KOH	227.9 Fg^{-1} at 2 mV s^{-1}	-1 to 0 V	-	106% after 5000 cycles	[63]
Boron-doped carbon	H_2SO_4	228 Fg^{-1} at 1 mV s^{-1}	0 to 1 V	8.65 W h kg^{-1}	100% after 1000 cycles	[64]
Carbon nanotube	KOH	180 Fg^{-1}	0 to 0.9 V	6.5 W h kg^{-1}	-	[65]
N_2-doped carbon nanofibers	KOH	202 Fg^{-1} at 1 Ag^{-1}	-1 to 0 V	7.11 W h kg^{-1}	97% after 3000 cycles	[66]
Mesoporous carbon	KOH	128 Fg^{-1} at 50 mA g^{-1}	0.2 to 1 V	1.16 W h kg^{-1}	-	[67]
Mesoporous fullerene	KOH	172 Fg^{-1} at 0.5 Ag^{-1}	-1 to 0 V	-	Significant drop after 1000 cycles	[68]
TiO_2 anchored to CNT	KOH	130.4 Fg^{-1} at 1 Ag^{-1}	-0.05 to 0.5 V	4.47 W h kg^{-1}		[69]
$MnWO_4$/RGO	KOH	288 Fg^{-1} at 5 mV s^{-1}	-0.35 to 0.55 V	-	14.9% after 6000 cycles	[70]
$MnWO_4$	Na_2SO_4	386 Fg^{-1} at 5 mVs^{-1}	0 to 1 V	-	90% after 2000 cycles	[71]
$MnWO_4$	KOH	295 Fg^{-1} at 5 mVs^{-1}	-0.2 to 0.6 V	16 Wh kg^{-1}	> 100% after 3000 cycles	[72]
WO_3-RGO composite	H_2SO_4	495 Fg^{-1} at 1 Ag^{-1}	-0.4 to 0.3 V	-	87.5% after 1000 cycles	[73]
$MnWO_4$ micro flower	Na_2SO_4	324 Fg^{-1} at 1 mA cm^{-2}	0 to 1 V	34 W h kg^{-1}	93% after 8000	[74]
$MnWO_4$@aCNT	KOH	542.18 Fg^{-1} at 2 mVs^{-1}	-0.1 to 0.6 V	5.6 W h kg^{-1}	Above 100% after 15,000 cycles	This work

Similar kind of result was also observed for GCD measurements both for PM and SM respectively (Figure 4.24c). Two such devices in SM (arrangement 1) as well as four in series/parallel combination (arrangement 2) were charged up to 3.1 V with 20 mA current for 15 s across red light emitting diodes (LEDs) (detail of the device arrangement and digital image of device is

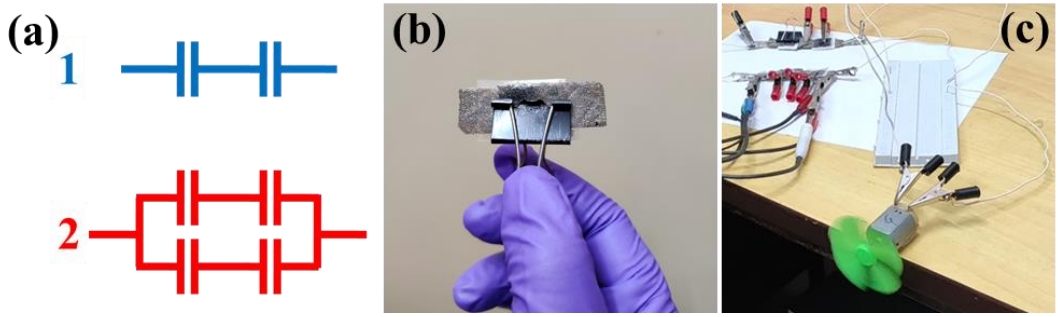

Figure 4.25: (a) **ASC** Device arrangement in series and series/parallel; (b) single ASC Device and (c) digital photographs of running motor fan.

presented in Figure 4.25a-b. Device "arrangement 1" lighted up a of 17 red LEDs connected in parallel in the form of 'JU' (acronym of our university) for 33 s. The same panel was stayed alight for 44 s by the device "arrangement 2" (Figure 4.24d). Devices in 'Arrangement 1" configuration was also managed to drive a digital display clock for nearly 40 minutes (Figure 4.24e). Again, the devices in "arrangement 2" was charged up to 3.2 V by 90 mA current for 12 s, which stored sufficient charge to drive a high-speed small motor fan (3 V, 80 mA) for ~7 s Associated movie clips of LED glow, digital clock and fan in operation are presented in supporting information (Figure 4.25c). All these results verify the competency of the as fabricated devices for their potential usage in modern day applications.

4.4. Conclusions

In summary, we have successfully prepared $MnWO_4$-aCNT hybrid via simple, budgetary protocol with high yield. aCNTs have been synthesized firstly via low temperature solid state method and have been grafted with $MnWO_4$ nanorods by in situ hydrothermal process. The as-fabricated electrodes based on aCNT, $MnWO_4$, $MnWO_4$-aCNT were subjected to CV, GCD and EIS tests. CV analysis of all fabricated electrodes suggested highest specific capacitance of 542.18 Fg^{-1} at a scan rate of 2 mVs^{-1} for $MnWO_4$-aCNT sample. By combining benefits of EDLC character of aCNT and pseudocapacitive features of secondary grown $MnWO_4$ nanorods, this hybrid showed improved electrochemical behaviour than both the individual building blocks. Distinct differences in electrochemical performance were thoroughly investigated on the basis of surface area, electron transport process and electrolyte diffusion. ASC device has been further devised using $MnWO_4$-aCNT hybrid, activated carbon and polymer gel electrolyte (PVA/KOH). The device delivered an energy density of 5.6 Wh kg^{-1} at a power density of 893.6 W kg^{-1} corresponding to the current density of 1 Ag^{-1}. High capacitance retention by the device was confirmed as it also held ~100 % of its initial capacitance even after 6000 long cycle runs. Series and parallel combination of the ASC devices were also able to power commercial red LEDs, rotate small motor fan with no external battery connection. Such designing of low temperature processed aCNT and multi-metallic oxide-based hybrid with creditable electrochemical features suggests its prospect as a building unit of modern long lusting storage devices.

4.5 References

[1] Gür TM. Review of electrical energy storage technologies, materials and systems: challenges and prospects for large-scale grid storage. Energy Environ Sci 2018; 11: 2696–767.

[2] Panda PK, Grigoriev A, Mishra YK, Ahuja R. Progress in supercapacitors: roles of two dimensional nanotubular materials. Nanoscale Adv 2020; 2: 70–108.

[3] Bairi P, Maji S, Hill JP, Kim JH, Ariga K, Shrestha LK. Mesoporous carbon cubes derived from fullerene crystals as a high rate performance electrode material for supercapacitors. J Mater Chem A Mater 2019; 7: 12654–60.

[4] Park SH, Jeong J-M, Kim SJ, Kim KH, Lee SH, Bae NH, et al. Large-area and 3D polyaniline nanoweb film for flexible supercapacitors with high rate capability and long cycle life. ACS Appl Energy Mater 2020; 3: 7746–55.

[5] Chaichi A, Venugopalan G, Devireddy R, Arges C, Gartia MR. A solid-state and flexible supercapacitor that operates across a wide temperature range. ACS Appl Energy Mater 2020; 3: 5693–704.

[6] Sun Z, Wang Y, Chen Z, Li X. Min-max game based energy management strategy for fuel cell/supercapacitor hybrid electric vehicles. Appl Energy 2020; 267: 115086.

[7] Wang Y, Xu F, Mao S, Yang S, Shen Y. Adaptive online power management for more electric aircraft with hybrid energy storage systems. IEEE Transactions on Transportation Electrification 2020; 6: 1780–90.

[8] Li L, Jia C, Zhu X, Zhang S. Utilization of cigarette butt waste as functional carbon precursor for supercapacitors and adsorbents. J Clean Prod 2020; 256: 120326.

[9] Yan J, Li S, Lan B, Wu Y, Lee PS. Rational design of nanostructured electrode materials toward multifunctional supercapacitors. Adv Funct Mater 2020; 30: 1902564.

[10] Yang B, Wang J, Zhang X, Wang J, Shu H, Li S, et al. Applications of battery/supercapacitor hybrid energy storage systems for electric vehicles using perturbation observer based robust control. J Power Sources 2020; 448: 227444.

[11] Zhang L, Zhang F, Yang X, Long G, Wu Y, Zhang T, et al. Porous 3D graphene-based bulk materials with exceptional high surface area and excellent conductivity for supercapacitors. Sci Rep 2013; 3: 1408.

[12] Sheberla D, Bachman JC, Elias JS, Sun C-J, Shao-Horn Y, Dincă M. Conductive MOF electrodes for stable supercapacitors with high areal capacitance. Nat Mater 2017; 16: 220–4.

[13] Chen L-F, Lu Y, Yu L, Lou XWD. Designed formation of hollow particle-based nitrogen-doped carbon nanofibers for high-performance supercapacitors. Energy Environ Sci 2017; 10: 1777–83.

[14] Wang F, Chen L, Li H, Duan G, He S, Zhang L, et al. N-doped honeycomb-like porous carbon towards high-performance supercapacitor. Chinese Chemical Letters 2020; 31: 1986–90.

[15] Stoller MD, Magnuson CW, Zhu Y, Murali S, Suk JW, Piner R, et al. Interfacial capacitance of single layer graphene. Energy Environ Sci 2011; 4: 4685–9.

[16] Ramirez-Castro C, Schütter C, Passerini S, Balducci A. Microporous carbonaceous materials prepared from biowaste for supercapacitor application. Electrochim Acta 2016; 206: 452–7.

[17] Boukhalfa S, Evanoff K, Yushin G. Atomic layer deposition of vanadium oxide on carbon nanotubes for high-power supercapacitor electrodes. Energy Environ Sci 2012; 5: 6872–9.

[18] Sahoo S, Rout CS. Facile electrochemical synthesis of porous manganese-cobalt-sulfide based ternary transition metal sulfide nanosheets architectures for high performance energy storage applications. Electrochim Acta 2016; 220: 57–66.

[19] Meng Q, Cai K, Chen Y, Chen L. Research progress on conducting polymer based supercapacitor electrode materials. Nano Energy 2017; 36: 268–85.

[20] Hu Q, Jiang X, He M, Zheng Q, Lam KH, Lin D. Core-shell nanostructured MnO_2@ Co9S8 arrays for high-performance supercapacitors. Electrochim Acta 2020; 338: 135896.

[21] Sk MM, Yue CY, Ghosh K, Jena RK. Review on advances in porous nanostructured nickel oxides and their composite electrodes for high-performance supercapacitors. J Power Sources 2016; 308: 121–40.

[22] Yao S, Xing L, Dong Y, Wu X. Hierarchical WO_3@ $MnWO_4$ core-shell structure for asymmetric supercapacitor with ultrahigh cycling performance at low temperature. J Colloid Interface Sci 2018; 531: 216–24.

[23] Pandit B, Dubal DP, Gómez-Romero P, Kale BB, Sankapal BR. V_2O_5 encapsulated MWCNTs in 2D surface architecture: complete solid-state bendable highly stabilized energy efficient supercapacitor device. Sci Rep 2017; 7: 43430.

[24] Harichandran G, Divya P, Radha S, Yesuraj J. Facile and controllable CTAB-assisted sonochemical synthesis of one-dimensional $MnWO_4$ nanorods for supercapacitor application. J Mol Struct 2020; 1199: 126931.

[25] Wu C, Cai J, Zhu Y, Zhang K. Hybrid reduced graphene oxide nanosheet supported Mn–Ni–Co ternary oxides for aqueous asymmetric supercapacitors. ACS Appl Mater Interfaces 2017; 9: 19114–23.

[26] Muthamizh S, Suresh R, Giribabu K, Manigandan R, Kumar SP, Munusamy S, et al. $MnWO_4$ nanocapsules: synthesis, characterization and its electrochemical sensing property. J Alloys Compd 2015; 619: 601–9.

[27] Tang J, Shen J, Li N, Ye M. Facile synthesis of layered $MnWO_4$/reduced graphene oxide for supercapacitor application. J Alloys Compd 2016; 666: 15–22.

[28] Raj BGS, Acharya J, Seo M-K, Khil M-S, Kim H-Y, Kim B-S. One-pot sonochemical synthesis of hierarchical $MnWO_4$ microflowers as effective electrodes in neutral electrolyte for high performance asymmetric supercapacitors. Int J Hydrogen Energy 2019; 44: 10838–51.

[29] Li F, Xu X, Huo J, Wang W. A simple synthesis of $MnWO_4$ nanoparticles as a novel energy storage material. Mater Chem Phys 2015; 167: 22–7.

[30] Naik KK, Gangan AS, Pathak A, Chakraborty B, Nayak SK, Rout CS. Facile Hydrothermal Synthesis of $MnWO_4$ Nanorods for Non-Enzymatic Glucose Sensing and Supercapacitor Properties with Insights from Density Functional Theory Simulations. ChemistrySelect 2017; 2: 5707–15.

[31] Shim H, Lim A, Kim J, Lee G, Kim D. Hydrothermal realization of a hierarchical, flowerlike $MnWO_4$@ MWCNTs nanocomposite with enhanced reversible Li storage as a new anode material. Chemistry–An Asian Journal 2013; 8: 2851–8.

[32] Ganguly D, Pahari D, Das NS, Howli P, Das B, Banerjee D, et al. All-amorphous CNT-MnO_2 nanoflaky hybrid for improved supercapacitor applications. Journal of Electroanalytical Chemistry 2016; 778: 12–22.

[33] Lei S, Tang K, Fang Z, Huang Y, Zheng H. Synthesis of $MnWO_4$ nanofibres by a surfactant-assisted complexation–precipitation approach and control of morphology. Nanotechnology 2005; 16: 2407.

[34] Maiti UN, Maiti S, Majumder TP, Chattopadhyay KK. Ultra-thin graphene edges at the nanowire tips: a cascade cold cathode with two-stage field amplification. Nanotechnology 2011; 22: 505703.

[35] Tong W, Li L, Hu W, Yan T, Guan X, Li G. Kinetic control of $MnWO_4$ nanoparticles for tailored structural properties. The Journal of Physical Chemistry C 2010; 114: 15298–305.

[36] Gao G, Dang W, Wu H, Zhang G, Feng C. Synthesis of $MnWO_4$@C as novel anode material for lithium ion battery. Journal of Materials Science: Materials in Electronics 2018; 29: 12804–12.

[37] Maity S, Das B, Samanta M, Das BK, Ghosh S, Chattopadhyay KK. $MoSe_2$-amorphous CNT hierarchical hybrid core–shell structure for efficient hydrogen evolution reaction. ACS Appl Energy Mater 2020; 3: 5067–76.

[38] Tiwari A, Singh V, Nagaiah TC. Tuning the $MnWO_4$ morphology and its electrocatalytic activity towards oxygen reduction reaction. J Mater Chem A Mater 2018; 6: 2681–92.

[39] Senthilkumar ST, Selvan RK, Melo JS. Redox additive/active electrolytes: a novel approach to enhance the performance of supercapacitors. J Mater Chem A Mater 2013; 1: 12386–94.

[40] Pujari RB, Lokhande VC, Patil UM, Lee DW, Lokhande CD. Controlled sulfurization of $MnCO_3$ microcubes architectured MnS_2 nanoparticles with 1.7 fold capacitance increment for high energy density supercapacitor. Electrochim Acta 2019; 301: 366–76.

[41] Panigrahi K, Howli P, Chattopadhyay KK. 3D network of V_2O_5 for flexible symmetric supercapacitor. Electrochim Acta 2020; 337: 135701.

[42] Jagadale AD, Jamadade VS, Pusawale SN, Lokhande CD. Effect of scan rate on the morphology of potentiodynamically deposited β-$Co(OH)_2$ and corresponding supercapacitive performance. Electrochim Acta 2012; 78: 92–7.

[43] Ivanishchev A V, Bobrikov IA, Ivanishcheva IA, Ivanshina OY. Study of structural and electrochemical characteristics of $LiNi_{0.33}Mn_{0.33}Co_{0.33}O_2$ electrode at lithium content variation. Journal of Electroanalytical Chemistry 2018; 821: 140–51.

[44] Ivanishchev A V, Churikov A V, Ivanishcheva IA, Ushakov A V, Sneha MJ, Babbar P, et al. Models of lithium transport as applied to determination of diffusion characteristics of intercalation electrodes. Russian Journal of Electrochemistry 2017; 53: 706–12.

[45] Ivanishchev A V, Ushakov A V, Ivanishcheva IA, Churikov A V, Mironov A V, Fedotov SS, et al. Structural and electrochemical study of fast Li diffusion in $Li_3V_2(PO_4)_3$-based electrode material. Electrochim Acta 2017; 230: 479–91.

[46] Arunkumar M, Paul A. Importance of electrode preparation methodologies in supercapacitor applications. ACS Omega 2017; 2: 8039.

[47] Singh KP, Bhattacharjya D, Razmjooei F, Yu J-S. Effect of pristine graphene incorporation on charge storage mechanism of three-dimensional graphene oxide: superior energy and power density retention. Sci Rep 2016; 6: 31555.

[48] Taberna PL, Simon P, Fauvarque J-F. Electrochemical characteristics and impedance spectroscopy studies of carbon-carbon supercapacitors. J Electrochem Soc 2003; 150: A292.

[49] Ashraf CM, Anilkumar KM, Jinisha B, Manoj M, Pradeep VS, Jayalekshmi S. Acid washed, steam activated, coconut shell derived carbon for high power supercapacitor applications. J Electrochem Soc 2018; 165: A900.

[50] Bairi P, Sardar K, Chanda K, Samanta M, Thakur S, Panigrahi K, et al. Shape-shifting via salt crystallization: conversion of a nanostructured polymer into a site-selective nitrogen-doped carbon sheet with enhanced supercapacitive performance. ACS Appl Energy Mater 2020; 3: 5984–92.

[51] Zhao YL, Barman AR, Dhar S, Annadi A, Motapothula M, Wang J, et al. Scaling of flat band potential and dielectric constant as a function of Ta concentration in Ta-TiO_2 epitaxial films. AIP Adv 2011; 1.

[52] Mott NF. The theory of crystal rectifiers. Proc R Soc Lond A Math Phys Sci 1939; 171: 27–38.

[53] Thakur S, Maiti S, Paul T, Besra N, Sarkar S, Chattopadhyay KK. Geometrically intricate sheet-on-pillar/flake hierarchy embracing cobaltosic and manganese oxides

over flexible carbon scaffold for binder-free high-energy-density supercapacitor. CrystEngComm 2018; 20: 6183–96.

[54] Xu Y, Lin Z, Huang X, Liu Y, Huang Y, Duan X. Flexible solid-state supercapacitors based on three-dimensional graphene hydrogel films. ACS Nano 2013; 7: 4042–9.

[55] Kang YJ, Chung H, Han C-H, Kim W. All-solid-state flexible supercapacitors based on papers coated with carbon nanotubes and ionic-liquid-based gel electrolytes. Nanotechnology 2012; 23: 065401.

[56] Choi BG, Chang S-J, Kang H-W, Park CP, Kim HJ, Hong WH, et al. High performance of a solid-state flexible asymmetric supercapacitor based on graphene films. Nanoscale 2012; 4: 4983–8.

[57] Khomenko V, Raymundo-Pinero E, Frackowiak E, Beguin F. High-voltage asymmetric supercapacitors operating in aqueous electrolyte. Applied Physics A 2006; 82: 567–73.

[58] Sidhu NK, Rastogi AC. Electrochemical performance of supercapacitors based on carbon nanofoam composite and microporous poly (3, 4-ethylenedioxythiophene) thin film asymmetric electrodes. Mater Chem Phys 2016; 176: 75–86.

[59] An KH, Kim WS, Park YS, Moon J, Bae DJ, Lim SC, et al. Electrochemical properties of high-power supercapacitors using single-walled carbon nanotube electrodes. Adv Funct Mater 2001; 11: 387–92.

[60] Yu H, Wu J, Lin J, Fan L, Huang M, Lin Y, et al. A Reversible Redox Strategy for SWCNT-Based Supercapacitors Using a High-Performance Electrolyte. ChemPhysChem 2013; 14: 394–9.

[61] Yu H, Fan L, Wu J, Lin Y, Huang M, Lin J, et al. Redox-active alkaline electrolyte for carbon-based supercapacitor with pseudocapacitive performance and excellent cyclability. RSC Adv 2012; 2: 6736–40.

[62] Roldán S, González Z, Blanco C, Granda M, Menéndez R, Santamaría R. Redox-active electrolyte for carbon nanotube-based electric double layer capacitors. Electrochim Acta 2011; 56: 3401–5.

[63] Bairi P, Sardar K, Chanda K, Samanta M, Thakur S, Panigrahi K, et al. Shape-shifting via salt crystallization: conversion of a nanostructured polymer into a site-selective nitrogen-doped carbon sheet with enhanced supercapacitive performance. ACS Appl Energy Mater 2020; 3: 5984–92.

[64] Wu Z-S, Winter A, Chen L, Sun Y, Turchanin A, Feng X, et al. Three-dimensional nitrogen and boron co-doped graphene for high-performance all-solid-state supercapacitors. Advanced Materials 2012; 24.

[65] An KH, Kim WS, Park YS, Choi YC, Lee SM, Chung DC, et al. Supercapacitors using single-walled carbon nanotube electrodes. Advanced Materials 2001; 13: 497–500.

[66] Chen L-F, Zhang X-D, Liang H-W, Kong M, Guan Q-F, Chen P, et al. Synthesis of nitrogen-doped porous carbon nanofibers as an efficient electrode material for supercapacitors. ACS Nano 2012; 6: 7092–102.

[67] Prabaharan SRS, Vimala R, Zainal Z. Nanostructured mesoporous carbon as electrodes for supercapacitors. J Power Sources 2006; 161: 730–6.

[68] Benzigar MR, Joseph S, Baskar A V, Park D, Chandra G, Umapathy S, et al. Ordered mesoporous C70 with highly crystalline pore walls for energy applications. Adv Funct Mater 2018; 28: 1803701.

[69] Sun X, Xie M, Travis JJ, Wang G, Sun H, Lian J, et al. Pseudocapacitance of amorphous TiO_2 thin films anchored to graphene and carbon nanotubes using atomic layer deposition. The Journal of Physical Chemistry C 2013; 117: 22497–508.

[70] Tang J, Shen J, Li N, Ye M. Facile synthesis of layered MnWO4/reduced graphene oxide for supercapacitor application. J Alloys Compd 2016; 666: 15–22.

[71] Yesuraj J, Elanthamilan E, Muthuraaman B, Suthanthiraraj SA, Merlin JP. Bio-assisted hydrothermal synthesis and characterization of $MnWO_4$ nanorods for high-performance supercapacitor applications. J Electron Mater 2019; 48: 7239–49.

[72] Li F, Xu X, Huo J, Wang W. A simple synthesis of $MnWO_4$ nanoparticles as a novel energy storage material. Mater Chem Phys 2015; 167: 22–7.

[73] Chu J, Lu D, Wang X, Wang X, Xiong S. WO_3 nanoflower coated with graphene nanosheet: synergetic energy storage composite electrode for supercapacitor application. J Alloys Compd 2017; 702: 568–72.

[74] Raj BGS, Acharya J, Seo M-K, Khil M-S, Kim H-Y, Kim B-S. One-pot sonochemical synthesis of hierarchical $MnWO_4$ microflowers as effective electrodes in neutral electrolyte for high performance asymmetric supercapacitors. Int J Hydrogen Energy 2019; 44: 10838–51.

Chapter 5: Synthesis of Different Manganese Tungstate Nanostructures for Enhanced Charge Storage Application: Theoretical support of the Experimental Finding

5.1. Introduction

In contemplation of the burgeoning energy demand, greenhouse gases level increment globally and ever impending depletion of conventional fossil-based fuels, alternative energies are now of great demand due to its all-aspect environment friendliness [1].

Though there are various systems that can store or convert energy, but supercapacitor (SC) particularly the electrochemical SCs are considered to be one of the most effective due to their ability to store more energy compared to the normal capacitors. This particular system has gained the central attraction of the associated industries for its several unique features that include favourable charging-discharging, long-time stable performance at a wide temperature range, environment friendliness, low maintenance cost and other features [2–5]. Such outstanding properties make SCs provide extensive efficacy in automobile, aerospace, electronic communications, energy sector etc. [6–10]. SCs are broadly classified into two types i.e., electrochemical double layer capacitors (EDLCs) and pseudo capacitors. In the first category, the charge gets stored by electrostatic ion adsorption in the electrolyte whereas in the second category, redox reaction at the interface between electrode and electrolyte store the charges. Different carbonaceous materials like carbon nanoparticles, nanotubes and graphene are commonly used as electrode in EDLC because of their favourable features like high surface area, conductivity and chemical stability [11–15]. EDLCs based on nano-porous carbonaceous materials are capable of delivering large power density but only low specific capacitance [16–18]. In the contrary, transition metal oxide (TMO), sulphide and polymer-based pseudo capacitors are capable of offering higher storage and rate capability compared to the EDLCs [19–22]. TMOs gained higher attention presently as SC electrode material due to their easy availability, favourable reaction kinetics, green features including less toxicity and high storage capability [23]. Numerous TMOs such as MnO_2, Co_3O_4, V_2O_5, NiO, SnO_2, etc. have been investigated widely in this respect [24–28]. However, these materials suffer

from their inherent poor electrical conductivity that negatively affects electron transport in them [29]. It is likely that multi-metallic oxide may show much enhancement in charge storing as they show higher electronic conductivity and may be associated with multiple oxidation states thus leaving the possibilities of richer redox reaction compared to single component TMOs [30]. Manganese tungstate ($MnWO_4$), as a bimetallic oxide gathered substantial attention due to its astonishing catalytic, magnetic, and electrochemical properties. Due to this, the material found its applications in different fields like photocatalysis, optical communication, sensing and others [31]. $MnWO_4$ has a monoclinic structure where Mn and W atom form an octahedral coordination surrounded by six O atoms. These oxygen atoms are so arranged that they develop distorted hexagonal close pack structure [25,29]. In comparison to pure tungstate oxides, its' binary form gives higher conduction because of the incorporation of the second atom [32]. Thus, the simultaneous presence of both Mn and W atoms makes $MnWO_4$ a promising candidate as electrode material for SCs [33]. Several reports are available in literature regarding the electrochemical aspects of $MnWO_4$. However, the capacitive performances of those electrode materials are still unsatisfactory. [34,35]. Also, the long cycle stability remained as one of the major issues hindering the material to be used in practical industry scale operation [25]**.** Thus, electrode materials with enhanced electrochemical features such as high specific capacitance and long cycle stability are the need of hour.

In the present work, we have synthesized $MnWO_4$ nanostructures of different aspect ratio by subtle tuning over reaction temperature and reaction time. As an immediate utility of the size-controlled nanostructures, the electrochemical properties of the as-synthesized $MnWO_4$ nanostructures have been studied. The detail study shows that specific capacitance (C_s) values of the samples get highly enhanced for the sample synthesized for the longest time duration. It is believed that simultaneous presence of porosity and efficient electron

transport collectively helps diffusion of the electrolyte significantly. Not only that, it has been observed that the change in the synthesis condition has a marked influence on the surface area which in turn governs the charge storage properties of the samples. Through density functional theory (DFT) calculation it has been found that $MnWO_4$ has different favourable aspects that helps the system to act as an efficient energy storage material as confirmed experimentally. The presence of electronic states near Fermi level with the maximum quantum capacitance value of 6700 $\mu F/cm^2$, as found from DFT calculation, is mainly attributed to the density of electrons in 'd' orbitals of Mn.

Such preeminent electrochemical performance obtained from the bi metallic tungstate oxide sample will help researchers designing electrode materials with different multi-metallic oxides.

5.2. Experimental and Characterization

The basic experimental technique for synthesizing $MnWO_4$ has been described in our previous work [36]. Briefly, in a typical run, the materials taken were manganese (II) acetate tetrahydrate crystals ($(CH_3COO)_2Mn$, $4H_2O$) and sodium tungstate dihydrate (Na_2WO_4, $2H_2O$). (Taken analytical grade without further purification).

In a typical experiment, 0.5 M of $(CH_3COO)_2Mn$ and 0.5 M of Na_2WO_4 were mixed in deionized water through stirring. The homogeneous solution was then taken into an autoclave (Teflon lined) maintained at 573 K for three different times 12, 18 and 24 hours. Thus, three samples were obtained and named as MWO12, MWO18 and MWO24 respectively. However, in each cases the final sample was obtained after washing the product generated in autoclave with deionized water followed by filtering and drying the residue over-night at 80 $^{\circ}C$.

The samples, thus developed were studied by X-ray diffraction (XRD, Bruker D8: Advance diffractometer), Raman spectroscopy (RAMAN, alpha 300, Witec, laser source of λ = 532

nm), X-ray photoelectron spectrometer (XPS, SPECS, HAS-3500), field emission scanning electron microscope (FESEM, Hitachi S-4800), transmission electron microscope (HRTEM, JEOL, JEM 2100), BET surface area analyser (Nova 1000e, Quantachrome, United States) and thermo-gravimetric analysis.

The electrochemical measurement was performed by using Gamry Interface 1000 (potentiostat/galvanostat/ZRA) in three-electrode configuration using 1 M KOH aqueous solution as the electrolyte. In the three electrodes system Pt wire and Ag/AgCl were chosen as the counter and reference electrodes respectively. To prepare the working electrode active material, carbon black and polyvinylidene fluoride were taken as 8:1:1 (wt %) ratio. N-methyl-2-pyrrolidone was taken to convert the system into a slurry paste which was subsequently coated on nickel foam (1 × 1 cm^2) and dried to get the final product [32]. During the Cyclic voltammetry (CV) measurement, a potential window between -0.1 to 0.6 V (vs. Ag/AgCl) was chosen. Charging-discharging (GCD) characteristics and electrochemical impedance spectroscopy (EIS) was also performed for the samples.

The theoretical calculation was done using DFT that has been employed to the monoclinic structures of $MnWO_4$ with the space group of P2/c (JCPDS Card No 13-0434) in accordance with the experimental sample. Vienna ab-initio simulation package (VASP) [37,38] was implemented to carry out the first principles calculations along with the projector augmented wave (PAW) [39] method within the generalized gradient approximation (GGA). The exchange-correlation terms were included in the calculations via the Perdew-Burke-Ernzerhof (PBE) functional [40]. The plane wave basis set cut-off was set at 500 eV. Γ centred two k-point grids of (5×5×5) and (8 × 8 × 8) were implemented during the geometry optimization and electronic properties study of bulk $MnWO_4$ respectively. For the optimization of the structure system, relaxation was continued till the convergence of the free energy value came below 10^{-5} eV/atom. A 24 Å Vacuum slab was constructed perpendicular

to the computational surface slab for the optimization and electronic calculation of the (-1 1 1) surface to cancel spurious interactions between periodic images. The effect of dispersive forces was taken into account via the DFT + D2 (Grimme's) method [41] as implemented in VASP. The computed unit cell lattice parameters for bulk $MnWO_4$ are a = 4.63, b = 5.58, c = 4.91 Å considering on-site interaction of oxygen in GGA+U method with U values of 3.90 and 6.20 for the electrons of Mn and W atoms [42,43]. The values of the lattice parameters are close with the reported literature [44]

5.3. Results and Discussions:

5.3.1. Phase confirmation through XRD and Raman analysis

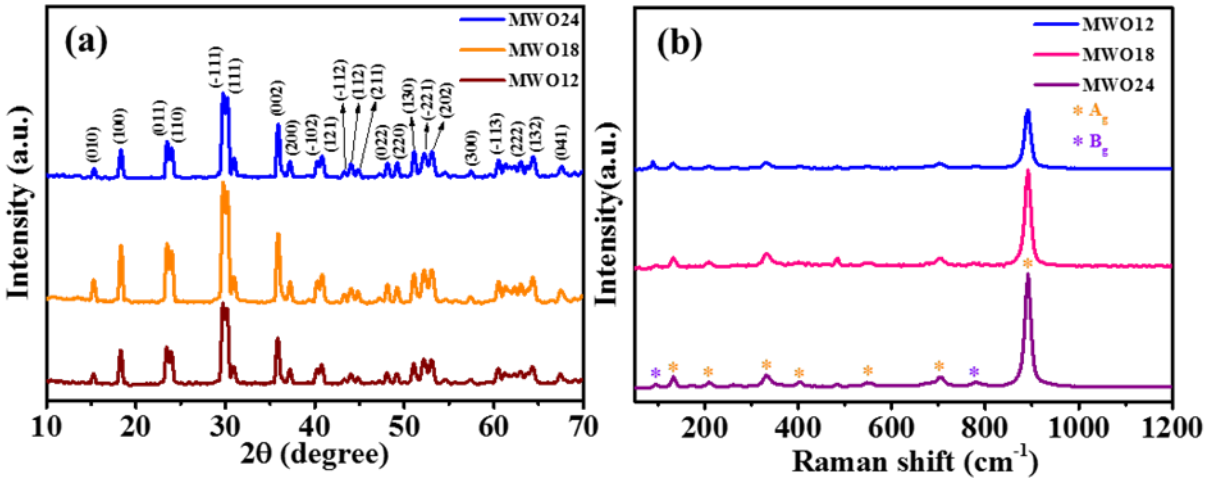

Figure 5.1: (a) XRD (b) RAMAN spectra of all the samples.

Figure 5.1a shows the XRD patterns of all the samples. The spectra show almost identical pattern with several distinct peaks all of which have been indexed to the monoclinic phase of $MnWO_4$ and the corresponding values of lattice constants come out to be a = 4.829 Å, b = 5.759 Å, and c = 4.998 Å [43,45] [JCPDS Card No 13-0434]. The sets of distinct peaks and the absence of any impurity induced peak confirm the phase purity of the sample. The mean

crystallite sizes of the as prepared $MnWO_4$ samples were evaluated using the Scherrer formula:

$$D = \frac{0.9\lambda}{\beta cos\,\theta} \quad (1)$$

Here, D denotes crystallite size. **λ**, β and θ stand for wavelength of X-ray source, full width at half maximum and diffraction angle. The average crystallite sizes for MWO24, MWO18 and MWO12 come out to be 14.5, 15.9 and 17 nm respectively.

Room temperature Raman analysis of all the samples were further carried out and are shown in Figure 5.1b. Here also one can see almost identical spectra for all the samples. Figure 5.1b shows that there are several peaks of which the peak with highest intensity is centred at 877 cm^{-1} and carries the signature of the presence of W-O bond (symmetric stretching) in $MnWO_4$ [46]. Peaks around 767 and 690 cm^{-1} respectively are associated with the asymmetric and symmetric stretching vibration of W–O–W bond. The small band at ~122 cm^{-1} carries the signature of the translational mode of tungsten [31]. Thus, the Raman spectra can indirectly be used as another secondary means to confirm the successful phase formation of the sample and thereby validates the XRD results.

5.3.2. Microscopic study:

Figure 5.2a-c shows the FESEM images of the samples. It has clearly been seen that with the increase of the reaction time there is profound change in the morphologies of the sample. With the increase of reaction time, the elongated particles take nearly square-like morphology. For the MWO12 sample, the dimension is around 300 nm in length and around 30 – 40 nm in breadth, thus giving considerable aspect ratio. For other two samples i.e., MWO18 and MWO24, the breadth remains almost the same whereas the length decreases giving lesser aspect ratio. To have a better understanding about the microstructures, HRTEM studies have been carried out for the MWO24 sample which has given the best electrochemical performance discussed in the coming section.

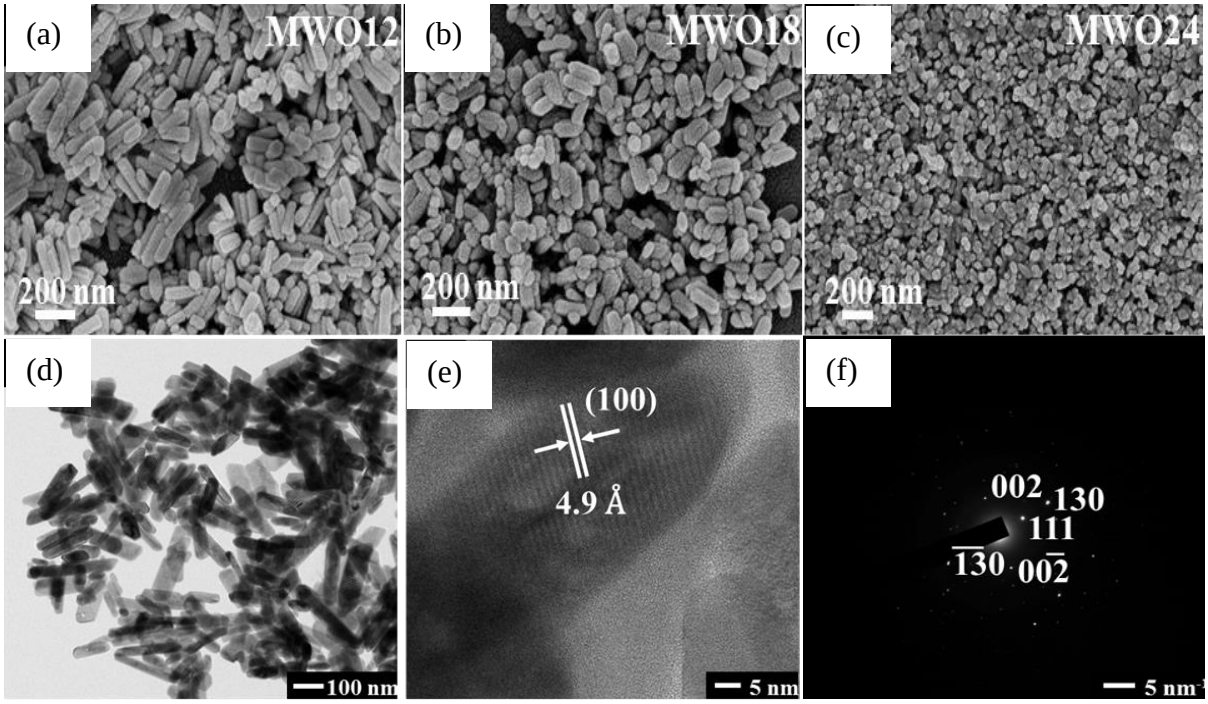

Figure 5.2: FESEM images of (a) MWO12 (b), MWO18 (c) and MWO24; (d) HRTEM image of MWO24; (e) corresponding lattice image (f) and SAED pattern.

The HRTEM image of MWO24 has been depicted in Figure 5.2d-f along with lattice image and SAED pattern. From Figure 5.2a the distinct morphological features of MWO24 may be seen which shows that length of these randomly oriented elongated MWO24 nanostructure takes the values within the range of 40-200 nm whereas from the histogram analysis (Figure 5.3a-b) it is seen that most of the nanostructures have length within the range of 100 to 120 nm and diameters between 30-40 nm. The lattice spacing as can be seen from Figure 5.2e has value 4.9 Å confirming the presence of (100) plane. The SAED pattern shown in Figure 5.2f indicates the presence of different planes like (002), (111), (130) suggesting the polycrystalline nature of the sample, as already revealed from XRD.

5.3.3. X-ray photoelectron spectroscopic study:

For the comprehensive investigation of the constituting elements present in the as developed samples with corresponding oxidation states, XPS analysis of MWO24 was performed and shown in Figure 5.4a-d. From Figure 5.4a it is seen that there are several distinct peaks

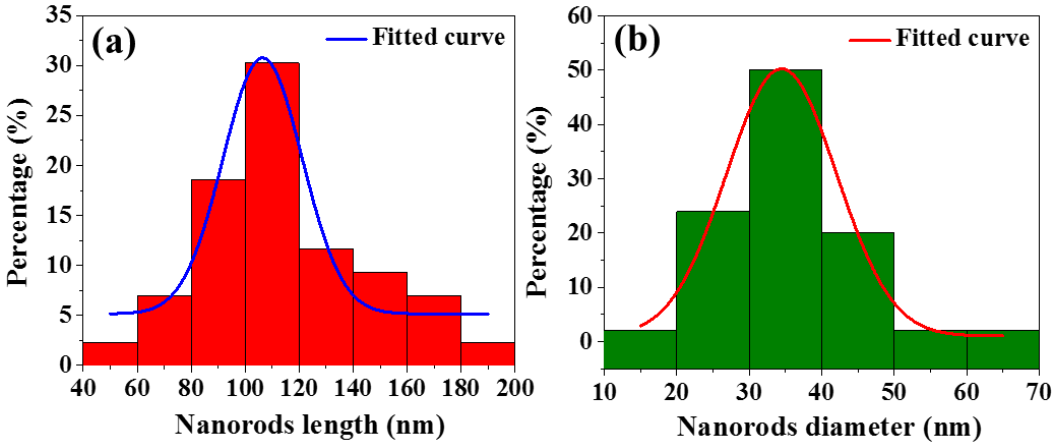

Figure 5.3: Percentage distribution of (a) rod length and (b) rod diameter of MWO24 from TEM analysis.

centred at binding energy values ~653.5, 641.5, ~530.7, 425.9, 283.6, 259.4, 246.2, ~35.3 and ~37.4 eV. Among this, the peaks at ~653.5 and 641.5 respectively carry the signature of Mn $2p_{3/2}$ and Mn $2p_{1/2}$. The peak at ~530.7 eV corresponds to O 1s state and is associated with the O^{-2} forming oxide together with Mn and W. De-convolution of the peak as shown in Figure 5.4b shows a small hump at ~532.3 eV due to surface hydration, which inexorably exists in the nanoforms, mostly in case of wet chemical synthesis techniques. Carbon 1s peak w r t which the background correction of the spectra is done can be seen centring at 283.9 eV. Peaks at very lower binding values like ~35.3 and ~37.4 eV are related with W $4f_{7/2}$ and W

$4f_{5/2}$ energy levels and de-convoluted in Figure 5.4c. Similarly, de-convolution of the peaks, associated with Mn $2p_{3/2}$ and Mn $2p_{½}$ respectively, has been done and shown in Figure 5.4d. Such elemental analysis confirms the successful foundation of $MnWO_4$ with oxidation state of Mn and W to be +2 and +6 respectively [47]. Atomic percentage (%) of the constituent elements present in $MnWO_4$ is assessed from XPS spectrum and the corresponding ratio for Mn: W: O is found to be 16: 15: 70, which corroborates well with literature [31].

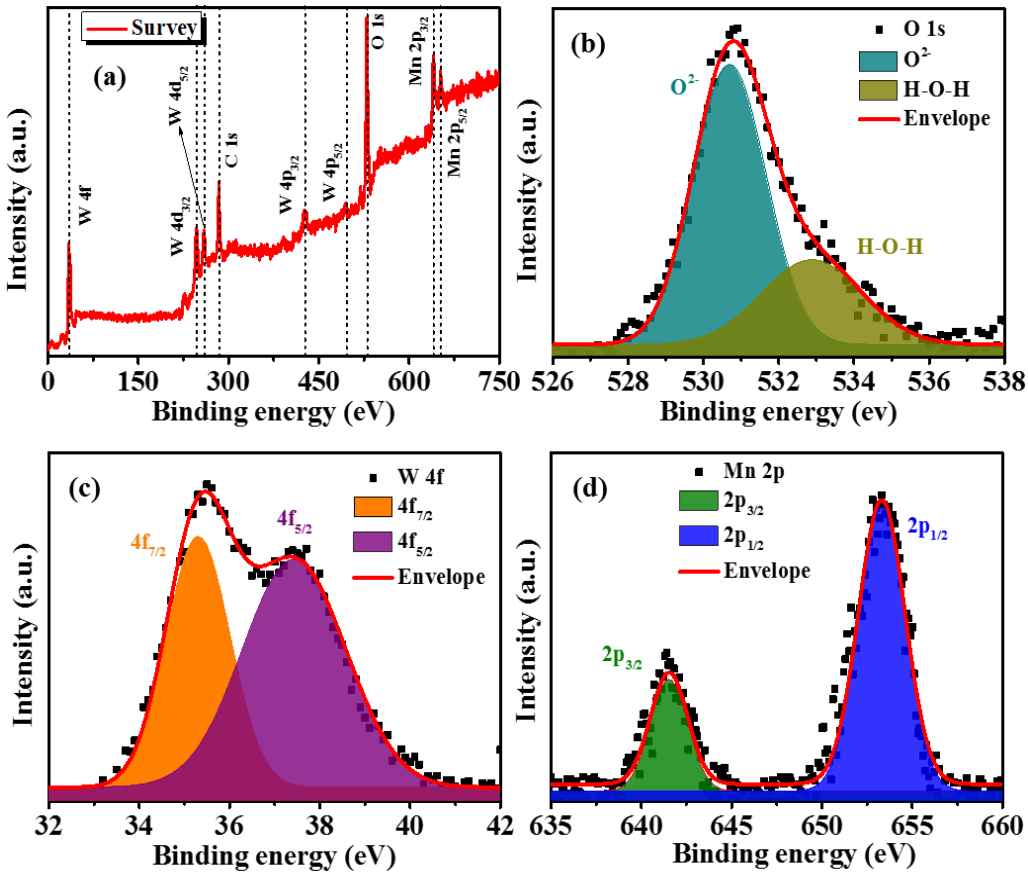

Figure 5.4: XPS spectra of MWO24; (a) survey spectra; de-convolution of (b) O 1s, (c) W 4f and (d) Mn 2p peak.

5.3.4. BET study

It is noteworthy that porosity and surface area are two crucial factors that manage the electrochemical performances of any surface. Keeping this in mind, the surface textural properties of all the samples were studied by nitrogen sorption measurements. N_2 adsorption–desorption isotherms of the samples have been shown in Figure 5.5a. From the Figure 5.5a**,** specific surface areas of MWO24, MWO18 and MWO12 are found to be 24.3, 19.7, and 15.8 $m^2\ g^{-1}$ respectively. Higher surface area for MWO24 arises due to the high porosity of the corresponding sample. The variations of pore volume with pore diameter for all the samples are shown in Figure 5.5b. As obvious, the porosity of MWO24 has values considerably higher than the other two samples. Higher porosity and surface area lead to higher ion and electron transport and greater contact area between samples and electrolyte, which in turn gives promising electrochemical performance from MWO24.

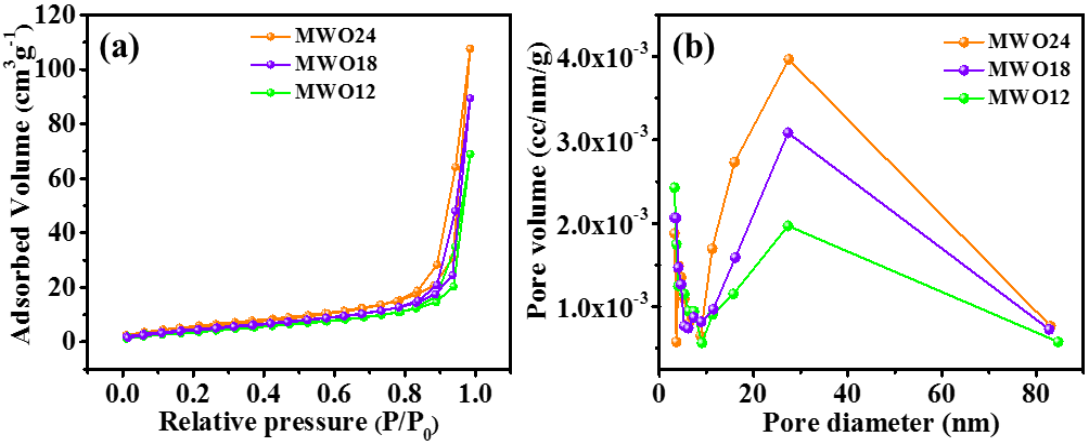

Figure 5.5: (a) N_2 adsorption–desorption isotherms and (b) pore distributions of all the samples.

5.3.5. Thermal study:

The thermo-gravimetric (TG) study along with the corresponding derivative curve of all the samples have been done and the corresponding thermograms are shown in Figure 5.6a and 5.6b. The thermograms were taken from room temperature up to 1073 K with a heating rate of 10 K/minute.

From Figure 5.6a it has been seen that in the entire region, all the samples show extremely high thermal stability with maximum percentage of weight loss not more than 4%. However, in this small weight loss, MWO24 shows little fastness compared to the other.

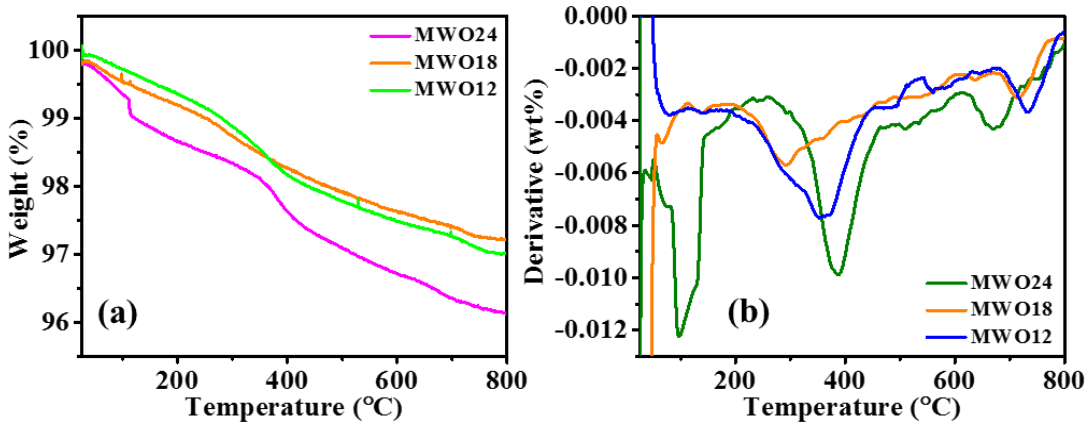

Figure 5.6: TGA (a), and corresponding derivative curves (b) of all the samples.

Derivative of the TGA thermogram (DTG) has been shown in Figure 5.6b. It is seen that here also the curve associated with MWO24 shows a prominent difference from the other two. It is seen that the rate of weight loss for this particular sample is significant at 95, 388 and 668 ^{o}C. For the other two samples, there is no significant weight loss at 95 ^{o}C. However, one can see a relatively lesser rate of mass loss at around 350 and 730 ^{o}C.

5.3.6. Electrochemical analysis

The electrochemical behaviour of all the samples has been shown in Figure 5.7a-c in the form of capacitance-voltage (C-V) loops with different scan rates. It is seen that all the samples exhibited reversible redox behaviour. No significant changes in the loop of all the samples were observed even at higher scan rates. However, heightening in the capacitance values is recorded with the increase of scan rate which stipulates excellent capacitive behaviour of the electrode material. Intercalation/de-intercalation to the active sites of electrode material with K^{+} ions of redox species is the basic cause behind the origin of redox mechanism [48,49].

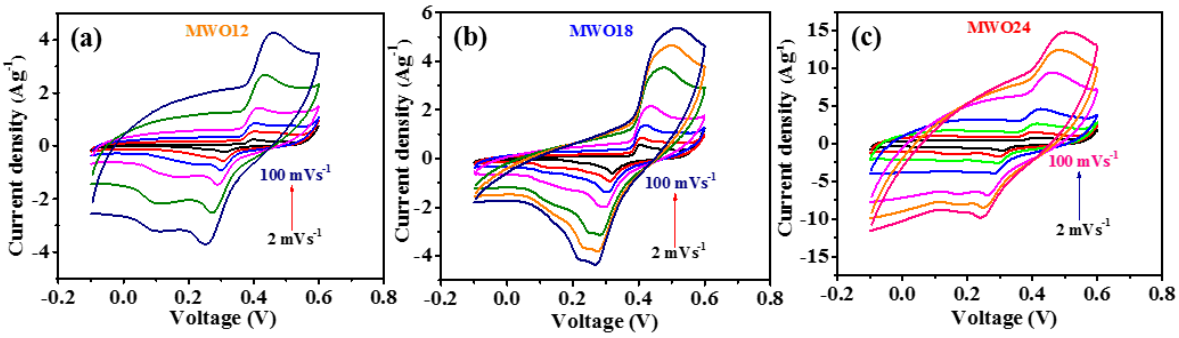

Figure 5.7: Capacitance – voltage relationship (C-V loop) of (a) MWO12, (b) MWO18, and (c) MWO24.

C_s values of the samples were determined with the formula as follows:

$$C_s = \frac{Q}{V} = \frac{\int I(V)dV}{\Delta V \times \upsilon \times \Delta m} \quad (2)$$

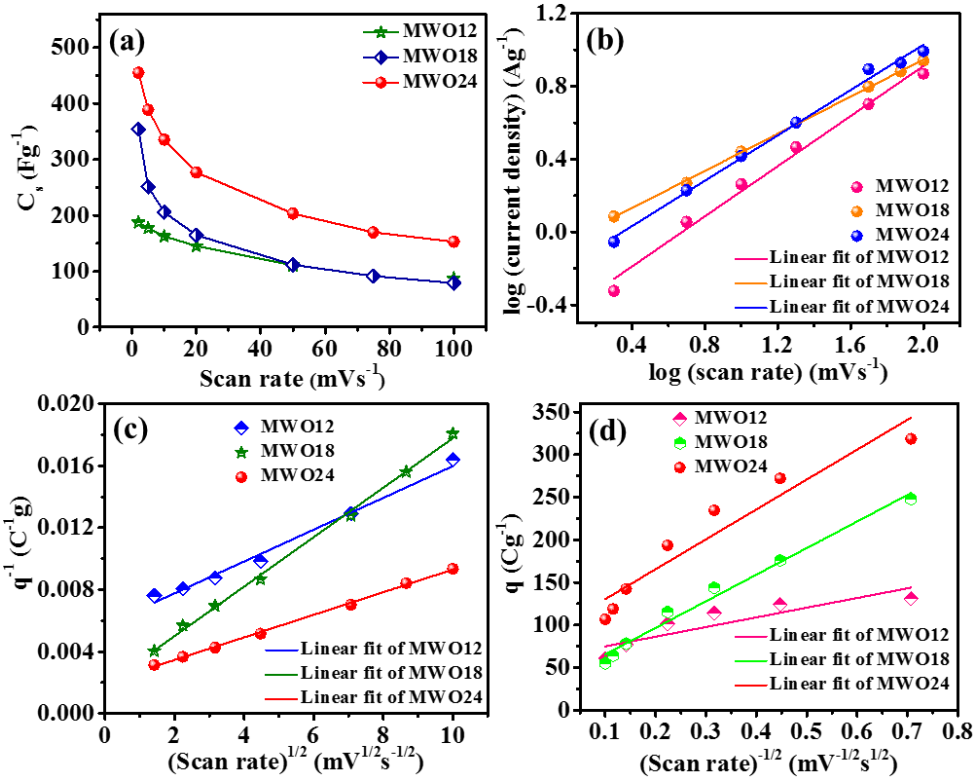

Figure 5.8: (a) Variation in C_s values with scan rate for all the samples, (b) log (current density) vs log (scan rate) plot of all samples; (c) inverse voltammetric charge (q^{-1}) vs square root of scan rate of all the samples and (d) Voltammetric charge (q) vs inverse square root of scan rate.

Here $\int I(V)dV$ gives the area under CV loop, υ denotes rate of scan in mVs^{-1}, ΔV (V) gives the value of potential window and Δm (g) gives mass of the active electrode. Figure 5.8a shows the variations in C_s with V.

To investigate the charge storage mechanism from CV analysis, the cathode peak current density (i_p) of all the samples have been plotted against scan rate in logarithmic scale. The corresponding plots have been shown in Figure 5.8b.

The i_p and the scan rate (υ) are supposed to be related to each other through a power law equation given below:

$$i_p = a\upsilon^b \quad (3)$$

The adjustment parameters a and b in equation 3 may be obtained from the intercept and slope of the plot shown in Figure 5.8b.

It is well known that for capacitive charge storage mechanism the value of b should be unity. On the other hand, "b" value of 0.5 denotes semi-infinite diffusion induced charge storage [49]. In our case, sample MWO24, MWO18 and MWO12 give b values of 0.62, 0.51 and 0.69 respectively confirming the existence of combined charge storage mechanism i.e., surface capacitive (q_s) process as well as diffusion controlled (q_d) technique. It is to be noted that at higher scan rates, due to the time constraints the electrolyte ions diffusion to available cavities of the electrolyte is restricted. Such hindrance in the diffusion resulted into a fall in charge (q) values with the scan rates as supported in Figure 5.8a [50]. Charge storage mechanism of all the $MnWO_4$ samples can be written as the sum of following two terms:

$$q = q_s + q_d \quad (4)$$

Here q_s denotes combination of induced charges and charges generated electrostatically due to double layer formation at the interface. Inner charge (q_d) contribution originates from the redox reactions governed by the slow diffusion of K^+ ions in the pores, voids, grain

boundaries, cracks, and crevices [26,51]. Overall charge for all the samples were calculated from the q^{-1} vs $\upsilon^{1/2}$ (Figure 5.8c) plots assuming υ goes to zero. Similarly, the outer charge contribution (q_s) was also evaluated for all the samples from plots of q vs $\upsilon^{-1/2}$ (Figure 5.8d). Intersections of the fitted lines on q axis of q vs $\upsilon^{-1/2}$ plot give the q_s value of the material, assuming υ goes to infinity [26]. The quantitative contribution percentage of diffusion and capacitive control processes for MWO24 electrode at different scan rates are shown in Figure 5.9. This rises of the specific capacitance value mostly due to diffusion controlled redox reaction at electrode-electrolyte interface. Result shows capacitive contribution upsurges with scan rates which accredits to the small ion diffusion and fast electron transfer into electrode.

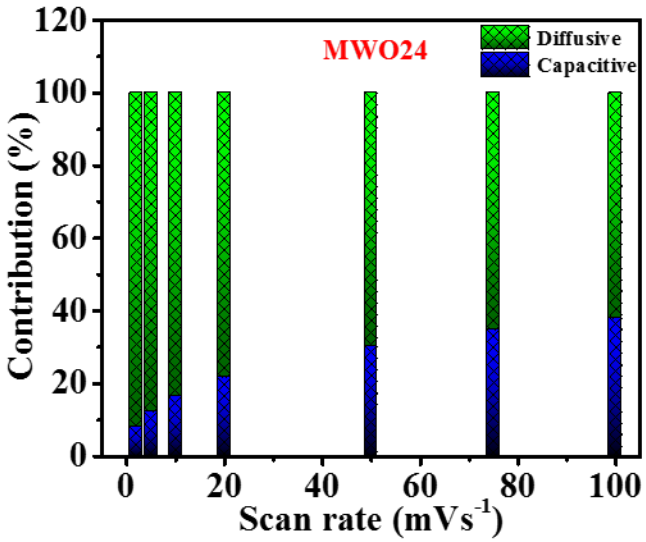

Figure 5.9: Capacitive and diffusive contribution curve of MWO24.

The Galvanometric charge-discharge (GCD) profiles for all the samples at a current density of 1 Ag^{-1} have been shown in Figure 5.10a. It is seen that decay curves of the GCD profiles contain acute non-linear nature with three distinct regions among which first region gives the voltage drop due to internal resistance, second region corresponds to the linear decay comes from EDL action and the last region is associated with the reversible electrochemical actions as observed by Jagadale et al. [52]. GCD also gives the value of C_s when analysed with the following equation:

$$C = \frac{i\Delta t}{m\Delta V} \quad (5)$$

Here i (A) and Δt (s) respectively give discharging current and time.

The discharge characteristics as shown in Figure 5.10a give the value of C_s at current density 1 Ag^{-1} to be 239.07, 155.43, and 127.06 Fg^{-1} for the samples MWO24, MWO18, and MWO12 respectively. Figure 5.10b summarizes discharge characteristics of MWO24 at different current densities.

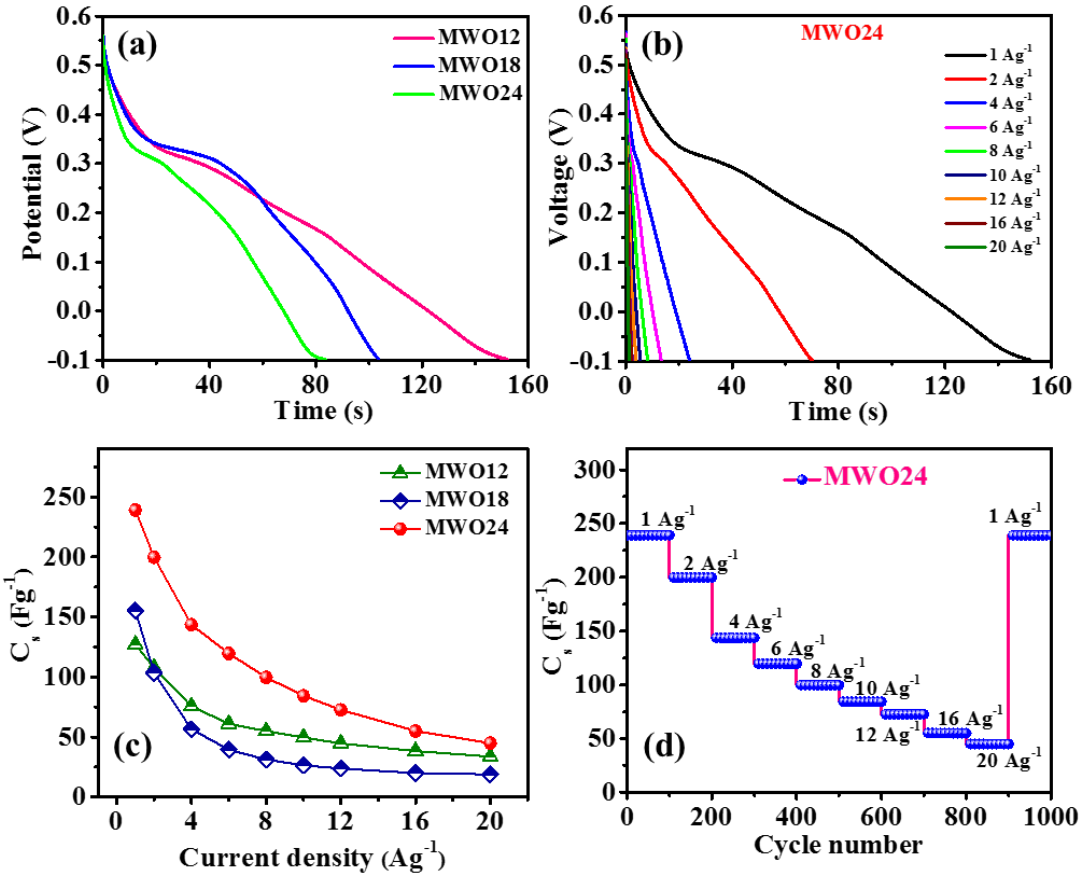

Figure 5.10: Galvanostatic charge–discharge curves of (a) all samples and (b) MWO24 at different current densities (c) Specific capacitance variation with current density (d) Cycling stability of MWO24 with gradually varied current density.

Figure 5.10c shows the variation of C_s with current densities for all the samples. The decreasing nature of C_s with current densities is more acute in MWO24 and is in well agreement with Figure 5.8a. The decrease of C_s with the rise of current density values may be due to the presence of less-amount of active materials. Figure 5.10d represents the

recyclability performance of the sample MWO24 which is extremely essential for any practical uses.

Figure 5.11a. shows the EIS characteristics of all the samples. The study was done with AC amplitude 5 mV within frequency range 0.01 to 10^5 Hz. The intersection of EIS curves (Figure 5.11a) with real impedance axis provides the solution resistance (R_s) which comes out be 1.01, 1.34 and 1.5 Ω for MWO24, MWO18 and MWO12 respectively. Furthermore, the diameter of the semicircle in high to medium frequency region of the plot designates the charge transfer resistance (R_{ct}) which can be accounted for the faradic reactions during electrochemical measurement [53]. The R_{ct} values of MWO24, MWO18 and MWO12 electrodes are 1.55 Ω, 26.97 Ω and 2.99 Ω respectively. Low R_{ct} value for MWO24 suggests faster redox reaction compared to other two samples. From the same Figure 5.11a, it is seen that the at lower frequency region the EIS spectra become almost parallel to the imaginary Y axis specially in case of MWO24 suggesting good capacitive nature of the sample. This also suggests easy ion diffusion at the aforesaid interface.

Figure 5.11b shows the plots of both real and imaginary parts of the capacitance vs. frequency. It is found that total impendence of a system can be written as:

$$Z(\omega) = Z'(\omega) + Z''(\omega) \quad (6)$$

Similarly, complex capacitance can also be written as:

$$C(\omega) = C'(\omega) + C''(\omega) \quad (7)$$

$$\text{with } C'(\omega) = \frac{Z''(\omega)}{\omega|Z|^2} \text{ and } C''(\omega) = \frac{Z'(\omega)}{\omega|Z|^2} \quad (8)$$

The detail significance of C' and C" may be found in our previous work and that of other workers [36,54,55].

The assessed values of real capacitances of all the electrodes from the frequency dependent real capacitance profiles (Figure 5.11b) are in well accord with the capacitance measured

from GCD profile at 0.01 Hz. Figure 5.11b also shows the variation of C" known as loss capacitance with frequency. The specific frequency where C" increases suddenly with a peak is known as peak frequency (f_0), the inverse of which is nothing but the dielectric relaxation time constant (τ_0). τ_0 basically gives the transition time when the system changes its behaviour from resistive to capacitive. The ideas about the figure of merit of the system can also be obtained from this characteristics time [54,56]. The value of τ_0 for the sample MWO24 comes out to be as small as 0.86 s only, thus indicating quick charging.

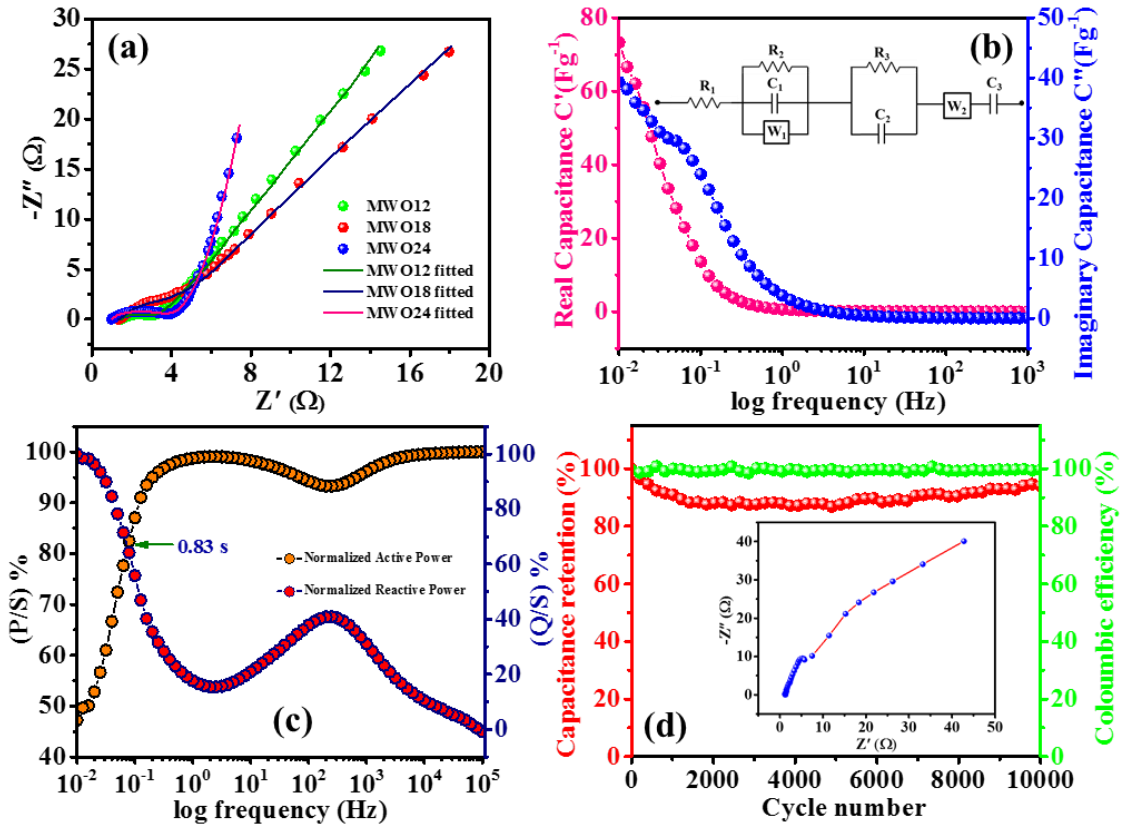

Figure 5.11: (a) Fitted electrochemical impedance spectra for all samples; (b) real and imaginary capacitance vs frequency; inset shows Equivalent circuit representation, based on the data obtained from Nyquist; (c) Active power and reactive power vs frequency; (d) Retention capacity and coulombic efficiency vs cycle number; inset shows Nyquist plot of MWO24 electrode after 10000 cycles.

The complex power S(ω) which is given by

$$S(\omega) = P(\omega) + j\, Q(\omega) \quad (9)$$

gives the idea about the dissipative nature of system.

Here P(ω) and Q(ω) represents active power and reactive power respectively and formulated as $P(\omega) = \omega\, C''(\omega)\, |\Delta Vrms|^2$ and $Q(\omega) = -\omega\, C'(\omega)\, |\Delta Vrms|^2$.

Normalised P(ω) signifies the power dissipation in the system (Figure 5.11c) that in turn indicates the transition of the system from capacitive to resistive state as ω increases [56,57]. On the other hand, Q(ω) shows a decrease with increasing ω. Thus, the system oscillates between these two states. Figure 5.11c shows a time interval of 0.83 s for the sample MWO24 which matches well with τ_0 value obtained from Figure 5.11b.

Figure 5.11d shows the capacitance retention as well as the Coulombic efficiency (at 10 Ag^{-1}) of the sample MWO24 over 10000 cycles thus indicating the performance of the same under long run. The capacitance value initially reduces over first couple of hundred cycles probably because of the accumulation of different oxygen containing functional groups at the sample surface. These groups are reportedly acting as obstacles for electrode-electrolyte interaction [58]. However, with higher cycles activation of both ionic species and electro-active surfaces takes place gradually [3,58] and ion exchange gets started. As a result, it is seen that even after 10000 cycles the sample can retain 94 % of its capacitance which is a good achievement for the as-developed system. Coulombic efficiency of the sample also remains almost constant after the long operation cycle which suggests promising candidature of the material for related applications.

The information obtained from Nyquist plot may be used for drawing the equivalent circuit as shown in inset of Figure 5.11b. During drawing the equivalent circuit, we have considered the different circuit components like resistance (R), Capacitance (C) and impedance (W) where the last term comes from diffusion mainly (W_s and W_k). Capacitance

has three components, first is geometrical capacitance (C_s), second is double layer capacitance (C_{dl}) whereas last comes from the intercalation (C_{int}). Resistance has also three components; electrolyte resistance (R_{el}), series resistance (R_s) and charge transfer resistance (R_{ct}). The significance of different terms may be found in our previous work [36] as well as in other works [59–61]. In circuit diagram, R_{el}, R_s, R_{ct} are labelled as R_1, R_2, R_3; whereas W_s and W_k are presented as W_1 and W_2 respectively. Finally, the capacitances C_s, C_{dl} and C_{int} are termed as C_1, C_2, C_3 respectively. The corresponding values are provided in Table 5.1.

Table 5.1: Values of equivalent circuit components.

Component	Value		
	MWO24	**MWO18**	**MWO12**
R_1 (ohm)	**0.51**	**1.18**	**2.36**
R_2 (ohm)	**1.01**	**1.34**	**1.50**
R_3 (ohm)	**1.55**	**26.97**	**2.99**
W_1 (ohm $S^{-1/2}$)	**45.49**	**59.7**	**55.22**
W_2 (ohm $S^{-1/2}$)	**0.86**	**3.01**	**2.24**
C_1 (F)	**0.152×10^{-3}**	**1.514**	**0.129×10^{-3}**
C_2 (F)	**0.117**	**0.079**	**0.912**
C_3 (F)	**0.99**	**2.87**	**0.62**

Change in the electrode material after long cycles operation is also scrutinized from the evaluated values of R_s and R_{ct} which are found to be ~1.26 and ~7.88 Ω respectively after 10000 cycles (inset of Figure 5.11d). FESEM image of MWO24 electrode after 10000 cycles is depicted in Figure 5.12.

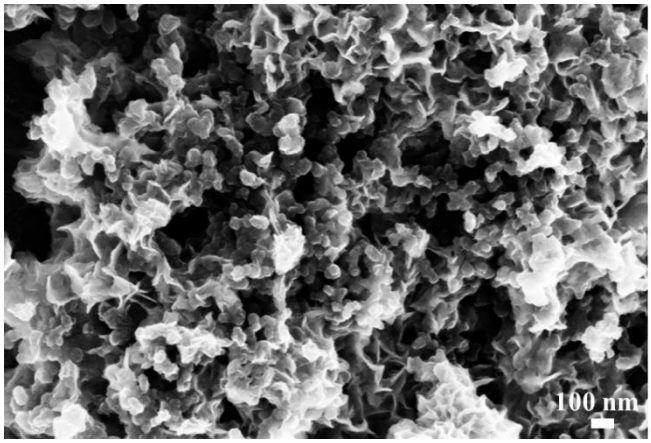

Figure 5.12: FESEM image of MWO24 electrode after 10000 cycles.

The nature and flat band potential of the sample prepared may be obtained from the well-known Mott-Schottky plot given by the equation [62]

$$\frac{1}{C^2} = \frac{2}{\varepsilon\varepsilon_0 e A^2 N_A}\left(V\text{-}V_{fb}\text{-}\frac{kT}{e}\right) \quad (10)$$

Here C is the capacitance; ε and ε_o are material and free space permittivity. Also, A is active surface are, N_A signifies donor density. V and V_{fb} stand for applied potential and flat band potential. K, T and 'e' stand for the Boltzmann constant, temperature and elementary charge respectively. The corresponding plot for MWO24 is shown in Figure 5.13 wherefrom the flat band potential has come out to be -1.03 V.

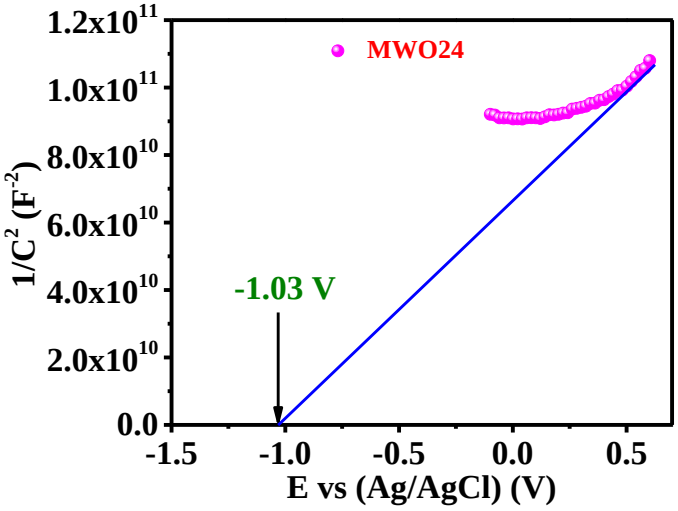

Figure 5.13: Mott Schottky plot of the MWO24 electrode.

Table 5.2: Electrochemical performance comparison.

Electrode material	Electrolyte	Specific capacitance	Potential window	Cycling stability	Ref.
$MnWO_4$/ RGO	6 M KOH	288 Fg^{-1} at 5 mV s^{-1}	-0.35 to 0.55 V	14.9% after 6000 cycles	[63]
$MnWO_4$	1 M Na_2SO_4	386 Fg^{-1} at 5 mVs^{-1}	0 to 1 V	90% after 2000 cycles	[64]
$MnWO_4$	1 M KOH	295 Fg^{-1} at 5 mVs^{-1}	-0.2 to 0.6 V	> 100% after 3000 cycles	[65]
$MnWO_4$ micro flower	1 M Na_2SO_4	324 Fg^{-1} at 1 mA cm^{-2}	0 to 1 V	93% after 8000	[66]
$MnWO_4$ (using DNA scaffold)	0.1 M Na_2SO_4	34 Fg^{-1} at 0.5 mA cm^{-2}	0 to 1 V	-	[67]
$MnWO_4$ (using CTAB)	1 M H_2SO_4	27 Fg^{-1} at 5 mVs^{-1} and 16 Fg^{-1} at 1.3 mA cm^{-2}	-0.2 to 1 V and 0 to 1 V	increased after 1000 cycles	[68]
$MnWO_4$@ aCNT	1 M KOH	542.18 Fg^{-1} at 2 mVs^{-1}	-0.1 to 0.6 V	Above 100% after 15,000 cycles	[69]
$MnWO_4$	0.1 M NaOH	199 Fg^{-1} at 2 mVs^{-1}	0 to 0.5 V	62% after 1200 cycles	[70]
WO_3-RGO composite	0.5 M H_2SO_4	495 Fg^{-1} at 1 Ag^{-1}	-0.4 to 0.3 V	87.5% after 1000 cycles	[71]
WO_3	0.5 M H_2SO_4	319.26 Fg^{-1} at 0.7 Ag^{-1}	-0.41 to 0 V	83.2% after 6000 cycles	[72]
WO_3	1 M Na_2SO_4	266 Fg^{-1} at 10 mVs^{-1}	-0.7 to 0.4 V	81% after 1000 cycles	[73]
WO_3–$WO_3 \cdot 0.5 H_2O$	0.5 M H_2SO_4	290 Fg^{-1} at 25 mVs^{-1}	-0.6 to 0.2 V	72% after 100 cycles	[74]
$MnWO_4$	KOH	455.07 Fg^{-1} at 2 mVs^{-1}	-0.1 to 0.6 V	94% after 10,000 cycles	This work

5.4. Theoretical Computations

Figure 5.14 shows the crystal structure of $MnWO_4$ that clearly indicates the presence of both MnO_6 and WO_6 and their linkage oxygen ligand. Density of States (DOS) of bulk $MnWO_4$ has been calculated through GGA + U method and is shown in Figure 5.15a. The predicted value of 2.2 eV obtained from GGA + U method matches well with reported value of experimental band gap of 2.65 eV [75]. Here on-site interaction of Tungsten has been considered as it is the rare earth element and implemented U = 7.00 V for Mn 3d orbital within the GGA+U method in DOS calculation [76]. The validity of the simulation approach is confirmed from the agreement of different reported experimental values of various parameters like lattice parameters and band gap.

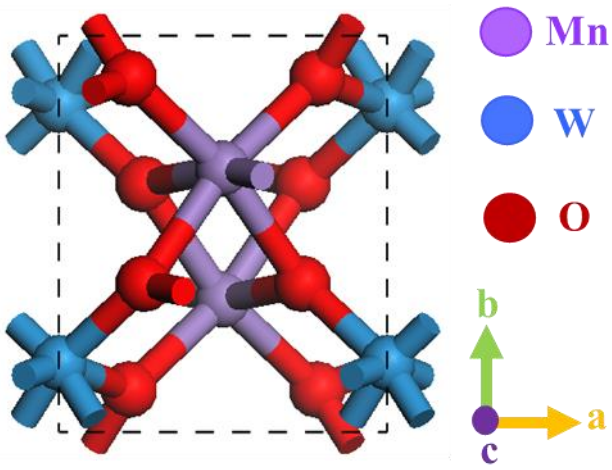

Figure 5.14: Bulk structure of $MnWO_4$ with W and Mn in octahedral/monoclinic environment, here violet, blue, and red spheres indicated Mn, W and O atoms respectively.

To gain more insight to the electronic properties of the as synthesized nanostructures we have calculated the Total density of states (TDOS) for the (-111) surface of $MnWO_4$ in Figure 5.15a which shows crowded arrangement of electronic states near the fermi level of (-111) surface. This result leads to build the possible reason behind good conductivity and specific capacitance as supported by experimental findings.

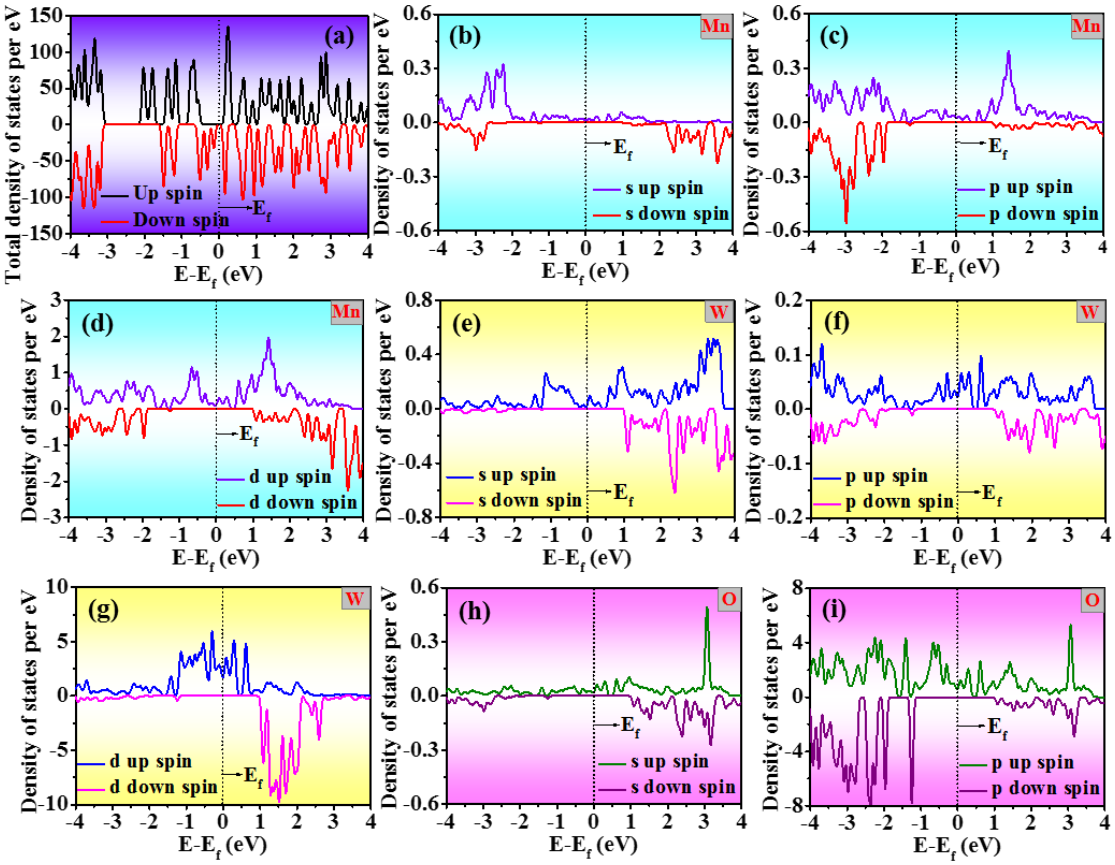

Figure 5.15: (a) Total density of states (TDOS) for (-111) surface of $MnWO_4$, Partial density of state (PDOS) [(-111) surface of $MnWO_4$] for (b) Mn s orbital, (c) Mn p orbital, (d) Mn d orbital, (e) W s orbital, (f) W p orbital, (g) W d orbital (h) O s orbital and (i) O 2p orbital in 2D configuration. The Fermi level is indicated by the dotted line.

The partial density of states (PDOS) of 2D configuration for each of s, p and d orbitals of Mn, W and O are presented in Figure 5.15b-i. PDOS analysis indicates that the conduction (bottom) and valence (top) bands are respectively contributed by W 'd' and O 'p' orbitals. From the figure it is clear that the electronic states near Fermi level at the top of valence band is mostly contributed by Mn and W 'd' orbitals and O 'p' orbitals. The total density of states (TDOS) along with partial density of states (PDOS) of 3D configuration for the same is presented in Figure 5.16a-i.

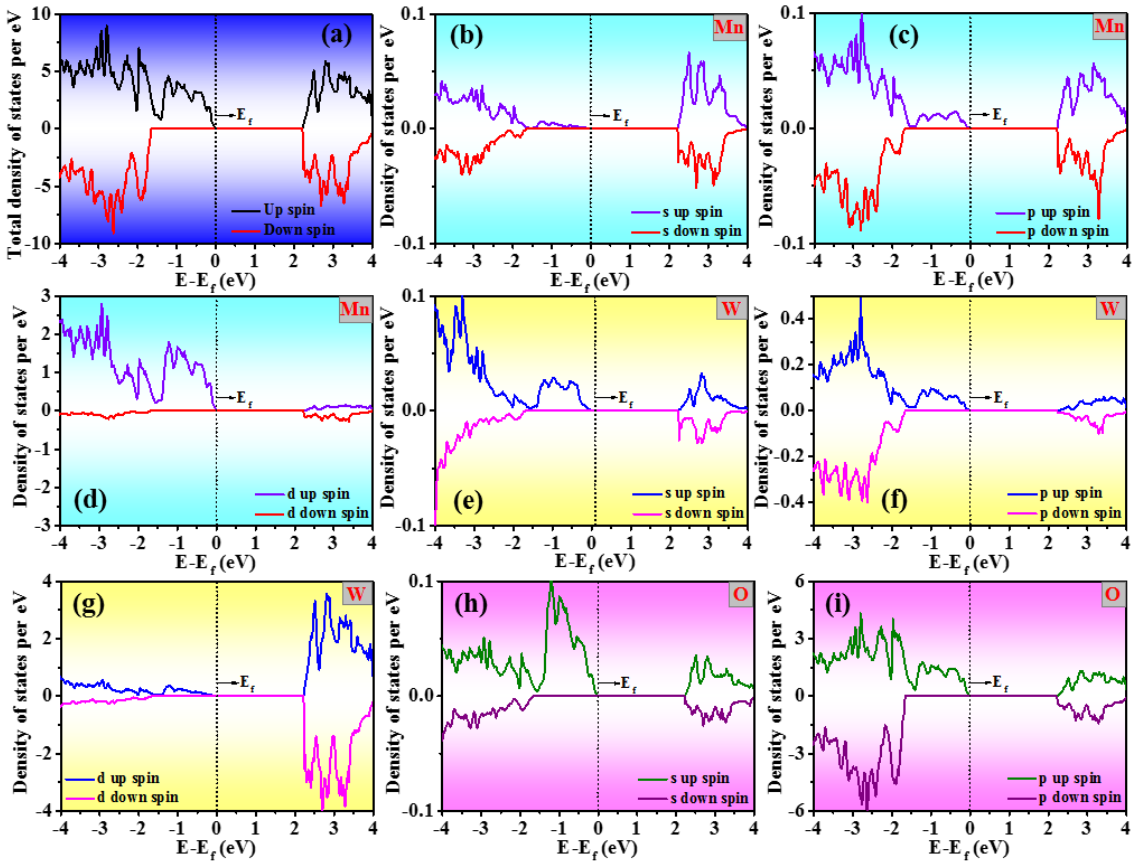

Figure 5.16: (a) Total density of states (TDOS) for (-111) surface of $MnWO_4$, Partial density of state (PDOS) [(-111) surface of $MnWO_4$] for (b) Mn s orbital, (c) Mn p orbital, (d) Mn d orbital, (e) W s orbital, (f) W p orbital, (g) W d orbital (h) O s orbital and (i) O 2p orbital in 3D configuration. The Fermi level is indicated by the dotted line.

We have computed theoretically the quantum capacitance for the (-111) surface of $MnWO_4$. Using the density of states, the quantum capacitance can be determined from the following relation: [35, 64]

$$C_Q = e^2 \int_{\infty}^{\infty} D(E)\, F_T\,(E - e\phi_G)\, dE \qquad (11)$$

Here D(E) denotes density of states, whereas Φ_G indicates the electrode potential. The thermal broadening function can be written as: [35,64]

$$F_T = (4kT)^{-1}\, \mathrm{sech}^2\,(E/2kT) \qquad (12)$$

It is clear from Figure 5.17 that the quantum capacitance which is noteworthy for the lower dimensional system yield the maximum value of 6700 μF/cm^2 at the potential of -4 V. The

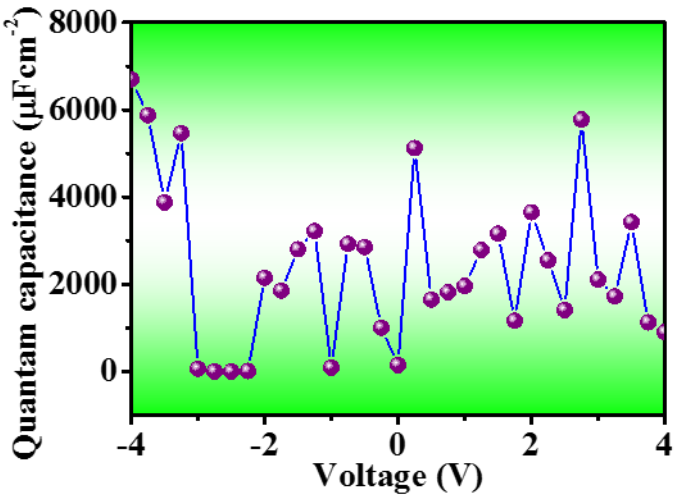

Figure 5.17: Variation of quantum capacitance of $MnWO_4$ surface as a function of voltage.

experimentally obtained total capacitance can be correlated with the quantum capacitance from the following relation: [35]

$$\frac{1}{C_T} = \frac{1}{C_Q} + \frac{1}{C_{EDL}} \tag{13}$$

where C_{EDL} indicates capacitance due to the electrical double layer.

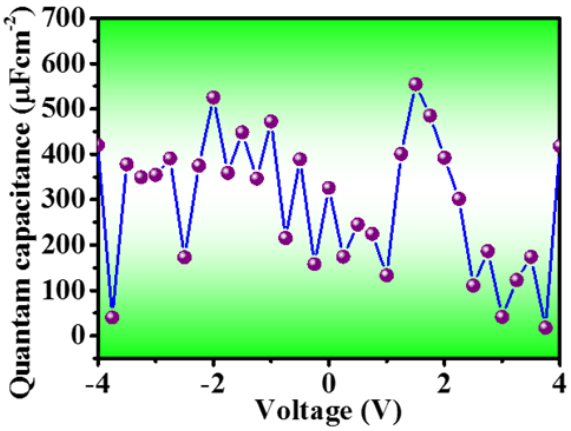

Figure 5.18: Variation of quantum capacitance of $MnWO_4$ surface as a function of voltage using DFT D3-BJ method.

We have also calculated quantum capacitance using DFT D3-BJ method [77,78] and the result has been shown in Figure 5.18. The TDOS and PDOS of 2D configuration for each of s, p and d orbitals of Mn, W and O are depicted in Figure 5.19a-i.

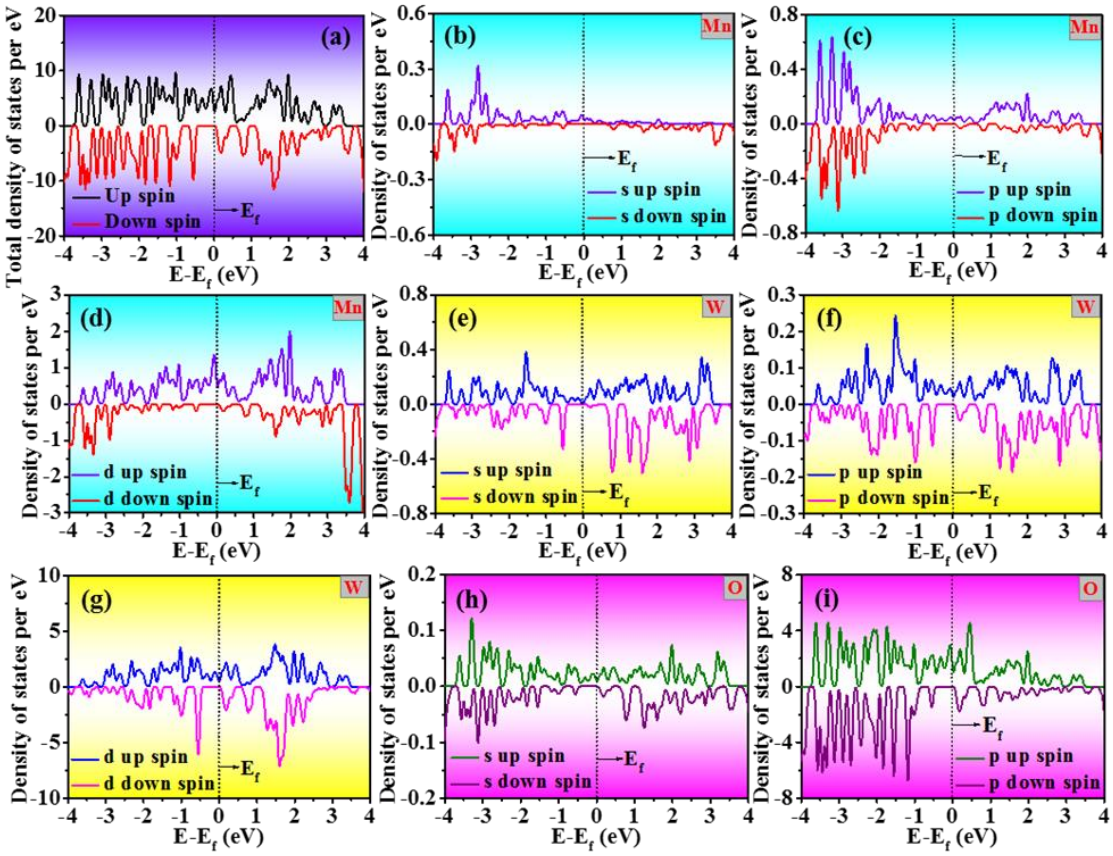

Figure 5.19: (a) Total density of states (TDOS) for (-111) surface of $MnWO_4$, Partial density of state (PDOS) [(-111) surface of $MnWO_4$] for (b) Mn s orbital, (c) Mn p orbital, (d) Mn d orbital, (e) W s orbital, (f) W p orbital, (g) W d orbital (h) O s orbital and (i) O 2p orbital in 2D configuration (using DFT D3-BJ method). The Fermi level is indicated by the dotted line.

5.5. Conclusions

In conclusion, we have successfully prepared $MnWO_4$ nanostructures of different aspect ratio via simple, budgetary, low temperature hydrothermal process with high yield. The as prepared samples were studied by XRD, FESEM, HRTEM, XPS, TGA, and BET analysis. The electrodes developed from as-developed $MnWO_4$ samples were subjected to CV, GCD and EIS analysis. Thorough investigation in electrochemical performance on the ground of surface area, electron transport process and electrolyte diffusion were carried out. It is seen that the sample prepared for the longest time shows best electrochemical results with the

maximum specific capacitance value of 455.07 Fg^{-1} at a scan rate of 2 mVs^{-1} and high capacitance retention of ~94% after 10000 cycles. Mott Schottky analysis was further carried out to explore charge transfer process at electrode-electrolyte interface. This proposes n-type semiconducting nature at the interface. Theoretical insight on the experimental results is highlighted from DFT simulations. The presence of electronic states near Fermi level and the enhanced quantum capacitance ensures excellent charge storage performance of the as synthesized $MnWO_4$. The encouraging electrochemical features of the electrode material facilitates the user to use it as a building block of advanced devices in energy storage applications.

5.6. References

[1] Gür TM. Review of electrical energy storage technologies, materials and systems: challenges and prospects for large-scale grid storage. Energy Environ Sci 2018; 11: 2696–767.

[2] Panda PK, Grigoriev A, Mishra YK, Ahuja R. Progress in supercapacitors: roles of two dimensional nanotubular materials. Nanoscale Adv 2020; 2:7 0–108.

[3] Park SH, Jeong J-M, Kim SJ, Kim KH, Lee SH, Bae NH, et al. Large-area and 3D polyaniline nanoweb film for flexible supercapacitors with high rate capability and long cycle life. ACS Appl Energy Mater 2020; 3: 7746–55.

[4] Bairi P, Maji S, Hill JP, Kim JH, Ariga K, Shrestha LK. Mesoporous carbon cubes derived from fullerene crystals as a high rate performance electrode material for supercapacitors. J Mater Chem A Mater 2019; 7: 12654–60.

[5] Chaichi A, Venugopalan G, Devireddy R, Arges C, Gartia MR. A solid-state and flexible supercapacitor that operates across a wide temperature range. ACS Appl Energy Mater 2020; 3: 5693–704.

[6] Sun Z, Wang Y, Chen Z, Li X. Min-max game based energy management strategy for fuel cell/supercapacitor hybrid electric vehicles. Appl Energy 2020; 267: 115086.

[7] Wang Y, Xu F, Mao S, Yang S, Shen Y. Adaptive online power management for more electric aircraft with hybrid energy storage systems. IEEE Transactions on Transportation Electrification 2020; 6: 1780–90.

[8] Li L, Jia C, Zhu X, Zhang S. Utilization of cigarette butt waste as functional carbon precursor for supercapacitors and adsorbents. J Clean Prod 2020; 256: 120326.

[9] Yan J, Li S, Lan B, Wu Y, Lee PS. Rational design of nanostructured electrode materials toward multifunctional supercapacitors. Adv Funct Mater 2020; 30: 1902564.

[10] Yang B, Wang J, Zhang X, Wang J, Shu H, Li S, et al. Applications of battery/supercapacitor hybrid energy storage systems for electric vehicles using perturbation observer based robust control. J Power Sources 2020; 448: 227444.

[11] Zhang L, Zhang F, Yang X, Long G, Wu Y, Zhang T, et al. Porous 3D graphene-based bulk materials with exceptional high surface area and excellent conductivity for supercapacitors. Sci Rep 2013; 3: 1408.

[12] Sheberla D, Bachman JC, Elias JS, Sun C-J, Shao-Horn Y, Dincă M. Conductive MOF electrodes for stable supercapacitors with high areal capacitance. Nat Mater 2017; 16: 220–4.

[13] Chen L-F, Lu Y, Yu L, Lou XWD. Designed formation of hollow particle-based nitrogen-doped carbon nanofibers for high-performance supercapacitors. Energy Environ Sci 2017; 10: 1777–83.

[14] Roy D, Sarkar S, Bhattacharjee K, Panigrahi K, Das BK, Sardar K, et al. Site specific nitrogen incorporation in reduced graphene oxide using imidazole as a novel reducing agent for efficient oxygen reduction reaction and improved supercapacitive performance. Carbon N Y 2020; 166: 361–73.

[15] Bairi P, Sardar K, Samanta M, Chanda K, Chattopadhyay KK. Nanoporous nitrogen-doped graphitic carbon hollow spheres with enhanced electrochemical properties. Mater Chem Front 2021; 5: 7645–53.

[16] Wang F, Chen L, Li H, Duan G, He S, Zhang L, et al. N-doped honeycomb-like porous carbon towards high-performance supercapacitor. Chinese Chemical Letters 2020; 31: 1986–90.

[17] Stoller MD, Magnuson CW, Zhu Y, Murali S, Suk JW, Piner R, et al. Interfacial capacitance of single layer graphene. Energy Environ Sci 2011; 4: 4685–9.

[18] Ramirez-Castro C, Schütter C, Passerini S, Balducci A. Microporous carbonaceous materials prepared from biowaste for supercapacitor application. Electrochim Acta 2016; 206: 452–7.

[19] Boukhalfa S, Evanoff K, Yushin G. Atomic layer deposition of vanadium oxide on carbon nanotubes for high-power supercapacitor electrodes. Energy Environ Sci 2012; 5: 6872–9.

[20] Sahoo S, Rout CS. Facile electrochemical synthesis of porous manganese-cobalt-sulfide based ternary transition metal sulfide nanosheets architectures for high performance energy storage applications. Electrochim Acta 2016; 220: 57–66.

[21] Meng Q, Cai K, Chen Y, Chen L. Research progress on conducting polymer based supercapacitor electrode materials. Nano Energy 2017; 36: 268–85.

[22] Chanda K, Thakur S, Maiti S, Acharya A, Paul T, Besra N, et al. Hierarchical heterostructure of MoS_2 flake anchored on TiO_2 sphere for supercapacitor application. AIP Conf Proc, vol. 1953, AIP Publishing; 2018.

[23] Hu Q, Jiang X, He M, Zheng Q, Lam KH, Lin D. Core-shell nanostructured MnO_2@ Co_9S_8 arrays for high-performance supercapacitors. Electrochim Acta 2020; 338: 135896.

[24] Sk MM, Yue CY, Ghosh K, Jena RK. Review on advances in porous nanostructured nickel oxides and their composite electrodes for high-performance supercapacitors. J Power Sources 2016; 308: 121–40.

[25] Yao S, Xing L, Dong Y, Wu X. Hierarchical WO_3@ $MnWO_4$ core-shell structure for asymmetric supercapacitor with ultrahigh cycling performance at low temperature. J Colloid Interface Sci 2018; 531: 216–24.

[26] Tamboli MS, Dubal DP. Inamuddin, AM Asiri, P. Gomez-Romero, BB Kale and DR Patil. Chem Eng J 2017; 307: 300–10.

[27] Chanda K, Maiti S, Sarkar S, Bairi P, Thakur S, Sardar K, et al. Hierarchical assembly of MnO_2 nanosheet on $CuCo_2O4$ nanoflake over fabric scaffold for symmetric supercapacitor. ACS Appl Nano Mater 2021; 4: 1420–33.

[28] Thakur S, Maiti S, Sardar K, Besra N, Bairi P, Panigrahi K, et al. New class of trimetallic oxide hierarchical mesoporous array on woven fabric: electrode for high-performance and stable battery type ultracapacitor. J Energy Storage 2021; 35: 102249.

[29] Harichandran G, Divya P, Radha S, Yesuraj J. Facile and controllable CTAB-assisted sonochemical synthesis of one-dimensional $MnWO_4$ nanorods for supercapacitor application. J Mol Struct 2020; 1199: 126931.

[30] Wu C, Cai J, Zhu Y, Zhang K. Hybrid reduced graphene oxide nanosheet supported Mn–Ni–Co ternary oxides for aqueous asymmetric supercapacitors. ACS Appl Mater Interfaces 2017; 9: 19114–23.

[31] Muthamizh S, Suresh R, Giribabu K, Manigandan R, Kumar SP, Munusamy S, et al. $MnWO_4$ nanocapsules: synthesis, characterization and its electrochemical sensing property. J Alloys Compd 2015; 619: 601–9.

[32] Tang J, Shen J, Li N, Ye M. Facile synthesis of layered $MnWO_4$/reduced graphene oxide for supercapacitor application. J Alloys Compd 2016; 666: 15–22.

[33] Raj BGS, Acharya J, Seo M-K, Khil M-S, Kim H-Y, Kim B-S. One-pot sonochemical synthesis of hierarchical $MnWO_4$ microflowers as effective electrodes in neutral electrolyte for high performance asymmetric supercapacitors. Int J Hydrogen Energy 2019; 44: 10838–51.

[34] Li F, Xu X, Huo J, Wang W. A simple synthesis of $MnWO_4$ nanoparticles as a novel energy storage material. Mater Chem Phys 2015; 167: 22–7.

[35] Naik KK, Gangan AS, Pathak A, Chakraborty B, Nayak SK, Rout CS. Facile Hydrothermal Synthesis of $MnWO_4$ Nanorods for Non-Enzymatic Glucose Sensing and Supercapacitor Properties with Insights from Density Functional Theory Simulations. ChemistrySelect 2017; 2: 5707–15.

[36] Sardar K, Thakur S, Maiti S, Besra N, Bairi P, Chanda K, et al. Amalgamation of $MnWO_4$ nanorods with amorphous carbon nanotubes for highly stabilized energy efficient supercapacitor electrodes. Dalton Transactions 2021; 50: 5327–41.

[37] Kresse G, Hafner J. Ab initio molecular dynamics for liquid metals. Phys Rev B 1993; 47: 558.

[38] Kresse G, Hafner J. Ab initio molecular-dynamics simulation of the liquid-metal–amorphous-semiconductor transition in germanium. Phys Rev B 1994; 49: 14251.

[39] Blöchl PE. Projector augmented-wave method. Physical review B. 1994; 15; 50(24): 17953.

[40] Perdew JP, Burke K, Ernzerhof M. Generalized gradient approximation made simple. Phys Rev Lett 1996; 77: 3865.

[41] Grimme S. Semiempirical GGA-type density functional constructed with a long-range dispersion correction. J Comput Chem 2006; 27: 1787–99.

[42] Mal P, Bera G, Rambabu P, Turpu GR, Chakraborty B, Ramaniah LM, et al. Electronic, magnetic and spectroscopic properties of doped $Mn_{(1-x)}A_xWO_4$ (A= Co, Cu, Ni and Fe) multiferroic: an experimental and DFT study. Journal of Physics: Condensed Matter 2016; 29: 075901.

[43] Munro JM, Latimer K, Horton MK, Dwaraknath S, Persson KA. An improved symmetry-based approach to reciprocal space path selection in band structure calculations, NPJ. Comput. Mater. 2020; 6: 1–6.

[44] Cai L-G, Liu F-M, Zhang D, Zhong W-W. Dependence of optical properties of monoclinic $MnWO_4$ on the electric field of incident light. Physica B Condens Matter 2012; 407: 3654–9.

[45] Muthamizh S, Suresh R, Giribabu K, Manigandan R, Kumar SP, Munusamy S, et al. $MnWO_4$ nanocapsules: synthesis, characterization and its electrochemical sensing property. J Alloys Compd 2015; 619: 601–9.

[46] Tong W, Li L, Hu W, Yan T, Guan X, Li G. Kinetic control of $MnWO_4$ nanoparticles for tailored structural properties. The Journal of Physical Chemistry C 2010; 114: 15298–305.

[47] Tiwari A, Singh V, Nagaiah TC. Tuning the $MnWO_4$ morphology and its electrocatalytic activity towards oxygen reduction reaction. J Mater Chem A Mater 2018; 6: 2681–92.

[48] Senthilkumar ST, Selvan RK, Melo JS. Redox additive/active electrolytes: a novel approach to enhance the performance of supercapacitors. J Mater Chem A Mater 2013; 1: 12386–94.

[49] Pujari RB, Lokhande VC, Patil UM, Lee DW, Lokhande CD. Controlled sulfurization of $MnCO_3$ microcubes architectured MnS_2 nanoparticles with 1.7 fold capacitance increment for high energy density supercapacitor. Electrochim Acta 2019; 301: 366–76.

[50] Pandit B, Dubal DP, Gómez-Romero P, Kale BB, Sankapal BR. V_2O_5 encapsulated MWCNTs in 2D surface architecture: complete solid-state bendable highly stabilized energy efficient supercapacitor device. Sci Rep 2017; 7: 43430.

[51] Panigrahi K, Howli P, Chattopadhyay KK. 3D network of V_2O_5 for flexible symmetric supercapacitor. Electrochim Acta 2020; 337: 135701.

[52] Jagadale AD, Jamadade VS, Pusawale SN, Lokhande CD. Effect of scan rate on the morphology of potentiodynamically deposited β-$Co(OH)_2$ and corresponding supercapacitive performance. Electrochim Acta 2012; 78: 92–7.

[53] Thakur S, Maiti S, Paul T, Besra N, Sarkar S, Chattopadhyay KK. Geometrically intricate sheet-on-pillar/flake hierarchy embracing cobaltosic and manganese oxides over flexible carbon scaffold for binder-free high-energy-density supercapacitor. CrystEngComm 2018; 20: 6183–96.

[54] Arunkumar M, Paul A. Importance of electrode preparation methodologies in supercapacitor applications. ACS Omega 2017; 2: 8039.

[55] Singh KP, Bhattacharjya D, Razmjooei F, Yu J-S. Effect of pristine graphene incorporation on charge storage mechanism of three-dimensional graphene oxide: superior energy and power density retention. Sci Rep 2016; 6: 31555.

[56] Taberna PL, Simon P, Fauvarque J-F. Electrochemical characteristics and impedance spectroscopy studies of carbon-carbon supercapacitors. J Electrochem Soc 2003; 150: A292.

[57] Ashraf CM, Anilkumar KM, Jinisha B, Manoj M, Pradeep VS, Jayalekshmi S. Acid washed, steam activated, coconut shell derived carbon for high power supercapacitor applications. J Electrochem Soc 2018; 165: A900.

[58] Bairi P, Sardar K, Chanda K, Samanta M, Thakur S, Panigrahi K, et al. Shape-shifting via salt crystallization: conversion of a nanostructured polymer into a site-selective nitrogen-doped carbon sheet with enhanced supercapacitive performance. ACS Appl Energy Mater 2020; 3: 5984–92.

[59] Ivanishchev A V, Bobrikov IA, Ivanishcheva IA, Ivanshina OY. Study of structural and electrochemical characteristics of $LiNi_{0.33}Mn_{0.33}Co_{0.33}O_2$ electrode at lithium content variation. Journal of Electroanalytical Chemistry 2018; 821: 140–51.

[60] Ivanishchev A V, Churikov A V, Ivanishcheva IA, Ushakov A V, Sneha MJ, Babbar P, et al. Models of lithium transport as applied to determination of diffusion characteristics of intercalation electrodes. Russian Journal of Electrochemistry 2017; 53: 706–12.

[61] Ivanishchev A V, Ushakov A V, Ivanishcheva IA, Churikov A V, Mironov A V, Fedotov SS, et al. Structural and electrochemical study of fast Li diffusion in $Li_3V_2(PO_4)_3$-based electrode material. Electrochim Acta 2017; 230: 479–91.

[62] Zhao YL, Barman AR, Dhar S, Annadi A, Motapothula M, Wang J, et al. Scaling of flat band potential and dielectric constant as a function of Ta concentration in Ta-TiO_2 epitaxial films. AIP Adv 2011; 1.

[63] Tang J, Shen J, Li N, Ye M. Facile synthesis of layered $MnWO_4$/reduced graphene oxide for supercapacitor application. J Alloys Compd 2016; 666: 15–22.

[64] Yesuraj J, Elanthamilan E, Muthuraaman B, Suthanthiraraj SA, Merlin JP. Bio-assisted hydrothermal synthesis and characterization of $MnWO_4$ nanorods for high-performance supercapacitor applications. J Electron Mater 2019; 48: 7239–49.

[65] Li F, Xu X, Huo J, Wang W. A simple synthesis of $MnWO_4$ nanoparticles as a novel energy storage material. Mater Chem Phys 2015; 167: 22–7.

[66] Raj BGS, Acharya J, Seo M-K, Khil M-S, Kim H-Y, Kim B-S. One-pot sonochemical synthesis of hierarchical $MnWO_4$ microflowers as effective electrodes in neutral electrolyte for high performance asymmetric supercapacitors. Int J Hydrogen Energy 2019; 44: 10838–51.

[67] Nithiyanantham U, Ede SR, Kesavan T, Ragupathy P, Mukadam MD, Yusuf SM, et al. Shape-selective formation of $MnWO_4$ nanomaterials on a DNA scaffold: magnetic, catalytic and supercapacitor studies. RSC Adv 2014; 4: 38169–81.

[68] Saranya S, Senthilkumar ST, Sankar KV, Selvan RK. Synthesis of $MnWO_4$ nanorods and its electrical and electrochemical properties. J Electroceram 2012; 28: 220–5.

[69] Sardar K, Thakur S, Maiti S, Besra N, Bairi P, Chanda K, et al. Amalgamation of $MnWO_4$ nanorods with amorphous carbon nanotubes for highly stabilized energy efficient supercapacitor electrodes. Dalton Transactions 2021; 50: 5327–41.

[70] Naik KK, Gangan AS, Pathak A, Chakraborty B, Nayak SK, Rout CS. Facile Hydrothermal Synthesis of $MnWO_4$ Nanorods for Non-Enzymatic Glucose Sensing and Supercapacitor Properties with Insights from Density Functional Theory Simulations. ChemistrySelect 2017; 2: 5707–15.

[71] Chu J, Lu D, Wang X, Wang X, Xiong S. WO_3 nanoflower coated with graphene nanosheet: synergetic energy storage composite electrode for supercapacitor application. J Alloys Compd 2017; 702: 568–72.

[72] Yao S, Qu F, Wang G, Wu X. Facile hydrothermal synthesis of WO_3 nanorods for photocatalysts and supercapacitors. J Alloys Compd 2017; 724: 695–702.

[73] Shinde NM, Jagadale AD, Kumbhar VS, Rana TR, Kim J, Lokhande CD. Wet chemical synthesis of WO_3 thin films for supercapacitor application. Korean Journal of Chemical Engineering 2015; 32: 974–9.

[74] Chang K-H, Hu C-C, Huang C-M, Liu Y-L, Chang C-I. Microwave-assisted hydrothermal synthesis of crystalline WO_3–$WO_3 \cdot 0.5H_2O$ mixtures for pseudocapacitors of the asymmetric type. J Power Sources 2011; 196: 2387–92.

[75] Raja VR, Karthika A, Suganthi A, Rajarajan M. Facile synthesis of $MnWO_4$/BiOI nanocomposites and their efficient photocatalytic and photoelectrochemical activities under the visible-light irradiation. Journal of Science: Advanced Materials and Devices 2018; 3: 331–41.

[76] Karmakar S, Mistari CD, Shajahan AS, More MA, Chakraborty B, Behera D. Enhancement of pseudocapacitive behavior, cyclic performance, and field emission characteristics of reduced graphene oxide reinforced $NiGa_2O_4$ nanostructured electrode: a first principles calculation to correlate with experimental observation. The Journal of Physical Chemistry C 2021; 125: 7898–912.

[77] Reckien W, Janetzko F, Peintinger MF, Bredow T. Implementation of empirical dispersion corrections to density functional theory for periodic systems. J Comput Chem 2012; 33: 2023–31.

[78] Ilawe N V, Zimmerman JA, Wong BM. Breaking badly: DFT-D2 gives sizeable errors for tensile strengths in palladium-hydride solids. J Chem Theory Comput 2015; 11: 5426–35.

Chapter 6: Two-Dimensional Layered $CsPb_2Br_5$ Perovskite as High-Performance Electrode Material for Supercapacitor Application

6.1. Introduction

Inspired by their intriguing features like long diffusion lengths, a large absorption coefficient, high carrier mobility, and a tunable spectral absorption window, all inorganic perovskites have found immense utility in modern photovoltaic [1]. A solar cell based on these perovskites has delivered substantial performance improvements. All inorganic perovskites possess the standard formula ABX_3 (where A and B are two different metallic cations that have different valencies, whereas X = halogens like I, Br, Cl, and mixed Cl/Br and Br/I systems). From this family, lead-based tri-halides have sparked broad interest in recent years for display and solar cell applications [2,3]. However, due to its questionable instabilities, it is still a problem in a number of device applications. Thus, the hotspot of frontier research is composition variation and surface treatment of these perovskites, aiming for improved stability. Currently, few works related to compositionally related materials like hexagonal Cs_4PbBr_6 and tetragonal $CsPb_2Br_5$ show desired stability and optoelectronic features [4,5]. Banking on inherent unique features, they showed usage perspectives in LEDs, memory devices, nanogenerators, li-ion batteries, CO_2 reduction, photo-detectors, etc. [6–11]. However, the value of these perovskites in other applications is still unexplored. Therefore, exploration of these materials both in synthesis and in application aspects is quite important.

Increasing demand for energy and fears of climate change necessitate the search for substitutes for energy conversion and storage. Thus, the facile design and engineering of low-cost energy materials for energy storage applications is the present need of the hour. As an energy storage device, supercapacitors (SCs) have shown huge potential, with numerous favourable features like wide operational temperature ranges, long cycle life, rapid charging and discharging rates, low maintenance costs, environmental friendliness, and safe operation. SCs' outstanding properties make them suitable for many diverse applications, such as hybrid electric vehicles, aircraft, smart grids, and so on [12–14]. SCs showed the potential to bridge

the energy-power gap between capacitors and conventional batteries. Electrochemical double layer capacitors (EDLCs), which hold electrostatic charges at the surface of the electrode material, via electrostatic non-Faradic processes. Instead, the pseudocapacitor stores charges through quick and reversible redox reactions that take place within the electrode substance. Till now, most of the research on pseudocapacitors has been confined to metal oxides (MnO_2, NiO, Co_3O_4, TiO_2, $MnWO_4$, etc.), which frequently necessitate complex process control for synthesis [15–19]. They also often suffer from low energy density compared to conventional batteries. Compositionally related perovskite could be an interesting alternative in the search for forthcoming energy materials for device-level performance.

Here, we adopted a wet chemical approach with a zero-thermal budget to synthesize phase-pure $CsPb_2Br_5$. Two highlights of this method are its simplicity and high sample yield. Using X-ray diffraction, the phase purity of the as-prepared sample was evaluated, and the XRD profile was further refined using the Rietveld method, which confirmed that $CsPb_2Br_5$ is found in the tetragonal lattice system. Utilizing EDX and XPS, the chemical composition and oxidation states of the synthesized sample were examined. The optical quality of the sample is explored using photoluminescence (PL) spectroscopy. As prepared, $CsPb_2Br_5$, was further used for the fabrication of SCs. The electrochemical features of the $CsPb_2Br_5$ based electrode were examined in detail. The specific capacitance (C_s) of the $CsPb_2Br_5$-based electrode is 886 Fg^{-1} at 2 mVs^{-1}. Detailed analysis suggested that the specific current values rise when the scan rate is increased, pointing to the electrode material's exceptional supercapacitive behavior. The as fabricated device retained ~76% of its initial specific capacitance and remarkable Columbic efficiency even after 5000 operation cycles. Such electrochemical performance observed in the synthesized sample serves as motivation for the rational design of further electrode materials that utilizes a variety of all-inorganic halide perovskites and semiconductor halides.

6.2. Experimental

6.2.1 Chemicals

The analytical grade cesium acetate (CH_3COOCs), lead bromide ($PbBr_2$), hydrobromic acid (HBr), and ethanol were utilized without further purification.

6.2.2 Synthesis of $CsPb_2Br_5$ perovskite

For the synthesis of $CsPb_2Br_5$, 2 mmol (384 mg) of cesium acetate (CH_3COOCs) was firstly added to deionized (DI) water and ethanol mixture comprising 1 mL DI water and 3 mL ethanol via ultra-sonication for 5 minutes. Afterwards, 2.5 mmol (~918 mg) $PbBr_2$ was mixed with the aforementioned mixture. The entire mixture was stirred vigorously for another 40 minutes. Once the precipitate gathered at the bottom of the beaker, HBr was further added to remove the impurities. The product was then thoroughly cleaned with DI water before being dried in a vacuum oven.

6.2.3 Preparation of working electrode

In an 8:1:1 weight ratio, $CsPb_2Br_5$, carbon black, and PVDF were combined to create the working electrode. A few drops of NMP were mixed with the aforementioned mixture to make a homogenous paste. The paste was then applied to a nickel foam substrate that had already been cleaned. The foam substrate was then dried in a vacuum oven for an entire night at 80°C.

6.3. Characterizations

The X-ray diffraction (XRD) pattern of $CsPb_2Br_5$ was monitored using a Bruker D8 Diffractometer. The HITACHI S4800 electron captures the FESEM image. EDX spectroscopy was used to analyse the sample composition. The constituent elements' oxidation states were determined using X-ray photoelectron spectroscopy (XPS) (NEXA base Thermo scientific).

PL spectra were recorded using a Horiba-Jobin Yvon Fluorolog-3 spectrophotometer**.** A three-electrode Gamry Interface 1000 cell was used for electrochemical studies.

6.4. Results and Discussion

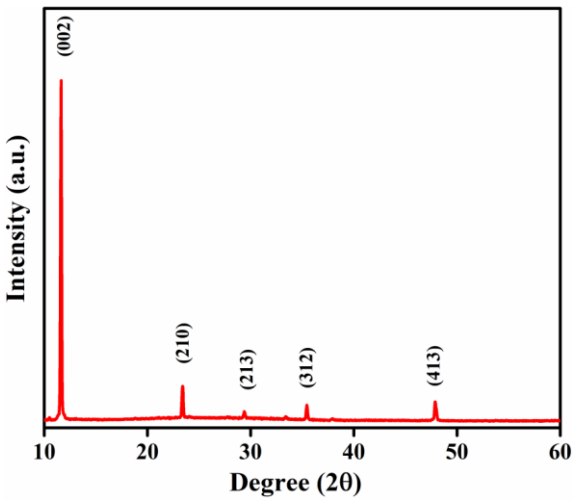

Figure 6.1: XRD of the $CsPb_2Br_5$.

An XRD measurement was performed to analyse the as-synthesized perovskite sample crystallinity. The XRD profile shown in Figure 6.1 reveals that the $CsPb_2Br_5$ sample is in the pure tetragonal phase (JCPDS no. 25-0211) [20]. At 11.62°, 23.47°, 29.41°, 35.43°, and 47.93°, several diffraction peaks are observed that agree with the (hkl) planes of (002), (210), (213), (312), and (413). According to the literature value [21,22], all peaks are well matched. XRD profile refined with FullProf software (Figure 6.2a) confirms that $CsPb_2Br_5$ is in a tetragonal lattice system having a *I4/mcm* space group. The lattice constants are a=b= 8.49 $\AA$ and c= 15.19 $\AA$, respectively. VESTA software is used to draw the crystal structure of a $CsPb_2Br_5$ unit cell. Figure 6.3 displayed an array of three unit-cell of $CsPb_2Br_5$ along the X, Y and Z. We measured PL at ambient to investigate the luminescence properties of $CsPb_2Br_5$. The PL spectrum of $CsPb_2Br_5$ shown in Figure 6.2b suggests strong emission ~ 519 nm, which corresponds to the green region in visible spectra. The origin of the narrow spectral width lies in the uniformity of size, shape, and composition. The absence of any abnormality related to the emission band

spectra substantiates the near band-edge emission of $CsPb_2Br_5$ in the registered spectra. The FESEM image (Figure 6.2c) discloses sheet

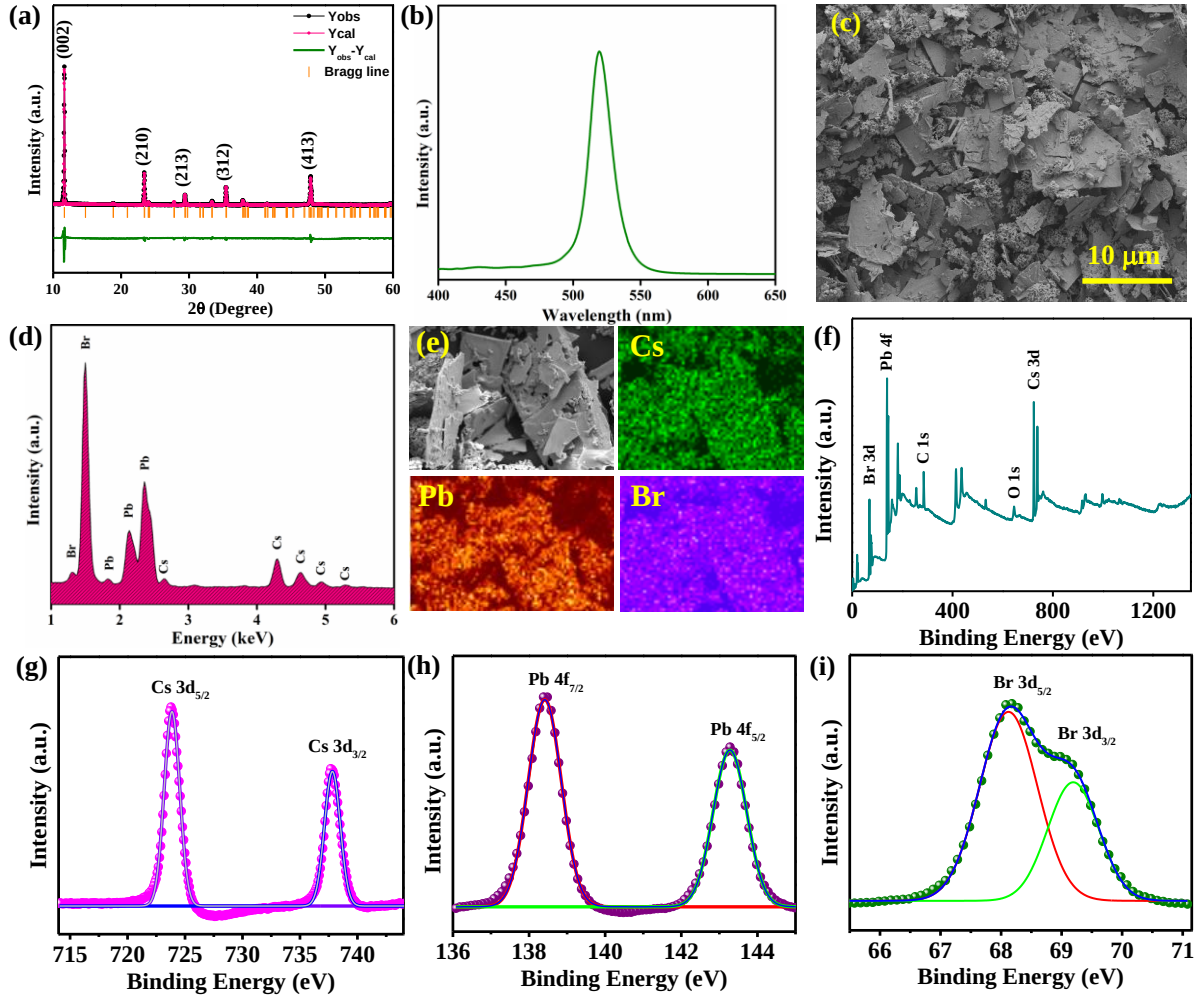

Figure 6.2: (a) XRD and Rietveld refinement, (b) PL spectra, (c) FESEM, (d) EDX and (e) elemental mapping of $CsPb_2Br_5$. (f) XPS survey scan of $CsPb_2Br_5$, core level XPS spectra of (g) Cs, (h) Pb, and (i) Br.

like structures, with a size of 5–6 μm. This image also confirms morphological uniformity on a large scale. EDX analysis is used to determine the elemental composition of the sample. Elemental compositions using EDX suggest only being of Cs, Pb and Br (Figure 6.2d). The atomic ratio ~12:25:63 of the constituent elements matches well with actual stoichiometry.

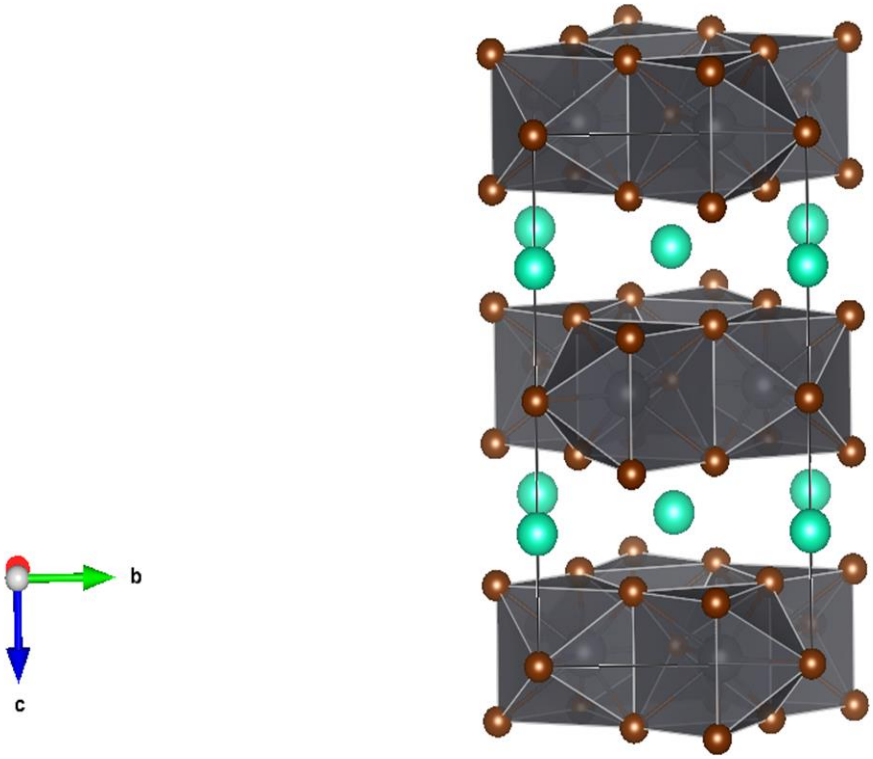

Figure 6.3: Crystal structure of the $CsPb_2Br_5$.

No impurity element-related peaks in EDX spectrum validate the pure phase and corroborate the XRD results. Elemental mapping of $CsPb_2Br_5$ demonstrates homogenous distributions of Cs, Pb, and Br (Figure 6.2e).

XPS is used to analyse the surface composition of the sample as well as the oxidation states of its constituent parts. The binding energies were charge-corrected to the reference value of the C 1s peak at 284.6 eV. The survey scan of $CsPb_2Br_5$ is presented in Figure 6.2f. It suggests the existence of peaks related to the constituent elements. High-resolution spectra of the component elements, Cs, Pb, and Br, are shown in Figure 6.2g-i. Peaks at 737.8 and 723.8 eV in the Cs 3d spectrum (Figure 6.2g) match to Cs $3d_{3/2}$ and Cs $3d_{5/2}$, separately. The 1^+ oxidation state of Cs in $CsPb_2Br_5$ is confirmed by this finding. Two peaks can be seen in Figure 6.2h, at 143.3 and 138.4 eV for Pb $4f_{5/2}$ and Pb $4f_{7/2}$, respectively. It verifies that the oxidation state of Pb is 2^+. Figure 6.2i shows fitted peaks of the Br 3d at 68.1 and 69.2 eV, which are related to the Br $3d_{5/2}$ and Br $3d_{3/2}$, respectively. According to this positioning, Br is in

oxidation state 1^-. Thus, XPS signals show that each of the constituent elements is in its typical oxidation state [21–23].

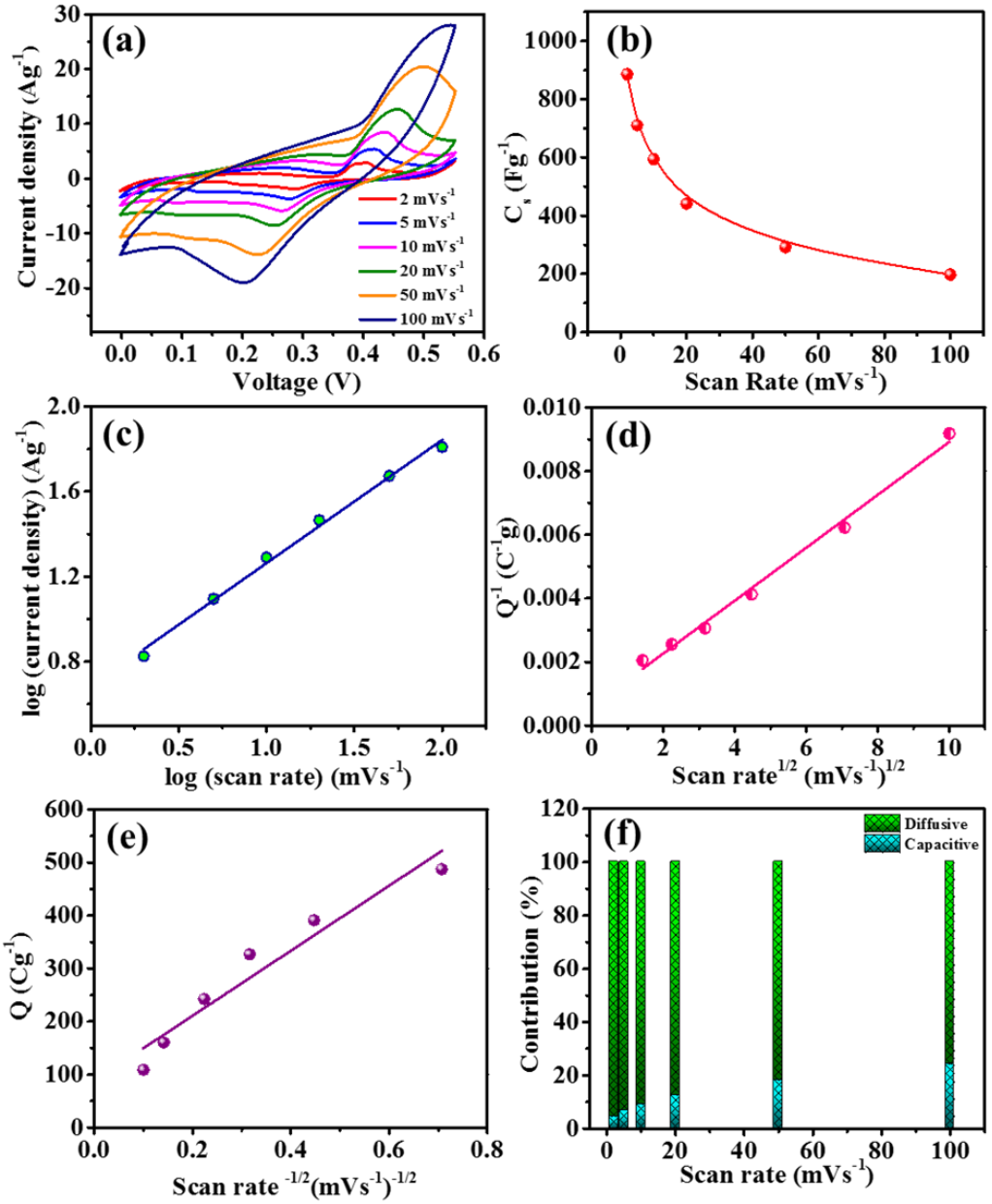

Figure 6.4: (a) CV, (b) C_s variation at different scan rate, (c) log (current density) vs. log (scan rate). Variation in (d) Q^{-1} and (e) Q with respect to $(\text{scan rate})^{-1/2}$ and (f) capacitive contribution of $CsPb_2Br_5$ electrode.

The electrochemical study of $CsPb_2Br_5$ was performed in a three-electrode system in a 1 M aqueous KOH electrolyte. Within the potential range of 0 to 0.55 V, CV curves (Figure 6.4a) were measured at various scan rates spanning from 2 to 100 mVs^{-1}. It is observed that the

electrode material shows significant faradic activity. Based on the CV curve pattern, the origin of the peaks could be attributed to the K^+ ion intercalation/de-intercalation via the following reaction:

$$CsPb_2Br_5 + xK^+ + xe^- \leftrightarrow CsPb_2Br_5Kx$$

The prominent redox peaks at lower scan rates could be attributed to the accessibility of K+ ions at the electroactive surfaces of the electrode for a sufficiently longer period. It is also observed that the specific current values are increased with increase of scan rates suggesting the outstanding supercapacitive behaviour of the electrode material. The electrode's specific capacitance (C_s) was estimated using the preceding equation:

$$C_s = \frac{Q}{V} = \frac{\int I(V)dV}{\Delta V \times \upsilon \times \Delta m}$$

The region under the CV curve is indicated here by the symbol $\int I(V)dV$. υ is the scan rate. Potential window range, voltage, and mass of the working electrode are each represented by (mV/s), ΔV (V), and Δm (g), respectively. Maximum value of C_s for $CsPb_2Br_5$ is found 886 Fg^{-1} at 2 mVs^{-1}. The difference in C_s values as a function of scan rate is depicted in Figure 6.4b and corresponding values are presented in Table 6.1.

Table 6.1: Specific capacitance variation with respect to scan rate.

Sample	Scan rate (mV/s)	Specific capacitance (F/g)
$CsPb_2Br_5$	**2**	**886**
	5	**711**
	10	**594**
	20	**441**
	50	**292**
	100	**198**

The logarithmic plot of the electrode's current density vs. scan rate follows power law: $i_p=a\upsilon^b$. Here, i_p is the cathodic peak current density. Scan rate is denoted by υ. Here, “a” and “b” are two adjustment parameters. “a” and “b” are the intercept and slope of the curve presented in Figure 6.4c. A value of “b” equal to 1 indicates capacitive charge-storage, whereas a value of "b" equal to 0.5 denotes diffusion-induced charge storage (Figure 6.4c). The assessed value of "b" is 0.58, confirming the presence of a combined charge-storage mechanism. This charge-storage mechanism of the $CsPb_2Br_5$ can be written as: $Q= Q_s + Q_d$. The term “Q_s” refers to the total charges induced, which generated electrostatically as a result of the double layer formation at the interface. Charges due to the ion diffusion process in the electrode are denoted by “Q_d”. The total charge obtained from the Q^{-1} vs $\upsilon^{1/2}$ plot (Figure 6.4d) is 1648.87 Cg^{-1}. Simultaneously, the outer charge contribution (Q_s) is 88.43 Cg^{-1}, evaluated from Q vs $\upsilon^{-1/2}$ plot (Figure 6.4e). These values indicate that reversible redox reactions (94.6%) dominate the overall C_s of the $CsPb_2Br_5$ electrode. The quantitative contribution of capacitive and diffusion control processes at various scan speeds is shown in Figure 6.4f. The aforesaid processes were calculated following the equation:

$$I(\upsilon)=k_1\upsilon +k_2\upsilon^{1/2}$$

where $I(\upsilon)$ is total redox current and $k_1\upsilon$ *and* $k_2\upsilon^{1/2}$denotes for capacitive and diffusion-controlled response. It implies that capacitive contribution increases with scan speeds, which is attributed to both fast electron transport into the electrode and small ion diffusion.

Figure 6.5a presents galvanostatic charge-discharge (GCD) profiles of the electrode as a function of current densities. The decay curve's nonlinearity is explained by the following variables: i) Internal resistance (IR)-induced IR drop; ii) electrochemical double layer action-induced linear portion; and iii) reversible electrochemical activities-induced curved section [13,24]. Specific capacitance was assessed from GCD, following the equation:

$$C= \frac{i\Delta t}{m\Delta V}.$$

Where the symbols for discharge current i (A) and discharge time Δt (s) correspondingly. The potential window range is denoted by ΔV (V), and the active mass of the electrode is denoted by m (g). The maximum C_s value is 495.6 Fg^{-1} at 1 Ag^{-1}. The variation in C_s values at different current densities is presented in Figure 6.5b and Table 6.2. This figure confirms a good agreement between GCD and CV values and is well in accord with Figure 6.4b. Cycling stability for SCs was tested by performing GCD for multiple cycles (Figure 6.5c). Going through 1200 cycles at different current densities, C_s still recovers its initial capacitance value fully, which suggests high cyclic stability of the electrode. The frequency range employed in the Electrochemical Impedance Spectroscopy (EIS) investigation was 0.01 -10^5 Hz. A. C. amplitude was fixed at 5 mV (Figure 6.5d). This plot well fits an equivalent circuit (inset of Figure 6.5d). The corresponding values of the fitted parameters are provided in Table 6.3.

Table 6.2: Specific capacitance variation with respect to current density.

Sample	Current density (Ag^{-1})	Specific capacitance (Fg^{-1})
CsPb2Br5	1	495.6
	2	370.7
	4	259.0
	5	223.4
	8	176.0

Table 6.3: Equivalent circuit parameters.

Component	Value
	$CsPb_2Br_5$
R_{el} (Ω)	**0.51**
R_s (Ω)	**1.91**
R_{ct} (Ω)	**4.1**
W_s (Ω $S^{-1/2}$)	**19.45**
W_k (Ω $S^{-1/2}$)	**13.57**
C_s (F)	**0.23×10^{-15}**
C_{dl} (F)	**1.2×10^{-3}**
C_{int} (F)	**231.3**

Nomenclature of parameters:

R_{el} = active electrolyte resistance

R_s = equivalent series resistance

R_{ct} = charge transfer resistance

W_s = diffusion impedance in parallel

W_k = diffusion impedance in series

C_s = geometrical capacitance

C_{dl} = double layer capacitance

C_{int} = intercalated capacitance

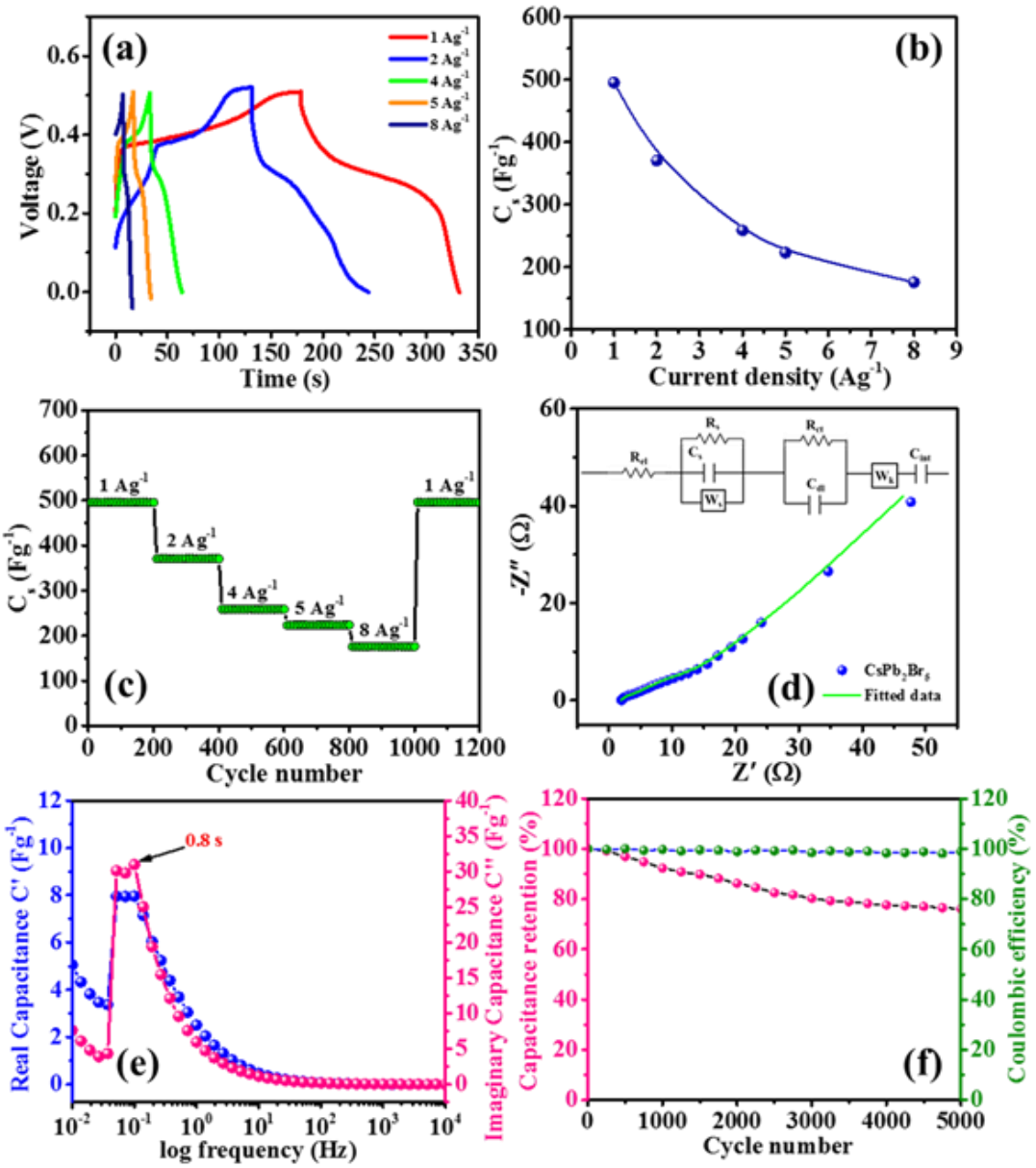

Figure 6.5: (a) GCD curve (b) C_s variation at different current density, (c) cycling stability curve at gradually varied current density, (d) EIS spectra, (e) C'(ω) and C''(ω) vs. log (frequency), (f) Columbic efficiency and retention capacity of $CsPb_2Br_5$.

For more insights on capacitive behaviour, C'(ω) and C''(ω) are plotted against frequency (Figure 6.5e). The equation for a system's total impedance is $Z(\omega) = Z'(\omega) + Z''(\omega)$, where Z'(ω) and Z''(ω) are the electrode material's real and imaginary impedances, respectively.

The total a.c. complex impedance is represented by the symbol Z(ω). Complex capacitance is as follows: $C(\omega) = C'(\omega) + C''(\omega)$

Here $C'(\omega) = \frac{Z''(\omega)}{\omega|Z|^2}$ and $C''(\omega) = \frac{Z'(\omega)}{\omega|Z|^2}$. where C' stands for the complex capacitance's real component. This is considered as the system's capacitance and measured by GCD at a very low frequency. The above equation's C'' stands for the capacitance's loss component and is connected to energy loss during charging process [13,14]. The dielectric relaxation time constant (τ_0) is levelled here as the inverse of peak frequency (f_0). This is the amount of time it takes for a cell to go from a resistive state to a capacitive one [14]. The time takes to reach the value τ_0 is 0.8 seconds. The low τ_0 value suggests fast charging.

The frequency dependent complex power equation was used to further explore the dissipative nature: $S(\omega)=P(\omega)+j\ Q(\omega)$. In this equation $P(\omega) = \omega\ C''(\omega)\ |\Delta Vrms|^2$ and $Q(\omega) = -\omega\ C'(\omega)\ |\Delta Vrms|^2$. Here, active power is P(ω). The reactive power symbol is Q(ω). The power dissipation within the cell is represented by the normalised active power. When the frequency is increased ($\omega \rightarrow \infty$), the cell's behaviour changes from capacitive to resistive, resulting in such power dissipation. In fact, as frequency increases, the normalised Q(ω) values decrease (Figure 6.6a). Pure capacitive behaviour at low frequencies ($\omega \rightarrow 0$) led to such a reduction. In between two extreme frequencies, the cell oscillates. After an interval of 0.9 s, the cell switches its behaviour from capacitive to resistive. These values agree well with the τ_0 value, obtained from Figure 6.5e.

Long-term stability was further evaluated at 20 Ag^{-1} for 5000 cycles (Figure 6.5f). $CsPb_2Br_5$ electrode exhibited ~76% capacitance retention after 5000 cycles. Even after the same number of cycles, Columbic efficiency remained greater than 99%. Such stability and long life indicate its potential as an electrode material. The electrochemical performance of

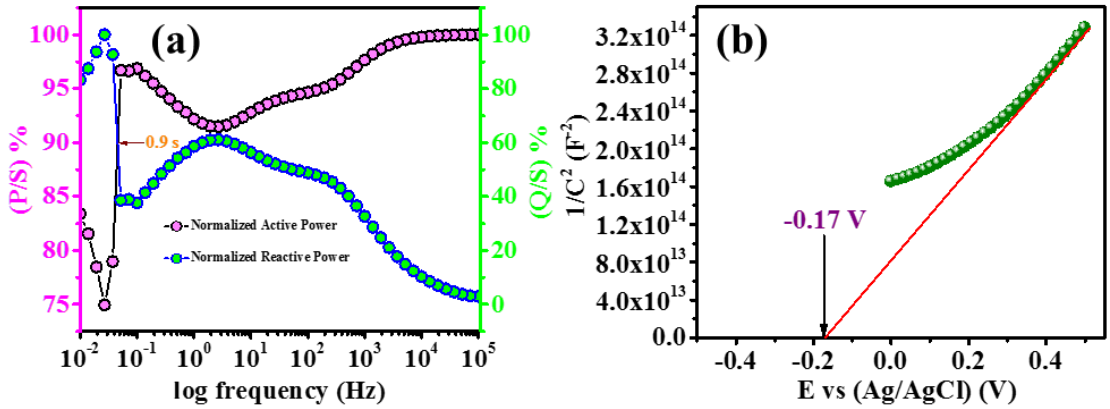

Figure 6.6: (a) Active power and reactive power vs log(frequency) and (b) Mott Schottky plot of the $CsPb_2Br_5$.

the electrode was further compared with previous perovskite-based reports, which suggest it has merit (Table 6.4).

The charge transfer mechanism of the junction capacitor can be easily understood by Mott-Schottky analysis. It illustrates how junction capacitance behaves in relation to applied bias. Here, 0.5 M Na_2SO_4 was used as the electrolyte in a three-electrode setup. The Mott-Schottky plot for the $CsPb_2Br_5$ electrode (Figure 6.6b) indicates n-type behaviour. Using this plot as a starting point, following equation is used to determine the Flat-band potential:

$$\frac{1}{C^2} = \frac{2}{\varepsilon\varepsilon_0 eA^2N_A}\left(V\text{-}V_{fb}\text{-}\frac{k_BT}{e}\right)$$

Here, C symbolizes for capacitance, while ε and ε_o stand for the material's respective dielectric constants and the permittivity of free space. Active surface area and donor density are abbreviated as A and N_A, respectively. V_{fb} is the flat band potential, while V denotes the applied potential. The Boltzmann constant, temperature, and elementary charge are each represented by the letters k_B, T, and e, respectively. The as measured flat band potential for $CsPb_2Br_5$, is ~ -0.17 V. The placement of the flat band potential on the negative side and the high donor density improved charge transfer across the interface, resulting in good electrochemical results.

Table 6.4: Electrochemical performance comparison of perovskite samples.

Perovskite sample	Scan rate/current density	Specific capacitance	Retention	References
$CsPbBr_{2.9}I_{0.1}$	0.1 mA cm^{-2}	150 mF cm^{-2}	88% (2000 cycle)	[25]
$CsPbI_3$	2 mV s^{-1}	7.23 mF cm^{-2}	65.5% (1000 cycles)	[26]
$La_{0.75}Sr_{0.25}Cr_{0.5}Mn_{0.5}O_3$	1 mV s^{-1}	751 F g^{-1}	79% (5000 cycles)	[27]
Y_2NiMnO_6	30 mA g^{-1}	77.76 F g^{-1}	70.17% (1800 cycles)	[28]
La_2CuMnO_6	0.25 A g^{-1}	205.5 F g^{-1}	78% (1000 cycles)	[29]
$La_{1-x}Sr_xMnO_3$	1 A g^{-1}	102 F g^{-1}	50% (5000 cycles)	[30]
$CsPb_2Br_5$	2 mV s^{-1}	886 F g^{-1}	76% (5000 cycles)	**Present work**

6.5. Conclusions

In conclusion, we have realized $CsPb_2Br_5$ via a facile chemical approach in ambient condition. The phase structure investigation and chemical composition is confirmed using XRD, XPS, and EDS. The PL spectrum of $CsPb_2Br_5$ suggests strong emission ~ 519 nm, which corresponds to the green region in the visible spectra, which, related to the emission band spectra substantiates the near band-edge emission of $CsPb_2Br_5$ in the registered spectra. The FESEM image discloses sheet-like structures, with a size of 5–6 µm. When $CsPb_2Br_5$ is used as a SC electrode material, it exhibits a specific capacitance value of 886 Fg^{-1} at 2 mVs^{-1}. The electrode retained ~76% of its original capacitance even after 5000 cycles. The interface of the $CsPb_2Br_5$ electrode plays a pivotal role in the charge storage process within the SC. Driven by these results, $CsPb_2Br_5$ can be used for advanced supercapacitor-based devices. We expect our

work will inspire others to adopt this high-yield synthesis technique for the realization of other inorganic perovskites and their usage in futuristic energy storage devices.

6.6. References

[1] Kojima A, Teshima K, Shirai Y, Miyasaka T. Organometal halide perovskites as visible-light sensitizers for photovoltaic cells. J Am Chem Soc 2009; 131: 6050–1.

[2] Paul T, Sarkar PK, Maiti S, Chattopadhyay KK. Multilevel programming and light-assisted resistive switching in a halide-tunable all-inorganic perovskite cube for flexible memory devices. ACS Appl Electron Mater 2020; 2: 3667–77.

[3] Paul T, Maiti S, Mukherjee U, Mondal S, Sahoo A, Chattopadhyay KK. Cube shaped FAPbBr3 for piezoelectric energy harvesting devices. Mater Lett 2021; 301: 130264.

[4] Shen W, Ruan L, Shen Z, Deng Z. Reversible light-mediated compositional and structural transitions between $CsPbBr_3$ and $CsPb_2Br_5$ nanosheets. Chemical Communications 2018; 54: 2804–7.

[5] Makani NH, Kumar P, Paul T, Maiti S, Sahoo A, Singh M, et al. Cathodoluminescence properties of phase pure low-dimensional Cs_4PbBr_6 perovskite and its stability under high-energy electron beams. MRS Commun 2022; 12: 1212–9.

[6] Hassan Y, Park JH, Crawford ML, Sadhanala A, Lee J, Sadighian JC, et al. Ligand-engineered bandgap stability in mixed-halide perovskite LEDs. Nature 2021; 591: 72–7.

[7] Siddik A, Haldar PK, Paul T, Das U, Barman A, Roy A, et al. Nonvolatile resistive switching and synaptic characteristics of lead-free all-inorganic perovskite-based flexible memristive devices for neuromorphic systems. Nanoscale 2021; 13: 8864–74.

[8] Mondal S, Maiti S, Paul T, Sahoo A, Bhattacharjee S, Das NS, et al. All-inorganic halide perovskite tuned robust mechanical-energy harvester: Self driven posture monitor and power source for portable electronics. Appl Mater Today 2022; 26: 101385.

[9] Paul T, Maiti S, Chatterjee BK, Bairi P, Das BK, Thakur S, et al. Electrochemical performance of 3D Network $CsPbBr_3$ perovskite anodes for Li-ion batteries: experimental venture with theoretical expedition. The Journal of Physical Chemistry C 2021; 125: 16892–902.

[10] Makani NH, Singh M, Paul T, Sahoo A, Nama J, Sharma S, et al. Photoelectrocatalytic CO2 reduction using stable lead-free bimetallic $CsAgBr_2$ halide perovskite nanocrystals. Journal of Electroanalytical Chemistry 2022; 920: 116583.

[11] Besra N, Sardar K, Maiti S, Sarkar PK, Paul T, Thakur S, et al. Incorporation of V_2O_5 nanorods into perovskite photodetectors as an alternative approach to enhance device performance: a step towards stability against ambient water species. Dalton Transactions 2020; 49: 15788–99.

[12] Sardar K, Thakur S, Maiti S, Besra N, Bairi P, Chanda K, et al. Amalgamation of $MnWO_4$ nanorods with amorphous carbon nanotubes for highly stabilized energy efficient supercapacitor electrodes. Dalton Transactions 2021; 50: 5327–41.

[13] Sardar K, Thakur S, Das A, Besra N, Banerjee D, Majumdar G, et al. Synthesis of different manganese tungstate nanostructures for enhanced charge-storage applications: theoretical support for experimental findings. Physical Chemistry Chemical Physics 2022; 24: 28271–82.

[14] Thakur S, Maiti S, Sardar K, Besra N, Bairi P, Panigrahi K, et al. New class of trimetallic oxide hierarchical mesoporous array on woven fabric: electrode for high-performance and stable battery type ultracapacitor. J Energy Storage 2021; 35: 102249.

[15] Chanda K, Maiti S, Sarkar S, Bairi P, Thakur S, Sardar K, et al. Hierarchical assembly of MnO_2 nanosheet on $CuCo_2O_4$ nanoflake over fabric scaffold for symmetric supercapacitor. ACS Appl Nano Mater 2021; 4: 1420–33.

[16] Ma L, Sun G, Ran J, Lv S, Shen X, Tong H. One-pot template-free strategy toward 3D hierarchical porous nitrogen-doped carbon framework in situ armored homogeneous NiO nanoparticles for high-performance asymmetric supercapacitors. ACS Appl Mater Interfaces 2018; 10: 22278–90.

[17] Vijayakumar S, Ponnalagi AK, Nagamuthu S, Muralidharan G. Microwave assisted synthesis of Co_3O_4 nanoparticles for high-performance supercapacitors. Electrochim Acta 2013; 106: 500–5.

[18] Chanda K, Thakur S, Maiti S, Acharya A, Paul T, Besra N, et al. Hierarchical heterostructure of MoS_2 flake anchored on TiO_2 sphere for supercapacitor application. AIP Conf Proc, vol. 1953, AIP Publishing; 2018.

[19] Yao S, Xing L, Dong Y, Wu X. Hierarchical WO_3@ $MnWO_4$ core-shell structure for asymmetric supercapacitor with ultrahigh cycling performance at low temperature. J Colloid Interface Sci 2018; 531: 216–24.

[20] Dursun I, De Bastiani M, Turedi B, Alamer B, Shkurenko A, Yin J, et al. $CsPb_2Br_5$ single crystals: synthesis and characterization. ChemSusChem 2017; 10: 3746–9.

[21] Paul T, Sarkar PK, Maiti S, Sahoo A, Chattopadhyay KK. Solution-processed light-induced multilevel non-volatile wearable memory device based on $CsPb_2Br_5$ perovskite. Dalton Transactions 2022; 51: 3864–74.

[22] Sahoo A, Paul T, Maiti S, Banerjee R. Temperature-dependent dielectric properties of $CsPb_2Br_5$: a 2D inorganic halide perovskite. Nanotechnology 2022; 33: 195703.

[23] Sahoo A, Paul T, Makani NH, Maiti S, Banerjee R. High piezoresponse in low-dimensional inorganic halide perovskite for mechanical energy harvesting. Sustain Energy Fuels 2022; 6: 4484–97.

[24] Pandit B, Dubal DP, Gómez-Romero P, Kale BB, Sankapal BR. V_2O_5 encapsulated MWCNTs in 2D surface architecture: complete solid-state bendable highly stabilized energy efficient supercapacitor device. Sci Rep 2017; 7: 43430.

[25] Ng CH, Lim HN, Hayase S, Zainal Z, Shafie S, Lee HW, et al. Cesium lead halide inorganic-based perovskite-sensitized solar cell for photo-supercapacitor application under high humidity condition. ACS Appl Energy Mater 2018; 1: 692–9.

[26] Maji P, Ray A, Sadhukhan P, Roy A, Das S. Fabrication of symmetric supercapacitor using cesium lead iodide ($CsPbI_3$) microwire. Mater Lett 2018; 227: 268–71.

[27] Rehman ZU, Raza MA, Tariq A, Chishti UN, Maqsood MF, Lee N, et al. $La_{0.75}Sr_{0.25}Cr_{0.5}Mn_{0.5}O_3$ perovskite developed for supercapacitor applications. J Energy Storage 2020; 32: 101951.

[28] Alam M, Karmakar K, Pal M, Mandal K. Electrochemical supercapacitor based on double perovskite Y_2NiMnO_6 nanowires. RSC Adv 2016; 6: 114722–6.

[29] Singh J, Goutam UK, Kumar A. Hydrothermal synthesis and electrochemical performance of nanostructured cobalt free La_2CuMnO_6. Solid State Sci 2019; 95: 105927.

[30] Lang X, Mo H, Hu X, Tian H. Supercapacitor performance of perovskite $La_{1-x}Sr_xMnO_3$. Dalton Transactions 2017; 46: 13720–30.

Chapter 7: Grand conclusion of Thesis & Future Prospect

7.1 Grand conclusion

The important conclusions of this dissertation will be covered in this chapter. The primary areas of interest in this thesis include transition metal-based semiconductors, their hybrids with carboneous materials such as amorphous carbon nanotubes (aCNTs), and perovskite materials for energy-related applications. The application of electrochemical energy to supercapacitors has focused on the use of electrodes made of

(i) $MnWO_4$-aCNT hybrid,

(ii) $MnWO_4$ nanostructures with varying aspect ratios, and

(iii) $CsPb_2Br_5$ perovskite.

Thus, the following summarises the significant discoveries of these works:

- Using a straightforward, cost-effective procedure, $MnWO_4$-aCNT hybrid was successfully developed with a good yield. The aCNTs were first synthesised using a low temperature solid state approach before being grafted with $MnWO_4$ nanorods using an in situ hydrothermal process. CV, GCD, and EIS experiments were performed on the electrodes made from aCNT, $MnWO_4$, and $MnWO_4$-aCNT. The CV measurement of all manufactured electrodes revealed that the $MnWO_4$-aCNT sample had the highest specific capacitance of 542.18 Fg^{-1} at a scan rate of 2 mVs^{-1}. Even after 15,000 cycles of operation, the $MnWO_4$-aCNT based electrode in the three-electrode system demonstrated a high-rate capacity with around 100% capacitance retention and approximately 100% coulombic efficiency. This hybrid demonstrated better electrochemical behaviour than either of the separate building blocks by combining the benefits of aCNT's EDLC with the pseudocapacitive properties of secondary produced $MnWO_4$ nanorods. Surface area, electron transport method, and electrolyte diffusion were used to study significant changes in electrochemical performance. With the use of

polymer gel electrolyte (PVA/KOH), activated carbon, and $MnWO_4$-aCNT hybrid, the ASC device has been further developed. In accordance with the current density of 1 Ag^{-1}, the apparatus produced an energy density of 5.6 Wh kg^{-1} at a power density of 893.6 W kg^{-1}. It was confirmed that the device had high capacitance retention since, even after 6000 long cycle runs, it retained around 100% of its initial capacitance. The ASC devices worked in both series and parallel configurations to power commercial red LEDs and rotate a small motor fan without the need for an external battery connection.

- With a straightforward, cost-effective, low-temperature hydrothermal technique, we have effectively created $MnWO_4$ nanostructures with varying aspect ratios and high yields. The samples were examined using XRD, FESEM, HRTEM, XPS, TGA, and BET analysis as they were prepared. The electrodes made from the MnWO4 samples as-developed were analysed using CV, GCD, and EIS. Extensive research was conducted on the electrochemical performance based on surface area, electron transport mechanism, and electrolyte diffusion. As can be observed, the sample that was produced for the longest period of time exhibits the best electrochemical findings, with a high capacitance retention of almost 94% after 10,000 cycles and a maximum specific capacitance value of 455.07 Fg^{-1} at a scan rate of 2 mVs^{-1}. To learn more about the charge transfer process at the electrode-electrolyte interface, a Mott Schottky study was performed. This suggests that the contact has n-type semiconducting character. DFT simulations provide theoretical insight into the experimental results. Excellent charge storage performance of the as synthesised $MnWO_4$ is ensured by the improved quantum capacitance and the existence of electronic states near Fermi level.
- $CsPb_2Br_5$ has been produced in ambient conditions using a simple chemical method. XRD, XPS, and EDS are used to confirm the phase structure analysis and chemical composition. In relation to the emission band spectra, the PL spectrum of CsPb2Br5

indicates significant emission at ~ 519 nm, which correlates to the green region in the visible spectra and supports the near band-edge emission of $CsPb_2Br_5$ in the registered spectra. Sheet-like nanoforms of 5-7 µm in size are visible in the FESEM image. The specific capacitance value of $CsPb_2Br_5$ at 2 mVs^{-1} is 886 Fg^{-1} when utilised as a SC electrode material. Even after five thousand cycles, the electrode still had roughly 76% of its initial capacitance. The interface of the $CsPb_2Br_5$ electrode plays an important role in the charge storage process within the Supercapacitor.

7.2 Future Prospect

This thesis includes a detailed investigation of transition metal-based materials such as $MnWO_4$ nanostructures with varying aspect ratios, as well as hybrids with carbonaceous materials such as aCNT and perovskite materials such as $CsPb_2Br_5$, for use in energy production and storage. However, there is still a lot of room for improvement in terms of device construction, the use of appropriate composite materials, and so on. The optical properties of a material can be optimised through shape and morphological tuning, which can have positive effects on applications such as photodetectors, sensors, and photocatalysis. In addition to these, we are developing a self-powered gadget that integrates energy harvesting and storage. Supercapacitors will be charged by the energy stored in the piezoelectric driven nanogenerator. Because MTMOs, perovskites and their hybrid with carbon nanomaterials have more advantages than TMOs, such as improved electrical and electronic conductivity and a synergistic impact from the addition of additional ions, we have selected them as a possible option for supercapacitors. These semiconductors can also be combined with other carbon nanomaterials, perovskite-based compounds, conducting polymers like polypyrrole or polyaniline, and other materials to form new hierarchies and composite materials that can be used to make supercapacitor electrodes and other energy applications like electrochemical HER, ORR, and OER, Na- or Li-ion batteries, etc. of course. Finally, but as important, all of

these research projects must be properly planned for and supported by operational laboratory equipment and supplies. As we move forward with these endeavours, we have already seen some exciting outcomes, which we expect to share soon along with a thorough explanation.

Phd Thesis

ORIGINALITY REPORT

4%

SIMILARITY INDEX

MATCH ALL SOURCES (ONLY SELECTED SOURCE PRINTED)

★S. Thakur, S. Maiti, K. Sardar, N. Besra, P. Bairi, K. Panigrahi, K. Chanda, T. Paul, K.K. Chattopadhyay. "New Class of Trimetallic Oxide Hierarchical Mesoporous Array on Woven Fabric: Electrode for high-Performance and Stable battery type Ultracapacitor", Journal of Energy Storage, 2021 3%

Crossref

EXCLUDE QUOTES	ON	EXCLUDE SOURCES	< 1%
EXCLUDE BIBLIOGRAPHY	ON	EXCLUDE MATCHES	< 10 WORDS